



University Library

Author/Filing Title *SHARAF, A.M.*

.....
Class Mark *T*

**Please note that fines are charged on ALL
overdue items.**

--	--	--

0403604494



**Investigation of All-Wheel-Drive Off-Road Vehicle
Dynamics Augmented by Visco-Lock Devices**

By

AL-Hossein Mostafa Sharaf


BSc , MSc

A thesis submitted in partial fulfilment of the requirements for the award of the degree
Doctor of Philosophy of Loughborough University

**Wolfson School of Mechanical and Manufacturing Engineering
Loughborough University**

November 2007



	
Date	19/12/08
Class	T
Acc No.	0403604494

*This Thesis Is Dedicated To MY Mother and
The Memory of My Beloved Father*

Abstract

A peculiarity of AWD off-road vehicles is that their behaviour depends not only on the total power, provided by the engine, but also on its distribution among the drive axles/wheels. In turn, this distribution is largely regulated by the drivetrain layout and its torque distribution devices. At the output of the drivetrain system, the torque is constrained by the interaction between the wheels and the soft soil. For off-road automotive applications, the design of drivetrain systems has usually been largely dominated by the mobility requirements. With the growing demand to have a multi-purpose on/off road vehicle with improved manoeuvrability over deformable soil, particularly at higher speed, the challenges confronting vehicle designers have become more complex.

The thesis presents a novel integrated numerical approach to assess the dynamic behaviour of all-wheel-drive vehicles whilst operating over deformable soil terrain. A full drivetrain system including all aspects of rotational inertial dynamics, friction, damping and stiffness properties is integrated within a fourteen-degrees-of-freedom vehicle model. For off-road simulations, the terra-mechanical phenomena between tyres and deformable soils has also been taken into account. The integration of all modules resulted in a fairly complex generic model which is implemented in the MATLAB/Simulink/SimDriveline environment.

In addition to the conventional mechanical torque distribution devices, particular attention has been paid to the modelling of various visco-lock devices, including the viscous couplings of shafts and visco-lock limited-slip differentials. In the present work, these devices are represented by fully parameterised physical models which capture the torque transmission mechanism represented by various thermodynamic, hydrodynamic, structural and mechanical modules. The characteristics of these devices can easily be altered so that comparisons can be made between different types. In addition, the influence of a wide range operating conditions, vehicle design parameters and tyre characteristics can also be made over various deformable soils. Both viscous shear and self-torque amplification (hump) have been considered. In order to validate the proposed modules of visco-lock devices, a test rig is devised. The results of the experimental work conform to those obtained from the numerical models.

A number of simulation studies, during longitudinal and cornering manoeuvres, are conducted to investigate the contribution of significant parameters. In addition, the influences of different drivetrain arrangements are presented. The obtained results delineated that both traction and cornering response of AWD off-road vehicles are highly affected by the way driving torque is distributed between axles/wheels. Also, It was demonstrated that, by appropriate selection of silicone fluid rheological properties, vehicle behaviour can be tuned in a simulation environment, avoiding time consuming and costly experimental procedures.

Keywords: 4x4 off-road vehicles modelling, terramechanics, AWD vehicle performance, viscous coupling, visco-lock devices, drivetrain dynamics.

Acknowledgements

Firstly I would like to thank my supervisors, Professor Homer Rahnejat and Mr. Paul King for their invaluable advice and encouragement during the course of my research.

I would like to gratefully acknowledge the Egyptian Ministry of Defence for the financial support extended to this research project.

I wish to express my gratitude to Dr. Sankar Mohan (Magna Powertrain) who greatly illuminated valuable aspects to me about the theory of rotary viscous coupling. I would like to extend special thanks to Dr. C. Harnisch and Dr. B. Lach (AESCO) for their technical support regarding the tyre model. I am deeply indebted to Mr. Heinrich Huchtkoetter (GKN Driveline) who supported me with all the required visco-lock differentials as well as the technical data to validate the numerical models.

A special word of thanks goes to Dr. George Mavros who made the whole PhD experience much more interesting and rewarding.

Finally, I would like to express my deepest gratitude to my wife Eman who allowed me to focus on my research through her love and looking after our sons Mohamed and Ahmed.

List of Contents

Abstract	I
Acknowledgements	II
List of Contents	III
List of Figures	IX
Nomenclature	XV
Glossary of Terms	XXXII

Chapter 1: Introduction

1.1 Research Overview.....	1
1.2 Problem Definition.....	2
1.3 Overall Aims and Objectives.....	4
1.4 Structure of the Thesis.....	5

Chapter 2: Review of Literature

2.1 Introduction.....	7
2.2 Mechanics of Wheel-Soil Interaction.....	7
2.2.1 Empirical Approach.....	8
2.2.2 Finite Element Method (FEM) Approach.....	9
2.2.3 Analytical Approach.....	11
2.3 Off-Road Vehicle Dynamic Simulation.....	19
2.3.1 Contribution of Wong (The Canadian School).....	20
2.3.2 Contribution of Crolla (The British School).....	22
2.3.3 Contribution of Schmid (The German School)	23
2.4 Torque Management Devices Implemented in AWD Vehicles.....	27
2.4.1 Mechanical Differential (Open and Locked).....	30

2.4.2	Clutch-Type LSD.....	31
2.4.3	Torsen LSD.....	32
2.4.4	Visco-Lock Devices.....	34
2.4.5	Electronically Controlled LSD.....	38
2.5	Driveline Dynamics of AWD Vehicles.....	41
2.5.1	Driveline Simulation Tools.....	41
2.5.2	AWD Vehicle Dynamics Augmented by Torque Management Devices	44
2.6	Conclusion of Review of Literature.....	49

Chapter 3: Theoretical Background

3.1	Soil Characterization for Numerical Modelling.....	53
3.1.1	Pressure-Sinkage Relationship.....	55
3.1.2	Shear-Stress Shear-Displacement Relationship.....	57
3.2	Off-Road Tyre Modelling.....	59
3.2.1	Main Features and Limitations.....	59
3.2.2	Rigid Wheel Model.....	60
3.2.3	Simulation of Elastic Tyres on Elastic/Plastic Soil	62
3.2.3.1	Elastic/Plastic Soil Model.....	62
3.2.3.2	The Substitution Circle Geometry Calculations.....	65
3.2.3.3	The Substitution Circle Angles Calculations.....	67
3.2.4	Ground Pressure and Reaction Force.....	68
3.2.5	Rolling Resistance.....	69
3.2.6	Drive Torque and Tractive Force.....	70
3.2.7	Lateral Forces.....	72
3.2.8	Tyre Aligning Torque.....	74
3.2.9	Slip Sinkage Effect.....	74
3.2.10	Multi-pass Effect.....	75
3.2.11	Influence of the Friction between Tyre and Soil.....	77
3.2.12	Influence of the Tyre Tread.....	78

3.3	Equations of Motion of the Vehicle's Body.....	80
3.3.1	General Motion of a Particle.....	80
3.3.2	Relative Transforms in Rigid-Body Kinematics.....	82
3.3.3	Kinematic Equations of the Vehicle Body.....	84
3.3.4	Dynamic Equations of Motion.....	88

Chapter 4: 4x4 Off-Road Vehicle Model

4.1	Physical Description of the Vehicle Model.....	95
4.2	Mathematical Derivation of the Vehicle Model.....	98
4.2.1	Sprung Mass Dynamics.....	98
4.2.2	Unsprung Mass Dynamics.....	101
4.2.2.1	Unsprung Mass Vertical Dynamics.....	101
4.2.2.2	Wheel Driving Speed.....	104
4.2.3	Tyre Forces and Moments.....	105
4.2.4	Inclined Road Surfaces.....	108
4.2.5	Aerodynamic Force.....	109
4.2.6	Vehicle and Tyre Kinematics.....	110
4.2.7	The Steering System.....	113
4.2.8	The Drivetrain Model.....	115
4.3	Numerical Simulation.....	122
4.4	Simulation Results and Analysis.....	124
4.4.1	Traction Analysis.....	125
4.4.1.1	Effect of Soil Shear Strength Properties.....	126
4.4.1.2	Effect of Tyre Inflation Pressure.....	128
4.4.1.3	Effect of Differential Lock.....	130
4.4.2	Handling Analysis.....	131
4.4.2.1	Steady State Handling Response.....	132
4.4.2.1.1	Static Weight Distribution Ratio.....	132
4.4.2.1.2	Soil Shear Strength Properties.....	135

4.4.2.1.3 Driveline Configurations.....	137
4.4.2.2 Transient State Handling Response.....	139
4.4.2.2.1 Step Steer Manoeuvre.....	139
4.4.2.2.2 Lane Change Manoeuvre.....	141
 Chapter 5: Tribo-Dynamics' Modules of Visco-Lock Devices	
5.1 General Considerations.....	145
5.1.1 Automotive Applications of Visco-Lock Devices.....	145
5.1.1.1 Viscous Transmission Device (VT).....	145
5.1.1.2 Viscous Control Device (VC).....	146
5.1.2 Strategies of Traction Control system.....	148
5.2 Rheology of Silicone Fluids.....	149
5.2.1 General Properties.....	149
5.2.2 Viscosity-Temperature Dependency.....	149
5.2.3 Viscosity-Shear-Rate Dependency.....	150
5.3 Mathematical Model of Viscous Shear Torque.....	152
5.3.1 Newtonian Fluid Model.....	152
5.3.2 Isothermal and Non-Newtonian Fluid Model.....	154
5.3.3 Adiabatic and Non-Newtonian Fluid Model.....	155
5.4 Mathematical Model of Self Torque Induced Amplification.....	158
5.4.1 Hydrodynamic Pressure Model.....	160
5.4.2 Thermal Energy Calculations.....	168
5.4.2.1 Compression of The Gas Phase.....	169
5.4.2.2 Compression of The Liquid Phase.....	171
5.4.3 Moments Due to Coulomb Friction.....	172
5.4.4 Structural Deformation of The Inner Plate Tab.....	173
5.5 Experimental Methodology.....	178
5.5.1 Rheological Measurements for the Silicone Fluid.....	178
5.5.2 Test Rig Design.....	182

5.5.2.1	Visco-Lock Differential Casing.....	182
5.5.2.2	Torque Unit Assembly.....	183
5.5.2.3	The Drive Unit.....	184
5.5.3	Measuring Instruments.....	186
5.5.3.1	Temperature Measurement.....	186
5.5.3.2	Speed Measurement.....	187
5.5.3.3	Torque Measurement.....	187
5.6	Results and Analysis.....	189
5.6.1	Visco-Lock Limited Slip Differential.....	189
5.6.2	Viscous Coupling.....	192

Chapter 6: Analysis of AWD Vehicle Dynamics Augmented by Visco-Lock Devices

6.1	Implementation of Visco-Lock Devices into Dynamic Drivetrain Model.....	196
6.1.1	Viscous Control Differentials with Equal Torque Distribution.....	196
6.1.1.1	Shaft-To-Carrier Layout	196
6.1.1.2	Shaft-To-Shaft Layout	198
6.1.2	Viscous Control Differentials with Non-Equal Torque Distribution.....	199
6.1.3	Permanent Wheel Drive with Viscous Coupling Transmission.....	201
6.2	Evaluation Criteria.....	205
6.2.1	Traction Criterion.....	206
6.2.1.1	Drawbar Pull Characteristics.....	206
6.2.1.2	Tractive Efficiency.....	209
6.2.2	The Handling Criterion.....	210
6.3	Result and Analysis.....	212
6.3.1	Different Drivetrain Configurations.....	212
6.3.2	Static Split Ratio of Driving Torque Distribution.....	218
6.3.3	Visco-Lock Device Tuning.....	222
6.3.3.1	Viscous Coupling (O-VC-O).....	223
6.3.3.2	Visco-Lock Limited Slip Differential (O-LSD-O).....	227

Chapter 7: Conclusions and Suggestions for Future Work

7.1 Achievement of Aims and Contributions to Knowledge..... 232
7.2 Overall Findings and Conclusions..... 234
7.3 Critical Assessment of Approach..... 236
7.4 Suggestions for Future Work..... 237

List of References..... 238

Appendix A: Numerical Simulation Parameters..... A-1

Appendix B: Measuring Instruments Specifications..... B-1

Appendix C: Publications..... C-1

List of Figures

Chapter 2

2.1 : Common Approaches Used to Study the Mechanics of Wheel-Soil Interaction.....	8
2.2 : Simulation of the Wheel-Soil Interaction using FEM (after Aubel, 1994).....	11
2.3 : Optional Models for the Contact Geometry Proposed by Schmid (1995).....	16
2.4 : Lateral Shear Displacement and Tyre Deformation (after Schwanghart, 1968).....	17
2.5 : Lateral Shear Displacement and Tyre Deformation (after Grecenko, 1969)...	17
2.6 : Lateral Shear Displacement and Tyre deformation (after Crolla and El-Razaz, 1987a).....	18
2.7 : ORIS Program Main Structure (after Ruff and Jakobs, 1993).....	25
2.8 : ORSIS Program Main Structure (after Harnisch et al., 2003).....	26
2.9 : 4WD Traction Control Strategies, adopted from (Mohan and Williams, 1995).....	29
2.10 : Principles of Open Differential Gearing, adopted from (Heisler, 2002).....	31
2.11 : Clutch Type Limited Slip Differential, adopted from (Dick, 1995).....	32
2.12 : Torsen Limited Slip Differentials, adopted from (Chocholek, 1988).....	33
2.13 : Viscous Coupling Characteristics, adopted from Taureg and Herrmann (1988).....	35
2.14 : Passive versus Electronically Controlled LSD (after Kinsey, 2004).....	39
2.15 : Torque Vectoring Differential (after Park and Kroppe, 2004).....	41

Chapter 3

3.1	: Basic Components of a Bevameter (after Wong, 1989).....	55
3.2	: The Pressure-Sinkage Relationship (after Ruff, 1997).....	56
3.3	: The Shear-Stress Shear-Displacement Relationship (after Ruff, 1997).....	58
3.4	: Principle of the Rigid Wheel Model, adopted from (Ruff, 1997).....	61
3.5	: Substitution Circle Approach (after Harnisch and Lach, 2002b).....	63
3.6	: Substitution Circle Approach (No Multi-pass) (after AESCO, 2005).....	64
3.7	: Substitution Circle Approach (Multi-pass) (after Harnisch et al. (2005).....	64
3.8	: Substitution Circle Geometry, adopted from (Harnisch, 2001).....	66
3.9	: Angles of the Substitution Circle, adopted from (Harnisch, 2001).....	67
3.10	: Rolling Resistances at High Slip Angles, adopted from (Harnisch, 2001).....	69
3.11	: Rolling Resistances at High Slip Angles, adopted from (AESCO, 2005).....	70
3.12	: Trajectory of a Point on Tyre Circumference, adopted from (AESCO, 2005).	71
3.13	: Calculations of the Lateral Forces (after AESCO, 2005).....	73
3.14	: Principle of the Aligning Torque Calculation (after Harnisch (2001)).....	74
3.15	: Principle of the Slip Sinkage Effect (after Ruff (1997)).....	75
3.16	: Principle of the Multi-pass Effect (after Ruff (1997)).....	76
3.17	: Tyre Tread Model (after Harnisch et al, 2003).....	78
3.18	: Computational Structure of AS2TM Off-Road Tyre Model Adopted from (Harnisch, 2001).....	78
3.19	: Motion of a Point as Sensed in the Global Frame of Reference.....	81
3.20	: Relative Transformation between two Inertial Frames of References.....	83
3.21	: Application of the Kinematic Equations on the Study of Vehicle Dynamics...	85

Chapter 4

4.1	: Vehicle Local, Wheels and Global/Fixed Frames of References.....	96
4.2	: 14-DOF 4x4 Off-Road Vehicle Model.....	97
4.3	: Two Degrees of Freedom Quarter-Car Model.....	101
4.4	: Driving Wheel Spin Degree of Freedom.....	104
4.5	: Gravitational Force Analyses for Inclined Road Surfaces.....	109
4.6	: Velocities Transformation at the Wheel Hub.....	110
4.7	: Ackerman Steering Corrections.....	113
4.8	: Mathematical Representation of 4x4 Drivetrain Model.....	116
4.9	: Development of 4x4 Drivetrain Model using SimDriveline.....	116
4.10	: 14-DOF 4x4 Off-Road Vehicle Simulink Model.....	123
4.11	: Traction Performance of the Baseline Vehicle Configuration.....	125
4.12	: Effect of Soil Shear Strength on Traction Performance.....	127
4.13	: Effect of Tyre Inflation Pressure on Traction Performance.....	129
4.14	: Effect of Differential Lock on Traction Performance.....	130
4.15	: Effect of Static Weight Distribution Ratio between Axles.....	134
4.16	: Effect of Soil Shear Strength Properties.....	136
4.17	: Steady State Handling Response for Different Driveline Configurations (Weight Distribution 40% on front axle – 60% on rear axle).....	138
4.18	: Transient Response of a Step Steer Input on Sand Soil at 60 km/h.....	140
4.19	: Transient Response of a Double Triangular Steering Input at 60 km/h.....	143

Chapter 5

5.1	: Viscous Transmission Devices (VT) in AWD Vehicles.....	146
5.2	: Configurations of the Viscous Control Devices (VC) in AWD vehicles.....	147
5.3	: Common Methods of Installing the Viscous Unit within Differential.....	147

5.4	: VC Traction Control Strategy, adopted from (Taureg and Herrmann, 1988)...	148
5.5	: Mathematical Model of Viscosity Shear Rate Dependency (after Tung and Linden, 1985).....	151
5.6	: Simplified Model of One Inner and Two Outer Plates.....	153
5.7	: Viscous Shear Torque for Different Levels of Modelling Assumptions.....	156
5.8	: Flow Chart of Calculating Steps of the Viscous Torque.....	157
5.9	: Effect of Inner Plate Axial Movement on the Viscous Shear Torque.....	158
5.10	: Model of Self Induced Torque Amplification (STA).....	160
5.11	: Effect of Core Temperature on Bulk Pressure and Air Voids %.....	170
5.12	: Coulomb Friction Torque Model.....	172
5.13	: Structural Deformation of the Inner Plate Tab Model.....	174
5.14	: General Algorithm of Viscous Coupling Simulation in STA Mode.....	177
5.15	: Silicone Fluid Rheology Measurements.....	180
5.16	: The AR1000 Rheometer.....	180
5.17	: Viscosity-Shear Strain Rate Dependency at Different Temperatures.....	181
5.18	: Viscosity-Temperature Dependency at Nearly Zero Shear Rate.....	181
5.19	: Visco-Lock Differential Casing Assembly.....	183
5.20	: Torque Unit Assembly.....	184
5.21	: The Drive Unit Main Components.....	185
5.22	: Temperature Measurements using Comark Microprocessor Thermometer.....	186
5.23	: Rotational Speed Measurements using Laser Rotational Vibrometer.....	187
5.24	: Torque Measurements using Datum Torque Transducer and Torque Log...	188
5.25	: Test Rig Arrangement with Instrumentations.....	188
5.26	: Time History of Numerical Simulation Result during Short Time of Period...	190
5.27	: Comparisons between the Numerical and the Experimental Results During Long Period of Time.....	190
5.28	: Shear Torque-Speed Characteristics (Model versus Experiment).....	191

5.29 : Temperature Effect on Torque capacity of the Visco-Lock Differential..... 192
5.30 : Self-Torque Amplification in Rotary Viscous Couplings..... 194

Chapter 6

6.1 : Viscous Control Differential with Shaft-To-Carrier Arrangement..... 197
6.2 : Viscous Control Differential with Shaft-To-Shaft Arrangement..... 198
6.3 : Viscous Control Differentials with Non-Equal Torque Distribution..... 200
6.4 : Permanent Drivetrain System with Viscous Coupling Transmission..... 202
6.5 : Traction Performance of the Vehicle Fitted with Viscous Coupling..... 204
6.6 : Viscous Coupling Operational and Torque Characteristics..... 204
6.7 : Physical Simulation Library of Visco-Lock Devices..... 205
6.8 : Concepts of Tractive Forces–Slip Characteristics Measurement..... 207
6.9 : Tractive Force–Slip Characteristics(Locked Centre Differential on Clay Soil) 208
6.10 : Variation of Tractive Efficiency with Drawbar Pull on Clay Soil..... 211
6.11 : Variation of Tractive Efficiency with Drawbar Pull on Loam Soil..... 211
6.12 : Effect of Drivetrain Layouts on Traction Performance on Clay Soil..... 217
6.13 : Effect of Drivetrain Layouts on Traction Performance on different Soil..... 217
6.14 : Effect of Drivetrain Layouts on Handling over Clay Soil at High Speed..... 218
6.15 : Effect of Static Split Ratio on Traction Performance on Clay Soil..... 219
6.16 : Effect of Static Split Ratio on Traction Performance on different Soils..... 220
6.17 : Effect of Static Split Ratio on Handling over Clay Soil at Low Speed..... 221
6.18 : Effect of Static Split Ratio on Handling over Clay Soil at High Speed..... 221
6.19 : Effect of Viscous Coupling Fluid Rheology on Traction on Clay Soil..... 223
6.20 : Effect of Viscous Coupling Fluid Rheology on Traction on Different Soils... 224
6.21 : Consequences of the Hump Mode on the Longitudinal Slip of the Tyres..... 226
6.22 : Consequences of the Hump Mode on the Distribution of the Tractive Forces. 226

6.23	: Effect of Viscous Coupling Fluid Rheology on Handling on Clay Soil.....	227
6.24	: Effect of Visco-Lock LSD Fluid Rheology on Traction on Clay Soil.....	228
6.25	: Effect of Visco-Lock LSD Fluid Rheology on Traction on Different Soils.....	228
6.26	: Effect of Mechanical Differential Locking on Handling Characteristics.....	230
6.27	: Effect of Visco-Lock LSD Fluid Rheology on Handling on Clay Soil.....	231

Appendix A

A-1	: Basic Dimensions of the Reference Vehicle.....	A-1
A-2	: Performance Limitations of the Reference Vehicle.....	A-2
A-3	: Suspension System Characteristics.....	A-4
A-4	: Engine Torque-Speed Characteristics.....	A-6
A-5	: Silicone Fluid Shear Properties at 25 °C (after Payer, 2006).....	A-11

Nomenclature

Chapter 2

- A : Empirical constant (Equation 2.23)
- a : Empirical constant (Equation 2.18)
- b : Tyre width, or width of rectangular plate or radius of circular plate
- b : Empirical constant (Equation 2.18)
- C : Apparent cohesion of the soil terrain
- C_f : Biased torque resulting from clutch type limited slip differential
- D : Wheel diameter
- D^* : Substitute circle diameter
- F_r : Thrust developed by the running gear of the vehicle
- f : Coefficient of dynamic friction
- f_o : Wheel sinkage (Figure 2.3)
- i : Shear displacement along a rigid rim
- i : Longitudinal slip
- j : Soil shear displacement
- j_x : Longitudinal shear displacement
- j_y : Lateral shear displacement
- K : Plastic soil deformation moduli
- K_C : Cohesive moduli of soil deformation
- K_r : Shear displacement at maximum shear stress
- K_w : Ratio of the residual shear stress to the maximum shear stress
- K_ϕ : Frictional moduli of soil deformation

Nomenclature

k	: Shear deformation modulus
l	: Tyre contact length (Figure 2.3)
m	: Slope of viscosity-shear strain relationship
N	: Normal load applied to clutch disc
N_1	: Ratio of the lug area to carcass area.
n	: Soil sinkage exponent (Equation 2.1)
n	: Number of slipping surfaces (Equation 2.17)
P_n	: Normal ground pressure
p_c	: Pressure due to carcass stiffness
p_i	: Tyre inflation pressure
p_L	: Pressure acting on the tyre lug
R_1	: Outer clutch disc radius.
R_2	: Inner clutch disc radius
R_m	: Motion resistance
r	: Wheel rolling radius or plate radius
r_1	: Outer plate inner radius
r_2	: Inner plate outer radius
S	: Gap between plates
T	: Shear torque transmitted by the viscous coupling
T_c	: Torque applied to the differential carrier gear
T_{FR}	: Friction torque
T_r	: Torque applied to the differential ring gear
T_s	: Torque applied to the differential sun gear
u_d	: Soil displacement gradient
V_j	: Velocity of a point on the tyre rim
W	: Tyre vertical weight

Nomenclature

x	: Tyre contact length
Z	: Number of working surfaces inside viscous coupling
z	: Sinkage
z_o	: Static sinkage (Figure 2.3)
α	: Lateral slip angle
β	: Silicone fluid filling ratio in rotary viscous coupling
$\dot{\gamma}$: Silicone fluid shear strain rate
$\dot{\gamma}_B$: Silicone fluid critical shear strain rate
Δn	: Differential speed between inner and outer plates
$\Delta\omega$: Differential speed between inner and outer plates
η_y	: Tread wall deformation
θ	: Angle of tyre/soil contact (Equation 2.7)
θ	: Temperature
θ_1	: Tyre initial contact angle (Equation 2.8)
θ_o	: Room or nominal temperature
μ	: Silicone fluid dynamic viscosity
ν	: Silicone fluid kinematic viscosity
ν_B	: Silicone fluid kinematic viscosity at critical shear rate
ν_θ	: Silicone fluid kinematic viscosity at any temperature
ν_{θ_o}	: Silicone fluid kinematic viscosity at room or nominal temperature
ρ	: Silicone fluid density
τ	: Shear stress at the tyre-terrain interface
τ_{\max}	: Maximum shear strength
ϕ_s	: Angel of soil internal shearing resistance
ω	: Wheel angular speed

- ω_c : Carrier gear angular speed
 ω_r : Ring gear angular speed
 ω_s : Sun gear angular speed

Chapter 3

- \mathbf{a}_p : Acceleration vector of point (P) in the local frame of reference
 b : Tyre width, or width of rectangular plate or radius of the circular plate
 b^* : Track-width (elliptical contact patch)
 b^{**} : Track-width (rectangular contact patch)
 C : Apparent cohesion of the soil terrain
 C_B : Soil stiffness
 \mathbf{c} : Position vector measured in the local frame of reference
 D : Wheel diameter
 D^* : Substitute circle diameter
 d_z : Moulds of the tyre into the ground ($d_z = f_0 + z_0$)
 \mathbf{e} : Position vector of a particle (P) with respect to the local frame
 F_H : Horizontal force at the wheel contact area
 F_R : Rolling resistance force
 F_{RE} : External rolling resistance force
 F_{RI} : Internal rolling resistance force
 F_U : Tyre circumferential force
 F_x : Thrust developed by the wheel (section 3.2)
 F_x : Projection of the force on the local frame of reference, x-axis (section 3.3)
 F_y : Lateral or side force (section 3.2)
 F_y : Projection of the force on the local frame of reference, y-axis (section 3.3)

- F_{y_1} : Lateral force induced by lateral shear stress in the contact patch
- F_{y_2} : Lateral force component due to a bulldozing effect
- F_z : Ground vertical reaction force (section 3.2)
- F_z : Projection of the force on the local frame of reference, z-axis (section 3.3)
- f : Tyre deflection
- f_0 : Maximum tyre deflection
- g : Gravitational acceleration
- $h(\vartheta)$: Lever arms of the rotational axis
- I_w : Wheel moment of inertia around its spinning axis
- I_{xx} : Roll moment of inertia of the vehicle body/sprung mass
- I_{xy} : Product moment of inertia of the vehicle body/sprung mass
- I_{yy} : Pitch moment of inertia of the vehicle body/sprung mass
- I_{yz} : Product moment of inertia of the vehicle body/sprung mass
- I_{zx} : Product moment of inertia of the vehicle body/sprung mass
- I_{zz} : Yaw moment of inertia of the vehicle body/sprung mass
- i : Tyre longitudinal slip
- j : Shear displacement
- $j_l(\vartheta)$: Local shear displacement in the longitudinal direction
- $j_y(\vartheta)$: Local shear displacement in the lateral direction
- $j_{y,\max}$: Maximum lateral shear displacement
- K : Module of plastic soil deformation
- K_C : Cohesive module of soil deformation
- K_r : Shear displacement at maximum shear stress
- K_w : Ratio of the residual shear stress to the maximum shear stress
- K_ϕ : Frictional module of soil deformation
- k : Shear deformation modulus

- L : Sum of moments about the local frame of reference (x-axis)
- L : Transformation or rotation matrix
- l : Tyre contact length
- M : Sum of the moments along the local frame of reference (y-axis)
- M_D : Drive torque at the wheel (from drivetrain system)
- M_U : Tyre circumferential torque
- M_x : Roll moment about the local frame of reference (x-axis)
- M_y : Pitch moment about the local frame of reference (y-axis)
- M_z : Tyre aligning torque (section 3.2)
- M_z : Yaw moment about the local frame z-axis (section 3.3)
- m : Mass
- N : Sum of the moments along the local frame of reference (z-axis)
- n : Sinkage exponent
- O_i : Origin of the global frame of reference
- O_j : Origin of the local frame of reference
- p : Normal ground pressure (section 3.2)
- p : Angular velocity about the local frame of reference (x-axis) (section 3.3)
- $P(z)$: Normal ground pressure distribution as function of soil sinkage
- $p(\vartheta)$: Normal pressure distribution as a function of soil/tyre contact angle
- $p_{in}(\vartheta)$: Normal pressure at the inlet contact point of the substitute circle
- $p_{out}(\vartheta)$: Normal pressure at the outlet contact point of the substitute circle
- $p_{el}(\vartheta)$: Ground pressure due to soil elastic deformation
- $p_{pl}(\vartheta)$: Ground pressure due to soil plastic deformation
- P_{max} : Pre-compaction pressure
- p_T : Ground pressure in the track (pre-compaction)
- q : Angular velocity about the local frame of reference (y-axis)

- R_i : Global/fixed frame of reference
- R_j : Local/moving frame of reference
- r : Angular velocity about the local frame of reference (z-axis)
- r_d : Dynamic rolling radius of the wheel
- s_i : Position vector of the origin (O_j) with respect to the global frame
- s_j : Position vector of the particle (P) with respect to the global frame
- T : Transformation matrix from local to global frame of reference
- U : Translational velocity projected on the local frame of reference, x-axis.
- u : Forwarded velocity of point P in the local frame of reference
- V : Velocity of a point on the rim (section 3.2)
- V : Translational velocity projected on the local frame, y-axis. (section 3.3)
- V_i : Vector of velocity of a point in the local frame of reference
- V_j : Vector of velocity of a point in the global frame of reference
- v : Lateral velocity of point P in the local frame of reference
- W : Translational velocity projected on the local frame of reference, z-axis.
- w : Vertical velocity of point P in the local frame of reference
- X : Sum of forces along the local frame of reference, x-axis. (section 3.3)
- x : Forwarded displacement of a point in local frame (section 3.3)
- x_G : Longitudinal distance of the C.G from the origin of the local frame
- x_i, y_i, z_i : Global/fixed frame of reference coordinates
- x_j, y_j, z_j : Local/moving frame of reference coordinates
- x_0, y_0 : coordinates of the substitute circle centre (section 3.2)
- Y : Sum of forces along the local frame of reference (y-axis) (section 3.3)
- y : Lateral displacement of a point in the local frame (section 3.3)
- Z : Sum of forces along the local frame of reference (z-axis) (section 3.3)
- z : Vertical displacement of a point in the local frame (section 3.3)

Nomenclature

- z : Sinkage (section 3.2)
- z_0 : Static sinkage
- $z_{0,1}$: Static sinkage without multi-pass assumption
- $z_{0,2}$: Static sinkage with multi-pass assumption
- z_{el}, z_{pl} : Elastic and plastic deformation of the soil respectively
- $z_{el,in}$: Soil elastic deformation at the inlet contact point of substitute circle
- $z_{el,out}$: Soil elastic deformation at the outlet contact point of substitute circle
- $z_{T,1}$: Depth of the track
-
- α : Tyre lateral slip angel
- Δz_{el} : Soil elastic deformation
- θ : Angular displacement about the local frame of reference (x-axis)
- \mathcal{G} : Wheel shear-angles at the substitute circle
- \mathcal{G}_1 : Tyre initial contact angle
- \mathcal{G}_{in} : Contact angle at the inlet contact point of the substitute circle
- $\mathcal{G}_{el,in}$: Inlet contact angle at the substitute circle (elastic tyre assumption)
- $\mathcal{G}_{el,out}$: Outlet contact angle at the substitute circle (elastic tyre assumption)
- μ_{ts} : Adhesion
- τ : Shear stress
- τ_{max} : Maximum shear strength of the soil
- φ : Angel of internal shearing resistance (section 3.2)
- φ : Angular displacement about the local frame (y-axis) (section 3.3)
- ψ : Angular displacement about the local frame of reference (z-axis)
- Ω : Rotational velocity vector of the local frame of reference
- ω : Rotational wheel speed
- $\dot{\omega}$: Rotational wheel acceleration

Chapter 4

A	:	Vehicle characteristic area (assumed to be the frontal area)
a, b	:	Longitudinal location of the body C.G. from front and rear axles
b	:	Soil damping coefficient (Equation 4.20)
b	:	Width of the rectangular plate, or radius of the circular plate
b_e, b_t	:	Damping rates at the engine and transmission sides of the clutch.
C	:	Apparent cohesion of the soil terrain
C_d	:	Coefficient of aerodynamic resistance
C_i	:	Shock absorber damping coefficient ($i = 1:4$)
D^*	:	Substitute circle diameter
F_a	:	Aerodynamics force due to air resistance
F_{D_i}	:	Soil damping force at each wheel
$F_{G_x}, F_{G_y}, F_{G_z}$:	Components of gravitational force relative to local frame system
F_H	:	Horizontal force at the tyre-soil contact area
F_n	:	Normal force applied to the clutch friction plates
F_{Rl}	:	Tyre internal rolling (flexing) resistance force
F_{s_i}	:	Suspension forces at each wheel ($i = 1:4$)
F_{U_i}	:	Wheel circumferential force ($i = 1:4$)
$F_{X_i}, F_{Y_i}, F_{Z_i}$:	Tyre force at the wheel hub relative to the wheel coordinate system
F_x, F_y, F_z	:	Total forces affecting the vehicle body sprung mass
$F_{x_i}, F_{y_i}, F_{z_i}$:	Tyre force relative to the local frame of reference system
g	:	Gravitational acceleration
h_G	:	Initial height of the local frame origin to the global frame
I_e	:	Mass moment of inertia of the engine and flywheel
I_{sh}	:	Mass moments of inertia of a shaft

Nomenclature

I_t	: Mass moments of inertia of the transmission system
I_{w_i}	: Wheel moment of inertia around its spinning axis ($i = 1:4$)
I_{xx}, I_{yy}, I_{zz}	: Mass moments of inertia of the vehicle body sprung mass
I_{xz}	: Product moment of inertia of the vehicle body sprung mass
i_D	: Differential gear ratio
i_G	: Gear ratios
$j_j(\theta)$: Local shear displacement in the longitudinal direction
K	: Module of plastic soil deformation
K_C	: Cohesive module of soil deformation
K_i	: Suspension spring stiffness ($i = 1:4$)
K_ϕ	: Frictional module of soil deformation
k	: Shear deformation modulus
k_{sh}, b_{sh}	: Shaft rotational stiffness and damping coefficient
M_e	: Engine torque (applied at the flywheel)
M_{cl}	: Torque transmitted by clutch
$M_{f_{max}}$: Maximum torque capacity of the clutch
M_l, M_{o_1}, M_{o_2}	: Longitudinal and the lateral driving torques across the differential
$M_{w_i}, M_{B_i}, M_{U_i}$: Wheel driving, braking and circumferential torque ($i = 1:4$)
M_x, M_y, M_z	: Roll, pitch and yaw moment, about the local frame of reference
m_{q_i}	: Quarter of the vehicle body or sprung mass ($i = 1:4$)
m_s	: Vehicle body or sprung mass
m_{w_i}	: Wheel unsprung mass ($i = 1:4$)
N_c	: Number of friction surfaces used by the clutch
n	: Sinkage exponent
\bar{n}_B	: Road surface profile or normal vector
p	: Normal ground pressure

Nomenclature

p, q, r	: Rotational velocities about local frame of reference coordinates
\mathbf{R}	: Relative transformation matrix
R_m	: Clutch effective torque radius
$\bar{\mathbf{r}}_1, \bar{\mathbf{r}}_2, \bar{\mathbf{r}}_3, \bar{\mathbf{r}}_4$: Position vector of wheels relative to the local frame of reference
r_1, r_2	: Inner and outer plate radius of the clutch plate
r_{d_i}	: Wheel dynamic rolling radius ($i = 1:4$)
$[\bar{\mathbf{r}}_{OL}]_G$: Position of the local frame origin with respect to the global frame
$[\bar{\mathbf{r}}_w]_G$: Position of wheel hub with respect to the global frame of references
t_f, t_{rr}	: Front and rear wheel track
U, V, W	: Translational velocities along local frame of reference coordinates
X_G, Y_G, Z_G	: Coordinates of global/fixed frame of reference
x_L, y_L, z_L	: Coordinates of local/moving frame of reference
z	: Vehicle body bounce
z	: Sinkage (Equation 4.95)
$z_{b_i}, \dot{z}_{b_i}, \ddot{z}_{b_i}$: Vertical displacement, speed and acceleration of the vehicle corners
z_{R_i}	: Surface height at each wheel with respect to the global frame
$z_{w_i}, \dot{z}_{w_i}, \ddot{z}_{w_i}$: Vertical displacement, speed and acceleration of the wheel centre
δ_i	: Steering angle applied at each wheel ($i = 1:4$)
η_G	: Gear efficiencies
\mathcal{G}	: Wheel-terrain contact-angle at the substitute circle
θ, φ, ψ	: Vehicle body roll angle, pitch and yaw angle
θ, φ, ψ	: Euler angles (calculated by Equations 63:65)
$\theta_e, \ddot{\theta}_e$: Flywheel angular displacement and acceleration
θ_R, φ_R	: Road inclination and camber angles
μ_s, μ_k	: Kinetic and static coefficients of friction

$\left[v_{x_i}, v_{y_i} \right]_L$: Longitudinal and lateral velocities with respect to the local frame
$\left[v_{x_i}, v_{y_i} \right]_W$: Longitudinal and lateral velocities with respect wheel coordinates
ρ	: Air density
τ	: Shear stress
τ_{\max}	: Maximum shear strength of the soil
φ	: Angel of internal shearing resistance
$\omega_i, \dot{\omega}_i$: Wheel rotational speed and acceleration
$\omega_l, \omega_o, \omega_{o_2}$: Longitudinal and the lateral rotational speed across the differential

Chapter 5

A	: Empirical constant (Equation 5.1)
A	: Active area of the plates
a	: Half width of inner plate tab
a, h_1, h_2	: Dimensions used to define tab deflected geometry (Figure 5.10)
b	: Half thickness of the inner plate tab
C_F	: Ratio of fluid volume to housing void volume at filling temperature
c_f	: Specific heat coefficient of the silicone fluid
c_c	: Specific heat coefficient of the viscous coupling core
dF	: Elementary force
F_C	: Coulomb friction force
G	: Modulus of rigidity
h	: Gap height or fluid film thickness
$(h \cdot A)_s$: Convection parameter for steel housing surface
$\left(\frac{kA}{\Delta x} \right)_s$: Equivalent conduction parameter through the housing
K_c	: Empirical conditional factor

Nomenclature

K_F	: Bulk modulus of the Silicone fluid
K_P	: Empirical factor due to the presence of holes and perforations
K_t	: Calculated geometry constant for plate tab deflection
L	: Inner plate tab length
l	: Inner plate tab width
M_{TC}	: Twisting moment on plate tab due to Coulomb friction effect
M_v	: Twisting moment on plate tab due to viscous shear effect
m	: Slope of the regression line BC at the high shear rates (Figure 5.5)
m_c	: Masses of the steel core (including the plates and the drum)
m_f	: Masses of the silicone fluid
$(mc)_c$: Thermal mass of the coupling core
$(mc)_s$: Thermal mass of coupling steel housing
n	: Number of tabs on the inner plate
P	: Bulk pressure inside the viscous coupling unit
P_1, P_2	: Pressure from inner plate side-1 and side-2 respectively
P_{1-2}	: Differential force across side-1 and side-2 on plate
p	: Hydrodynamic pressure (around the inner plate tab)
P_e	: Equivalent differential pressure
p_o	: Atmospheric pressure
P_t	: Net axial force exerted on the inner plate tab
Q	: Thermal energy
Q_1	: Energy conducted from the viscous coupling core into the housing
Q_2	: Energy convected by the air from the housing to the surrounding air
q_x	: Volume flow rate per unit depth in the x-direction
R	: Universal gas constant
r_i	: Outer plate inner radius

Nomenclature

r_2	:	Inner plate outer radius
r_3	:	Inner plate slot radius
S	:	Gap between inner and outer plates
S_1, S_2	:	Gap width between inner and outer plate from side-1 and side-2
T_C	:	Coulomb friction torque
T_T	:	Total torque transmitted by one cell of plates
T_V	:	Viscous shear torque
t_i	:	Inner plate thickness
U	:	Tangential or slider velocity
u, v, w	:	Fluid velocity components in X, Y, Z directions respectively
V_a	:	Volume of air inside the viscous coupling
V_f	:	Volume of the silicone fluid in its free state
V_{f_i}	:	Initial fill volume of silicone fluid
V_{F_o}	:	Volume of the silicone fluid at any temperature
V_h	:	Volume of the viscous coupling's housing at any temperature
V_{h_i}	:	Initial volume of the viscous coupling housing
V_{h_o}	:	Volume of the viscous coupling's housing at any temperature
X, Y, Z	:	Tangential, axial and radial flow directions relative to the coupling unit
α	:	Coefficient line of thermal expansion
β_F	:	Coefficient volume of thermal expansion of the Silicone fluid
β_S	:	Coefficient volume of thermal expansion of the steel
$\dot{\gamma}, \dot{\gamma}_B$:	Shear strain rate and critical shear strain rate respectively
Δ	:	The net axial deflection of the tab tip
ΔP	:	Bulk pressure rise due incremental change in temperature
Δt	:	Time interval or step time

Nomenclature

$\Delta\mathcal{G}$:	Incremental change in temperature
δ	:	Inner plate tab inclination angle
δ_{ic}	:	Inner plate tab twisting angle due to Coulomb friction moment
δ_{tot}	:	Total twisting angle of the inner plate tab around its centroid
δ_{iv}	:	Inner plate tab twisting angle due to differential shear stress moment
η	:	Coefficient of Coulomb friction between plates
θ	:	Temperature
θ_a	:	Air temperature
θ_o	:	Nominal temperature
θ_s	:	Skin temperature
θ_i	:	Initial filling temperature
θ_f	:	Fluid temperature
μ	:	The dynamic viscosity at a specific temperature
μ_o	:	Dynamic viscosity at a nominal temperature and nearly zero shear rate
ν, ν_θ	:	Kinematic viscosity at any temperature
ν_o	:	Nominal kinematic viscosity (at room temperature)
\Re	:	Reynolds Number
\Re^*	:	Modified Reynolds' Number
\Re_h	:	Reynolds' Number defined for gap height
\Re_L	:	Reynolds' Number defined for tab length
ρ	:	Fluid density
τ	:	Shear stress
φ, ψ	:	Angles describing plate geometry
ω	:	Relative rotational speed between inner and outer plates

Chapter 6

F_d	:	Drawbar pull (force available at the drawbar)
I_F	:	Gear reduction of the front axle differential
I_{GB}	:	Gear box ratio
I_R	:	Gear reduction of the rear axle differential
i_f, i_r	:	Longitudinal slip at the front and rear axles respectively
J_F, J_R	:	Mass moment of inertia of the front and rear propeller shafts
K	:	Torque capacity of the viscous unit
M_{df}	:	Driving torque available at the front axle tyres
M_{di}	:	Driving torque available at the driven wheels
M_{dr}	:	Driving torque available at the rear axle tyres
M_E	:	Engine driving torque
P_d	:	Drawbar pull power
R_C, R_P	:	Radius of the carrier and pinion gears respectively
R_S, R_R	:	Radius of the sun and ring gears respectively
r_{di}	:	Dynamic rolling radius of the wheel ($i = 1:4$)
T_1, T_2	:	Torques applied at right and left axle (output from differential)
T_C	:	Input torque applied at the differential carrier through the ring gear
T_F, T_R	:	Torque applied to front and rear axles respectively
T_{GB}	:	Torque applied at gear box
T_{LF}	:	Torque applied at left front tyre
T_{LR}	:	Torque applied at left rear tyre
T_{RF}	:	Torque applied at right front tyre
T_{RR}	:	Torque applied at right rear tyre
T_V	:	Viscous shear torque transmitted by visco-lock devices

Nomenclature

V	:	Vehicle speed
ξ	:	Torque split ratio
ξ_{RS}	:	Ring-to-sun gear ratio
η_d	:	Tractive or driving efficiency
η_m	:	Motion efficiency
η_s	:	Slip efficiency
η_t	:	Transmission efficiency
$\sum_{i=1}^4 F_{xi}$:	Total tractive forces developed by the driving wheels
$\sum R$:	Total driving resistance
ω_1, ω_2	:	Rotational speed of the right and left axles (output from differential)
ω_C	:	Rotational speed of the differential carrier
ω_E	:	Engine rotational speed
$\omega_F, \dot{\omega}_F$:	Rotational speed and acceleration of the front axle tyres
ω_{GB}	:	Rotational speed of the output shaft of gear box
ω_{LF}	:	Rotational speed of the left front tyre
ω_{LR}	:	Rotational speed of the left rear tyre
ω_P	:	Rotational speed of the pinion gear
ω_R, ω_S	:	Rotational speed of the ring and sun gears respectively
$\omega_R, \dot{\omega}_R$:	Rotational speed and acceleration of the rear axle tyres
ω_{RF}	:	Rotational speed of the right front tyre
ω_{RR}	:	Rotational speed of the right rear tyre

Glossary of Terms

4WD	:	Four-Wheel Drive or (4×4)
ABS	:	Anti-Lock-Braking System
ADAMS	:	Automatic Dynamic Analysis of Mechanical Systems
AESCO	:	Automotive Engineering, Software & Consulting
AS ² TM	:	AESCO Soft Soil Tyre Model
AWD	:	All Wheel Drive
AWS	:	All Wheel Steering
BS	:	British Standard
DOF	:	Degree of Freedom
FEM	:	Finite Elements Method
FWD	:	Front Wheel Drive
HIL	:	Hardware in the Loop
HMMWV	:	High Mobility Multi-Wheeled Vehicle
IKK	:	Institute for Automotive Engineering
ISO	:	International Organization for Standardization
LAV	:	Light Armoured Vehicle
LSD	:	Limited Slip Differential
LSD-O-O	:	Visco-Lock Limited Slip Differential (front axle) – Open central differential – Open differential (rear axle)
LSD(SS)	:	Visco-Lock Limited Slip Differential (Shaft to Shaft) layout
LSD(SC)	:	Visco-Lock Limited Slip Differential (Shaft to Carrier) layout
MATLAB	:	MATrix LABoratory
NATO	:	North Atlantic Treaty Organization
NRMM	:	NATO Reference Mobility Model

NTVPM	:	Nepean Tracked Vehicle Performance Model
NWVPM	:	Nepean Wheeled Vehicle Performance Model
O-O-O	:	Open differential (front axle) – Open central differential – Open differential (rear axle)
O-L-O	:	Open differential (front axle) – Locked central differential – Open differential (rear axle)
O-VC-O	:	Open differential (front axle) – Viscous Coupling – Open differential (rear axle)
O-LSD-O	:	Open differential (front axle) – Visco-Lock Limited Slip Differential – Open differential (rear axle)
O-O-LSD	:	Open differential (front axle) – Open central differential – Visco-Lock Limited Slip Differential (rear axle)
ORIS	:	Off Road Interactive Simulation
ORSIS	:	Off Road Systems Interactive Simulation
PID	:	Proportional-Integral-Derivative controller
RTVPM	:	Rigid Tracked Vehicle Performance Model
RWD	:	Rear Wheel Drive
STA	:	Self-Torque Amplification
SUV	:	Sports Utility Vehicles
TACOM	:	Tank Automotive COMmand
TBR	:	Torque Bias Ratio
TCS	:	Traction Control System
TMD	:	Torque Management Devices
TORSEN	:	Torque Sensing
VDAS	:	Vehicle Dynamics Analysis Software
VENUS	:	Vehicle-Nature Simulation
WES	:	U.S. Army Waterways Experiment Station

Chapter 1: Introduction

1.1 Research Overview

Wheeled vehicles which are used in sports utility, military or by some emergency services have to fulfil several key requirements. One requirement concerns their mobility, which is defined as the ability of the vehicle to cope with arduous cross-country terrains. Unlike the prepared surfaces of solid infrastructure (referred to hereinafter as on-road or made roads), off-road terrains are characterized by deformable irregular surfaces with abrupt slopes and obstacles of distinctive nature. It is commonly recognized that, the interaction between wheeled vehicles and soft terrain is complex and strongly dominated by the terrain's mechanical properties. Furthermore, some soils can behave excessively in terms of sinkage and slippage according to the applied wheel normal load and driving torque.

The continual demand for improved mobility over an increasingly wider range of terrains has stimulated a great deal of interest in the field of drivetrain research. Originally, the concept of rigid four wheel drive was adopted such that both the front and rear axles were rigidly coupled to a transfer-case without a speed differential between them. While this layout offers a better tractive performance, serious problems may still arise on dry roads, especially during cornering manoeuvres. High wind-up torques in the drivetrain may occur, as well as severe tyre wear. The most common solution is to incorporate an ordinary open differential at both the front and rear axles and within the transfer-case itself in order to absorb shaft speed variations between the axles/wheels. In addition, for serious driving situations, these differentials can be manually locked. However, there are significant operational requirements in eliminating the manual intervention by employing permanent torque management devices, which would automatically adapt to the tyre-terrain conditions.

These aspects have emerged with the recent demands for multi-purpose on/off road vehicles, not only with a higher traction and acceleration potential, but also with

improved manoeuvrability over deformable soils. Although improving traction performance is a main consideration for off-road vehicle applications, the desired increase in mobility must be achieved without making any compromises regarding safety or ease of operation or driver comfort. Furthermore, for modern vehicles, handling behaviour is an important aspect which requires a potential to sustain high lateral accelerations, whilst maintaining a good level of directional stability.

With recent achievements in ride quality, which promotes unprecedented opportunity to increase vehicle speed over soft terrains, the challenges for vehicle designers have become more complex. Off-road vehicles can be more sensitive to these demands than passenger cars due to the basic requirement for high ground clearances and hence high centres of mass. Therefore, during cornering manoeuvres, large lateral weight transfers can cause significant changes in tyre-soil contact conditions such as sinkage and longitudinal slip, affecting lateral forces. Furthermore, the vehicle side-slip and yaw motion are dependent on, not only vehicle design parameters and tyre characteristics, but also on the mechanical properties of the terrain.

1.2 Problem Definition

With respect to the aforementioned requirements, it is obvious that the striking challenge is to design an efficient torque management device to optimally distribute the driving torque between the axles/wheels, not only for better traction performance, but also to achieve an acceptable cornering stability.

Over the years, it has been shown that, for off-road applications, the concept of all-wheel-drive propulsion offers better performance and improved mobility. Nowadays various components are available for AWD drivelines, including simple differentials, limited slip differentials through to fully electronically-controlled differentials.

To construct a driveline and achieve the desired vehicle performance, the designer is, therefore, confronted with a bewildering range of options. The relationships between vehicle body, drivetrain, suspensions, tyres, steering, terrain conditions, and so on, are

quite complicated for an AWD off-road vehicle. Therefore, employing numerical modelling techniques and simulation studies for such situations is unavoidable.

The prospective model should provide design engineers with the capability to investigate the effects of various components and aid future developments for control systems and automatic optimization of off-road 4×4 vehicles.

Over the past two decades, a considerable volume of research has been carried out to investigate 4×4 vehicle behaviour, fitted with different drivetrain configurations. However, the mechanism of tyre force generation was simply represented by empirical on-road tyre models and the road conditions were approximated and reduced to representation by a coefficient of adhesion. This approach should not be extended to off-road vehicles, because the interactions between pneumatic tyres and deformable soil are complex and include many effects such as sinkage, multi-pass and slip sinkage.

Among the wide variations of permanent AWD systems, visco-lock devices, including viscous coupling of shafts and visco-lock limited-slip differentials, are widely used. The elegant design and economical construction have attracted many designers to employ visco-lock devices, not only to fulfil torque split and transfer function, but also to act as self-controlling devices.

The choice of visco-lock devices for off-road vehicles has been largely dominated by terrain mobility requirements. With growing demands to improve off-road vehicle handling, these devices need to be tuned before installing in the vehicle. The tuning process involves reconditioning the device torque distribution characteristics, which in turn regulates tractive force distribution and contributes to the generation of significant yaw moments and tyre slip angles in a direct manner.

In reality, the selection and tuning of such devices are usually based on a trial and error approach, which is time consuming and can be prohibitively expensive. Moreover, the contribution of any empirical approach to the improvement of the existing knowledge on visco-lock devices would be rather limited.

Hitherto, there has been a lack of an integrated approach for implementation of visco-lock devices in a full vehicle simulation environment, especially for AWD off-road vehicles.

1.3 Overall Aims and Objectives

The aim and objectives of the present research follow directly from the problems stated in the preceding sections. A set of well-defined tasks have been performed and are outlined below:

- Development of a 14 DOF multi-physics numerical simulation model by integrating vehicle body dynamics, kinematics, vertical dynamics, and the terra-mechanical phenomena between elastic tyres and soft soils.
- Development of a complex 4×4 drivetrain model, which represents a full drivetrain system, incorporating all aspects of rotational inertial dynamics, friction, damping and stiffness properties.
- Integrating the drivetrain model with the vehicle dynamic model and carrying out a comprehensive investigation of traction and handling performance of 4×4 vehicles during typical manoeuvres under different operating conditions.
- Development of detailed tribo-dynamics' modules to numerically simulate different visco-lock devices, including viscous couplings of shafts and visco-lock limited-slip differentials. The mechanism of viscous-shear torque generation takes into account the rheology of silicone fluid, shear rate, temperature effect and the humping (Self-Torque-Amplification) phenomenon in rotary viscous couplings.
- Design and manufacture of a laboratory test rig to validate the derived tribo-dynamics' modules for different visco-lock devices.
- Integrating the tribo-dynamics' modules of different visco-lock devices with the overall vehicle multi-physics model.
- Carrying out an investigation to evaluate the tractive performance and cornering stability of AWD off-road vehicles, fitted with visco-lock devices, as well as ordinary drivetrain systems. Additionally, from point of view of traction performance and cornering stability, the tuning processes for visco-lock devices needed to be established in a numerical environment by altering the rheology of the silicone fluid.

The multi-physics modelling approach adhered to the following requirements:

- The model should be generic and appropriate for the simulation of a wide variety of conditions, including ride and handling tests. However, the main strength of the model should include detailed drivetrains for accurate prediction of tractive forces.
- Possibilities should exist for future incorporation of advanced control strategies and automatic optimization of off-road 4×4 vehicles. Furthermore, total control over the generation of model's equations should be provided in order to facilitate for implementation of an in-house written code.
- Implementation on a PC with a common programming language environment (MATLAB, Simulink), so that the model applications can be widely accessible.
- The concepts of modularity, flexibility, and user-friendliness should be emphasized during model development.

1.4 Structure of the Thesis

The work is organised in seven chapters. A brief description of the issues discussed in each chapter is given below, in order to provide an overview of the approach followed in the thesis.

CHAPTER 1 : INTRODUCTION

The future challenges for off-road AWD vehicles are briefly highlighted. As a result, the aim and objectives of the investigations are clearly stated and a brief description for the research framework is outlined.

CHAPTER 2 : REVIEW OF LITERATURE

An in-depth review of the state of the art in the field of AWD off-road vehicle dynamics is presented. The review covers the aspects of mechanics of wheel-soil interactions, off-road vehicle simulation and various strategies for torque distribution control in AWD vehicles, particularly for visco-lock devices.

CHAPTER 3 : THEORETICAL BACKGROUND

This chapter presents the necessary theoretical background on terramechanics principles and the mechanism of tyre force generation over deformable soils. Additionally, some fundamental considerations about coordinate systems, rigid body motions in space and the implementation in vehicle dynamics are presented.

CHAPTER 4 : 4×4 OFF-ROAD VEHICLE MODEL

This chapter presents the mathematical derivations for a 4×4 off-road vehicle model, integrating the terramechanics of tyre-soil contact, the vehicle body dynamics, and suspension and drivetrain systems. Different simulations are carried out, based on standard test manoeuvres, to investigate 4×4 vehicle traction performance and handling characteristics under typical operational conditions.

CHAPTER 5 : TRIBO-DYNAMIC MODULES OF VISCO-LOCK DEVICES

This chapter presents detailed mathematical derivation of different tribodynamics' modules for visco-lock devices. Additionally, issues related to test rig design, instrumentations and results of measurements are discussed. Furthermore, experimental results for typical components are compared with the numerical predictions.

CHAPTER 6 : ANALYSIS OF AWD VEHICLE DYNAMICS USING VISCO-LOCK DEVICES

This chapter presents an overall investigation by numerical modelling, especially the results for the implementation of visco-lock devices in the overall vehicle model. Furthermore, the dynamic performance of AWD off-road vehicles, coupled with different drivetrain layouts, is addressed in terms of traction and directional stability. Additionally, the tuning process for visco-lock devices is presented using alternative silicone fluids.

CHAPTER 7 : CONCLUSION AND SUGGESTIONS FOR FUTURE WORK

This chapter summarises the major findings of the presented research. The main outcomes, a critical assessment of the approach undertaken, as well as some suggestions for future research work.

Chapter 2: Review of Literature

2.1 Introduction

This chapter describes previous work reported in the field of AWD off-road vehicle dynamics. In particular, the issues of off-road tyre modelling, off-road vehicle dynamic simulation, and various torque management devices implemented in AWD vehicles are reviewed. Attention is paid to the use of passive control visco-lock devices in AWD vehicles. The following sections critically analyse the most appropriate reported work, whilst a significant amount of supporting literature concerning, for instance, numerical methods for use in vehicle dynamics, or the modelling of tribo-dynamics' modules of visco-lock devices are referred to later in the thesis when dealing with these issues.

The review of literature is divided into the following areas, according to the specific topics discussed:

- (1) Mechanics of wheel-soil interactions (terramechanics).
- (2) Off-road vehicle dynamic simulation.
- (3) Torque management devices implemented in AWD vehicles.
- (4) Driveline dynamics of AWD vehicles.

2.2 Mechanics of Wheel-Soil Interaction

Since its invention nearly 5000 years ago, the wheel has played a crucial role in off-road transportation. One of the fundamental aspects in off-road vehicle studies is the mechanics of wheel-soil interaction. The interaction between pneumatic tyre and deformable soil is very complex and includes many effects such as sinkage, multi-pass and slip sinkage. The performance of a driven wheel is usually characterized by its thrust, resistance to motion, sinkage, slip, driving torque, and angular speed. Accurate predictions of these parameters are of prime interest to all designers of off-road vehicles.

In recent years, a variety of methods have been proposed to study the interactions of pneumatic tyres with deformable soils (Wong, 1989). They range from entirely empirical approaches to highly theoretical ones, figure 2.1. In this section, the main features of some of the well-known off-road tyre models are highlighted. As a result of evaluation, an appropriate off-road tyre model is subsequently selected to be employed in the present research.

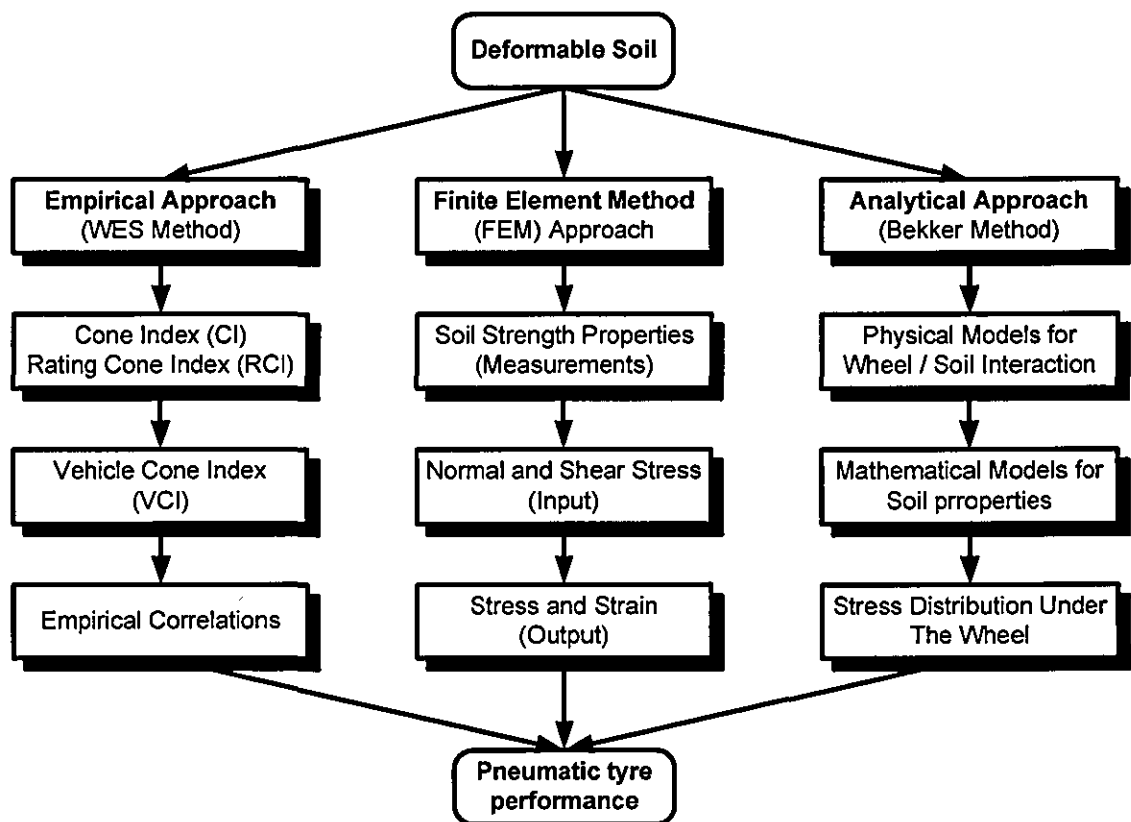


Figure 2.1 Common Approaches Used to Study the Mechanics of Wheel-Soil Interaction

2.2.1 Empirical Approach

This approach is best exemplified by the work of U.S. Army Waterways Experiment Station (WES, 1973). The method was first introduced during the Second World War in order to support the military with a simple and quick means to measure terrain mobility, based on a ‘go/no go’ basis. The WES method is based on the use of a standard cone in measuring the soil penetration resistance to describe the soil properties and the wheel

numeric based on some tyre variables to describe the wheel characteristics. The models, describing the wheel performance are developed from field, and therefore this method is considered to be worthy for in-situ decision-making during tactical missions (Wong, 1989).

On a higher level of sophistication, the NATO Reference Mobility Model '*NRMM*' (Ahlvin and Haley, 1992), including the WES philosophy, is useful for mission planning. The NRMM is a set of equations and algorithms that predict a particular vehicle's performance in a prescribed terrain, based on the vehicle attributes and the terrain properties. The main prediction module considers a combination of vehicle, terrain, and weather conditions in order to determine the maximum possible speed versus the resisting force characteristics at which the vehicle can operate. The primary prediction target of NRMM is the vehicle's 'speed-made-good' (i.e. effective maximum speed) per terrain unit. Thus, speed predictions and limiting force calculations can be determined for on-road, off-road, and obstacle crossing manoeuvres.

In 1992, WES and TACOM (Tank Automotive Command) developed '*NRMM-II*' to include enhanced mobility algorithms, a better organised modular structure and a more flexible user interface (Sullivan, 1999). NRMM-II is used to determine on-road/off-road platform mobility characteristics, e.g. to predict vehicle speeds over terrains, often used to compare two vehicles over a given terrain. Predictions are made using terrain characteristics (e.g., soil strength, vegetation, slope, roughness), vehicle attributes (e.g., tractive effort curve, weight, aerodynamic properties, dimensions), and scenario parameters (e.g., dry, wet, snow, sand). Traction, ride quality, and visibility are examples of speed limitations.

2.2.2 Finite Element Method (FEM) Approach:

Finite Element Method (FEM) was first introduced into the study of tyre-terrain interactions by Perumpral et al. (1970) in an attempt to predict the stress distributions and soil deformation with the soil mass under a tractor tyre. This method requires the geometry of the contact patch and the stress distributions on the tyre-soil interface to be

specified at the outset. It can only be used to analyse the strain, stress and displacement fields within the soil mass.

Yong et al. (1978) developed a model to study the stress and strain fields in the soil beneath the tyre using FEM. Their model described the tyre as a linear elastic body and the terrain as a piecewise linear elastic finite element. Normal and shear stress data were used as inputs and the length of the contact patch between the two elastic bodies was predicted using modified Hertzian theory. This model improved the prediction of the tyre-contact geometry, but it should be noted that if the normal and shear stress distributions at the tyre surface are known, the performance of the tyre is already defined.

Based on readily available information from the tyre manufacturers (generalised deflection, load, and contact area charts), Nakashima and Wong (1993) developed a finite element tyre model. The analysis procedures were used to determine two equivalent Young's moduli of elasticity for the tread and the side-wall.

Chen (1993) incorporated the Nakashima and Wong finite element tyre methodology into a tyre terrain model to study the effect of tyre slip-sinkage. The terrain was modelled using Bekker's semi-empirical normal pressure and shear stress equations. The tyre was assumed to rotate about its point of entry into the terrain as it experiences slip-sinkage. Thus, a well-matched slip sinkage was obtained from the wheel geometry and the rotational conditions. Furthermore, an equation was proposed to predict the slip sinkage, based on the data obtained during shear tests conducted at various normal loads.

Aubel (1994) developed the basis of a comprehensive FEM model called '*VENUS*', an abbreviation of '*VEHicle-NatUre Simulation*', see figure 2.2. The model consists of sub-modules for the soil, the tyre and the tyre-soil interaction. The soil was assumed to have elasto-plastic properties, with strength limits under tri-axial state of stress. Furthermore, in addition to simulating the frictional properties of the soils, the FEM-soil model was modified to consider the cohesive properties as well. The tyre was considered as three concentric rings (tread, carcass and wheel-rim), each of which as a homogenous medium with certain elastic properties. The interaction model considered the contact conditions,

especially during rolling with and without circumferential slip. The main output of the model was the deformation in both the soil and the tyre. Therefore, the shape of the contact area, sinkage, rolling resistance and circumferential force, as well as circumferential slip could be computed.

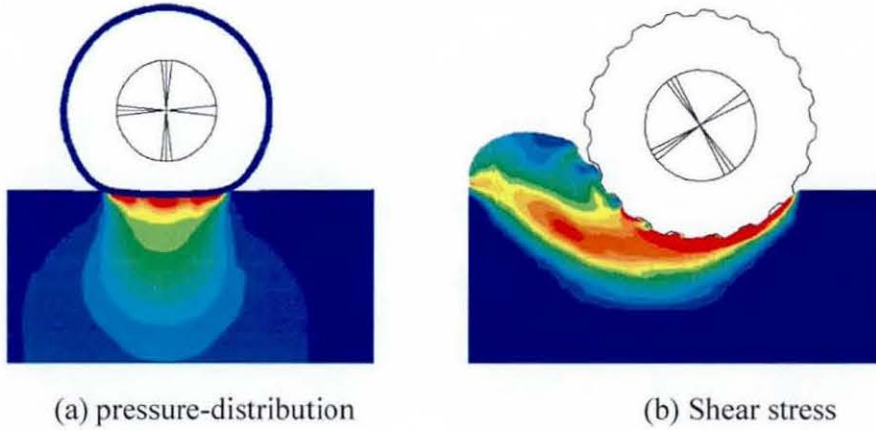


Figure 2.2 Simulation of the Wheel-Soil Interaction using FEM (after Auel, 1994)

2.2.3 Analytical Approach:

While providing little insight into the empirical and FEM approaches of wheel-soil mechanics, analytical (or semi-empirical) models have become very popular and are also computationally very effective. The work of some of the pioneers concerning analytical modelling of wheel-soil interaction is presented in text books by Bekker (1956, 1960, 1969) and Wong (1989, 2001).

In the early 1950's, Bekker proposed several analytical models of a pneumatic tyre operating over soft soil. He initially analysed a rigid tyre rolling over a deformable terrain. He assumed that the normal ground pressure (P_n) acting on the wheel rim, was equal to the pressure under a plate at the same sinkage (z). The derived semi-empirical equation is called the '*Bekker pressure-sinkage equation*', and represents the basis for most of the off-road analytical tyre models:

$$P_n = \left(\frac{K_C}{b} + K_\phi \right) \cdot z^n = K \cdot z^n \quad (2.1)$$

Where: (K_c, K_ϕ) are the cohesive and frictional moduli of soil deformation, (n) is the soil sinkage exponent, and (b) is the width of the rectangular plate, or the radius of a equivalent circular plate. Based on this assumption, Bekker developed a formula for predicting the resistance to the wheel motion (R_m) and its sinkage (z) as follows:

$$R_m = b \cdot K \cdot \frac{z^{n+1}}{n+1} \quad (2.2)$$

$$z = \left(\frac{3 \cdot W}{b \cdot (3-n) \cdot K \cdot \sqrt{D}} \right)^{\frac{2}{2n+1}} \quad (2.3)$$

Bekker found that satisfactory results from equations (2.2) and (2.3) could be obtained for moderate values of tyre sinkage $\left(z < \frac{D}{6} \right)$, where (D) is the wheel diameter and (W) is the vertical reaction of the terrain.

Later, Bekker developed an equation to define the critical inflation pressure at which the tyre may be considered to behave in elastic mode. According to this equation; if the sum of the inflation pressure (p_i) and the pressure produced by the stiffness of the carcass (p_c) is less than the pressure that the terrain can support at the lowest point of the tyre circumference, the terrain is considered to be firm and the tyre contact area would be flattened and could no longer be modelled as a rigid rim, see equation (2.4).

$$p_i = \frac{W \cdot (n+1)}{b \cdot \left(\frac{3 \cdot W}{(3-n) \cdot b \cdot K \cdot \sqrt{D}} \right)^{\frac{1}{2n+1}} \cdot \sqrt{D - \left(\frac{3 \cdot W}{(3-n) \cdot b \cdot K \cdot \sqrt{D}} \right)^{\frac{2}{2n+1}}} - p_c \quad (2.4)$$

Furthermore, Bekker proposed that the sum of (p_i) and (p_c) could be expressed by the average ground pressure. The average ground pressure at a specific tyre at a given normal

load and inflation pressure is equal to the normal load carried by the tyre divided by its projected ground contact area on a hard surface.

To characterize the soil shear strength properties, Bekker (1969) developed a test facility called 'Beviameter' device. This apparatus was used to obtain shearing torque versus displacement curves using a shear annulus head at various normal loads.

The well known "shear stress-shear displacement equation" proposed by Janosi and Hanamoto (1961) is widely used to fit the shearing torque-displacement data and predict the shear stress at the tyre-terrain interface by assuming the following simplified form:

$$\tau = (C + P_n \cdot \tan \varphi_s) \cdot (1 - e^{-j/k}) \quad (2.5)$$

It is observed that the first part of equation (2.5) is the basic Coulomb friction, consisting of two separate terms. The former corresponds to the apparent cohesion of the terrain (C) and referred to as the cohesive portion of the shear strength. The latter is due to the frictional portion of the shear strength ($P_n \cdot \tan \varphi_s$), where (φ_s) is the angle of terrain shearing resistance. (j) is referred to as shear displacement and (k) is the shear deformation modulus.

Later another modified equation was proposed by Wong and Preston-Thomas (1983) to describe the shear stress-displacement curve that displays a 'hump' of maximum shear stress and then decreases with increasing shearing displacement to a constant value of residual stress. Moreover, the procedure for applying the proposed equation, describing the shear stress-displacement relationship to the prediction of the thrust-slip relation of a vehicle running gear was also developed as:

$$\tau = \tau_{\max} \cdot K_r \left(1 + \left(\frac{1}{K_r \cdot (1 - 1/e)} - 1 \right) \cdot e^{-\frac{j}{K_w}} \right) \cdot \left(1 - e^{-\frac{j}{K}} \right) \quad (2.6)$$

Where (K_w) is equal to the shear displacement at maximum shear stress, (K_r) is the ratio of the residual shear stress to the maximum shear stress.

Wong and Reece (1966, 1967a, 1967b) developed a modified model of rigid wheel-soil interaction. Their model followed the Bekker's approach. An improved method was developed to predict the shear displacement (j) along a rigid rim, based on the consideration of the slip velocity of a point on the rim (V_j) as follows:

$$V_j = \omega \cdot r \cdot (1 - (1 - i) \cdot \cos \theta) \quad (2.7)$$

This resulted in an equation for the shear displacement (j) as a function of the tyre longitudinal slip (i) and the wheel rotational speed (ω) as follows:

$$j = \int_0^i V_j \cdot dt = \int_0^{\theta_1} \omega \cdot r \cdot (1 - (1 - i) \cdot \cos \theta) \cdot \frac{d\theta}{\omega} \quad (2.8)$$

They used the above equation (2.8) to enhance equation (2.6) for predicting the shear stress at the wheel-soil interface.

Based on the soil shear deformation, the shear stress (τ) can be calculated, consequently the thrust developed by the running gear (F_x) of a vehicle can be predicted by integrating the shear stress over the projected contact area, and tyre-terrain contact angles (θ, θ_1), where (b, D) are tyre width and diameter respectively.

$$F_x = \left(\frac{b \cdot D}{2} \right) \cdot \int_0^{\theta_1} \tau \cdot \cos \theta \cdot d\theta \quad (2.9)$$

Wong and Reece have shown that motion resistance is a function of slip and that the actual normal pressure distribution beneath a wheel has its peak value well forward of the tyre bottom centre and moving forward with increasing slip. They proposed a method to improve the prediction of the normal pressure beneath a wheel, when working on sand. They divided the normal pressure distribution into a front and rear region with the transition point being the peak pressure value. They used a separate equation to model each of these regions. An equation from experimental data was used to determine the

relation between the location of this peak and the amount of slip. Equations (2.2) and (2.9) were then used to determine the motion resistance and the thrust of the wheel. Their model gave better accuracy than that of Bekker's.

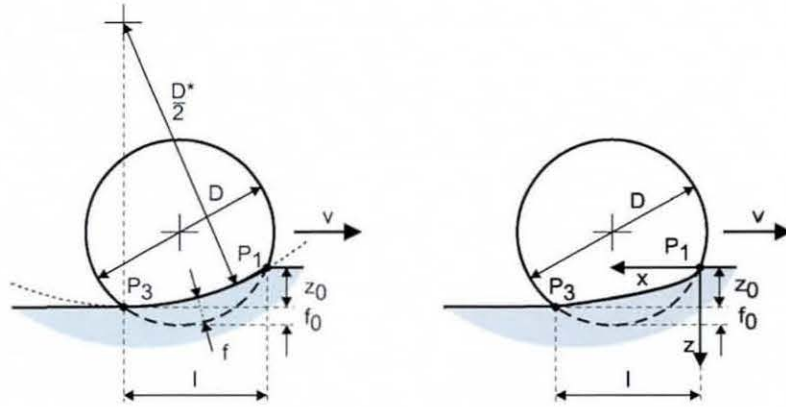
According to the value of the normal ground pressure beneath the wheel (P_n), Wong and Preston-Thomas (1986) developed another model to distinguish between rigid and elastic modes of a tyre operating on soft soil. Their approach was similar to that of Bekker's model and improved the operating mode predictions. Furthermore, they proposed that a transition sinkage boundary can be found by equating the nominal pressure with the average ground pressure, and then calculate the vertical reaction of the terrain. If this reaction is greater than the normal load, the tyre was assumed not to have sunk into the transition sinkage, and thus remained rigid. If the vertical reaction was less than the normal load, the tyre was assumed to have a certain amount of deflection, and thus could no longer be modelled as a rigid rim.

$$P_n = (N_1) \cdot p_L + (1 - N_1) \cdot p_c \quad (2.10)$$

Where (N_1) is the ratio of the lug area to the carcass area. (p_L, p_c) are the pressures acting on the lug and the carcass respectively.

Schmid (1995) presented an in-depth review of the state of the art in the field of tyre-terrain interaction. He summarised the results from ten years of research, which are presented in 34 papers and more than six doctoral theses carried out at the Institute of Automotive Engineering, (IKK), of the University of the Federal Armed Forces, Hamburg. In an attempt to improve the calculation of the tyre-terrain contact shape, Schmid and Ludewig (1991) proposed the assumption of a parabolic shape for the contour. The parabolic model approximates the circle-section (D^*) very closely, and allows a much more elegant mathematical treatment, because there is no necessity for cut-away terms in a mathematical form, as is in the case of a circular section, figure 2.3. The diameter of the substitute circle (D^*) is calculated from equilibrium condition between the vertical reaction force of the ground and the vertical reaction of the tyre. This equilibrium is obtained through an iteration process. The vertical reaction of the ground is

the result of numerical integration of the local pressures under the wheel. The tyre reaction force was computed from the measured tyre characteristics. Furthermore, they proposed an equation to calculate the tyre deformation on the flat road as a function of tyre inflation pressure.



(a) Surrogate-diameter model for the tyre (b) Parabolic model for the contact contour

Figure 2.3 Optional Models for the Contact Geometry Proposed by Schmid (1995)

While most off-road research has been devoted to the evaluation of tractive performance and mobility over unprepared area, there is a considerable volume of research to investigate the behaviour of pneumatic tyres over soft soil during cornering manoeuvres.

Schwanghart (1968) considered an un-driven off-road tyre with deep treads rolling on a soft terrain. He assumed that the total lateral displacement, resulted from components of tread wall deformation (η_y), soil deformation and shearing (j_y) as well as slip (α) after exceeding maximum soil deformation, figure 2.4. The governing equation was given as:

$$j_y + \eta_y = x \cdot \tan \alpha \quad (2.11)$$

Grecenko (1969) included both longitudinal slip and slip angle (α) to model the behaviour of an off-road tyre, subjected to combined longitudinal and lateral forces. The longitudinal shear displacement (j_x) is represented by an expression similar to the rigid track ($j_x = x_l$) the lateral shear displacement (j_y) is given by the following equation:

$$j_y = (x - j_x) \cdot \tan \alpha \tag{2.12}$$

Grecenko, also, introduced the soil displacement gradient (u_d) to remain constant along the contact length. The resultant shear stress ($j = u_d \cdot x$), where (u_d) is given as follows:

$$u_d = \sqrt{\left(1 - \frac{j_x}{x}\right)^2 \cdot \frac{j_y^2}{(x - j_x)^2} + \frac{j_x^2}{x^2}} \tag{2.13}$$

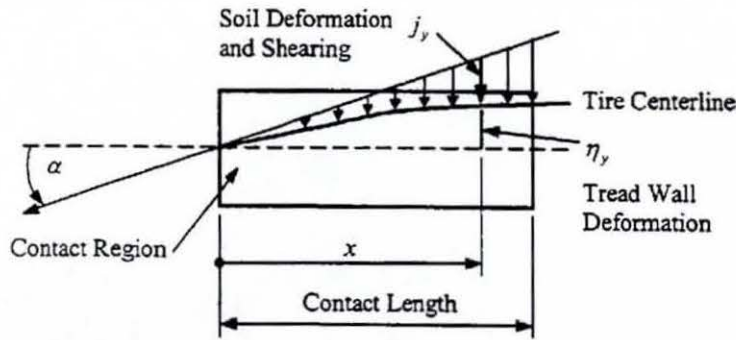


Figure 2.4 Lateral Shear Displacement and Tyre Deformation (after Schwanghart, 1968)

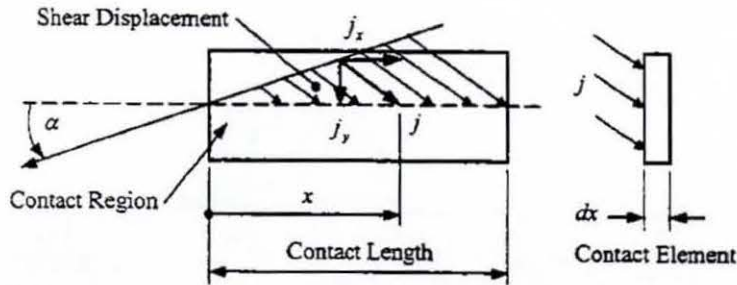


Figure 2.5 Lateral Shear Displacement and Tyre Deformation (after Grecenko, 1969)

Crolla and El-Razaz (1987a and 1987b) assumed that terrain is isotropic. Alternatively, the behaviour of the tyre in lateral shearing direction is similar to that in the longitudinal direction. They introduced separate terms for shearing deformation in the longitudinal

(j_x) and lateral (j_y) directions. Furthermore, the resultant shear displacement (j) is the vector sum of both of these as follow, figure 2.6.

$$j = \sqrt{j_x^2 + j_y^2} \quad (2.14)$$

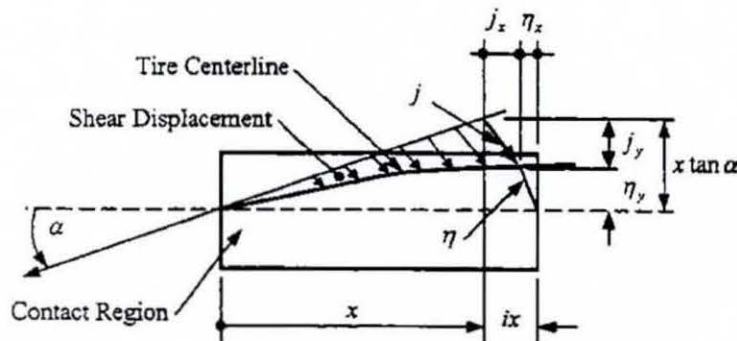


Figure 2.6 Lateral Shear Displacement and Tyre deformation
(after Crolla and El-Razaz, 1987a)

Based on a semi-empirical model for the lateral behaviour of off-road tyres, Metz (1993) found that the magnitude of the cornering stiffness for off-road tyre is reduced, because an additional lateral shearing displacement takes place. He considered this to be true, because the shear strength of soil is usually less than the friction between the tyre and dry pavement. Metz also indicated that, cornering stiffness and lateral force capability are half of the same tyre when on paved surfaces. Since the relationship between the shear stress and shear displacement for a deformable terrain is usually of an exponential form, Metz assumed the relation between lateral force and slip angle is also an exponential function.

Wu (2000) derived a new off-road tyre model for predicting tyre forces under combined longitudinal slip and slip angle deformation. The developed tyre model takes into account tyre lateral deformation, direction of slip velocity, contact trajectory, lateral bulldozing force, sidewall shearing, and terrain properties. The model predicts the relationship between the tyre lateral force and drawbar pull at different slip angles and tyre inflation pressure values in both cases of rigid and elastic modes.

Based on the research at the former Institute for Automotive Engineering (IKK) Harnisch (2001) developed a new off-road tyre model. His model is based on the substitution circle approach, described earlier. He calculated the lateral forces on soft soils, including the shear stress in the contact area, as well as a side component of the rolling resistance. Another improvement is the consideration of the elastic soil properties. With these additions the dynamic reactions of the vehicle to the topography of the environment and to the roughness of the soil can be simulated. These are mainly the vertical oscillations of the vehicle induced by uneven terrains. Furthermore, the deformation of the soft soil by the dynamic wheel loads is calculated, which results in a varying rut's depth and precompaction of the soil. Depending on speed and vehicle conditions this effect can lead to self-excitation of the vehicle by rut of the first wheel.

Furthermore, Harnisch et al. (2005) optimised the off-road tyre model for use in MATLAB/Simulink dynamics simulation environment (S-function). Currently, this tyre model is a commercially available software tool, which is called AS²TM (AESCO Soft Soil Tyre Model (AESCO GbR, 2005).

2.3 Off-road Vehicle Dynamic Simulation

The continual demand for improvement in vehicle mobility over a wider range of terrains and in many applications, such as in farming, forestry, military or in emergency operations has stimulated a great deal of interest in the simulation of vehicles over unprepared area. According to (Wong, 1989), generally, there are two objectives for off-road vehicle simulation:

- The first is to describe the behaviour of an off-road vehicle by functional relationships in terms of its design parameters, as well as soil mechanical properties. An accurate method of predicting off-road vehicle performance under different operating conditions is of prime interest to the designer and the users of off-road vehicles, e.g. (Ruff, 1997).
- The second objective is to study the change in terrain conditions caused by the passage of an off-road vehicle. This is of great interest to the agricultural engineers to evaluate soil compaction caused by farm vehicles, e.g. (Taylor and Burte, 1987).

Although various methods for analyzing tyre-terrain interaction and for predicting individual tyre performance have been in use for many decades, most of these have not been integrated into an appropriate procedure for predicting the dynamic performance of wheeled vehicles. The terramechanical phenomena between the pneumatic tyres and the deformable soil should be integrated into the dynamics of the vehicle. All the influential parameters, described thus far, should be included in an overall vehicle dynamic simulation study of off-road vehicles.

In this section, the main findings of some of the well known integrated off-road vehicle dynamics studies are reported. It should be mentioned that, all the previous research reported here are based on analytical (semi-empirical) approach of tyre-soil mechanics, which was originally introduced by Bekker (1956, 1960, 1969).

2.3.1 Contribution of Wong (The Canadian School)

Wong and Preston-Thomas (1986) developed a computer aided method for predicting the steady state tractive performance of multi-axle wheeled vehicles over unprepared terrains. The major features of their simulation model may be summarised as follows:

- The response characteristics of the terrain to repetitive loading were taken into account in predicting the sinkage and rut depth of different tyres.
- The dynamic load transfer between axles due to drawbar pull and gradient was taken into consideration.
- The effect of independent suspensions on the load distribution among axles was also taken into account.

Furthermore, these researchers used their computer simulation model for a parametric evaluation of the wheeled vehicle performance. The effects of tyre configuration, inflation pressure, and static load distribution over two types of terrain were investigated.

Wu (2000) investigated the handling characteristics of a six-wheel-drive (6WD) front-wheel-steering military vehicle on hard ground and on deformable soil. Based on a computer-aided simulation program called '*AUTOSIM*', a 17-DOF model to simulate

handling behaviour of off-road vehicles was developed. In comparison with the steady state handling behaviour on hard ground, the handling characteristics on deformable terrain demonstrated quite low tyre lateral forces and a considerable time-lag existed in the response with respect to the steering input.

Wong and Huang (2006a, 2006b) presented an investigation to compare the thrust developed by a multi-axle Light Armoured Vehicle (LAV, 8×8) with that of a tracked vehicle. Their investigation was carried out, based on various computer-aided simulation models for predicting wheeled and tracked vehicle performance, which were developed under collaboration with Vehicle Systems Development Corporation. These models, known as RTVPM, NTVPM and NWVPM, can be used to support vehicle designers and procurement managers in the selection of a suitable vehicle configuration for a given mission and environment from the traction performance viewpoint.

NTVPM '*Nepean Tracked Vehicle Performance Model*' was used for performance evaluation of vehicles with rubber-belt tracks or link tracks with relatively short-track pitch, commonly used in high-speed tracked vehicles, such as military vehicles (Wong, 1995, 1998a).

RTVPM, '*Rigid Tracked Vehicle Performance Model*' was used for performance evaluation of vehicles with link tracks having relatively long track pitch commonly in use in low-speed agricultural and construction tractors.

NWVPM, '*Nepean Wheeled Vehicle Performance Model*' is a comprehensive computer simulation model for performance evaluation of off-road wheeled vehicles. The major design parameters of the vehicle and of the tyre are considered. The computer model consists of two modules; the tyre module and the vehicle module. The tyre module predicts the operating mode of the tyre, normal and shear stress distributions on the tyre–terrain interface. The main outputs from tyre module are thrust, motion resistance and sinkage. The vehicle module takes into account the dynamic interaxle load transfer as well as the multi-pass effects. Terrain strength properties are presented in both vertical and horizontal directions, as well as its response to repetitive normal and shear loading.

2.3.2 Contribution of Crolla (The British School)

Crolla (1991) summarized his contributions over 20 years of research in the field of off-road vehicle dynamics. This includes more than 64 research papers covering the following aspects: analysis and improvement of off-road vehicle ride vibration using active suspension control, steering behaviour and lateral stability of tractor, braking, slope stability, tyre modelling, and power-take-off drivelines. The majority of these research works were devoted to automotive-agricultural applications like; the ride quality whilst moving on unprepared surfaces; the handling of the tractor and the combined tractor and trailer; and the vibration problems in a tractor power take-off unit. The following papers, from Crolla's contributions, which are related to the current topic, are highlighted here.

Crolla (1975) developed a computer program to simulate the field performance of an agricultural tractor operating under varying loading conditions. The predicted work-rates under dynamic and steady state conditions were compared. Several aspects of tractor design which influence dynamic performance were discussed and design criteria were suggested to control the variations in load caused by change in depth or soil resistance.

In an attempt to predict the tractor lateral response, while conducting off-road manoeuvres, Crolla and Hales (1979) produced a table summarising results obtained from various field measurements. This empirical process has led to some important concluding remarks. They found that, lateral forces were approximately related to the slip angle by an exponential relationship. Furthermore, the lateral force characteristic at small slip angles was found to be non-linear. Also, lateral force coefficient reduced with an increase in tyre vertical force and the presence of braking or tractive force reduced the lateral force. Compared to on-road tyres, they noticed that, at a given slip angle off-road tyres generate lower lateral force, the maximum value of which increases as tyre inflation pressure decreases, in a manner analogous to tractive force behaviour.

Crolla (1983a) proposed a 4-DOF mathematical model to examine the common problems concerning lateral stability of a tractor and a trailer combination, such as overturning and jack-knifing. Off-road tractor-trailer combinations were shown to exhibit similar

problems to their road vehicles counterparts; oversteer instability (at much lower speeds than the road vehicles) and the well-known jack-knife and trailer swing instabilities under braking conditions. The results indicated that weight distribution and tyre inflation pressure were dominant in determining the safe operating conditions.

Using the classical vehicle dynamics methods, Crolla and Horton (1983b) proposed appropriate methods to model the special features of off-road vehicle steering systems. Some of the special problems were addressed, including the role of tyre/soil interaction in the generation of tyre forces, effect of tyre dynamic response, hydrostatic system characteristics and articulated-frame steer vehicles.

Since all the analytical models are subjected to limitations resulting from the inherent difficulties in precisely modelling tyre forces, Crolla and El-Razaz (1987b) proposed a tyre model to predict the combined lateral and longitudinal forces generated by off-road tyres on deformable soil. Their model was based on the idea that, in the tyre-ground contact region the force due to soil shear must equal that due to deflection at any point.

Furthermore, this tyre model was modified to study the interaction between tyre and the terrain for different assumptions, including straight and angled lugs, cambered tyre, in addition to inclusion of a new description for the pressure-sinkage relationship and shear stress-shear displacement relationships. A computer program using MATLAB software was developed, and the results were shown in the form of tyre forces and moments in the three directions summed over the tyre contact length. The effect of many parameters such as slip angle, soil deformation modulus, lug dimensions and lugs spacing on tyre forces and moments was discussed (El-Gawwad et al., 1999a, 1999b, 1999c, 1999d).

2.3.3 Contribution of Schmid (The German School)

Based on research of more than two decades at the former Institute for Automotive Engineering (IKK) under the management of Schmid, various computer programs to simulate off-road vehicle dynamics have been developed. The following contributions, which are related to the current research topic, are discussed.

Ruff et al. (1991, 1993, 1994, 1997) developed a program for interactive simulation of the mobility of off-road vehicles. The program was called 'ORIS' (Off Road Interactive simulation) and composed of several sub-models, which described wheel-soil interaction, motion resistance and driveline power transmission, see figure 2.7.

ORIS was written in the programming language C under ANSI standard. The description of the wheel-soil interaction and the dynamic calculation of slip were the basis of the program. The theory of rigid wheel proposed by Bekker (1956, 1960) and the assumption of a parabolic shape for the contour proposed by Schmid and Ludewig (1991) were used. For calculation of motion resistance the air resistance, slope gradient, rolling resistance and accelerative resistances were considered. Within the driveline sub-model, engine and transmission characteristics were considered, as well as basic torque distribution devices, such as torque converter with mechanically open and locked differentials. Based on ORIS, many investigations have been carried out to assess the interaction between the vehicle sub-systems and the terrain as follows:

Lach (1996) investigated the influence of tyre inflation pressure on the traction performance of a 4x4 military truck over two different soils (loam and sand). He carried out a comparison between simulated results using the ORIS programme and experimental test-drives, with regard to the circumferential force, the rolling resistance, and the tractive force. The results confirmed the well-known benefits of reduced tyre inflation pressure, such as lower rolling resistance and higher traction capabilities.

Furthermore, Lach (1997, 1999) discussed some possible strategies for a tyre inflation pressure control system. He proposed some measured parameters for controlling the inflation pressure such as rolling resistance, sinkage and wheel slip. The control strategy outlined that it would be better to control the tyres which face higher sinkage or slip rather than controlling the inflation pressure for all the tyres. Moreover, the ruts from the previous tyres should be exploited by the following tyres traversing the same path. This improves the general characteristics of the control system, whilst also increasing the tyre life and decreasing the time to refill the tyres and recover 'on-road' mobility.

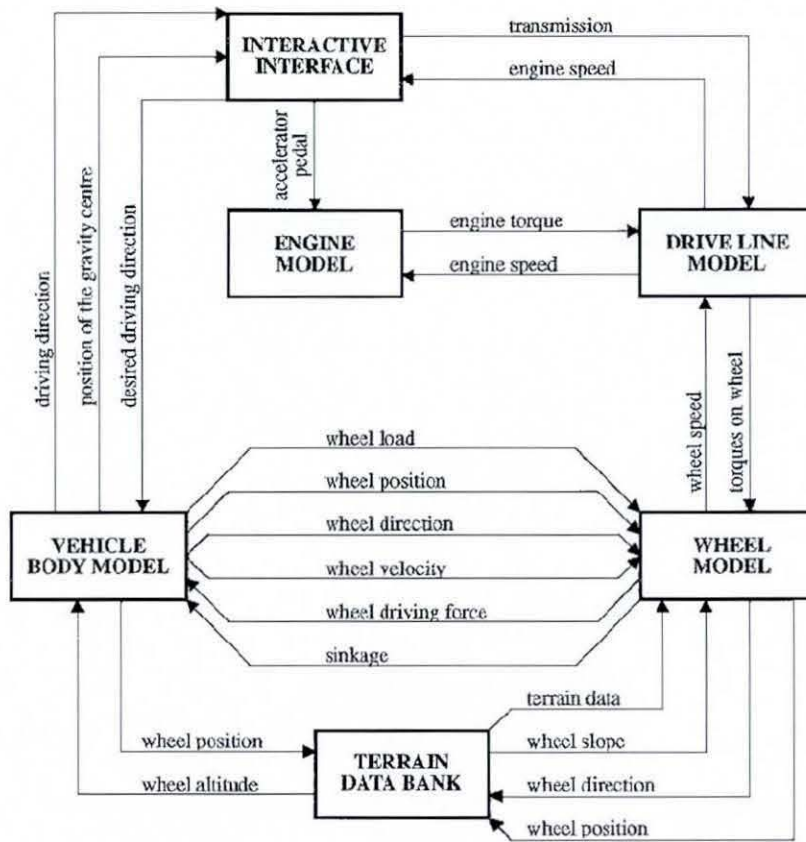


Figure 2.7 ORIS Program Main Structure (after Ruff and Jakobs, 1993)

Harnisch (1997) investigated the consequences of increasing the number of axles from the perspective of efficient off-road truck design. The advantages of higher drawbar pull, better climbing ability are encountered by extra expenditure due to the required higher propulsion power and additional design complexity. The results of the simulated multi-axle vehicle showed a remarkable lower rolling resistance due to the multi-pass effect.

Furthermore, Harnisch (1999) investigated the contribution of multi-pass effect, resulting from the ruts of the wheels, on the process of cornering of multi-axle-steer vehicles. The results showed that, during lateral manoeuvres of multi-axle vehicle, the multipass-effect was reduced, causing a significant higher rolling resistance. Moreover, this negative effect could be reduced by considering multi-axle-steering layout, where the steady-state cornering response was improved, especially for the case of symmetric all-wheel steering systems (AWS). However, compared to the standard steering systems, an increased rolling resistance at the beginning of a cornering procedure was noted, especially when

manoeuvring in confined space with fast changes to the steering angle. The author recommended development of a control system as an optimal solution to this problem.

Harnisch (2001), in his PhD dissertation, increased the capabilities of the ORIS program and added more features to the tyre model itself, such that the new version was able to simulate multi-drive-axles and multi-steer-axles. Furthermore, due to its real-time capability, it is also possible to include test stands (HIL, Hardware in the Loop), as well as driving simulators with motion systems. The new version of the simulation programme is called 'ORSIS' (Off Road Systems Interactive Simulation). The main structure of ORSIS program is shown in figure 2.8.

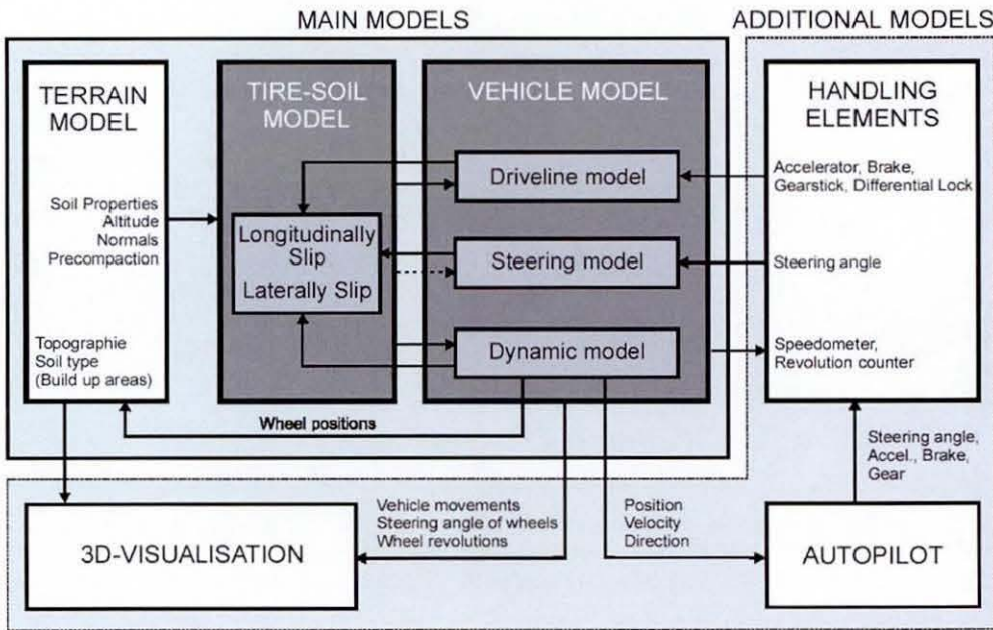


Figure 2.8 ORSIS Program Main Structure (after Harnisch et al., 2003)

ORSIS is written in the C++ programming language and has a modular structure, which allows easy and fast adaptations. It can be run on different computer platforms. Later, ORSIS became a commercial tool for off-road vehicle simulation and AESCO took over the distribution, support and further development of the simulation program. Details and capabilities of ORSIS are introduced in numerous publications, for example (Harnisch and Lach, 2002a; Harnisch and Lach, 2002b; Harnisch et al. 2003; Harnisch et al. 2007).

2.4 Torque Management Devices Implemented in AWD Vehicles

A peculiarity of AWD off-road vehicles is that their running abilities (higher traction, tractive efficiency, and improved mobility) depend not only on total tractive effort available by the power-plant, but also on its distribution between the driving wheels. The latter is determined by actuating vehicle systems and characteristics of the power dividing mechanisms e.g. inter-wheel, inter-axle reduction gear and transfer cases. The locking characteristics of these mechanisms regulate the circumferential force distribution between driving wheels. Accordingly, they can control both the longitudinal performance and the handling characteristics of the vehicle (Vantsevich, 1997).

There are almost as many different types of four-wheel-drive systems as there are four-wheel-drive vehicles. It seems that every manufacturer has several different schemes for providing power to all the wheels. The language used by different carmakers can sometimes be a little confusing, so prior to discussing some of the most important torque management devices it is useful to clear up some terminology (Dick, 1995; Mohan and Williams, 1995; Stone and Ball, 2004).

Part-Time Four-Wheel Drive: It has a separate transfer case after the transmission. It is referred to as part-time, because it can be used only to prevent wheel slip under special circumstances, where the vehicle moves on an off-road area. For on-road manoeuvres, the power is derived as (4×2), while on purpose the transfer case provides torque from the engine to the other wheels (4×4). Both the front and rear axles are rigidly coupled to the transfer axle. There is no difference in speed between front and rear axles. It should be noted that this mechanism is not allowed for on-road driving, otherwise serious drivetrain damage may occur, which is referred to as '*transmission wind-up*'.

On-Demand –Four-Wheel Drive: An open differential is incorporated between the front and rear axles. The open differential absorbs the variations in the speed between the front and rear shafts. However, being an open differential, torque transmitted is regulated by the axle with the least amount of resistance. This system allows driving on on-road, but will increase the fuel consumption of the vehicle. The driver may use two-wheel drive,

when there is no need for four-wheel drive. This arrangement is called ‘*on-demand*’. In certain serious situations, it is possible to lock the differentials by means of an electric or a vacuum locking system.

Full-Time (Permanent) Four-Wheel Drive: This system has differential everywhere, at both the front and rear axles and within the transfer case. This allows the vehicle to be 4WD on on-road. However, the open differential would transfer torque to the wheel with the least traction. The differentials can be locked to prevent this effect, or sometimes a limited slip differential is added to prevent excessive slip between the axles or the wheels.

All-Wheel Drive (AWD) (Automatic): In this case there is no selectable transfer case. Generally, these vehicles use the four-wheel drive concept to maintain stability. Usually, a traction control system is implemented to direct power from the spinning wheels to the gripping wheels. The system operates automatically and requires no driver intervention.

The construction layout and design considerations of all these four-wheel-drive systems are explained in many text books, for example (Dick, 1995; Heisler, 1885, 2002; Garrett, 2001). In addition, some selective papers are reviewed to cover and explore various classifications and industrial trends of those systems as follows:

Lanzer (1986) conducted a comparison between permanent and part time 4WD systems from the point of view of a torque split mechanism. He proposed a torque split factor to evaluate the influence of tractive force on drivability, handling, ease of operation, cost, and compatibility with the ABS system for different 4WD systems.

Mohan and Williams (1995) organized the various AWD traction control systems, including passive and active devices, by the general principles used and their implementation and strategies, figure 2.9. In addition, several examples of the major traction control systems made by automobile manufacturers are described in some detail.

Williams et al. (1995) described an approach for identifying and understanding the common market trend for development of 4WD systems. Based on a building block approach, they categorized the available 4WD systems available in the market, such that,

the systems were separated into main components and rated according to their effect on the overall performance and safety.

Vantsevich (1997) presented a statistical analysis of 4WD agricultural tractors and their differentials with data on more than 4000 tractor models produced since 1970. The obtained results have led to the creation of construction systems of a unified limited slip differential and a technique to select geometrical parameters for it.

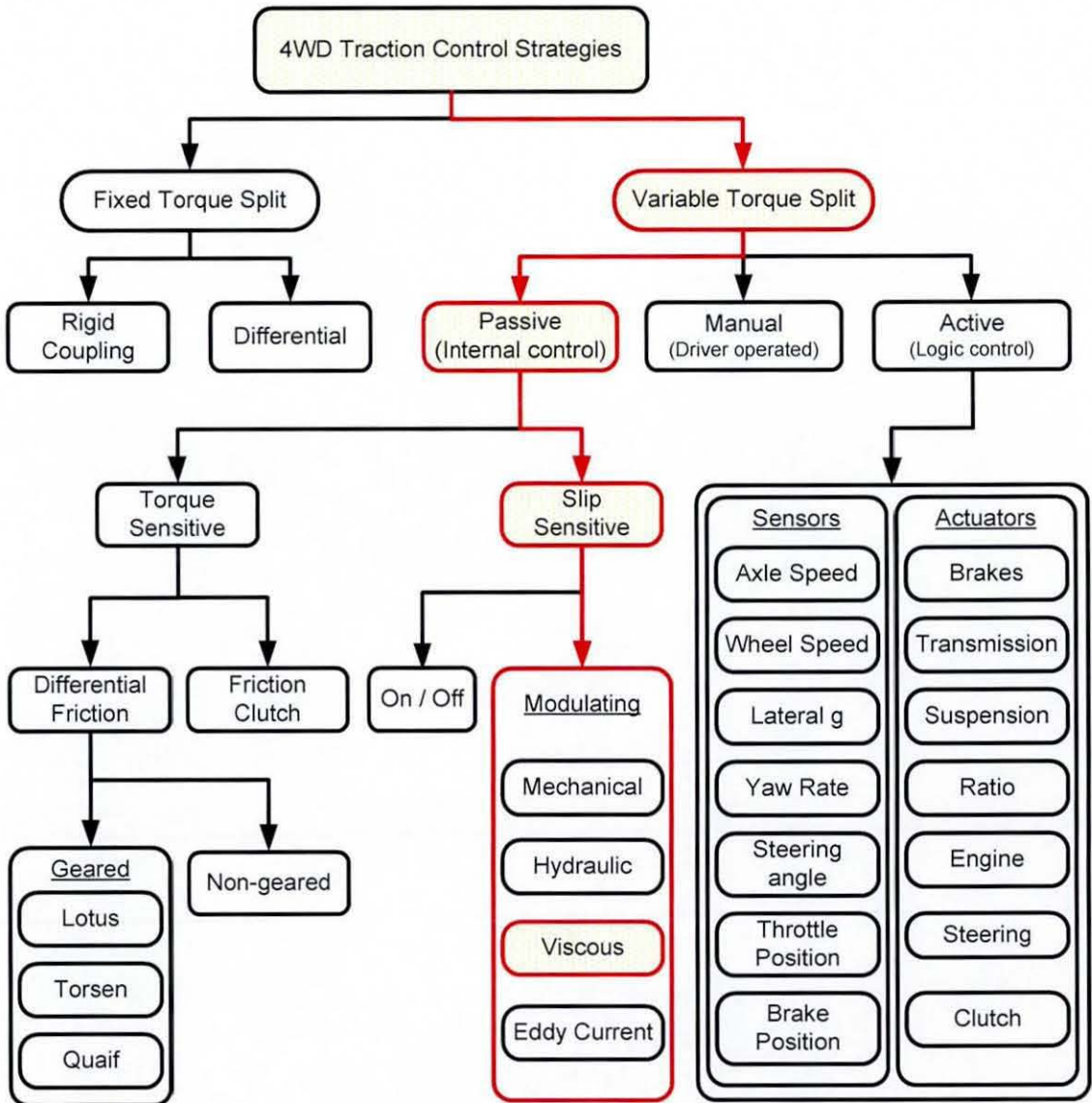


Figure 2.9 4WD Traction Control Strategies, adopted from (Mohan and Williams, 1995)

According to this review, it is obvious that the driveline components available to carry out a driveline for 4WD are a number and, considering a same nominal typology, the characteristics can vary significantly from one supplier to another. Such differences permit establishment of the desired performance by the appropriate selection of the driveline components. An extensive literature survey for the various devices used to produce torque bias has been carried out. Some of the well-known examples incorporating friction clutch, high friction worm gearing (Torsen differential), viscous coupling and electronically controlled limited slip differentials are introduced below.

2.4.1 Mechanical Differential (Open and Locked):

The conventional open differential has been the standard device for an automotive powertrain for a long time. This device is simple and effective in providing the necessary speed differential between the driving wheels during vehicle turning, see figure 2.10. However, because of the inherent equal-torque characteristics, it cannot take full advantage of the available traction at the driving wheels in roads with different levels of adhesion. Thus, the vehicle's maximum propelling power is restricted to twice the limiting torque at the low friction side of the driving wheels. Meanwhile, any attempt to increase the engine throttle simply makes the low friction side wheels to spin more, which would increase the slip sinkage in case of driving on an off-road area (Dick, 1995).

The conventional bevel-gear differential can be analyzed as a set of planetary gears, the gear attached to the left half-axle can be considered as the sun gear with angular speed (ω_s), the other gear attached to the right half-axle can be considered as the ring gear with an angular speed (ω_r). The crown wheel is considered as the planet carrier with an angular velocity (ω_c). The kinematic equation for planetary gears can be applied and from power and torque balance equations, the driving speed and torque along the lateral axes can be calculated as follow: (Stone and Ball, 2004).

$$\omega_c = \left(\frac{\omega_r + \omega_s}{2} \right) \quad \text{and} \quad T_s = T_r = \left(\frac{T_c}{2} \right) \quad (2.15)$$

To improve the traction characteristics of an open differential, the locking differential is useful for critical off-road conditions. The locked differential has the same parts as an open differential, but adds an electric, pneumatic, hydraulic or frictional mechanism to lock the two output pinions together. This mechanism is usually activated manually by a switch, and when activated, both the wheels spin at the same speed, equation (2.16). If one wheel leaves the ground, the other wheel is not affected.

$$\omega_c = \omega_r = \omega_s \quad \text{and} \quad T_c = (T_s + T_r) \quad (2.16)$$

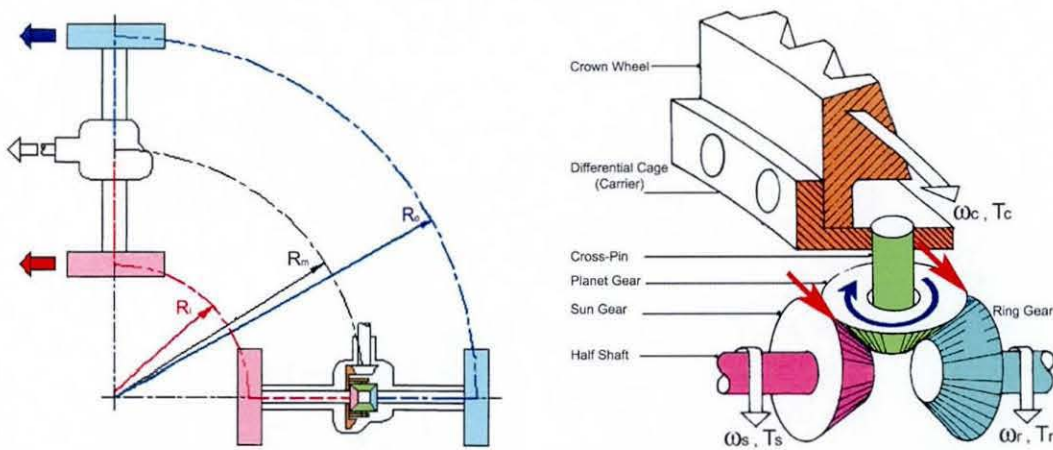


Figure 2.10 Principles of Open Differential Gearing, adopted from (Heisler, 2002)

2.4.2 Clutch-Type LSD

One way to introduce torque bias to the system is to add a friction clutch, figure 2.11. The clutch type LSD has all of the same components as an open differential, but it adds a spring pack and a set of clutches. Some of these have a cone clutch that acts like the synchronizers in a manual transmission. The spring pack pushes the side gears against the clutches, which are attached to the cage. Both side gears spin with the cage when both the wheels are moving at the same speed, and the clutches are not needed. The only time the clutches act is when one wheel spins faster than the other. The clutches resist this behaviour, forcing both wheels to rotate at the same speed. If one wheel tends to spin faster, then it must overcome the resistance of the clutch. The stiffness of the springs combined with the friction of the clutch determines how much torque it takes to overcome

the clutch resistance. The main disadvantage is, since frictional forces are continually active to resist slip, the frictional clutches tend to wear, resulting in deterioration of differential performance (Garrett, 2001).

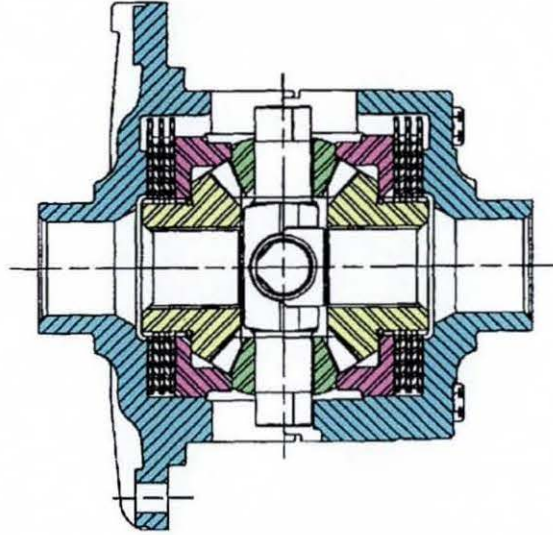


Figure 2.11 Clutch Type Limited Slip Differential, adopted from (Dick, 1995).

The general expression for the biased torque due to a total force applied in the friction disc is given by Danesin et al. (2004) as:

$$C_f = n \cdot f \cdot N \cdot \left(\frac{R_1 + R_2}{2} \right) \cdot \text{sgn}(\Delta\omega) \quad (2.17)$$

Where, (n) is the number of slipping surfaces, (f) is the clutch dynamic coefficient of friction. (N) is the normal load applied on the clutch disc. (R_1, R_2) are the outer and inner clutch disc radii. $(\Delta\omega)$ is the differential angular speed of the rotating discs.

2.4.3 Torsen LSD

Since 1983, Torsen differential has been employed in the powertrain driveline. These devices are often used in high-performance AWD vehicles. Torsen differential is purely a mechanical device, figure 2.12. The Torsen (from Torque Sensing) works as an open

differential when the amount of torque transferred to each wheel is the same. As soon as one wheel starts to lose traction, the difference in torque causes the gears in the Torsen differential to engage them. The design of gears determines the torque bias ratio. For instance, if a Torsen differential is designed with (5:1) bias ratio, it is capable of applying up to five times more torque to the wheel with good traction (Shih and Bowerman, 2002). The basic operating principles of a Torsen differential, as well as a functional comparison with an open differential are given by Chocholek (1988). Moreover, he derived a simplified mathematical model for the basic frictional relationships within a Torsen differential, which are responsible for achieving the bias torque between the drive axles.

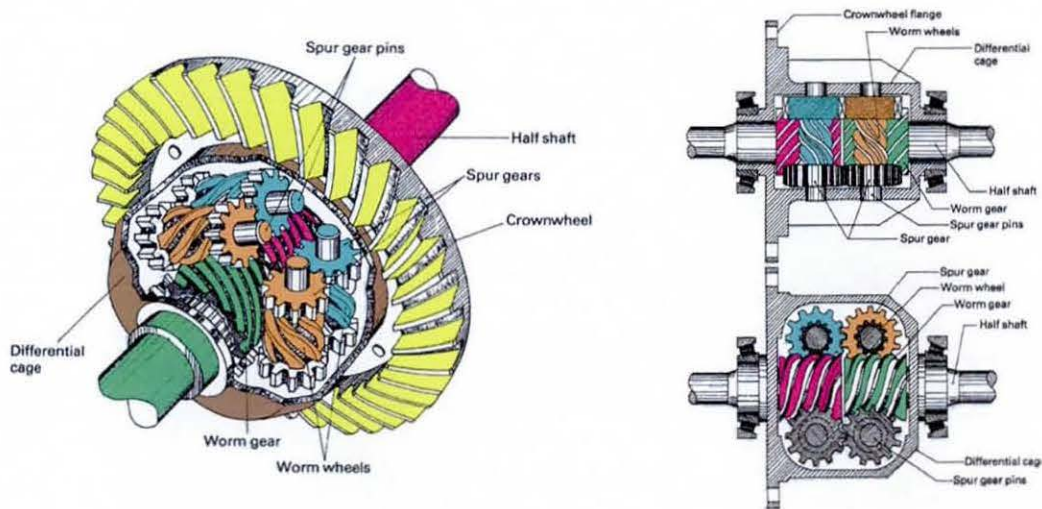


Figure 2.12 Torsen Limited Slip Differentials, adopted from (Chocholek, 1988)

Egnaczak (1994) presented an overview of a modified torque sensing geared LSD called '*Torsen-II*', which is designed with parallel axle helical gearing, further to its compatibility with Antilock Braking System (ABS). The bias ratio starts from (1.6:1) to (2.5:1). It has a similar function to the older type described previously.

Based on a numerical simulation model, as well as experimental results, Shih and Bowerman (2002) compared the torque bias ratio and the efficiency of friction clutch based LSD, Torsen differentials and Lockable differential devices. The authors also investigated the effect of helical angle and bearing arrangement on both the torque bias ratio and power loss.

It should be noted that this kind of LSD differential biases torque as a function of the available torque at the slipping wheel. Thus, if a wheel is off the ground with no carried torque, the differential cannot produce a torque bias to the contacting wheel. For this reason, many torque sensitive differentials are designed with a preload. Even with a wheel off the ground, there is some torque available to the wheel with good traction. Preload must be limited to prevent adverse handling effects in the vehicle, limiting its effectiveness (Kinsey, 2004).

2.4.4 Visco-Lock Devices

Rotary viscous couplings have been in use since the 1920s as torsional dampers or as torque transmission devices. However, their full potential was not realized until the use of AWD vehicles. These couplings are commonly used in AWD to connect the rear axle with the front axle such that, the transmitted torque is a function of the relative rotational speed between them. In its simplest form, a viscous coupling consists of a sealed housing and a splined hub. A set of thin plates are alternately connected to the housing and the hub. The intervening space between the plates and the housing is partially filled with high viscosity silicone oil as shown in figure 2.13. When one set of wheels tries to spin faster, the set of plates corresponding to those wheels spin faster than the others. The viscous fluid, entrained/entrapped between the plates, adheres to the faster disks, thus dragging the slower disks along with it. This transfers additional torque to the slower moving wheels or the wheels which are not slipping (Dick, 1995; Heisler, 2002).

The viscous coupling unit constitutes the core of the entire family of products known as visco-lock devices. They can be used in a driveline in series as a viscous transmission called '*viscous coupling*', or they can be employed within the differential unit to act as a viscous control element called '*visco-lock limited slip differential*'. In the parallel connection, there are two common ways of installing the viscous unit. These are: the shaft-to-carrier and the shaft-to-shaft layouts. In a shaft-to-carrier layout, one set of plates is splined to the differential carrier, whilst the other set of plates is splined to the differential gear on one side which, in turn, is of course splined to its shaft. On the other hand, with a shaft-to-shaft arrangement, the plates are connected alternately, one set to each of the differential gears (Garrett, 2001).

Taureg and Herrmann (1988) illustrated some typical applications of viscous coupling in all wheel drive vehicles. In addition, they proposed a simple empirical description of the transmitted viscous torque (T) as a function of the speed difference (Δn) and the friction torque (T_{FR}) as follow:

$$T = T_{FR} + a \cdot (\Delta n)^b \quad (2.18)$$

Their method of calculation has been supported by numerous experimental measurements to find the empirical constants (a , b) as follows:

$$a = \frac{\log\left(\frac{T_2 - T_{FR}}{T_1 - T_{FR}}\right)}{\log\left(\frac{\Delta n_2}{\Delta n_1}\right)} \quad \text{and} \quad b = \frac{(T_2 - T_{FR})}{(\Delta n_2)^a} \quad (2.19)$$

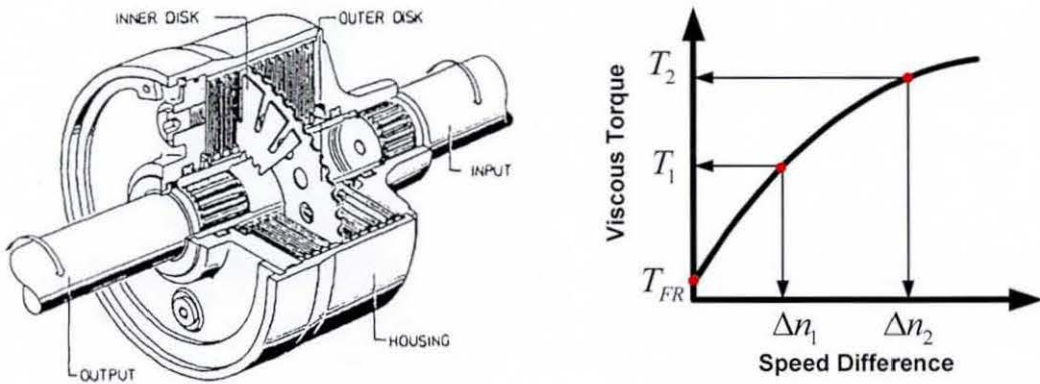


Figure 2.13 Viscous Coupling Characteristics, adopted from Taureg and Herrmann (1988)

Peschke (1986) presented an in-depth study of the operating and design considerations of viscous couplings. Based on the assumption of simple Couette flow between the plates of a unit cell with dynamic viscosity (μ), Peschke calculated the shear torque (T) transmitted by the viscous coupling as a function of the slip speed ($\Delta\omega$), inner and outer plate radii (r_1, r_2) and gap (or fluid film thickness) between the plates (S) as follows:

$$T = \frac{\pi \cdot \Delta\omega \cdot \mu}{2S} \cdot (r_2^4 - r_1^4) \quad (2.20)$$

Furthermore, Peschke clarified that due to the shearing of the oil, an equivalent amount of heat is generated; therefore the fluid temperature is raised and causes it to expand. At room temperature, the coupling is only partially filled with silicone fluid. At a certain critical temperature, when all the silicone fluid has expanded to fully fill the voids, the bulk pressure increases which causes the transmitted torque to sharply increase. Referring to the ‘*Self Torque Amplification*’ (STA) or ‘*hump phenomenon*’, Peschke described its onset to be at the time, when all the air within the housing is dissolved into the fluid. The temperature - pressure - volume expansion relationship is the key to this special mode of viscous coupling operation.

Taureg and Horst (1990) developed a more sophisticated model to calculate the viscous shear torque, by considering the effect of seal drag, the viscosity variation of the silicone with temperature, local shear rate and the contribution of two-phase flow.

$$T = \underbrace{T_{FR}}_{\text{Seals}} + \underbrace{\Delta n \cdot K_z(n)}_{\text{Relative and absolute speed}} \cdot \underbrace{\left(\frac{Z \cdot \pi^2}{15 \cdot S} \right) \cdot \rho(\theta) \cdot \nu(\theta, \beta(\theta)) \cdot \int_{r_1}^{r_2} \nu(r) \cdot r^3 \cdot dr}_{\text{Geometry + Fluid viscosity}} \quad (2.21)$$

Where (T_{FR}) is the friction torque due to seal. $(\Delta n \cdot K_z(n))$ accounts for the viscosity changes due to absolute and relative speed difference (n) . The rest of the terms account for geometry and viscosity effects, where, (Z) is the number of working surfaces, (r_1, r_2) are the radii of the inner and outer plates separated by gap (S) , which is filled with silicone fluid of density (ρ) , kinematic viscosity (ν) and filling ratio (β) . (θ) is referred to the fluid temperature. Furthermore, Taureg and Horst related the hump phenomena to the geometry of the plate slots. An additional objective was to develop externally controlled viscous coupling through controlling the pressure inside the unit, which is used to trigger the timing of the STA (hump) mode.

Further improvements in the calculation of viscous shear torque were carried out by Takemura and Niikura (1990). They incorporated the viscosity-shear rate relationship into the torque equation, which was originally developed by Tung and Linden (1985). The viscosity variation is related to shear rate according to the following equation:

$$\nu = \nu_B \cdot \left(\frac{\dot{\gamma}_B}{\dot{\gamma}} \right)^{-m} \quad (2.22)$$

Furthermore, they used a log-log model to relate the viscosity variation with temperature using the following equation:

$$\log(\nu_\theta) = \log(\nu_{\theta_0}) \cdot 10^{A \cdot \log\left(\frac{\theta}{\theta_0}\right)} \quad (2.23)$$

Where (A, m) are empirical constants, $(\nu_{\theta_0}, \nu_\theta)$ are viscosities at room and at any temperature. $(\dot{\gamma}, \dot{\gamma}_B)$ are shear and critical shear strain rates.

Takemura and Niikura proposed new sequences to explain the phenomena of self torque amplification. According to their explanation, the uneven distribution of air bubbles, which are collected in the plate holes, generates local temperature difference. This imbalance in thermal expansion is assumed to cause the differential pressure across the plate sides, resulting in metal contact of the plates and more torque to be transmitted.

Mohan et al. (1992) calculated the shear torque by considering the fluid viscosity dependency on shear rate, as well as on temperature. The silicone fluid is considered to exhibit pseudo-plastic behaviour under shear. Another empirical relationship is used to express viscosity variation with temperature which was originally proposed by Dow Corning Corporation (1962), see equation (2.24).

$$\log(\nu_\theta) = \left(\frac{722.5 + 0.000032 \cdot \nu_{\theta_0}}{\theta} \right) + 1.004 \cdot \log(\nu_{\theta_0}) - 2.447 \quad (2.24)$$

Furthermore, they claimed that as the plates approach each other, an axial pumping action occurs within the coupling, in addition to a reduction in the effective permeability for the

axial flow through the perforated plates. The combined effect was thought to set up a system of differential pressure cells that force the plate pairs together and hence lead to the occurrence of the hump phenomena.

Based on an elaborated numerical simulation as well as experimental observations of the fluid flow inside the viscous coupling, Wakamatsu et al. (1992) found that the flow field had nearly no radial component and any small radial component was close to the outer plate holes. Furthermore, they found that both the shape and number of holes of the plates had no significant effect on the transmitted torque.

Using a numerical model, Nakaoka et al. (1993) concentrated on the geometry of the inner plate tabs and the effect of a tab's camber particularly on the hump mechanism. They found that the viscous flow over a slight camber on the inner plate tabs caused a considerable torsional moment on them, resulting in an increase of the angle of attack of the blade and axial thrust on the inner disk.

Mohan (2002, 2003, 2004) described a comprehensive theory to define and explain the conditions necessary for initiating and sustaining STA in rotary viscous couplings. His work established and verified the processes that produce STA by proposing a sequence of events which are qualitatively viable and consistent with one another, with respect to a chain of causality. The various thermodynamic, hydrodynamic, structural and mechanical processes were delineated and tested using a methodology consisting of theoretical analysis, computational dynamic simulation and experimental observations. This investigation differs from others by studying the interaction between fluid mechanics and structural mechanics within the coupling. The structural response of the inner plate tabs on dynamic pressure generation in the gaps between the inner and outer plates were identified as the main cause of the sequence of events that results in STA.

2.4.5 Electronically Controlled LSD

The conventional passively controlled limited slip differential has limited capabilities due to its inherent design. By electronically controlling the differential's output, both traction

and handling can be easily optimized. Furthermore, if the vehicle is equipped with one of the advanced traction or braking control systems, the differential can resist by applying a torque to the wheel that is slowing down. This reduces the effectiveness of both the differential and the control systems. To allow compatibility, the differential needs to be de-tuned, reducing the tractive effort of the vehicle. Optimal mobility and handling can easily be achieved by programming the differential to react differently to specific external conditions. Figure 2.14 shows the torque transfer range of an electronically controllable differential compared with an ordinary viscous coupling LSD (Kinsey, 2004)

The majority of the current design solutions for electronically torque-biased LSD, used in AWD applications, are based on the use of wet-plate clutches. The amount of torque transferred by the coupling can be varied by modifying the number of friction plates engaged or by modulating the applied pressure. Several mechanisms are used for generating and controlling the pressure, including ball-ramp arrangements, gear-pumps, axial pistons/ cam plates, hydraulic valves etc.

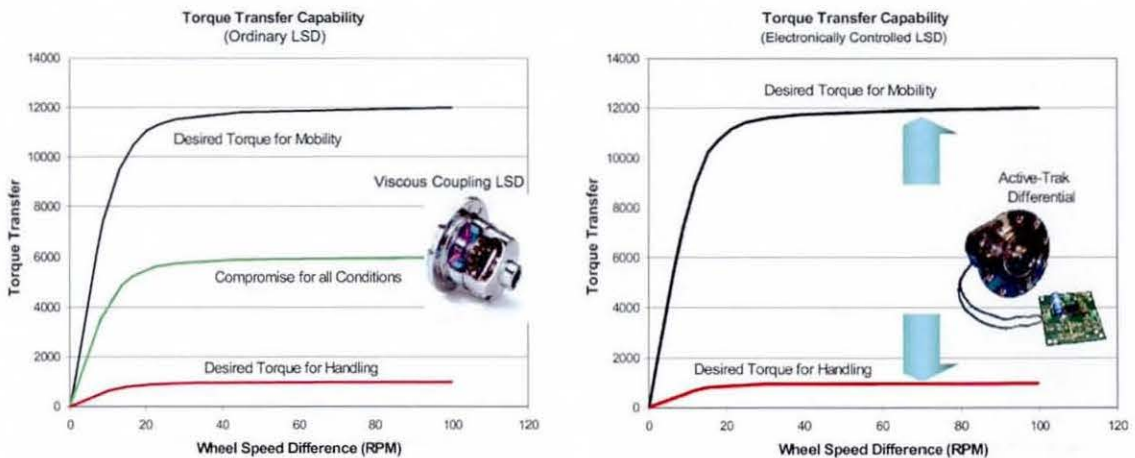


Figure 2.14 Passive versus Electronically Controlled LSD (after Kinsey, 2004)

Some examples using ball-ramp arrangements are given by (Gill et al., 2002; Kinsey, 2004; Huchtkoetter and Gassmann, 2004). An electronically controlled valve is employed, consisting of an electromagnetic coil positioned above a ball covering an orifice. When the coil is energized, an armature, which is slightly offset, tries to align with the coil. This provides a force on the ball blocking the orifice. The amount of force

on the ball controls the pressure that can be generated on the clutch pack. When the coil is disengaged, the ball can move away from the orifice allowing pressure to bleed off.

A Proportional-Integral-Differential (PID) controller is used to calculate the engagement force. Several inputs are used to determine the condition of the vehicle. Inputs include individual wheel speeds, steering angle, throttle position, vehicle speed, brake status, transfer case mode, and temperature. Based on the inputs, theoretical wheel speeds are calculated. When the actual measured wheel speeds vary from the theoretical speeds the controller determines how much correction is needed.

Another coupling solution addresses the stringent requirement for controllability by employing a magnetic particle clutch, coupled, in a quasi-static torque split arrangement with a planetary gear system (Gradu, 2003). Magnetic particle clutches are well known for very good torque modulation capabilities and for torque characteristics that are independent of the differential speed in the clutch. The main control parameter of the clutch is the applied current, which energizes a coil and aligns the steel particles similarly to bridges in the gap between the clutch rotors. The torque is transferred between the rotors due to friction with the micron-sized steel particles. The torque split arrangement significantly increases the torque capacity of the coupling, directing only a fraction of the torque through the magnetic particle clutch.

Park and Kroppe (2004) presented a novel torque-vectoring called '*Differential System Dynamic Trak*' which can be applied to both the inter-axle and the inter-wheel differential systems. The '*Dynamic Trak*' has three multi-plate clutches, figure 2.15. The centre clutch located inside the differential case provides a limited-slip or complete lock-up capability. The two outboard clutches, positioned at either sides of the differential case, selectively adjust the torque flow to the left or right shafts/wheels. An electronic control unit and a hydraulic circuit unit control the three clutches, effecting the active management of the torque to the two output shafts/wheels. The '*Dynamic Trak*' can provide a maximum of 100% torque bias, while maintaining an open differential feature.

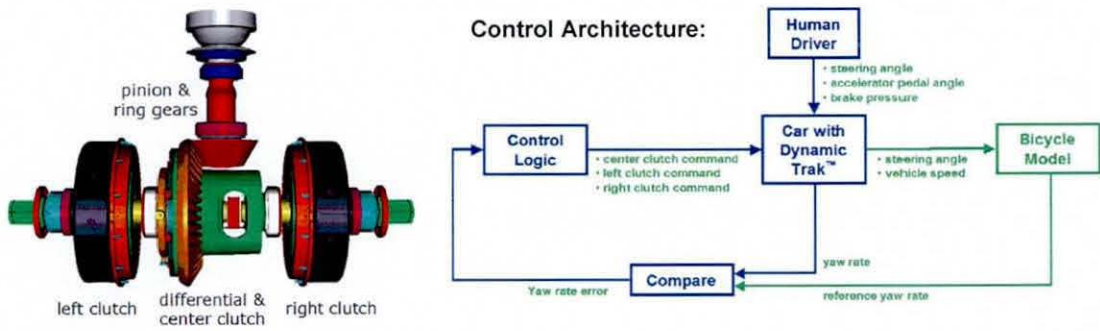


Figure 2.15 Torque Vectoring Differential (after Park and Kroppe, 2004)

2.5 Driveline Dynamics of AWD Vehicles

The driveline is a fundamental part of a vehicle. It transmits the energy from the engine combustion to propel the vehicle body through the wheels. In addition to the driveability and ease of operation, it is of great importance that this action is achieved as efficiently as possible, which would lead to better performance and lower fuel consumption. To achieve this, it is important to be able to mathematically model and numerically simulate the individual elements of the power train including engine, transmission, torque distribution devices, axles and so on. Next, the relationships between driveline characteristics and vehicle subsystems including body, suspensions, steering system and tyres must be clearly identified. Finally, with reference to special measuring criteria, the vehicle dynamics in terms of longitudinal, lateral and vertical responses should be evaluated.

2.5.1 Driveline Simulation Tools

Numerical simulation of dynamic systems has long been recognized as an important and effective tool in the design and analysis of drivetrain systems. Over the years many simulations have been developed which are application-specific, for example (Somayaji, 1993; Assanis et al., 1999). In the process of constructing such simulations, the differential equations which describe the motion of the system are repeatedly derived in a form which is appropriate to a particular application. The equations of motion are coded and debugged. This time-consuming process is repeated for each application before any useful results can be obtained from the simulation. A need emerges to quickly construct

flexible simulations which allow rapid and safe evaluation of alternative components and system configurations. In this section, several driveline analysis programs with various levels of complexity are discussed and compared, which assists selection of the right simulation tool.

With a support from Ricardo Consulting Engineers Ltd. and Boeing Computer Services, Ciesla and Jennings (1995) have constructed a library of powertrain component models in a modular form. This library is called '*Powertrain Dynamic Simulation Library*' (PDSL). These macro models have been derived in a consistent manner and have been designed to handle the causality issues that are important in a general purpose library. Models built using the PDSL components have been validated to ensure that the results predicted by the model are sensible. These modules have been developed using the EASY5 simulation language environment (MSC Software Co.). Each model in the library represents a basic component, commonly found in drivetrain. This library allows users to easily and quickly develop complex models of a wide range of vehicle and transmission configurations.

IMAGINE Ltd. (1995-2006) issued powertrain library called '*AMESim*' including components for modelling powertrain, transmissions and driveline systems. This library enables the designer to address the various physical phenomena involved in powertrain system simulation. From the engine to tyres, a large set of component models are provided. A complete modelling facility is offered for applications such as design of a automatic gearbox, analysis of shaft or driveline vibration, improvement of gear shift quality, clutch design, sizing of dual mass flywheels, optimization of gearbox efficiency, for example, the work carried by Garcia and Kargar (2000).

Another multi-domain modelling language is called '*Modelica*' under the '*MathModelica*' environment (Modelica Association). Modelica is a standardized language for complex multi-domain dynamic modelling while MathModelica is a modelling and simulation environment building on the Modelica language. The language contains a standard library with ready to use components such that the user can use them and build a complete model by dragging components and drawing lines between them. Significant research is carried out to simulate full driveline system using '*Modelica*' for examples (Pettersson, 1996; Nobrant, 2001; Drogies and Bauer, 2002; Wallén, 2004).

The latest release of the Modelica includes special library called '*PowerTrain*', which is enriched by optional consideration of 3D effects, a simpler signal bus concept, new components and example models for flexible drivelines, 4WD drivelines and hybrid vehicles. In addition, various new driver models have been added. A number of components originally developed for the Power-Train library have been incorporated into the Modelica standard library since they are of general interest (Elmqvist et al., 2004)

The MathWorks Inc. (2004-2006) released a new toolbox called '*SimDriveline*', which is part of Simulink Physical Modelling, encompassing the modelling and design of systems according to basic physical principles. SimDriveline extends Simulink with tools for modelling and simulating the mechanics of driveline systems. These tools include components such as gears, rotating shafts, and clutches; standard transmission templates; and engine and tyre models. SimDriveline is optimized for ease of use and speed of calculation for driveline mechanics. It is integrated with the MathWorks control design and code generation products, such that, it is possible to design and test controllers in real time with the model of the mechanical system. SimDriveline can be used for a variety of automotive, aerospace, defence, and industrial applications. It is particularly suited to the development of controllers for automotive and aerospace transmission systems.

In order to include, in an effective manner, all the sources of drivetrain non-linearity, a multi-body dynamic methodology is most appropriate. MSC Software Corporation released '*ADAMS/Driveline*' which provides engineers and analysts with specialized tools for modelling and simulating driveline components and studying the dynamic behaviour of the entire driveline during different input conditions. It can also be used to explore interactions between driveline and chassis components, such as suspensions, steering systems, brakes, and the vehicle body (MSC Software Co.).

Another well-known algorithm called '*Bond Graphs Method*' can be used for modelling and simulation of driveline systems, for example (Vijayakumar and Chandran, 2002; Wehrwein and Mourelatos, 2005). Bond graphs are topological models that capture energy exchange pathways in physical processes. The generic elements in bond graphs are energy storage, energy dissipation, energy transformation, and input-output elements.

The connecting edges or '*bonds*' represent energy pathways between the elements. Each bond is associated with two variables; effort and flow. The product of effort and flow is power, i.e., the rate of energy transfer. Connections in the system can be modelled by two idealized elements (series or parallel) junctions. This domain independence makes bond graphs attractive in a multi-domain context. Furthermore, the equations associated with bond-graph elements can be automatically converted into a simulation code, thus releasing the modeller of writing computable code. A lot of publications are available to cover different definitions and concepts of bond graphs, e.g., (Borutzky, 1992).

2.5.2 AWD Vehicle Dynamics Augmented by Torque Management Devices

Although the primary objective of AWD vehicle is to improve propulsion, particular attention must be paid to other aspects of vehicle behaviour. Therefore, a series of research works are carried out to investigate the vehicle behaviour in terms acceleration, deceleration, braking and cornering under the condition of various configurations of 4WD.

Hall (1986) predicted the steady state cornering behaviour of a high mobility 4WD armoured vehicle fitted with different torque split devices between front and rear axle. Different modules were proposed to simulate different types of torque distribution devices such as visco-lock, torque and friction clutch LSD. The behaviour of the tyres was predicted using an empirical on-road tyre model with simplified representation of the coefficient of adhesion. With static weight equally divided between the front and rear axle, Hall found that compared to viscous type LSD, torque sensitive LSD generates greater lift-off oversteer effects. This is may be due to the capabilities of torque-sensitive LSD to bias a higher torque across the wheels.

Furthermore, Hall and Moss (1988) conducted research into the use of viscous coupling to alleviate the transmission wind-up in military vehicles, when driven on-road. Various computer simulation models were developed to investigate the steady state handling response of military vehicles fitted with H-type transmission and viscous coupling of different stiffness characteristics. The results obtained indicate that wind-up torque is considerably reduced when the vehicle negotiates tight turns on roads at low speeds, in

addition to a noticeable reduction in tyre wear. Moreover, if a viscous coupling is used with stiffer characteristics, wind up torque would be reduced while keeping a high level of traction capability on off-road areas.

MacLaurin and Crolla (1988) proposed an active system, using a double differential to control both overall wheel slip and the distribution of slip and torque between the wheels. To obtain data on combined longitudinal and lateral tyre forces, they used the PARDE mobile tester. Both the computer simulation and field testing showed that active control of the differential offers the potential for tailoring the vehicle response in a way which is not possible with conventional differentials. Additionally, the generated yaw rate for mechanically locked differential was found to be higher than that of an open differential and for LSD differentials; the behaviour is somewhere between open and locked case.

Furthermore, MacLaurin and Hall (1993) described in detail the computer simulation models used to predict the steady state handling behaviour of the vehicle. The effect of controllable and various types of limited slip differentials on vehicle handling and traction characteristics were investigated. To validate the numerical models, they carried out field tests of a military vehicle equipped with a controllable double differential. The results suggested that using an actively controlled differential would considerably change the potential for better steady state handling behaviour.

Minabe et al. (1986) developed a computer simulation model to study 4WD handling characteristics resulting from two concepts: geared centre differential (with different static torque split ratio) and viscous coupling device (with different viscous characteristics). The vehicle model was represented by four degrees of freedom for simulating longitudinal, lateral, yaw and roll motion. Calculations of tyre forces in both longitudinal and lateral directions were based on empirical maps as function of slip angle and coefficient of friction. Under certain prescribed manoeuvres, many simulations were carried out to evaluate cornering response of the vehicle in each case.

Maretzke and Richter (1986) investigated the effect of different types of 4WD on both longitudinal and lateral directions. A 3-DOF vehicle model was used to express forward,

lateral and rotational motions about the vertical axis. The tyre representation was based on a simplified on-road tyre model. On the basis of the given tyre characteristics, the tyre model calculated forces in both longitudinal and lateral directions in addition to the dependency of the friction conditions and wheel load. The driveline model represented various configurations of torque split mechanisms, such as rigid coupling, central differential and viscous coupling. The viscous coupling was described by simplified empirical relationships of the viscous torque, driving speed and operating temperature. Many simulations were carried out, such as traction, braking and handling to evaluate vehicle performance in terms of different drivetrain configurations. An overall result of their investigation indicated that introducing a controllable degree of freedom (viscous coupling) between front and rear axle improved the general performance of the vehicle.

Tani et al. (1987) followed a similar methodology of Marezke and Richter to investigate the vehicle response due to different static torque split ratios. The vehicle model was represented by 6-DOF, in addition to 10-DOF for a drivetrain model. Some useful mathematical equations of different driveline layouts were introduced. The authors found that if a relatively small resisting force is applied to the centre differential, higher acceleration and cornering performance would be obtained. Compared to the centre differential, the results reflected the advantage of using a visco-lock LSD as the torque distribution device, which was a suitable feature for passenger cars.

Lugner et al. (1987) compared the performance of eight different drivetrain configurations for the case of straight ahead acceleration on a μ -split surface, on high friction surface and the unilateral crossing of the low friction patch. They found that the configuration of a central differential with parallel viscous coupling and soft coupling at the rear differential can provide a good compromise for all the perceived driving duties. It should be mentioned that the authors based their model on empirical equations to represent visco-lock differentials. Additionally, they carried out simulations with on-road surface with different coefficient of adhesion.

Hopkins and Metz (1994) examined the effect of locked differential on oversteer/understeer behaviour of RWD racing car. The numerical simulation of the

steady state cornering behaviour showed that the actual effect is much more complicated, and is strongly affected by static weight distribution between front and rear axles, roll coupling distribution, available traction and the radius of negotiated turn.

Huchtkoetter et al. (1994 and 1996) presented a series of field tests which investigated the effect of viscous coupling implemented in a front-wheel-drive vehicle on both its traction and handling characteristics. The results from tests demonstrated substantial traction improvement while only slightly influencing steering torque. Factors affecting this steering torque in front-wheel-drive vehicles were described. Further testing demonstrated that a vehicle with viscous limited slip differential exhibited an improved stability under acceleration and throttle-off manoeuvres during cornering.

Rubin and Moskwa (1999) developed a dynamic powertrain system model of the High Mobility Multi-Wheeled Vehicle (HMMWV). The dynamic model contains separate modules for open, Torsen differential and automatic transmission, as well as several other powertrain components. The model was created in the Simulink graphical programming environment. The overall model, combining full vehicle and powertrain system, was simulated during different scenarios to examine acceleration capabilities of the vehicle over moderately steep hills. The results demonstrated only the longitudinal performance of the vehicle, including its shifting characteristics and speed up-time diagram.

In a series of five papers, the research engineers at Visteon Corporation, introduced a new modelling approach called '*VADSIM-DYNA*' to combine the dynamics of driveline systems within a full vehicle modelling environment. Using ADAMS/View, Alexander and Monkaba (2000) developed fully parametric modules to represent the critical components and assemblies of the driveline system, such as the hypoid gear set, the differential case and pinion shaft, full and semi-floating axles, and propeller shafts.

Later, Alexander et al. (2002) incorporated their driveline modules into a highly non-linear, multi-degree of freedom vehicle model, which was developed in the ADAMS program by Subramanyam et al. (2000). Then, the developed VADSIM-DYNA driveline model was modified to include the functions of torque control devices.

Liu et al. (2001) presented a co-simulation approach to integrate the vehicle control modules in the virtual prototyping environments to verify the vehicle traction/cornering performance. The controller modules were developed in MATLAB. ADAMS was used to create a high-fidelity virtual prototyping vehicle model. The vehicle model was then modified to integrate the function of torque bias control devices. The co-simulation of the controller modules with the vehicle model was performed using ADAMS/Controls.

Furthermore, Liu et al. (2002) introduced three types of driveline torque bias arrangements including an electro-magnetic coupler, twin couplers and an electro-magnetic limited slip differential to monitor the vehicle response with different driveline torque strategies. The simulations were used to study several winter test conditions on packed snow or icy road and were used to also validate the torque control strategies.

Huchtkoetter et al. (2004) described various driveline concepts using electronically controlled Torque Management Devices (TMD), ranging from on-demand (hang-on coupling) to full-time AWD systems with a centre differential. The influences of TMD on vehicle dynamics were investigated for various driveline layouts and TMD arrangements. Results from vehicle tests showed remarkable improvements in vehicle traction provided by TMD. Furthermore, TMD also showed a significant influence on vehicle handling and stability and safety in 4WD systems, as well as in 2WD applications.

According to standard manoeuvres and a set of criteria, Borio et al. (2004) suggested a methodology for the comparison of longitudinal and lateral performances of AWD vehicles with different drivetrain architectures (locking, self-locking, viscous coupling and active differentials). Their performance evaluation methodology was based on three indices. The first index was to evaluate the longitudinal performance, using Traction Capability Index (TCI). The second was to evaluate lateral performance using Handling objective Quality Index (HIQ), and the third index was to evaluate reaction of the car during power on/off considering the yaw and sideslip response after the throttle transient. Their findings can be summarized as follows: the presence of a self-locking or visco-coupling on the centre allows for better longitudinal performance under all conditions. However, at high lateral acceleration it becomes worst, because of deterioration in stability, due to the locking phenomenon.

Danesin et al. (2004) investigated the dynamics of a 4WD vehicle, considering drivelines with different layouts including an ordinary differential, torque sensing and friction-clutch-based LSD. A simulator was used to compare performance through virtual experimentation. In addition, some preliminary road tests were carried out. Regarding lateral stability, the authors found that, compared with central clutch hydraulically actuated LSD the Torque sensing layout tends to reduce the under-steering behaviour of the car. It should be noted that the main equations applied to model open, torque sensing and limited slip differentials were based on empirical coefficients which were picked-up from direct measurements of the employed devices.

2.6 Conclusion of Review of Literature

An in-depth review of the state of the art in the field of AWD off-road vehicle dynamics has been presented here. The review includes more than 95 research papers and eight doctoral theses covering the following aspects: mechanics of wheel-soil interaction, off-road vehicle simulation and various strategies to control torque distribution in AWD vehicles. These are critically analysed and summarised as follows:

In the field of wheel soil mechanics and off-road vehicle simulation:

- Among the different reported approaches of wheel-soil mechanics, the analytical approach, which is originated by Bekker (1956, 1960, 1969) possesses a distinctive and highly desired advantage, being easily adapted to numerical simulation environments. This approach is characterised by a well-established mathematical structure which accounts for the pressure-sinkage in the vertical direction, and the shear-tension-displacement in the horizontal direction. On the contrary other approaches, e.g. theoretical and empirical, are still striving to compete in terms of fidelity, computational time and ease of use.
- Undoubtedly, the most important aspect of any off-road vehicle simulation model is the mechanism of tyre force generation (i.e. a suitable tyre model). It should be emphasized that a tyre model can be judged from at least two different points of view. First, in terms of being an all-around performer i.e. being able to deliver sensible

results when used in simulations under a wide range of operating conditions. Second, it can be judged in terms of enabling the study and assessment of certain parameters that influence tyre force generation. To this end, a recently developed off-road tyre modelling method, called '*AS²TM*' (AESCO GbR, 2005), seems to be the model of choice. Since the tyre model is customized as a Simulink S-Function, it seems a sensible choice which offers great flexibility for future developments of the entire modelling domain, where it can include further features such as control systems and automatic optimization routines.

- With the latest advances in computer technology, various computer programs have been developed to simulate different aspects of wheeled vehicle dynamics over deformable terrains. Although some of them have succeeded in this aim, simulation with such models is either computationally expensive e.g., '*ORSIS*' (Harnisch et al., 2007) or confidentially restricted e.g., '*NRMM-IT*' (Sullivan, 1999). On the other hand, with recent demands concerning the application of control systems and automatic optimization in 4×4 off-road vehicles, there is a need to develop models with medium degree of sophistication, yet adequate to represent vehicle dynamics accurately. One should also provide total control over the equations of the model to facilitate the implementation of an in-house written code.

In the sections dedicated to various torque management devices and their effect on vehicle behaviour, the following overall conclusions can be made:

- It is obvious that, the concepts of 4WD-trains developed or under development range from types activated manually, automatically, or permanently applied, with different kinds and degrees of differential locks. More sophisticated concepts use data monitored from driving conditions to control the transmission properties of the central and the axle differential gears using various electronic systems (Lanzer, 1986; Mohan and Williams, 1995; Huchtkoetter and Gassmann, 2004). Among this variety, application of visco-lock devices offer a possibility to achieve permanent 4WD inexpensively, providing an automatically adjusted tractive force distribution through a relatively wide range of conditions (Lee and Atkinson, 2002)

- It is recognised by the majority of researchers that a vehicle with visco-lock devices exhibits an improved traction performance. However, undesirable over-steering effect may occur during cornering manoeuvres, depending to a great extent, on the coupling characteristics of these devices (Minabe et al., 1986; Hall et al., 1988; Huchtkoetter et al., 1994, 1996).
- It is observed that, while visco-lock devices were originally developed to improve vehicle performance during serious driving situations, such as for off-road areas, under slippery conditions or μ -split surfaces, the majority of research work carried out has been devoted to the study of slippery on-roads and the used mechanism of tyre force representation has been based on on-road empirical maps as functions of vertical load, slip angle and coefficient of friction (Maretzke and Richter, 1986; Tani et al., 1987; Rubin and Moskwa, 1999; Borio et al., 2004). At this point, it should be emphasized that, this approach should not be extended to off-road vehicles, because the interactions between pneumatic tyres and deformable soil are very complex and include many effects, such as sinkage, multipass and slip sinkage. Another shortcoming is that, the mechanism of viscous torque transmission has been treated in past researches in a simple manner, using empirical equations or look-up tables, including data fitted to experimental measurements.
- On the other hand, although various mathematical models for analyzing the mechanism of torque generation in rotary viscous couplings have been in existence for many years (Peschke, 1986; Takemura and Niikura, 1990; Nakaoka et al., 1993; Mohan, 2002, 2003, 2004), most of these have not been integrated into an appropriate procedure for predicting the dynamic performance of a vehicle. In addition, some of these models have only shed light on isolated effects such as the complex sequence of events that would result in self-induced torque amplification (hump).
- As a final conclusion, there has been a lack of integrated numerical approach for implementation of visco-lock devices in a full vehicle simulation environment, especially for off-road automotive applications. Moreover, the contribution of any empirical approach to the improvement of the existing knowledge on visco-lock devices has been rather limited.

The following observation can be made with regard to the reported numerical simulation tools:

- Over the years, modelling effort has concentrated on replicating the behaviour of individual system components or sub-systems as closely as possible. This has, in the main, led largely to multi-body dynamic models, created in codes such as *ADAMS*. Although very good agreement is often found with test data, the sheer size of such models often leads to long computation times. For the purpose of the present analysis a model is implemented in the *MATLAB/Simulink* environment. This choice offers the possibility of later incorporation of advanced control strategies and the use of the real-time toolbox in Simulink.
- Recently, a fair number of commercial tools for simulating driveline systems have been reported. These tools have the potential to simulate the individual components commonly found in automotive powertrains. The common feature of those programs is the inclusion of general purpose libraries, which enable users to easily and quickly develop complex models. Among this variety, *SimDriveline* toolbox seems to be the tool of choice. Since *SimDriveline* toolbox is a part of Simulink Physical Modelling, It provides the advantage of using the control design and other code generation products within the Simulink environment.

Chapter 3: Theoretical Background

Traditionally, working in off-road vehicle research requires a combined knowledge of terramechanics and vehicle dynamics. This chapter presents the necessary foundations both in the understanding of basic principles of terramechanics and the mechanism of tyre force generation over deformable soil. Furthermore, some fundamental considerations about coordinate systems, rigid body motions in 3-D space and the implementation in vehicle dynamics are presented. The Newton-Euler approach is chosen for the formulation of the system of differential equations of motion. The material provided in this chapter not only forms the basis for off-road vehicle model development, but also to interpret and analyze the simulation results.

3.1 Soil Characterization for Numerical Modelling

Performance evaluation of terrain-vehicle systems entails information about both the vehicle design parameters and the physical environment within which the vehicle may operate. For the purpose of numerical modelling of off-road vehicles, the characterization of soil mechanical properties is a fundamental task in order to be able to predict thrust, resistance, sinkage, slip, driving torque, and wheel speed. Generally, the soil mechanical properties can be categorized as soil physical properties and soil strength parameters.

Soil physical properties affect the vehicle performance by changing the soil strength characteristics under different conditions. In Nature, however, the soil strength values in a site vary stochastically. Furthermore, they may be altered by soil cultivation and by vegetation. Additionally, they change continually within short term due to climatic influences. Impacts due to agriculture and by nature cause tremendous uncertainties in the actual soil strength. In order to consider the influences of cultivation and of climate on soil strength influences such as those of density and of moisture content has to be investigated systematically prior to any modelling effort. For this purpose, various models have been developed to account for the changes in soil strength due to its moisture

content, e.g. (Hintze, 1990, 1991, 1994). Furthermore, in Nature, soil strength values in a given site are somewhat scattered. Therefore, a particular measured value is not regarded as reliable at all. Additionally, a mean measured value in a few measurements may not be trustworthy. To solve this problem, various statistical methods have been reported by different researchers e.g., (Heiming, 1987, 1989), where frequency distribution, mean value and standard deviation, and other statistical measures have been considered.

For off-road automotive applications, soil strength parameters are some of the main factors affecting the supporting, floating, shear, friction and other abilities of the soil under vehicle load. Prediction of off-road vehicle performance, to a large extent, depends on the proper evaluation and measurement of the strength parameters of the terrain, which has been the major objective of terrain-vehicle mobility studies.

To characterize the soil strength parameters, interactions between tyre and soft soil may be described in terms of two separate relationships; one is soil deformation in vertical direction using '*The Pressure-Sinkage Relationship*' and the other is to describe soil deformation in the horizontal direction using '*The Shear-Stress Shear-Displacement Relationship*'. Both relationships can be obtained experimentally using a device called '*Bevameter*', which was originally developed by Bekker (1969).

Figure 3.1 shows the basic components of a Bevameter facility. In the Bevameter shown, a hydraulic loading cylinder is mounted vertically at one end of the frame and is used to apply normal loads to the sinkage plate in pressure-sinkage tests. A shear annulus head is mounted at the other end of the bevameter frame and is rotated by the hydraulic ram through a chain drive. The idea is to subject the terrain to loading, similar to that imposed by a running gear. To simulate this, two separate tests are carried out as follows:

- The penetration tests: different plates with suitable sizes (b_1, b_2) are used to simulate the contact area of the vehicle running gear; hence the pressure-sinkage relationship (p, z) of the terrain can be obtained.
- The shear test: using a shear annulus ring, which is driven by a torque motor, the shear stress-shear displacement relationship (T, θ) at various normal pressures (P', P'', P''') can thus be obtained.

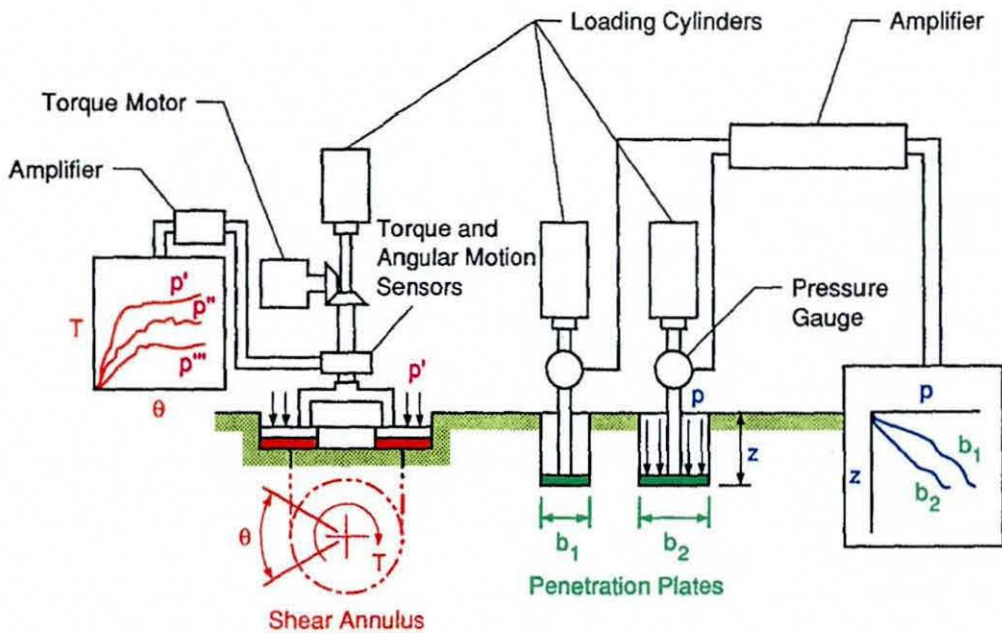


Figure 3.1 Basic Components of a Bevameter (after Wong, 1989)

The common approaches for predicting both relationships are highlighted as follows:

3.1.1 Pressure-Sinkage Relationship

A vehicle applies normal load to the terrain through its wheels, which results in sinkage. Alternatively, a wheel on soft soil penetrates into the ground to such a depth which results in a ground pressure balance against the applied wheel load. To predict the normal pressure distribution at the wheel-terrain interface, the response of the terrain to normal load and repetitive loading must be measured and then described by a mathematical relationship. This relationship is considered as semi-empirical, owing to the use of measured values, rather than being from first mathematical principles, such as by contact mechanics of poro-elastic solids, which would be highly involved in an analytical sense.

For the measurement of pressure-sinkage relationship, the vertical plate penetration test has thus become widely accepted, see figure 3.2. Different sizes of plates (b_1 , b_2) are used, and both the penetration force (F) and the sinkage (z) are recorded. The penetration speed is usually kept low to reduce the dynamic effect. This corresponds to

relaxation of the soil as a poro-elastic solid, similar to viscoelastic behaviour. Consequently, the pressure on the sinkage plate is obtained by dividing the penetration force by the contact area. The results of the calculated ground pressure (p) versus measured plate sinkage (z) can easily be plotted as shown in figure 3.2. This curve may be approximated by a simple exponential equation (3.1) which was originally proposed by Bekker (1956) as follows:

$$p = \left(\frac{K_C}{b} + K_\phi \right) \cdot z^n = K \cdot z^n \quad (3.1)$$

Where: (K) is the modulus of plastic soil deformation, (K_C, K_ϕ) are the cohesive and frictional moduli of soil deformation respectively, and (n) is the soil sinkage exponent.

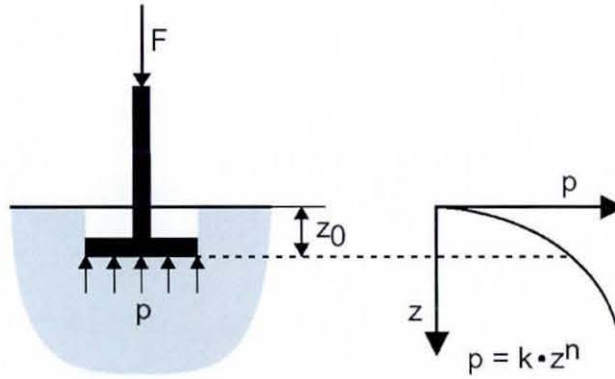


Figure 3.2 The Pressure-Sinkage Relationship (after Ruff, 1997)

To derive the soil strength parameters (K_C, K_ϕ, n), a weighted least squares method, which was originally developed by Wong (1980), is used. The weight error function is given as follows:

$$f(n, K) = \sum p^2 \cdot (\ln p - \ln K - n \cdot \ln z)^2 \quad (3.2)$$

By taking the partial derivative of $f(n, K)$ with respect to (n) and (K) and equating them to zero and solving for (n) and (K) the following expressions result:

$$n = \frac{(\sum p^2) \cdot (\sum p^2 \cdot \ln p \cdot \ln z) - \sum p^2 \cdot \ln p \cdot (\sum p^2 \cdot \ln z)}{(\sum p^2) \cdot (\sum p^2 \cdot (\ln z)^2) - \sum (p^2 \cdot \ln z)^2} \quad (3.3)$$

$$\ln K = \frac{\sum p^2 \cdot \ln p - n_{av} \cdot \sum p^2 \cdot \ln z}{\sum p^2} \quad (3.4)$$

For a given terrain, the sinkage exponent (n) should be the same, so the average exponent (n_{av}) can be calculated as follows:

$$n_{av} = \frac{(n)_{b=b_1} + (n)_{b=b_2}}{2} \quad (3.5)$$

Then, the values of (K_c , K_ϕ) can be calculated as follows:

$$K_c = \frac{(K)_{b=b_1} - (K)_{b=b_2}}{b_2 - b_1} \quad (3.6)$$

$$K_\phi = (K)_{b=b_1} - \left(\frac{(K)_{b=b_1} - (K)_{b=b_2}}{b_2 - b_1} \right) \cdot b_2 \quad (3.7)$$

A number of measured strength properties for soils are given by Wong (1989). Moreover, he introduced the response of a terrain to repetitive loading.

3.1.2 Shear-Stress Shear-Displacement Relationship

A vehicle applies a shear force (traction) to the terrain's surface through its wheels, which results in the development of thrust and an associated slip. To predict the tractive performance of an off-road vehicle, it is necessary to measure the relationship between shear stress and shear displacement under various normal pressures.

For the measurement of this relationship, two different types of shear plates can be used. The first one with grousers for measuring the internal shear strength, and the second is covered with natural rubber for measuring rubber-terrain shearing characteristics. During

the tests, different normal pressures are applied on the shear ring while the shear stress, shear displacement and slip sinkage are recorded. For each value of the normal pressure, the maximum shear stress is plotted versus the normal pressure. The single measurement points can be approximated by a line, see figure 3.3.

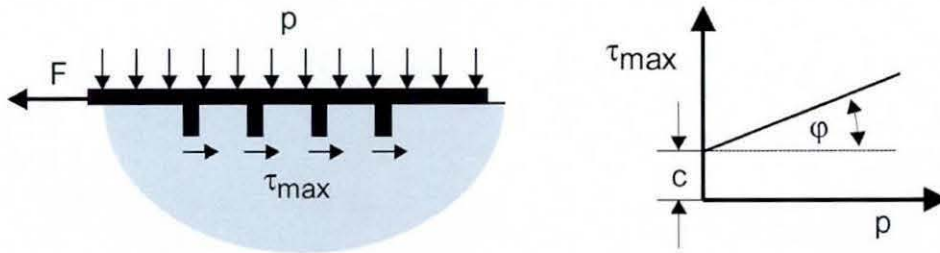


Figure 3.3 The Shear-Stress Shear-Displacement Relationship (after Ruff, 1997)

The slope of this line determines the soil internal friction angle (ϕ) and the intersection with the abscissa specifies the soil cohesion (C). The maximum shear strength (τ_{\max}) is assumed to be observed from the following Mohr-Coulomb failure criterion as follows:

$$\tau_{\max} = C + p \cdot \tan \phi \quad (3.8)$$

To fit the measured data and predict the shear stress as a function of shear deformation (j), Janosi and Hanamoto (1961) proposed the following simplified equation:

$$\tau = \tau_{\max} \cdot \left(1 - e^{-\frac{j}{k}}\right) = (C + p \cdot \tan \phi) \cdot \left(1 - e^{-\frac{j}{k}}\right) \quad (3.9)$$

Wong and Preston-Thomas (1983) proposed a different equation, composed of two exponential functions. Their equation describes the shear stress-displacement curve that displays a 'hump' of maximum shear stress and then decreases with an increase in shear displacement to a constant value of residual stress as follows:

$$\tau = \tau_{\max} \cdot K_r \left(1 + \left(\frac{1}{K_r \cdot (1 - 1/e)} - 1\right) \cdot e^{-\frac{j}{K_w}}\right) \cdot \left(1 - e^{-\frac{j}{k}}\right) \quad (3.10)$$

Where (k) is the tangent modulus of horizontal shear deformation, (K_w) is equal to the shear displacement at the maximum shear stress, (K_r) is the ratio of the residual shear stress to the maximum shear stress.

3.2 Off-Road Tyre Modelling

Calculation of the interactions between tyres and soil is the key challenge in off-road vehicle dynamics simulation. An extensive literature review is carried out to select a suitable off-road tyre model (see chapter 2). Among the different methods developed for wheel-soil mechanics, the AS²TM off-road tyre model was chosen (AESCO, 2005) for use in the current investigation.

The AS²TM uses an advanced version of the traditional analytical method, which is based on the principles introduced by Bekker (1956, 1960, 1969) and by Janosi and Hanamoto (1961). The main strength of this tyre model is the consideration of elastic tyres on soft soils, including multi-pass calculations. Furthermore, the deformed contact patch between the tyre and the soil is described by a large substitute circle. The main outputs of the model are the longitudinal, lateral, and vertical forces of elastic tyres on soft soils, driving torques acting on the wheel, sinkage, tyre deflection, rolling resistance, slip, slip angle and soil compaction. In this section, the main features, limitations, as well as the mathematical modelling of this tyre model are briefly introduced (Ruff et al., 1991, 1993, 1994, 1997; Schmid, 1995; Harnisch, 2001; Harnisch et al., 2003, 2005; AESCO, 2005).

3.2.1 Main Features and Limitations

Features:

- Tyre forces in longitudinal, lateral and vertical directions are calculated by assuming contact of an elastic tyre on soft soils.
- Calculating torques acting on the tyre relative to the wheel hub.
- Calculating slip in both longitudinal and lateral directions.
- Taking into account interactions between the longitudinal and the lateral forces.

- Calculating sinkage, resulting from assumption of elastic and plastic soil characteristics.
- Calculating rolling resistance, based on both soil compaction and tyre deformation.
- Calculating tyre deflection, taking into account tyre inflation pressure.
- Calculating slip-sinkage.
- Including the effects of repetitive loading or multi-pass (soil pre-compaction).
- Including influence of tyre-profile (i.e., lug height and tyre shape profile).
- Including the effect of slippery surfaces (e. g. grass, wet loam).
- Implementing the tyre model as an S-function in Matlab/Simulink environment.

Limitations:

Since the tyre model is approximated by a single-point-contact only, the simulation of crossing over-steep obstacles ($>80^\circ$) is not possible. The drawback of this assumption would mainly affect ride quality simulations. Even though a significant number of important effects can be described (e.g. deformation of the soil after crossing, planting of roughness) the wheel elevation curve, when crossing a tapered ditch, may not be geometrically correct.

3.2.2 Rigid Wheel Model

The preliminary approach in understanding off-road tyre modelling is to consider a rigid wheel with a circular geometry, which is a practical approximation of tyre over soft soils without pre-compaction, see figure 3.4. While the rigid wheel model is relatively simple, it represents an essential starting point for any analytical off-road tyre model.

The first step is to numerically calculate the local pressure under the wheel, see equation (3.1). The normal pressure distribution starts at zero, where the wheel enters the terrain ($z = 0$) and reaches its maximum at the bottom dead centre of the wheel ($z = z_0$).

Tyre vertical force (F_z) is calculated from the numerical integration of the pressure along the contact area, where (ϑ_1) is the contact angle given by: $\left(\vartheta_1 = \arccos\left(\frac{D-2 \cdot z_0}{D}\right) \right)$.

$$F_z = b \cdot \int_0^l P(z) \cdot dx = b \cdot \left(\frac{D}{2}\right) \cdot \int_0^{\theta_1} p(\theta) \cdot \cos \theta \cdot d\theta \quad (3.11)$$

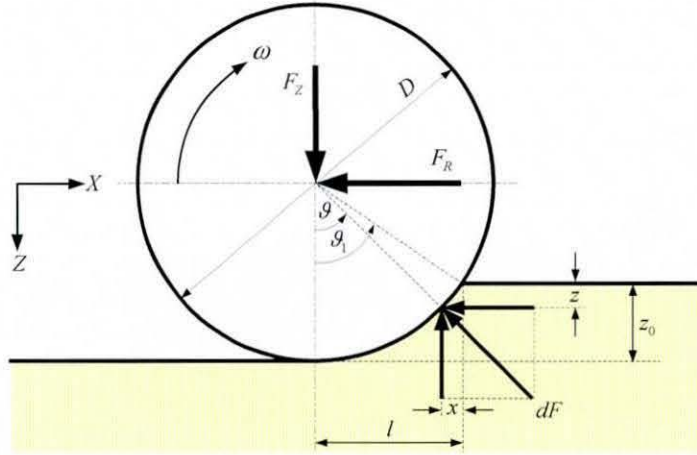


Figure 3.4 Principle of the Rigid Wheel Model, adopted from (Ruff, 1997)

From equations (3.1) and (3.11) an expression for the tyre sinkage can be obtained as:

$$z_0 = \left(\frac{3 \cdot F_z}{b \cdot (3-n) \cdot \left(\frac{K_C}{b} + K_\varphi\right) \cdot \sqrt{D}} \right)^{\frac{2}{2n+1}} \quad (3.12)$$

The resisting force can be calculated by integrating the horizontal component:

$$F_R = b \cdot \int_0^{z_0} P(z) \cdot dz = b \cdot \left(\frac{D}{2}\right) \cdot \int_0^{\theta_1} p(\theta) \cdot \sin \theta \cdot d\theta \quad (3.13)$$

$$F_R = b \cdot \left(\frac{K_C}{b} + K_\varphi\right) \cdot \left(\frac{z_0^{n+1}}{n+1}\right) \quad (3.14)$$

The transferred circumferential force (F_U) and its horizontal component (F_x) can be determined by integration of local shear stress over the contact area. The local shear stress ($\tau(\theta)$) can be computed, based on the local pressure and shear displacement, see equations (3.9) or (3.10).

$$F_U = b \cdot \left(\frac{D}{2}\right) \cdot \int_0^{\vartheta_1} \tau_{\max}(\vartheta) \cdot \left(1 - e^{-\frac{\vartheta}{k}}\right) \cdot d\vartheta \quad (3.15)$$

$$F_x = b \cdot \left(\frac{D}{2}\right) \cdot \int_0^{\vartheta_1} \tau_{\max}(\vartheta) \cdot \left(1 - e^{-\frac{\vartheta}{k}}\right) \cdot \cos \vartheta \cdot d\vartheta \quad (3.16)$$

The drawbar pull can be computed as the difference between the longitudinal force (F_x) and the resisting force caused by the soil (F_R).

3.2.3 Simulation of Elastic Tyres on Elastic/Plastic Soil

The pressures generated along the contact area depend on the local deformation of the ground, which are described by the tyre-soil contact contour. While maximum sinkage results from the equilibrium condition of wheel load and ground pressures, the shape of contact is an assumption in most analytical models. In the simplest case the contact contour consists of the section of a circle and a straight horizontal secant. For the elastic tyre assumption, the model uses a large substitute circle (D^*) to describe the deformed contact patch between the tyre and soil. This approximation allows a much more elegant mathematical treatment of the deflected elastic tyre contour, figure 3.5.

3.2.3.1 Elastic/Plastic Soil Model:

In straight line motion of a multi-wheeled off-road vehicle, an element of the terrain under the leading wheel is first subjected to a vertical load. As the leading wheel rolls over, the vertical load on the terrain element is reduced. However, the vertical load is reapplied again by the following wheel. Thus, a terrain element is subjected to repetitive loading. The loading-unloading-reloading cycle continues until the rear wheel of the vehicle has passed over the terrain. To predict the normal pressure distribution, sinkage and motion resistance, the response of the terrain to repetitive normal loads must be measured.

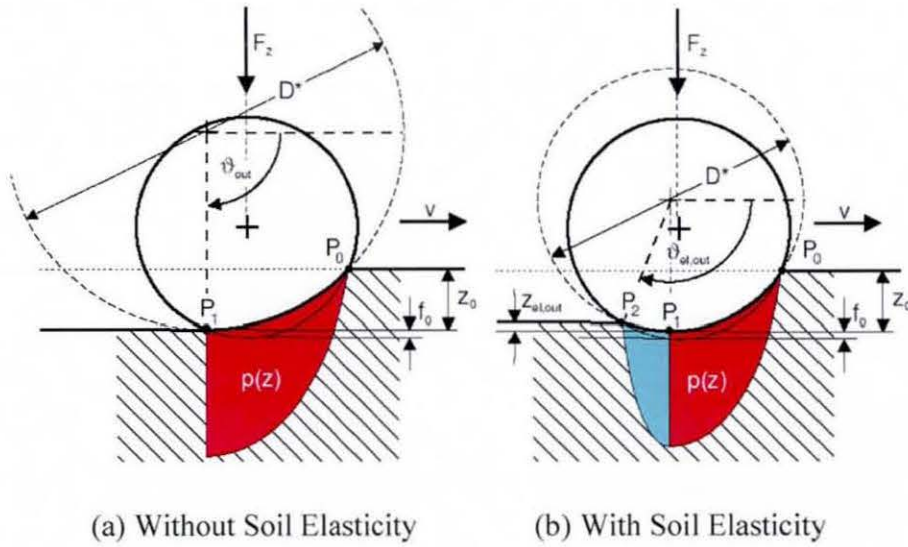


Figure 3.5 Substitution Circle Approach (after Harnisch and Lach, 2002b)

Soil elasticity is important for multi-pass calculations and also leads to a much more realistic pressure distribution under the wheel, figure 3.5. The response of the elastic soil to repetitive loading is considered similar to that of Wong (1989). When the load is first applied to the soil, the load-sinkage relationship follows the normal pattern, equations (3.1). If the load is reduced, a certain amount of elastic rebound (recovery) occurs. When the load is reapplied again, a certain amount of hysteretic response exists during the loading-unloading cycle. Consequently, additional sinkage occurs. Soil elasticity can be determined by means of plate-sink tests with repetitive loading. The soil stiffness (C_B) is assumed to be linear over the complete range of sinkage and can be obtained from measurements as follows:

$$C_B = \frac{P_{\max}}{\Delta z_{el}} \quad (3.17)$$

The ground pressure (p_{el}) during elastic deformation of the soil (z_{el}) can be easily calculated using the soil elasticity modulus (C_B) as follows:

$$p_{el} = C_B \cdot z_{el} \quad (3.18)$$

Figures 3.6 and 3.7 show the principle of the substitution circle model for the non multi-pass and the multi-pass cases. In the figures, the plastic (red) and the elastic soil deformations (green and blue) are shown. In multi-pass the pre-compaction of the soil is taken into account; the pressure sinkage relationship starts with an elastic portion, equation (3.1). To effect plastic soil deformation, the local pressure should increase above the pre-compaction pressure (p_{max}).

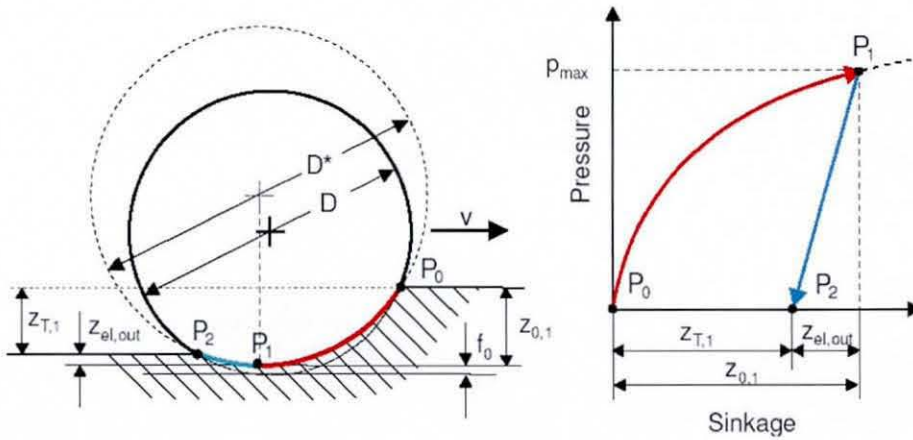


Figure 3.6 Substitution Circle Approach (No Multi-pass) (after AESCO, 2005)

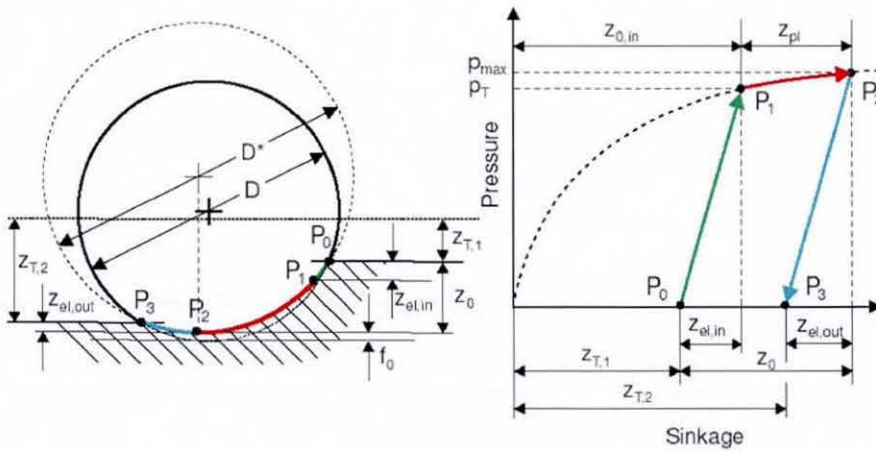


Figure 3.7 Substitution Circle Approach (Multi-pass) (after Harnisch et al. (2005))

Referring to figure 3.6, the elastic soil deformation ($z_{el,out}$) using substitution circle approach and non multi-pass case is calculated as follows:

$$z_{el,out} = \frac{p_{max}}{C_B} = \frac{K \cdot z_{0,1}^n}{C_B} \quad (3.19)$$

Referring to figure 3.7 and based on the soil elasticity modulus (C_B), the elastic soil deformation ($z_{el,in}$, $z_{el,out}$), using the substitution circle approach for multi-pass case, can be obtained as follow:

$$z_{el,in} = \frac{p_T}{C_B} = \frac{K \cdot z_{0,in}^n}{C_B} \quad (3.20)$$

$$z_{el,out} = \frac{p_{max}}{C_B} = \frac{K \cdot (z_{T,1} + z_0)^n}{C_B} \quad (3.21)$$

3.2.3.2 The Substitution Circle Geometry Calculations:

The diameter of the substitute circle (D^*) is calculated from equilibrium condition between the vertical reaction force of the soil and the vertical reaction of the tyre. Solution to the equilibrium condition is obtained via an iterative process, see figure 3.18:

- The vertical reaction of the ground is calculated by numerical integration of the local pressures under the wheel, see equation (3.30) and (3.33)
- The tyre reaction force is computed from the measured tyre characteristics. To determine these characteristics, the vertical load has to be measured versus the tyre deflection. The measured values are approximated by an analytical conversion formula, which was proposed by Schmid (1995), and is used by the model. Five parameters are employed to describe the non-linear tyre deflection characteristics (f), taking into account the influence of tyre inflation pressure. Due to the fact that, the geometry of the deflected tyre on soft soil is different from that on a flat hard road, the tyre reaction force must be modified to compensate for this effect.

For the calculation of the ground vertical reaction force, the geometry of the tyre deflection on soft ground must first be calculated, see figure 3.8.

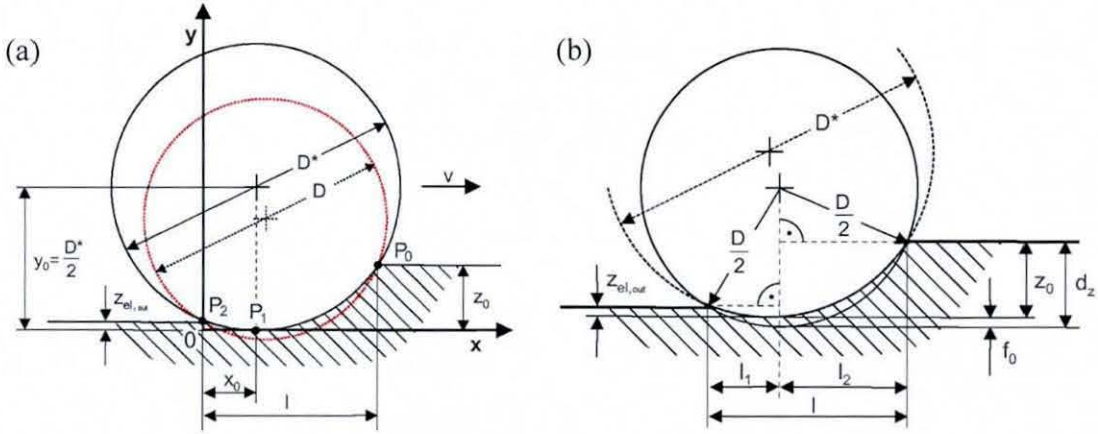


Figure 3.8 Substitution Circle Geometry, adopted from (Harnisch, 2001)

Referring to figure 3.8, the general equation for a circle can be applied as follows:

$$(x - x_0)^2 + (y - y_0)^2 = \left(\frac{D^*}{2}\right)^2 \quad (3.22)$$

The origin of the coordinate system is located at the intersection of the tangent at the substitution circle through (P_1) and the vertical line passing through (P_2) . As shown in figure 3.8, the following boundary conditions are also applied:

$$\left. \begin{aligned} x = 0 & \rightarrow y(x) = z_{el,out} \\ x = l & \rightarrow y(x) = z_0 \\ l = l_1 + l_2 & = \sqrt{D \cdot (f_0 + z_{el,out}) - (f_0 + z_{el,out})^2} + \sqrt{D \cdot d_z - d_z^2} \end{aligned} \right\} \quad (3.23)$$

From equation (3.22) and the assumptions given in equation (3.23), two quadratic equations are obtained and solved to obtain (x_0) and (D^*) as follows:

$$x_0 = \left(\frac{l \cdot z_{el,out}}{z_{el,out} - z_0} \right) \cdot \left(1 - \sqrt{1 - \left(1 - \frac{z_0}{z_{el,out}} \right) \cdot \left(1 + \frac{z_0 \cdot (z_0 - z_{el,out})}{l^2} \right)} \right) \quad (3.24)$$

$$D^* = z_0 + \frac{(l - x_0)^2}{z_0} \quad (3.25)$$

3.2.3.3 The Substitution Circle Angles Calculations:

Referring to figure 3.9b, the contact angle of the substitution circle without multi-pass can be calculated as follows:

$$\vartheta_{in} = \arcsin \left(1 - \frac{2 \cdot z_{0,1}}{D^*} \right) \quad (3.26)$$

Referring to figure 3.9a, the contact angles of the substitution circle with multi-pass can be calculated as follows:

$$\left. \begin{aligned} \vartheta_{el,in} &= \arcsin \left(1 - \frac{2 \cdot (z_{0,2} - z_{el,in})}{D^*} \right) \\ \vartheta_{el,out} &= \frac{\pi}{2} + \arcsin \left(1 - \frac{2 \cdot z_{el,out}}{D^*} \right) \end{aligned} \right\} \quad (3.27)$$

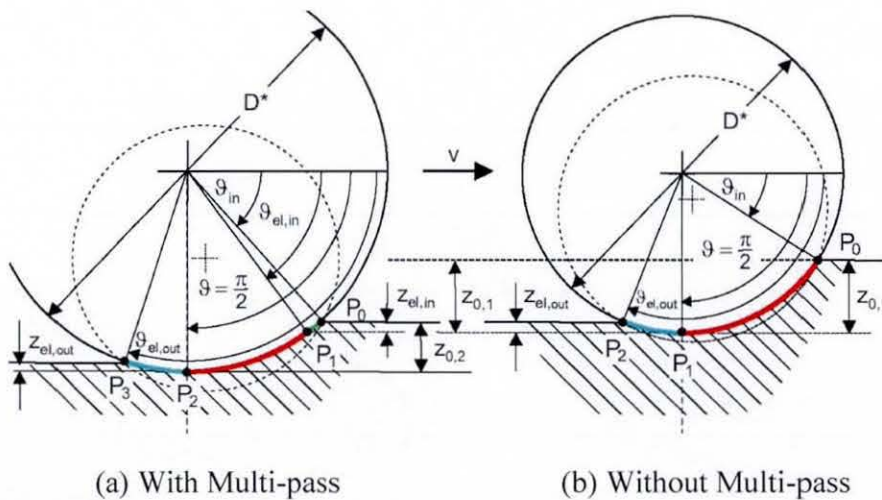


Figure 3.9 Angles of the Substitution Circle, adopted from (Harnisch, 2001)

3.2.4 Ground Pressure and Reaction Force

The numerical integration of the local pressure along the contact area gives the vertical reaction force. To take into account the effect of soil elasticity, the contact area is divided into plastic and elastic regions. The ground local pressure, and hence the vertical reaction are calculated.

For the non-multi-pass case; the ground pressure is given as:

$$\left. \begin{aligned} p_{pl} &= K \cdot \left(\frac{D^*}{2} \cdot (\sin \vartheta - \sin \vartheta_m) \right)^n \\ p_{out}(\vartheta) &= C_B \cdot \left(z_{el,out} - \frac{D^*}{2} \cdot (1 - \sin \vartheta) \right) \end{aligned} \right\} \quad (3.28)$$

The integration of local pressure under the tyre contact area gives the vertical reaction as:

$$\left. \begin{aligned} F_{Z,pl} &= b \cdot \frac{D^*}{2} \cdot K \cdot \int_{\vartheta_m}^{\frac{\pi}{2}} \left(\frac{D^*}{2} \cdot (\sin \vartheta - \sin \vartheta_m) \right)^n \cdot \sin \vartheta \cdot d\vartheta \\ F_{Z,out} &= b \cdot \frac{D^*}{2} \cdot C_B \cdot \int_{\frac{\pi}{2}}^{\vartheta_{el,out}} \left(z_{el,out} - \frac{D^*}{2} \cdot (1 - \sin \vartheta) \right) \cdot \sin \vartheta \cdot d\vartheta \end{aligned} \right\} \quad (3.29)$$

$$F_Z = F_{Z,pl} + F_{Z,out} \quad (3.30)$$

For the multi-pass case: the ground pressure is given by:

$$\left. \begin{aligned} p_m(\vartheta) &= C_B \cdot \left(\frac{D^*}{2} \cdot (\sin \vartheta - \sin \vartheta_m) + z_{o,1} \right) \\ p_{pl}(\vartheta) &= K \cdot \left(\frac{D^*}{2} \cdot (\sin \vartheta - \sin \vartheta_m) + z_{o,1} - z_{el,m} \right)^n \end{aligned} \right\} \quad (3.31)$$

The integration of local pressure under the tyre contact patch area gives the vertical reaction as:

$$\left. \begin{aligned} F_{Z,in} &= b \cdot \frac{D^*}{2} \cdot C_B \cdot \int_{\vartheta_{in}}^{\vartheta_{el,in}} \left(\frac{D^*}{2} \cdot (\sin \vartheta - \sin \vartheta_{in}) + z_{0,1} \right) \cdot \sin \vartheta \cdot d\vartheta \\ F_{Z,pl} &= b \cdot \frac{D^*}{2} \cdot K \cdot \int_{\vartheta_{el,in}}^{\frac{\pi}{2}} \left(\frac{D^*}{2} \cdot (\sin \vartheta - \sin \vartheta_{in}) + z_{0,1} - z_{el,in} \right)^n \cdot \sin \vartheta \cdot d\vartheta \end{aligned} \right\} \quad (3.32)$$

$$F_Z = F_{Z,in} + F_{Z,pl} + F_{Z,out} \quad (3.33)$$

3.2.5 Rolling Resistance

Similar to the rigid wheel model, the external rolling resistance (F_{RE}) due to compaction of the terrain is computed by integrating the horizontal component of the normal pressure over the tyre contact patch, figure 3.10. Equation (3.34) is used to calculate rolling resistance in case of non-multi-pass, while equation (3.35) is used for the multi-pass case:

$$F_{RE} = b \cdot K \cdot \left(\frac{z_{0,1}^{n+1}}{n+1} - \frac{1}{2} \cdot z_{0,1}^n \cdot z_{el,out} \right) \quad (3.34)$$

$$F_{RE} = b \cdot K \cdot \left(\frac{z_{0,i}^{n+1} - z_{0,1}^{n+1}}{n+1} - \frac{1}{2} \cdot (z_{0,i}^n \cdot z_{el,out,i} - z_{0,1}^n \cdot z_{el,in,i}) \right) \quad (3.35)$$

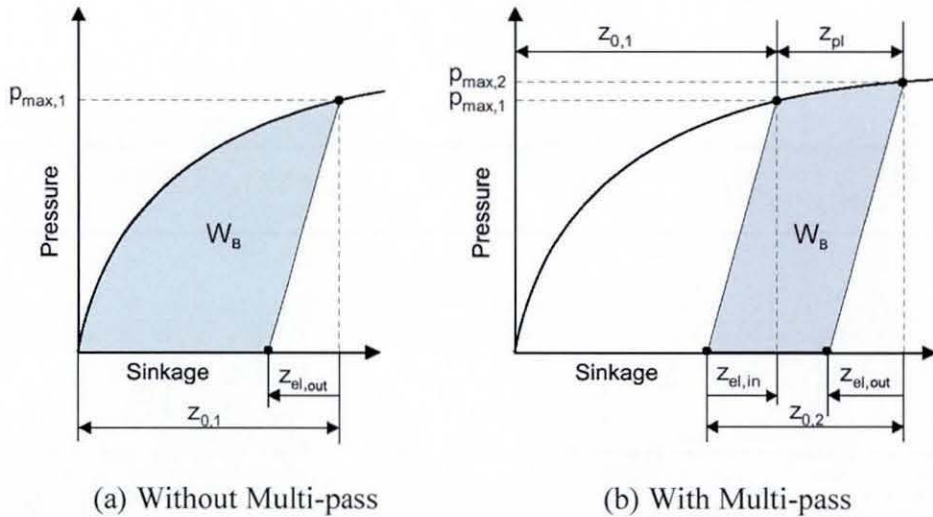


Figure 3.10 Rolling Resistances at High Slip Angles, adopted from (Harnisch, 2001)

Fundamentally, the external rolling resistance is always directed in opposite sense to the direction of travel. Furthermore, the change in track width due to high slip angle is taken into account. At high slip angles, the external rolling resistance has a lateral force component which is added to the lateral force caused by shear deformation, figure 3.11. In addition to the external rolling resistance, the internal rolling resistance (F_{RI}) due to the flexing work of the tyre (hysteresis losses) is also taken into account. It should be noted that, this portion of the rolling resistance does not affect the transmission of forces in the contact patch, equation (3.41). where (α) is the lateral slip angle.

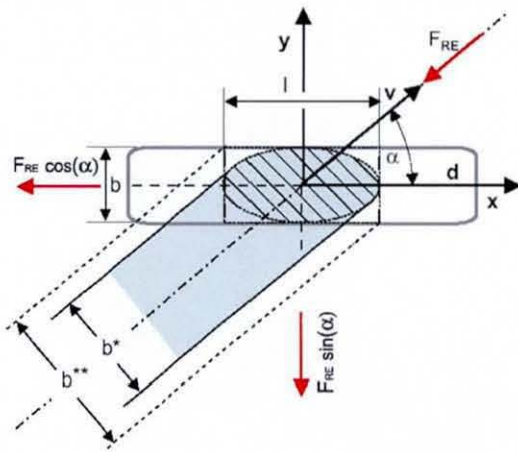


Figure 3.11 Rolling Resistances at High Slip Angles, adopted from (AESCO, 2005)

3.2.6 Drive Torque and Tractive Force

Both the wheel driving torque (M_D) and the tractive force (F_x) are calculated based on the local pressure ($p(\vartheta)$) and the local shear displacement ($j_l(\vartheta)$) in the contact patch. A method for the calculation of local shear displacement of rigid wheel was proposed by Wong and Reece (1967a, 1967b). This method is based on the analysis of slip velocity of a point (p) on the wheel circumference relative to the terrain, figure 3.12. The local differences between these speeds in the contact area are integrated over time to calculate the local shearing deformations, see equations (2.8) and (2.9):

$$j_l(\vartheta) = \frac{D}{2} \cdot \left((\vartheta_{el,out} - \vartheta_{in}) + (1-i) \cdot (\cos \vartheta_{el,out} - \cos \vartheta_{el,in}) \right) \quad (3.36)$$

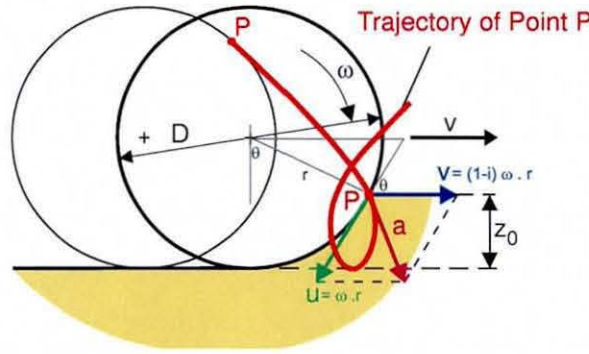


Figure 3.12 Trajectory of a Point on Tyre Circumference, adopted from (AESCO, 2005)

The slip returned by the model is calculated from internal values and matches the traditional slip definition only in stationary cases (V and ω are constant). There is no difference between pushed ($V \leq \omega \cdot r_d$) and pulled ($V > \omega \cdot r_d$) cases. Furthermore, it is considered that the soil is sheared rather than the tyre slipping over an invariable surface. The slip is limited to values between $(-1: +1)$ or $(\pm 100 \%)$ and can be calculated as:

$$i = \begin{cases} \frac{\omega \cdot r_d - V}{\omega \cdot r_d} & \rightarrow V \leq \omega \cdot r_d \\ \frac{V - \omega \cdot r_d}{V} & \rightarrow V > \omega \cdot r_d \end{cases} \quad (3.37)$$

Based on the local shearing displacement ($j_l(\vartheta)$), the local shear stress ($\tau(\vartheta)$) can be computed using equation (3.9) or alternatively equation (3.10). The integration of local shear stress ($\tau(\vartheta)$) over the contact patch gives the circumferential force (F_U) as:

$$F_U = b \cdot \left(\frac{D^*}{2} \right) \cdot \int_{\vartheta_m}^{\vartheta_{el, out}} (C + p(\vartheta) \cdot \tan \varphi) \cdot \left(1 - e^{\frac{-j_l(\vartheta)}{k}} \right) \cdot d\vartheta \quad (3.38)$$

The drive torque (M_D) is defined as a function of circumferential force (F_U), dynamic rolling radius (r_d), and internal flex-rolling (F_{Rl}) as:

$$M_D = M_U + I_w \cdot \dot{\omega} = (F_U + F_{Rl}) \cdot r_d + I_w \cdot \dot{\omega} \quad (3.39)$$

where $(\dot{\omega})$ is the rotational wheel acceleration and (I_w) is the wheel's mass moment of inertia around its spinning axle (i.e. polar moment of inertia). The rolling radius can be set to a fixed value or alternatively be defined by a mathematical function, which allows description of the dynamic rolling radius as a function of the wheel load (Hirschberg et al., 2002). Because of the curved contact patch there is a difference between the tractive force acting parallel to the ground surface and the circumferential force (F_U) , which acts parallel to the tyre surface.

The horizontal portion of local shear stress integration gives the tractive force as follows:

$$F_H = b \cdot \left(\frac{D^*}{2} \right) \cdot \int_{\vartheta_m}^{\vartheta_{el,out}} (C + p(\vartheta) \cdot \tan \varphi) \cdot \left(1 - e^{-\frac{j_l(\vartheta)}{k}} \right) \cdot \sin(\vartheta) \cdot d\vartheta \quad (3.40)$$

The net tractive force in longitudinal direction (F_x) can be computed as the difference between horizontal force and the external rolling resistance (F_{RE}) ; see figure 3.11.

$$F_x = F_H - F_{RE} \cdot \cos \alpha \quad (3.41)$$

3.2.7 Lateral Forces

Based on the local pressure $(p(\vartheta))$ under the wheel in combination with the local shear displacement in the lateral direction $(j_y(\vartheta))$, the local stress can be calculated. The results of integration of the local shear stress over the contact zone are the lateral and horizontal forces (F_{y_l}) . The mathematical approach for calculation of lateral forces is similar to the theory put forward by Schwanghart (1968), which also considers the influence of lateral force on the longitudinal force as has been proposed by Grecenko (1969). Figure 3.13 shows the basic principle for pure lateral force modelling.

$$F_{y_l} = b \cdot \left(\frac{D^*}{2} \right) \cdot \int_{\vartheta_m}^{\vartheta_{el,out}} (C + p(\vartheta) \cdot \tan \varphi) \cdot \left(1 - e^{-\frac{j_y(\vartheta)}{k}} \right) \cdot d\vartheta \quad (3.42)$$

According to the well known concept of friction circle, the dependencies between lateral and longitudinal forces are taken into account. Furthermore, the tyre lateral force is regulated by the maximum lateral shear displacement ($j_{y,max}$) and slip angle (α) as given by equation (3.43), where (l) is the tyre contact length, see figure 3.13.

$$j_{y,max} = l \cdot \tan \alpha \quad (3.43)$$

In addition to the lateral force induced by shear stress in the contact patch, a further lateral component (F_{y_2}) due to a bulldozing wave in the tyre side wall or the lateral component of rolling resistance, see figure 3.11, is also considered as follows:

$$F_{y_2} = F_{RE} \cdot \sin \alpha \quad (3.44)$$

The total lateral force (F_y) can thus be given as:

$$F_y = F_{y_1} + F_{y_2} \quad (3.45)$$

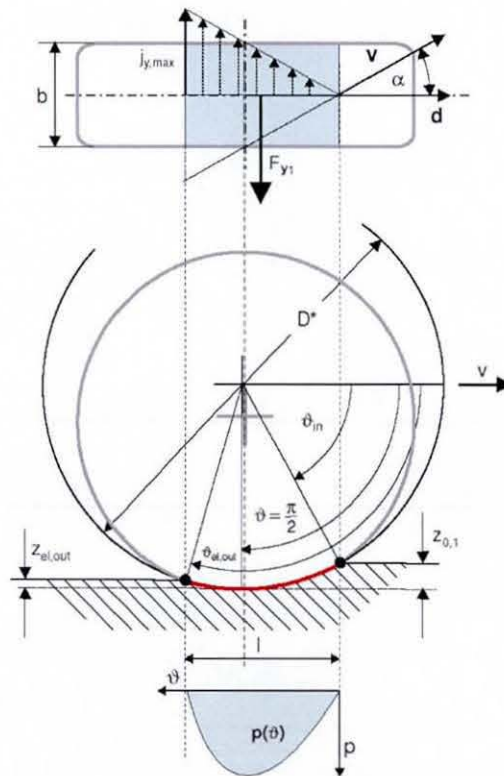


Figure 3.13 Calculations of the Lateral Forces (after AESCO, 2005).

3.2.8 Tyre Aligning Torque

Calculation of tyre aligning torque (M_z) is based on a simplified model using the local lateral shear stresses ($\tau_y(\vartheta)$) and the lever arm to the rotational axis ($h(\vartheta)$). The effect of lateral force component due to high slip angle is neglected. The local lever arm can be calculated according to the defined substitute circle dimensions, figure 3.14. The integration of the lateral shear stress multiplied by the lever arm over the contact area gives the tyre aligning torque as follows:

$$h(\vartheta) = \frac{D^*}{2} \cdot \cos \vartheta - \left(\sqrt{D \cdot (f_0 + z_{el,out}) - (f_0 + z_{el,out})^2} - x_0 \right) \quad (3.46)$$

$$M_z = b \cdot \left(\frac{D^*}{2} \right) \cdot \int_{\vartheta_{in}}^{\vartheta_{el,out}} h(\vartheta) \cdot \tau_y(\vartheta) \cdot d\vartheta \quad (3.47)$$

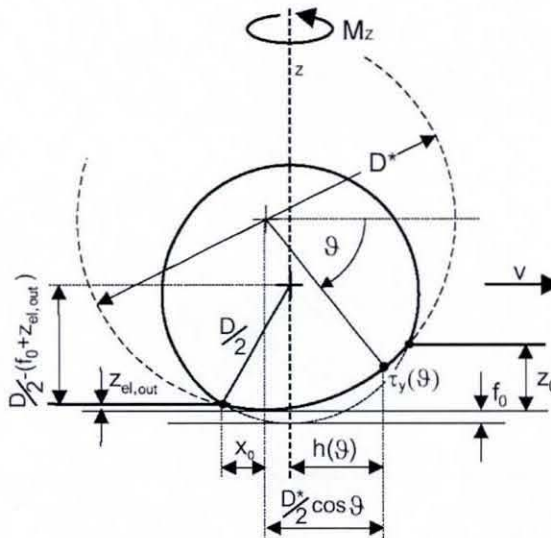


Figure 3.14 Principle of the Aligning Torque Calculation (after Harnisch (2001))

3.2.9 Slip Sinkage Effect

When the driving torque is applied at the wheel hub, both the longitudinal slip and the associated soil shearing deformation occur at the tyre-ground contact patch. At higher

driving torques, excessive slippage is generated, which causes additional sinkage called ‘*slip sinkage*’, mainly due to the wheel digging into the ground, figure 3.15. This phenomenon is mostly dependent on wheel slip (i), soil mechanical properties and tyre-soil contact area. For the calculation purposes two tyre parameters are required, the lug height (h_{st}) and the ratio between the positive and negative portion of the tyre tread (k_s). The basic idea of this model is to calculate the volume of the soil per unit time which is transported by the negative part of the tread. The slip sinkage (z_s) may thus be calculated as follow: (Ruff, 1997)

$$z_s = k_s \cdot h_{st} \cdot \left(\frac{i}{1-i} \right) \quad (3.48)$$

It should be noted that, the tyre model considers the additional rolling resistance due to slip sinkage, in addition to the effect of soil filling degree of the tyre tread.

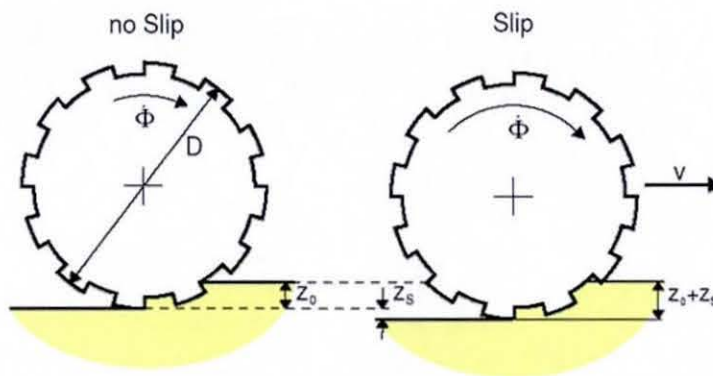


Figure 3.15 Principle of the Slip Sinkage Effect (after Ruff (1997))

3.2.10 Multi-pass Effect

Generally, in the field of off-road multi-axle vehicles, it is well known that, one of the most important effects is called the ‘*multi-pass effect*’. The multi-pass arises from the track or rut produced by a wheel which has rolled over the virgin terrain. Therefore, the wheel of the following axle will encounter conditions quite different from those of the first axle.

This phenomenon is mainly related to soil compaction and its response to repetitive loading as explained earlier in section 3.2.3.1. The multi-pass effect has a great impact in reducing the rolling resistance of the vehicle. In turn, both the mobility and fuel consumption are improved when driving on soft soils. The basic concept of multi-pass is depicted in figure 3.16. In the pre-compacted soil, the additional sinkage (Δz_{02}) of the wheel and the tyre contact length (l_2) is significantly lower, which translates to a lower rolling resistance.

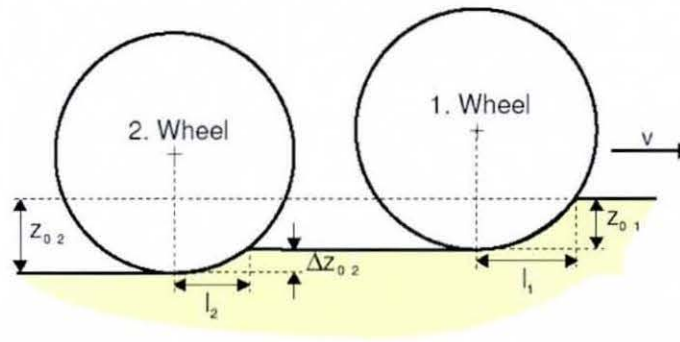


Figure 3.16 Principle of the Multi-pass Effect (after Ruff (1997))

For the calculation of multi-pass, it is assumed that the soil strength parameters do not change during compaction. The model for the multi-pass is based on the hypothesis that the pressure level of the following wheel has to be higher than that of the preceding wheel to cause an additional sinkage (Schmid, 1995; Ruff, 1994, 1997). Based on the assumptions of the rigid wheel model with a parabolic shape and neglecting the elasticity of the terrain, the numerical integration of the pressure distribution along the contact area is considered to be equivalent to the wheel load. Therefore, the additional static sinkage (Δz_{02}) due to multi-pass with vertical load (F_{z2}) for the follower wheel is calculated as:

$$\Delta z_{02} \approx \left(\frac{F_{z2}}{b \cdot K \cdot \sqrt{D} \cdot \sqrt{1 - \frac{\Delta z_{02}}{D} \cdot z_{01}^n} \cdot \left(1 + \frac{2 \cdot n}{3} \cdot \frac{\Delta z_{02}}{z_{01}} \right)} \right)^2 \quad (3.49)$$

With the assumption of elastic tyres with a parabolic shape on a compacted hard ground in the track, the pressure distribution in the contact area only depends on the tyre deformation not on the deformation of the ground. This requires an approach different from the method described above (Schmid and Ludewig, 1991). With this assumption, and based on experience, the maximum pressure is 25% higher than the average pressure. A simple equation for the additional sinkage is thus obtained as:

$$\left. \begin{aligned}
 p_2(x) &= p_{2_{\max}} \cdot \left(1 - \frac{16 \cdot x^4}{l_{h2}^4}\right) \\
 &= \underbrace{\left(1.25 \cdot \frac{F_{z2}}{b \cdot l_{h2}}\right)}_{p_{2_{\max}}} \cdot \left(1 - \frac{16 \cdot x^4}{l_{h2}^4}\right) \\
 \Delta z_{02} &= \left(1.25 \cdot \frac{F_{z2}}{b \cdot l_{h2}}\right)^{\frac{1}{n}}
 \end{aligned} \right\} \quad (3.50)$$

where (l_{h2}) is the equivalent contact length of the tyre, measured on the hard surface.

3.2.11 Influence of Friction between Tyre and Soil

The maximum shear strength of the soil (τ_{\max}) is calculated by the model in two different ways. The first is based on Coulomb friction, given by equation (3.8). The second is based on the adhesion between the tyre and the soil, which can be expressed as a function of the normal pressure (p) and the coefficient of friction (μ_{ts}) (Bekker, 1960):

$$\tau_{\max} = p \cdot \mu_{ts} \quad (3.51)$$

The typical range of the coefficient of friction is (0.3 : 1.0) and depends on the soil mechanical properties and the material of the tyre. The maximum shear strength is calculated according to the minimum value of adhesion, equation (3.51), and the internal soil friction, equation (3.8), thus:

$$\tau_{\max} = \min((C + p \cdot \tan \varphi) , p \cdot \mu_{ts}) \quad (3.52)$$

3.2.12 Influence of the Tyre Tread

The effect of tyre tread is taken into consideration in the model by the inclusion of two different parameters; the lug height and the profile factor (the relation between the positive and negative portions of the tyre tread). The basic idea of the model is to separate the calculations of normal pressure, as well as shear strength according to the positive and negative portions of the tread. In the area under the lug, the shear strength of the soil is calculated by equation (3.51) according to normal pressure (p_1). Between the lugs, the maximum shear strength of the soil is calculated by equation (3.8) according to normal pressure (p_2).

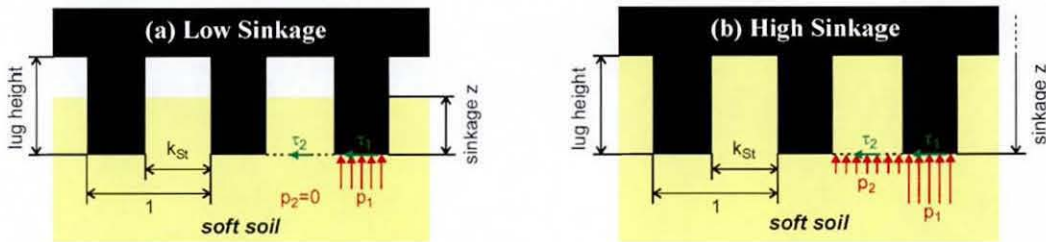


Figure 3.17 Tyre Tread Model (after Harnisch et al, 2003)

Furthermore, the effect of soil filling of the tyre tread is taken into account, see figure 3.17. The results obtained by Harnisch et al. (2003) show that, both the tyre tread profile factor and lug height have a high influence on the drive torque, as well as the rolling resistance. Figure 3.18 shows the general algorithm of the tyre model computational structure:

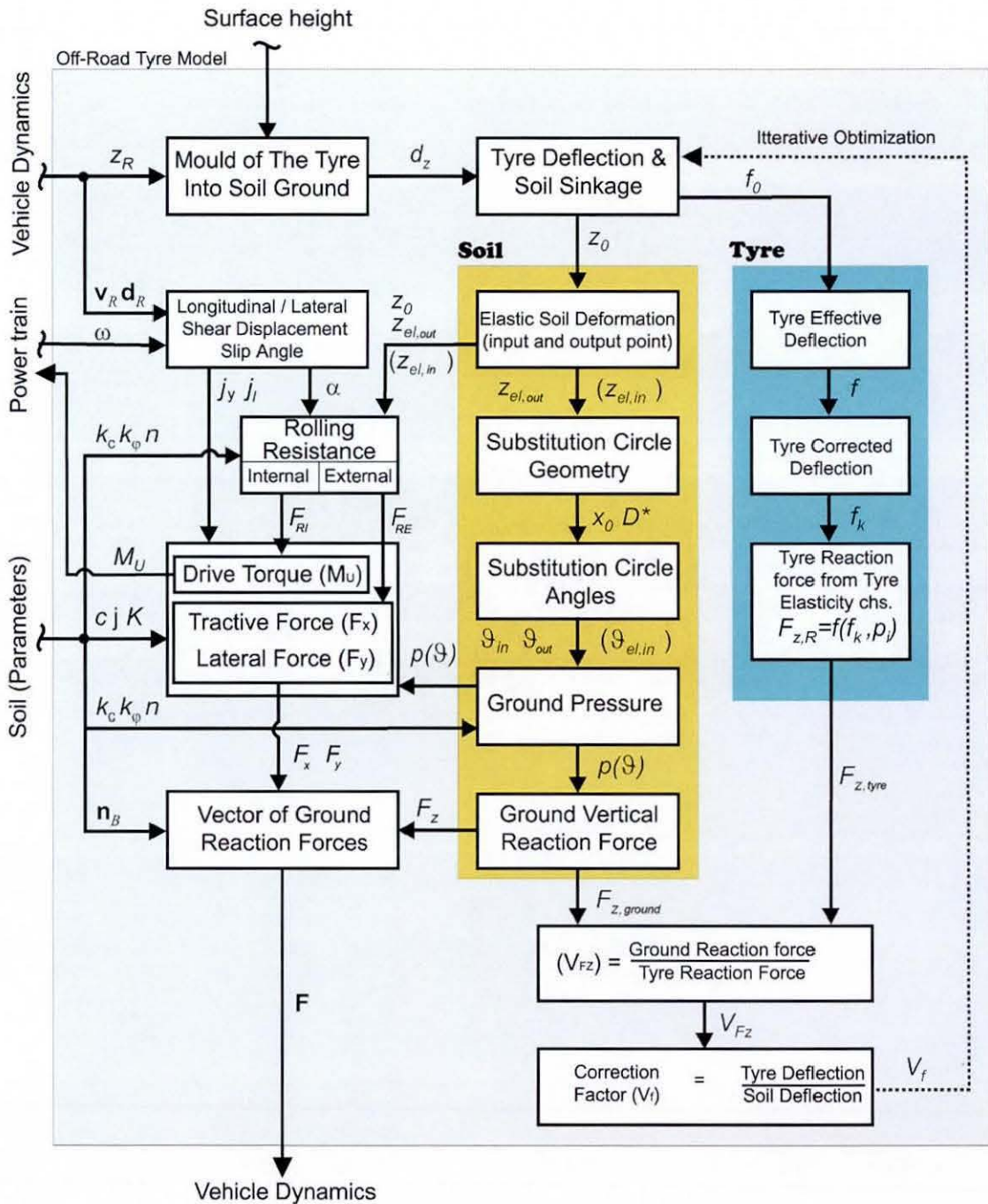


Figure 3.18 Computational Structure of AS²TM Off-Road Tyre Model
Adopted from (Harnisch, 2001)

3.3 Equations of Motion of the Vehicle's Body

Based on the Newton-Euler approach, the general form of the equations of motion of a rigid body with six degrees of freedom is derived from the first principles. The mathematical derivation is carried out for an elementary particle and then integrated over all the full rigid body to include the effect of the external forces and moments. The velocity and acceleration are defined with respect to two frames of reference. Furthermore, relative transformations are used to transform the data between these frames of reference.

3.3.1 General Motion of a Particle

The general motion of a particle (\mathbf{p}) in space may be described by considering two frames of reference as shown in figure 3.19. The global frame of reference is defined by (R_i) or (O_i, x_i, y_i, z_i) , while the local frame of reference is defined by (R_j) or (O_j, x_j, y_j, z_j) .

It is anticipated that, the local frame of reference may be moving with respect to the global frame through translational and/or rotational motions. Referring to figure 3.19, the position of the particle (\mathbf{p}) can be defined with respect to each frame of reference according to the following position vectors:

\mathbf{s}_j : Position vector of the particle (\mathbf{p}) with respect to the local frame of reference (R_j)

\mathbf{s}_i : Position vector of the particle (\mathbf{p}) with respect to the global frame of reference (R_i)

\mathbf{e} : Position vector of the origin (O_j) with respect to the global frame of reference (R_i)

The general relationship between all the aforementioned vectors can be written as follow:

$$\mathbf{s}_i = \mathbf{e} + \mathbf{s}_j \quad (3.53)$$

The time rate of change of the position vector (\mathbf{s}_j) with respect to the local frame of reference can be expressed by $(ds_j/dt)_{R_j}$. The time rate of change of the same position vector with respect to the global frame of reference can be expressed by the following equation (Rahnejat, 1998):

$$\left(\frac{ds_j}{dt} \right)_{R_i} = \left(\frac{ds_j}{dt} \right)_{R_j} + \boldsymbol{\Omega} \times \mathbf{s}_j \quad (3.54)$$

Where $(\boldsymbol{\Omega})$ is the rotational velocity vector of the local frame of reference.

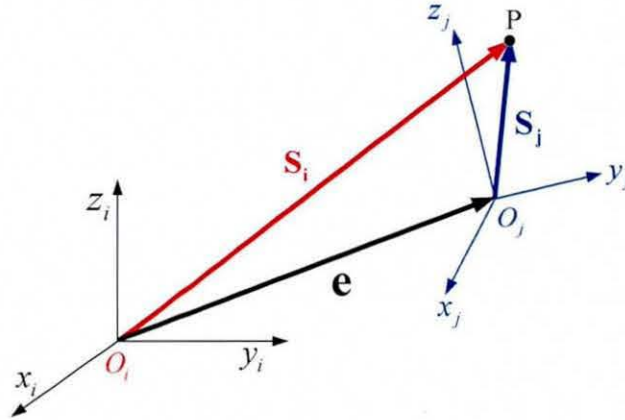


Figure 3.19 Motion of a Point as Sensed in the Global Frame of Reference

The following mathematical expressions are used to discriminate between the rate of change of a vector with respect to the global and local frames of reference:

$\frac{D(\)}{Dt} = \left(\frac{d(\)}{dt} \right)_{R_i}$: means time derivative of a vector relative to the global frame (R_i).

$\frac{d(\)}{dt} = \left(\frac{d(\)}{dt} \right)_{R_j}$: means time derivative of a vector relative to the local frame (R_j).

The velocity of the particle (p) with respect to the global frame reference (R_i) results from the differentiation of the position vector (\mathbf{s}_i) with respect to time. Referring to figure 3.19, the following relations are applied:

$$\left. \begin{aligned} \frac{D\mathbf{s}_i}{Dt} &= \frac{D\mathbf{e}}{Dt} + \frac{D\mathbf{s}_j}{Dt} \\ \frac{D\mathbf{s}_i}{Dt} &= \frac{D\mathbf{e}}{Dt} + \left(\frac{ds_j}{dt} + \boldsymbol{\Omega} \times \mathbf{s}_j \right) \\ \mathbf{V}_i(\mathbf{P}) &= \mathbf{V}_i(\mathbf{O}_j) + \mathbf{V}_j(\mathbf{P}) + \boldsymbol{\Omega} \times \mathbf{s}_j \end{aligned} \right\} \quad (3.55)$$

A similar procedure is carried out for the derivation of acceleration, knowing that acceleration is the time rate of change of the velocity vector. Equation (3.54) is applied to the velocity vector assuming that $(\mathbf{V}_i(O_j) = 0)$:

$$\begin{aligned}
 \frac{D^2 \mathbf{s}_i}{Dt^2} &= \frac{D}{Dt} \left(\frac{D\mathbf{s}_i}{Dt} \right) = \frac{D}{Dt} \left(\frac{d\mathbf{s}_j}{dt} + \boldsymbol{\Omega} \times \mathbf{s}_j \right) \\
 &= \frac{d}{dt} \left(\frac{d\mathbf{s}_j}{dt} + \boldsymbol{\Omega} \times \mathbf{s}_j \right) + \boldsymbol{\Omega} \times \left(\frac{d\mathbf{s}_j}{dt} + \boldsymbol{\Omega} \times \mathbf{s}_j \right) \\
 &= \frac{d^2 \mathbf{s}_j}{dt^2} + \frac{d}{dt} (\boldsymbol{\Omega} \times \mathbf{s}_j) + \boldsymbol{\Omega} \times \left(\frac{d\mathbf{s}_j}{dt} \right) + \boldsymbol{\Omega} \times (\boldsymbol{\Omega} \times \mathbf{s}_j) \\
 &= \underbrace{\frac{d^2 \mathbf{s}_j}{dt^2}}_{\text{Linear Acceleration}} + \underbrace{\left(\frac{d\boldsymbol{\Omega}}{dt} \right) \times \mathbf{s}_j}_{\text{Tangential Acceleration}} + \underbrace{\boldsymbol{\Omega} \times (\boldsymbol{\Omega} \times \mathbf{s}_j)}_{\text{Centripetal Acceleration}} + \underbrace{2 \cdot \boldsymbol{\Omega} \times \left(\frac{d\mathbf{s}_j}{dt} \right)}_{\text{Coriolis Acceleration}}
 \end{aligned} \tag{3.56}$$

3.3.2 Relative Transforms in Rigid-Body Kinematics

Fundamentally, kinematics of a rigid body is concerned with the analysis of position, velocity and acceleration of the body. Since the aforementioned vectors are relative, it is often necessary to define them with respect to the frames of reference. For this purpose it is essential to apply relative transforms, as a convenient way to switch between frames of reference. Ellis (1994) and Rahnejat (1998) describe the general theory of translational and rotational transformations that are used for expressing vector components in different frames of reference that are moving with respect to each other.

It is possible to move from a local frame of reference (R_j) to the global frame of reference (R_i) using three sequential rotations and a linear translation of (R_j) until (R_j) coincides with (R_i) . It should be noted that in this specific case, each rotation takes place with respect to the previous frame of reference, not the initial frame of reference. The transformation is, therefore, called ‘relative’. Each rotation results in a new set of axes, which are related to the previous set of axes by a transformation matrix (\mathbf{L}) , figure 3.21.

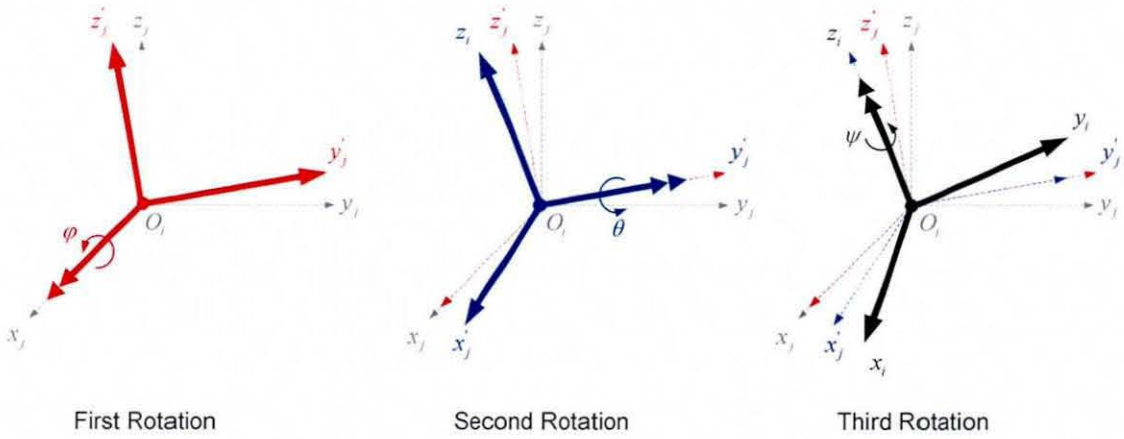


Figure 3.20 Relative Transformation between two Inertial Frames of References

The characterisation of the transformation by the sequence of numbers “1-2-3” implies that the first rotation is about x-axis ‘Roll’, the second about y-axis ‘Pitch’ and the third about z-axis ‘Yaw’. The frame transformation consists of the following steps:

- (1) Linear translation ($-\mathbf{e}$) resulting coincidence of (O_j) with (O_i) .
- (2) 1st rotation (φ) about axis (O_i, x_j) resulting to the frame (O_i, x'_j, y'_j, z'_j) as follows:

$$\begin{pmatrix} x'_j \\ y'_j \\ z'_j \end{pmatrix} = \underbrace{\begin{pmatrix} 1 & 0 & 0 \\ 0 & \cos \varphi & -\sin \varphi \\ 0 & \sin \varphi & \cos \varphi \end{pmatrix}}_{\text{Roll: } \mathbf{L}(\varphi)} \begin{pmatrix} x_j \\ y_j \\ z_j \end{pmatrix} \quad (3.57)$$

- (3) 2nd rotation (θ) about axis (O_i, y'_j) resulting to the frame (O_i, x''_j, y'_j, z_i) as follows:

$$\begin{pmatrix} x''_j \\ y'_j \\ z_i \end{pmatrix} = \underbrace{\begin{pmatrix} \cos \theta & 0 & \sin \theta \\ 0 & 1 & 0 \\ -\sin \theta & 0 & \cos \theta \end{pmatrix}}_{\text{Pitch: } \mathbf{L}(\theta)} \underbrace{\begin{pmatrix} 1 & 0 & 0 \\ 0 & \cos \varphi & -\sin \varphi \\ 0 & \sin \varphi & \cos \varphi \end{pmatrix}}_{\text{Roll: } \mathbf{L}(\varphi)} \begin{pmatrix} x_j \\ y_j \\ z_j \end{pmatrix} \quad (3.58)$$

(4) 3rd rotation (ψ) about axis ($O_i z_i$) resulting in coincidence with the frame ($R_i = O_i x_j y_j z_j$) as follows:

$$\begin{pmatrix} x_i \\ y_i \\ z_i \end{pmatrix} = \underbrace{\begin{pmatrix} \cos \psi & -\sin \psi & 0 \\ \sin \psi & \cos \psi & 0 \\ 0 & 0 & 1 \end{pmatrix}}_{\text{Yaw: } L(\psi)} \underbrace{\begin{pmatrix} \cos \theta & 0 & \sin \theta \\ 0 & 1 & 0 \\ -\sin \theta & 0 & \cos \theta \end{pmatrix}}_{\text{Pitch: } L(\theta)} \underbrace{\begin{pmatrix} 1 & 0 & 0 \\ 0 & \cos \phi & -\sin \phi \\ 0 & \sin \phi & \cos \phi \end{pmatrix}}_{\text{Roll: } L(\phi)} \cdot \begin{pmatrix} x_j \\ y_j \\ z_j \end{pmatrix} \quad (3.59)$$

The resulting matrix (\mathbf{T}) shown below is obtained by multiplying the three transformation matrices in the following order: ($\mathbf{T} = \mathbf{L}(\phi, \theta, \psi) = \mathbf{L}(\psi)\mathbf{L}(\theta)\mathbf{L}(\phi)$):

$$\mathbf{T} = \begin{pmatrix} \cos \theta \cdot \cos \psi & \sin \theta \cdot \sin \phi \cdot \cos \psi - \cos \phi \cdot \sin \psi & \sin \theta \cdot \cos \phi \cdot \cos \psi + \sin \phi \cdot \sin \psi \\ \cos \theta \cdot \sin \psi & \sin \theta \cdot \sin \phi \cdot \sin \psi + \cos \phi \cdot \cos \psi & \sin \theta \cdot \cos \phi \cdot \sin \psi - \sin \phi \cdot \cos \psi \\ -\sin \theta & \cos \theta \cdot \sin \phi & \cos \theta \cdot \cos \phi \end{pmatrix} \quad (3.60)$$

If angles (ϕ, θ, ψ) are relatively small, the above matrix can be simplified to the one shown below, since ($\cos(\phi, \theta, \psi) \approx 1$) and ($\sin(\phi, \theta, \psi) \approx \phi, \theta, \psi$):

$$\mathbf{T} = \begin{pmatrix} 1 & -\psi & \theta \\ \psi & 1 & -\phi \\ -\theta & \phi & 1 \end{pmatrix} \quad (3.61)$$

3.3.3 Kinematic Equations of the Vehicle Body

The kinematic relations for the vehicle body are obtained by considering two frames of reference, as shown in figure 3.22. Global (fixed) frame of reference (R_i) and local (moving) frame of reference attached to the vehicle body (R_j). Obviously, (R_j) is a moving frame of reference, thus, its position and orientation changes continually with respect to the fixed global frame of reference. The considered axis system is right handed. The positive rotation is clockwise around the axis when viewed from the origin along the positive direction. $[U \ V \ W]^T$ is the translational velocity vector including longitudinal,

lateral and vertical component of the origin of the local frame of reference. $[p \ q \ r]^T$ is the angular velocity vector including roll, pitch and yaw components around the local frame of reference coordinates.

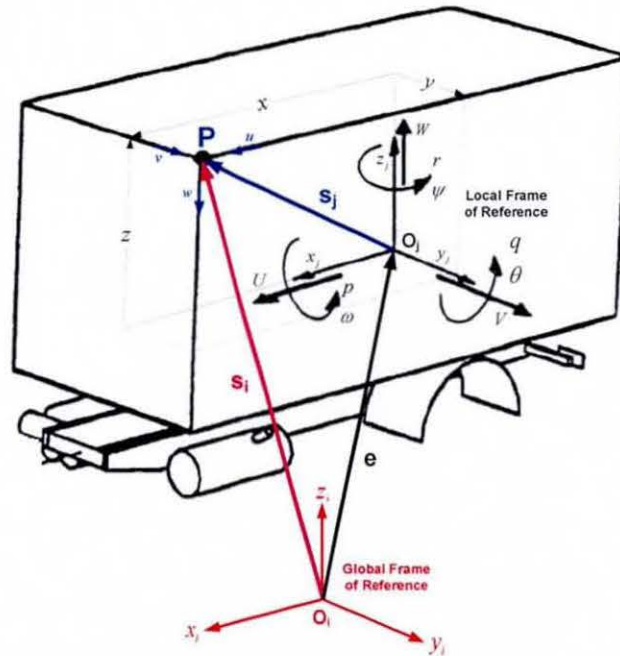


Figure 3.21 Application of the Kinematic Equations on the Study of Vehicle Dynamics

The velocity and acceleration of a point (p) on the vehicle body can be found by applying the kinematic equations in a matrix form. All velocities and accelerations are calculated with respect to the global frame of reference (R_i). Nevertheless, it is much more convenient to use the projection of these velocities to the local (moving) frame of reference (R_j). In this way, one can gain a better perception of the situation, as it is very important to know the velocity vectors in certain directions, specified by the local frame of reference attached to the vehicle body.

For the study of vehicle motion, equation (3.54) can be rewritten in a matrix form. In this case (s_j) represents the space vector of a point (p) of the vehicle with respect to the local (vehicle attached) frame, while (Ω) represents the space vector of the rotational velocity of the local frame of reference. Attention should be paid to the fact that while the velocity

obtained in equation (3.54) is sensed with respect to the global frame of reference, the actual components are still written for the local frame of reference (R_j). Consequently, equation (3.55) is half written for the global frame of reference ($\mathbf{V}_i(O_j)$) and half written for the local (moving) frame of reference ($\mathbf{V}_j(P) + \boldsymbol{\Omega} \times \mathbf{s}_j$).

Equation (3.55) includes the translational motion of the origin of the local frame of reference. In order to write this equation for the global frame of reference, it is essential to multiply the second term by the transformation matrix \mathbf{L} , so that the components of the rotational velocities are projected to the global frame of reference as:

$$\mathbf{V}_i(P) = \mathbf{V}_i(O_j) + \mathbf{L}(\mathbf{V}_j(P) + \boldsymbol{\Omega} \times \mathbf{s}_j) \quad (3.62)$$

Equation (3.62) represents the velocity of a point (p) on the vehicle, with respect to the global frame of reference. This velocity should now be projected onto the local frame of reference. This is achieved by pre-multiplying the velocity by the inverted transformation matrix (\mathbf{L}^{-1}) as follows:

$$\left. \begin{aligned} \mathbf{V}_j(P) &= \mathbf{L}^{-1} \cdot \mathbf{V}_i(P) = \mathbf{L}^{-1} [\mathbf{V}_i(O_j) + \mathbf{L}(\mathbf{V}_j(P) + \boldsymbol{\Omega} \times \mathbf{s}_j)] \\ &= \mathbf{L}^{-1} \mathbf{V}_i(O_j) + \mathbf{L}^{-1} \mathbf{L} (\mathbf{V}_j(P) + \boldsymbol{\Omega} \times \mathbf{s}_j) \\ &= \mathbf{L}^{-1} \mathbf{V}_i(O_j) + (\mathbf{V}_j(P) + \boldsymbol{\Omega} \times \mathbf{s}_j) \end{aligned} \right\} \quad (3.63)$$

Equation (3.63) is written in a condensed matrix form. It is easy to obtain the velocity components in all three directions in the local frame of reference, as follows:

Let $[UVW]^T$ be the projections of the translational velocity to the local frame of reference, so that $([U \ V \ W]^T = \mathbf{L}^{-1} \mathbf{V}_i(O_j))$. Also, let $(\boldsymbol{\Omega} = [\omega_x \ \omega_y \ \omega_z]^T = [p \ q \ r]^T)$.

The components of the velocity in the directions of the local axes can be written as:

$$\begin{bmatrix} u \\ v \\ w \end{bmatrix} = \begin{bmatrix} U \\ V \\ W \end{bmatrix} + \begin{bmatrix} dx/dt \\ dy/dt \\ dz/dt \end{bmatrix} + \begin{bmatrix} z \cdot q - y \cdot r \\ x \cdot r - z \cdot p \\ y \cdot p - x \cdot q \end{bmatrix} \quad (3.64)$$

Because point (p) belongs to the vehicle, which is considered as a rigid body, the middle term of the right hand-side of the above equation diminishes. Thus, the velocity becomes:

$$\begin{bmatrix} u \\ v \\ w \end{bmatrix} = \begin{bmatrix} U \\ V \\ W \end{bmatrix} + \begin{bmatrix} z \cdot q - y \cdot r \\ x \cdot r - z \cdot p \\ y \cdot p - x \cdot q \end{bmatrix} \quad (3.645)$$

In order to calculate the acceleration of point (p) one can start from equation (3.59):

$$\begin{aligned} \mathbf{a}_p &= \frac{d}{dt} \mathbf{V}_i(P) = \frac{d}{dt} (\mathbf{L}^{-1} \mathbf{V}_i(O_j) + (\mathbf{V}_i(P) + \boldsymbol{\Omega} \times \mathbf{s}_j)) \\ &= \frac{d}{dt} \mathbf{L}^{-1} \mathbf{V}_i(O_j) + \frac{d}{dt} (\mathbf{V}_i(P) + \boldsymbol{\Omega} \times \mathbf{s}_j) \\ &= \frac{d}{dt} \mathbf{L}^{-1} \mathbf{V}_i(O_j) + \frac{d}{dt} \left(\frac{d\mathbf{s}_j}{dt} + \boldsymbol{\Omega} \times \mathbf{s}_j \right) \\ &= \frac{d}{dt} \mathbf{L}^{-1} \mathbf{V}_i(O_j) + \frac{d^2 \mathbf{s}_j}{dt^2} + \left(\frac{d\boldsymbol{\Omega}}{dt} \right) \times \mathbf{s}_j + 2 \cdot \boldsymbol{\Omega} \times \left(\frac{d\mathbf{s}_j}{dt} \right) + \boldsymbol{\Omega} \times (\boldsymbol{\Omega} \times \mathbf{s}_j) \\ &= \frac{d}{dt} \mathbf{L}^{-1} \mathbf{V}_i(O_j) + \boldsymbol{\Omega} \times \mathbf{L}^{-1} \mathbf{V}_i(O_j) + \frac{d^2 \mathbf{s}_j}{dt^2} + \left(\frac{d\boldsymbol{\Omega}}{dt} \right) \times \mathbf{s}_j + 2 \cdot \boldsymbol{\Omega} \times \left(\frac{d\mathbf{s}_j}{dt} \right) + \boldsymbol{\Omega} \times (\boldsymbol{\Omega} \times \mathbf{s}_j) \end{aligned} \quad (3.66)$$

The above equation can be written in matrix form as follows:

$$\begin{pmatrix} A_x \\ A_y \\ A_z \end{pmatrix} = \begin{pmatrix} \frac{dU}{dt} \\ \frac{dV}{dt} \\ \frac{dW}{dt} \end{pmatrix} + \begin{pmatrix} -V \cdot r + W \cdot q \\ -W \cdot p + U \cdot r \\ -U \cdot q + V \cdot p \end{pmatrix} + \begin{pmatrix} -x \cdot (q^2 + r^2) + y \cdot \left(p \cdot q - \frac{dr}{dt} \right) + z \cdot \left(p \cdot r + \frac{dq}{dt} \right) \\ -y \cdot (r^2 + p^2) + z \cdot \left(q \cdot r - \frac{dp}{dt} \right) + x \cdot \left(p \cdot q + \frac{dr}{dt} \right) \\ -z \cdot (p^2 + q^2) + x \cdot \left(p \cdot r - \frac{dq}{dt} \right) + y \cdot \left(q \cdot r + \frac{dp}{dt} \right) \end{pmatrix} \quad (3.67)$$

Or as separate equations as follows:

$$\begin{aligned} A_x &= \frac{dU}{dt} - V \cdot r + W \cdot q - x \cdot (q^2 + r^2) + y \cdot \left(p \cdot q - \frac{dr}{dt} \right) + z \cdot \left(p \cdot r + \frac{dq}{dt} \right) \\ A_y &= \frac{dV}{dt} - W \cdot p + U \cdot r - y \cdot (r^2 + p^2) + z \cdot \left(q \cdot r - \frac{dp}{dt} \right) + x \cdot \left(p \cdot q + \frac{dr}{dt} \right) \\ A_z &= \frac{dW}{dt} - U \cdot q + V \cdot p - z \cdot (p^2 + q^2) + x \cdot \left(p \cdot r - \frac{dq}{dt} \right) + y \cdot \left(q \cdot r + \frac{dp}{dt} \right) \end{aligned} \quad (3.68)$$

3.3.4 Dynamic Equations of Motion

Since the velocity and acceleration of a point fixed to a body moving with six degrees of freedom are defined, the inertial equations can be obtained from a summation of the effects of the small elements of mass. The dynamic equations of motion are obtained by applying the Newton – Euler method as follows:

$$\left. \begin{aligned} \delta F_x &= D(\delta m \cdot u) / Dt \\ \delta F_y &= D(\delta m \cdot v) / Dt \\ \delta F_z &= D(\delta m \cdot w) / Dt \end{aligned} \right\} \quad (3.69)$$

Assuming that the vehicle's mass remains constant, the equations may be rewritten as:

$$\left. \begin{aligned} \delta F_x &= \delta m \cdot (Du / Dt) \\ \delta F_y &= \delta m \cdot (Dv / Dt) \\ \delta F_z &= \delta m \cdot (Dw / Dt) \end{aligned} \right\} \quad (3.70)$$

The effect of the sum of particles, which form the vehicle, is realised through integration:

$$\left. \begin{aligned} \int \delta F_x &= \int \delta m \cdot (Du / Dt) \\ \int \delta F_y &= \int \delta m \cdot (Dv / Dt) \\ \int \delta F_z &= \int \delta m \cdot (Dw / Dt) \end{aligned} \right\} \quad (3.71)$$

The following relations also apply:

$$\left. \begin{aligned} \int \delta m &= m \\ \int \delta m \cdot x &= m \cdot x_G \\ \int \delta m \cdot y &= m \cdot y_G \\ \int \delta m \cdot z &= m \cdot z_G \end{aligned} \right\} \quad (3.72)$$

Where (m) is the vehicle's total mass, $[x_G \ y_G \ z_G]^T$ is the vector of coordinates of the position of the vehicle centre of mass with respect to the moving frame of reference.

$$X = \Sigma F_x = \int \delta F_x \quad \text{is the sum of forces in the direction of axis } O_x \text{ of frame } (R_j)$$

$$Y = \Sigma F_y = \int \delta F_y \quad \text{is the sum of forces in the direction of axis } O_y \text{ of frame } (R_j)$$

$$Z = \Sigma F_z = \int \delta F_z \quad \text{is the sum of forces in the direction of axis } O_z \text{ of frame } (R_j)$$

Consequently, using equations (3.68) the following expressions for forces can be derived:

$$\left. \begin{aligned} \Sigma F_x &= m \cdot \left(\frac{dU}{dt} - V \cdot r + W \cdot q \right) - m \cdot \left[x_G \cdot (q^2 + r^2) - y_G \cdot \left(p \cdot q - \frac{dr}{dt} \right) - z_G \cdot \left(p \cdot r + \frac{dq}{dt} \right) \right] \\ \Sigma F_y &= m \cdot \left(\frac{dV}{dt} - W \cdot p + U \cdot r \right) - m \cdot \left[y_G \cdot (r^2 + p^2) - z_G \cdot \left(q \cdot r - \frac{dp}{dt} \right) - x_G \cdot \left(p \cdot q + \frac{dr}{dt} \right) \right] \\ \Sigma F_z &= m \cdot \left(\frac{dW}{dt} - U \cdot q + V \cdot p \right) - m \cdot \left[z_G \cdot (p^2 + q^2) - x_G \cdot \left(p \cdot r - \frac{dq}{dt} \right) - y_G \cdot \left(q \cdot r + \frac{dp}{dt} \right) \right] \end{aligned} \right\} \quad (3.73)$$

Euler moment equations for a single point (p) of the vehicle are expressed as:

$$\left. \begin{aligned} \delta M_x &= y \cdot [D \cdot (\delta m \cdot w) / Dt] - z \cdot [D \cdot (\delta m \cdot v) / Dt] \\ \delta M_y &= z \cdot [D \cdot (\delta m \cdot u) / Dt] - x \cdot [D \cdot (\delta m \cdot w) / Dt] \\ \delta M_z &= x \cdot [D \cdot (\delta m \cdot v) / Dt] - y \cdot [D \cdot (\delta m \cdot u) / Dt] \end{aligned} \right\} \quad (3.74)$$

By assuming again that the vehicle's mass is constant, the above equations can be written as follows:

$$\left. \begin{aligned} \delta M_x &= \delta m \cdot [y \cdot (Dw / Dt) - z \cdot (Dv / Dt)] \\ \delta M_y &= \delta m \cdot [z \cdot (Du / Dt) - x \cdot (Dw / Dt)] \\ \delta M_z &= \delta m \cdot [x \cdot (Dv / Dt) - y \cdot (Du / Dt)] \end{aligned} \right\} \quad (3.75)$$

Again, the effect of the sum of particles, which form the vehicle, is realised through integration:

$$\left. \begin{aligned} \int \delta M_x &= \int \delta m \cdot [y \cdot (Dw / Dt) - z \cdot (Dv / Dt)] \\ \int \delta M_y &= \int \delta m \cdot [z \cdot (Du / Dt) - x \cdot (Dw / Dt)] \\ \int \delta M_z &= \int \delta m \cdot [x \cdot (Dv / Dt) - y \cdot (Du / Dt)] \end{aligned} \right\} \quad (3.76)$$

Where L, M and N denote the sum of all moments in the direction of axes x,y,z respectively, so that:

$$L = \Sigma M_x = \int \delta M_x \quad \text{is the sum of moments in the direction of axis Ox of frame } (R_j)$$

$$M = \Sigma M_y = \int \delta M_y \quad \text{is the sum of moments in the direction of axis Oy of frame } (R_j)$$

$$N = \Sigma M_z = \int \delta M_z \quad \text{is the sum of moments in the direction of axis Oz of frame } (R_j)$$

$$\Sigma M_x = \int \delta m \cdot \left\{ \begin{aligned} &y \cdot \left[\frac{dW}{dt} - U \cdot q + V \cdot p - z \cdot (p^2 + q^2) + x \cdot \left(p \cdot r - \frac{dq}{dt} \right) + y \cdot \left(q \cdot r + \frac{dp}{dt} \right) \right] \\ &- z \cdot \left[\frac{dV}{dt} - W \cdot p + U \cdot r - y \cdot (r^2 + p^2) + z \cdot \left(q \cdot r - \frac{dp}{dt} \right) + x \cdot \left(p \cdot q + \frac{dr}{dt} \right) \right] \end{aligned} \right\} \quad (3.77)$$

$$\Sigma M_y = \int \delta m \cdot \left\{ \begin{aligned} &z \cdot \left[\frac{dU}{dt} - V \cdot r + W \cdot q - x \cdot (q^2 + r^2) + y \cdot \left(p \cdot q - \frac{dr}{dt} \right) + z \cdot \left(p \cdot r + \frac{dq}{dt} \right) \right] \\ &- x \cdot \left[\frac{dW}{dt} - U \cdot q + V \cdot p - z \cdot (p^2 + q^2) + x \cdot \left(p \cdot r - \frac{dq}{dt} \right) + y \cdot \left(q \cdot r + \frac{dp}{dt} \right) \right] \end{aligned} \right\} \quad (3.78)$$

$$\Sigma M_z = \int \delta m \cdot \left\{ \begin{aligned} &x \cdot \left[\frac{dV}{dt} - W \cdot p + U \cdot r - y \cdot (r^2 + p^2) + z \cdot \left(q \cdot r - \frac{dp}{dt} \right) + x \cdot \left(p \cdot q + \frac{dr}{dt} \right) \right] \\ &- y \cdot \left[\frac{dU}{dt} - V \cdot r + W \cdot q - x \cdot (q^2 + r^2) + y \cdot \left(p \cdot q - \frac{dr}{dt} \right) + z \cdot \left(p \cdot r + \frac{dq}{dt} \right) \right] \end{aligned} \right\} \quad (3.79)$$

Furthermore, the following relations apply for the mass and product moments of inertia:

$$\left. \begin{aligned}
 I_{xx} &= \int (y^2 + z^2) \cdot \delta m \\
 I_{yy} &= \int (x^2 + z^2) \cdot \delta m \\
 I_{zz} &= \int (x^2 + y^2) \cdot \delta m \\
 I_{yz} &= \int y \cdot z \cdot \delta m \\
 I_{zx} &= \int z \cdot x \cdot \delta m \\
 I_{xy} &= \int x \cdot y \cdot \delta m
 \end{aligned} \right\} \quad (3.80)$$

Introducing the definitions of mass and product moments of inertia into the Euler equations yields:

$$\left. \begin{aligned}
 \Sigma M_x &= I_{xx} \cdot \left(\frac{dp}{dt} \right) - (I_{yy} - I_{zz}) \cdot q \cdot r + I_{yz} \cdot (r^2 - q^2) - I_{zx} \cdot \left(p \cdot q + \frac{dr}{dt} \right) + I_{xy} \cdot \left(p \cdot r - \frac{dq}{dt} \right) \\
 &+ m \cdot y_G \cdot \left(\frac{dW}{dt} - U \cdot q + V \cdot p \right) - m \cdot z_G \cdot \left(\frac{dV}{dt} - W \cdot p + U \cdot r \right)
 \end{aligned} \right\} \quad (3.81)$$

$$\left. \begin{aligned}
 \Sigma M_y &= I_{yy} \cdot \left(\frac{dq}{dt} \right) - (I_{zz} - I_{xx}) \cdot p \cdot r + I_{xz} \cdot (p^2 - r^2) - I_{xy} \cdot \left(q \cdot r + \frac{dp}{dt} \right) + I_{yz} \cdot \left(q \cdot p - \frac{dr}{dt} \right) \\
 &+ m \cdot z_G \cdot \left(\frac{dU}{dt} - V \cdot r + W \cdot q \right) - m \cdot x_G \cdot \left(\frac{dW}{dt} - U \cdot q + V \cdot p \right)
 \end{aligned} \right\} \quad (3.82)$$

$$\left. \begin{aligned}
 \Sigma M_z &= I_{zz} \cdot \left(\frac{dr}{dt} \right) - (I_{xx} - I_{yy}) \cdot p \cdot q + I_{xy} \cdot (q^2 - p^2) - I_{yz} \cdot \left(r \cdot p + \frac{dq}{dt} \right) + I_{zx} \cdot \left(r \cdot q - \frac{dp}{dt} \right) \\
 &+ m \cdot x_G \cdot \left(\frac{dV}{dt} - W \cdot p + U \cdot r \right) - m \cdot y_G \cdot \left(\frac{dU}{dt} - V \cdot r + W \cdot q \right)
 \end{aligned} \right\} \quad (3.83)$$

Below, the six generic differential equations of motion obtained by the application of Newton-Euler method are grouped together:

$$\Sigma F_x = m \cdot \left(\frac{dU}{dt} - V \cdot r + W \cdot q \right) - m \cdot \left[x_G \cdot (\dot{q}^2 + r^2) - y_G \cdot \left(p \cdot q - \frac{dr}{dt} \right) - z_G \cdot \left(p \cdot r + \frac{dq}{dt} \right) \right] \quad (3.84)$$

$$\Sigma F_y = m \cdot \left(\frac{dV}{dt} - W \cdot p + U \cdot r \right) - m \cdot \left[y_G \cdot (r^2 + p^2) - z_G \cdot \left(q \cdot r - \frac{dp}{dt} \right) - x_G \cdot \left(p \cdot q + \frac{dr}{dt} \right) \right] \quad (3.85)$$

$$\Sigma F_z = m \cdot \left(\frac{dW}{dt} - U \cdot q + V \cdot p \right) - m \cdot \left[z_G \cdot (p^2 + q^2) - x_G \cdot \left(p \cdot r - \frac{dq}{dt} \right) - y_G \cdot \left(q \cdot r + \frac{dp}{dt} \right) \right] \quad (3.86)$$

$$\left. \begin{aligned} \Sigma M_x &= I_{xx} \cdot \left(\frac{dp}{dt} \right) - (I_{yy} - I_{zz}) \cdot q \cdot r + I_{yz} \cdot (r^2 - q^2) - I_{zx} \cdot \left(p \cdot q + \frac{dr}{dt} \right) + I_{xy} \cdot \left(p \cdot r - \frac{dq}{dt} \right) \\ &+ m \cdot y_G \cdot \left(\frac{dW}{dt} - U \cdot q + V \cdot p \right) - m \cdot z_G \cdot \left(\frac{dV}{dt} - W \cdot p + U \cdot r \right) \end{aligned} \right\} \quad (3.87)$$

$$\left. \begin{aligned} \Sigma M_y &= I_{yy} \cdot \left(\frac{dq}{dt} \right) - (I_{zz} - I_{xx}) \cdot p \cdot r + I_{xz} \cdot (p^2 - r^2) - I_{xy} \cdot \left(q \cdot r + \frac{dp}{dt} \right) + I_{yz} \cdot \left(q \cdot p - \frac{dr}{dt} \right) \\ &+ m \cdot z_G \cdot \left(\frac{dU}{dt} - V \cdot r + W \cdot q \right) - m \cdot x_G \cdot \left(\frac{dW}{dt} - U \cdot q + V \cdot p \right) \end{aligned} \right\} \quad (3.88)$$

$$\left. \begin{aligned} \Sigma M_z &= I_{zz} \cdot \left(\frac{dr}{dt} \right) - (I_{xx} - I_{yy}) \cdot p \cdot q + I_{xy} \cdot (q^2 - p^2) - I_{yz} \cdot \left(r \cdot p + \frac{dq}{dt} \right) + I_{zx} \cdot \left(r \cdot q - \frac{dp}{dt} \right) \\ &+ m \cdot x_G \cdot \left(\frac{dV}{dt} - W \cdot p + U \cdot r \right) - m \cdot y_G \cdot \left(\frac{dU}{dt} - V \cdot r + W \cdot q \right) \end{aligned} \right\} \quad (3.89)$$

By assuming that the centre of mass of the vehicle coincides with the origin (O_j) of the frame of reference, so $(x_G = y_G = z_G = 0)$. Also the vehicle is symmetrical about the plane defined by axes (O_jx) and (O_jz) , thus as a result $(I_{xy} = I_{yz} = 0)$. The above equations can be further simplified by introducing these relations into the generic equations as follows:

$$\Sigma F_x = m \cdot \left(\frac{dU}{dt} - V \cdot r + W \cdot q \right) \quad (3.90)$$

$$\Sigma F_y = m \cdot \left(\frac{dV}{dt} - W \cdot p + U \cdot r \right) \quad (3.91)$$

$$\Sigma F_z = m \cdot \left(\frac{dW}{dt} - U \cdot q + V \cdot p \right) \quad (3.92)$$

$$\Sigma M_x = I_{xx} \cdot \left(\frac{dp}{dt} \right) - (I_{yy} - I_{zz}) \cdot q \cdot r - I_{xz} \cdot \left(p \cdot q + \frac{dr}{dt} \right) \quad (3.93)$$

$$\Sigma M_y = I_{yy} \cdot \left(\frac{dq}{dt} \right) - (I_{zz} - I_{xx}) \cdot p \cdot r + I_{xz} \cdot (p^2 - r^2) \quad (3.94)$$

$$\Sigma M_z = I_{zz} \cdot \left(\frac{dr}{dt} \right) - (I_{xx} - I_{yy}) \cdot p \cdot q + I_{xz} \cdot \left(r \cdot q - \frac{dp}{dt} \right) \quad (3.95)$$

Chapter 4: 4x4 Off-Road Vehicle Model

Nowadays, implementing numerical simulation techniques in the process of vehicle development is an indispensable task. The exploitation of vehicle modelling in the commercial world has focused on either simplified models aimed at understanding fundamental issues or extremely complex models based on multi-body system dynamics' packages, e.g. ADAMS, aimed at understanding specific designs. Between these two extremes, however, it has become apparent that there is a class of models which can usefully be employed to explore design issues in relation to vehicle behaviour during different manoeuvres. While for on-road vehicles there are plenty of established codes covering this aspect, e.g. VDAS and veDYNA, there is a lack of similar tools for the off-road driving simulations.

The aim of this chapter is to present a medium degree of sophistication for 4x4 off-road vehicle models. Based on a multi-physics modelling approach, a full drivetrain system including all aspects of rotational inertial dynamics, friction, damping and stiffness properties is integrated within a fourteen-degrees-of-freedom vehicle model, including body dynamics, kinematics, suspension and wheel dynamics as well as the terramechanical phenomena between tyres and soft soils. The interaction between all these modules is implemented in the MATLAB/Simulink/SimDriveline environment.

The full integration of all these modules results in a multi-physics platform, which provides the design engineers with the capability to investigate the effects of various components and would aid the future development of control systems and automatic optimization of off-road 4x4 vehicles. The model is generic and appropriate for the simulation of a wide variety of conditions in the low-medium frequency range, including traction, ride and handling tests.

The contribution of a number of significant parameters on the traction performance as well as cornering response of 4x4 off-road vehicles are discussed, revealing the fidelity and robustness of the presented multi-physics vehicle model.

4.1 Physical Description of the Vehicle Model

Vehicle dynamics is concerned with the behaviour of vehicles through certain manoeuvres. In general, this behaviour may be described in terms of performance, ride and handling characteristics. Vehicle performance, in longitudinal direction, is mainly dependent on its power plant characteristics, drivetrain layout, tyre soil contact, and any employed control systems. Ride characteristics, in vertical direction, are devoted to the road surface profile and the induced vibration which affects passenger comfort. Handling characteristics, in lateral direction, are primarily concerned with the vehicle response to driver steering commands and its effect on the controllability and stability of the vehicle.

The vehicle response during certain manoeuvre is controlled by the forces imposed on the vehicle from the tyre-ground contact conditions, gravitational effect, and aerodynamics. For the theoretical analysis of vehicle dynamics, the equations of motion must be known, and the physical interactions between the various subsystems must be written in the form of mathematical expressions. The vehicle and its subsystems are modelled to determine what forces will be produced by each of these sources under particular manoeuvres.

For the purpose of numerical modelling, the vehicle is usually sub-divided into five masses. These are: the vehicle mass (sprung, or body mass concentrated at its centre of gravity) and located above the suspension springs, and four unsprung masses, which represent the assemblies: wheels, axles, and suspensions. The vehicle body is assumed to be rigid, with mass (m_s) and moments of inertia. The rigid body has six degrees of freedom, which includes three translations namely; forward velocity (U) in x_L -direction, lateral velocity (V) in y_L -direction and vertical velocity (W) in z_L -direction, in addition to three rotations namely; roll rate (p) about x_L -axis, pitch rate (q) about y_L -axis and yaw rate (r) about z_L -axis. The wheels are connected to the vehicle body via springs and shock absorbers. It is assumed that each wheel has two degrees of freedom, one for the vertical displacement (z_w), and the other for wheel rotational driving speed (ω_l). Thus, the total degrees of freedom are fourteen.

According to the SAE Recommended Practice System (SAE J670e), all the movements of the vehicle body are observed relative to the local/moving frame of reference, as shown in figure 4.1. The vehicle attitude and trajectory through the course of a manoeuvre are defined with respect to a right-handed orthogonal frame of reference, fixed on the ground, referred to as the global or fixed frame of reference. This is located directly beneath the local/moving coordinate system at the point, where the manoeuvre has commenced.

Another four coordinate systems for the wheels are added to represent each wheel motion independently. Transformations between all coordinates are based on relative transformations. The equations of motion for the non-linear, unsteady motion of the vehicle sprung mass are based on the Newton-Euler formulation for translational and rotational motions. These equations are derived with respect to the local frame of reference (see chapter 3 for the full mathematical derivation).

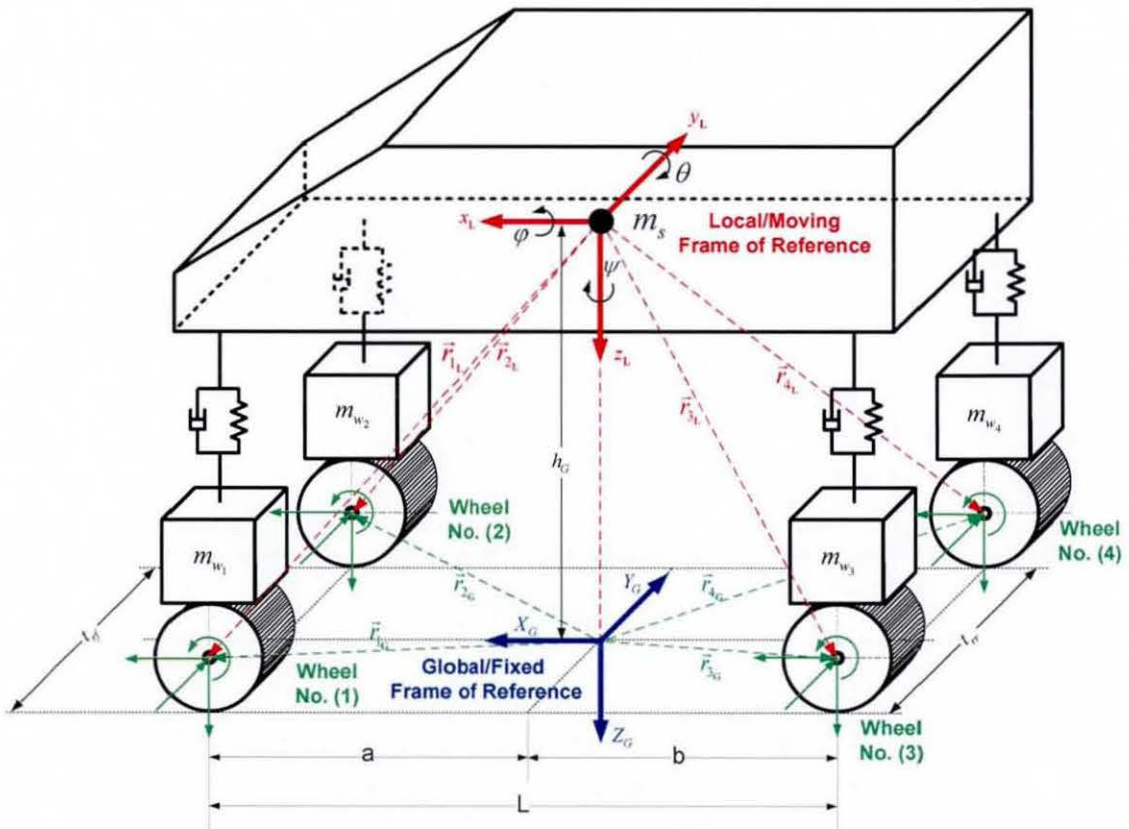


Figure 4.1 Vehicle Local, Wheels and Global/Fixed Frames of References

The forces and moments that govern the vehicle's motion are:

- Driving forces developed at the contact patch between the tyres and the terrain.
- Lateral forces on the tyres, as a result of the development of tyre slip angles.
- Tyre vertical forces resulting from the ground pressure-sinkage relationship.
- Rolling resistance forces (internal from the tyre and external from the terrain).
- Gravitational forces due to vehicle weight.
- Forces due to inclined or uneven roads.
- Aerodynamic force due to air resistance.
- Suspension system spring and damper forces.
- Soil damping force due to soil damping coefficient.
- All the moments that result from the aforementioned forces.

Figure 4.2 shows a free body diagram of the vehicle sprung and unsprung masses including all forces and moments affecting the vehicle motion.

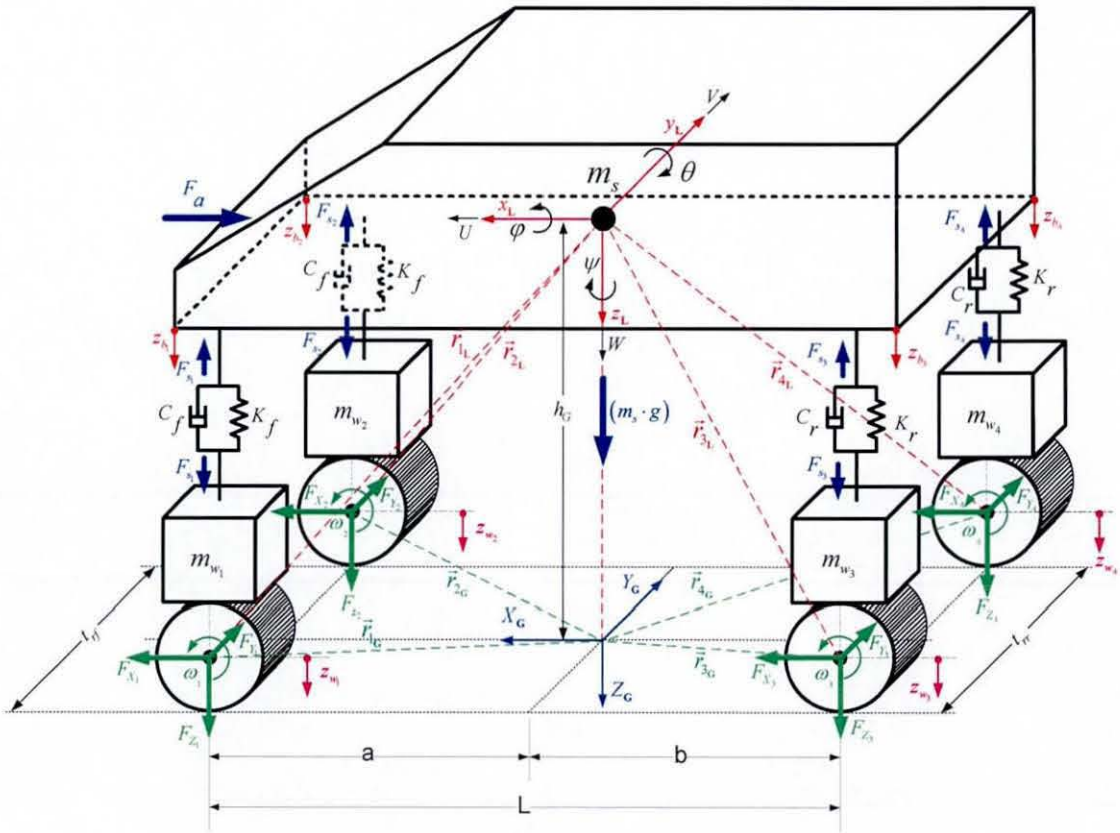


Figure 4.2 14-DOF 4x4 Off-Road Vehicle Model

4.2 Mathematical Derivation of the Vehicle Model

4.2.1 Sprung Mass Dynamics:

The general equations of motion of a body with six degrees of freedom are derived in chapter 3. Simplifications may be carried out by assuming the local frame of reference to be located at the vehicle sprung mass C.G. To further simplify the calculations, the vehicle is assumed to be symmetrical about the plane defined by axes x_L and z_L (Ellis, 1994). Based on the Newton-Euler formulation, the equations of motion of the vehicle sprung mass can be written in the following form:

$$\Sigma F_x = m_s \cdot (\dot{U} - V \cdot r + W \cdot q) \quad (4.1)$$

$$\Sigma F_y = m_s \cdot (\dot{V} - W \cdot p + U \cdot r) \quad (4.2)$$

$$\Sigma F_z = m_s \cdot (\dot{W} - U \cdot q + V \cdot p) \quad (4.3)$$

$$\Sigma M_x = I_{xx} \cdot \dot{p} - (I_{yy} - I_{zz}) \cdot q \cdot r - I_{xz} \cdot (p \cdot q + \dot{r}) \quad (4.4)$$

$$\Sigma M_y = I_{yy} \cdot \dot{q} - (I_{zz} - I_{xx}) \cdot r \cdot p + I_{xz} \cdot (p^2 - r^2) \quad (4.5)$$

$$\Sigma M_z = I_{zz} \cdot \dot{r} - (I_{xx} - I_{yy}) \cdot p \cdot q + I_{xz} \cdot (r \cdot q - \dot{p}) \quad (4.6)$$

In order to establish differential equations such that it would be more convenient to solve in MATLAB/ Simulink environment, the acceleration terms are separated on the left hand side and the rest of terms on the right hand side are rearranged as follows:

$$\text{Forward Dynamics : } m_s \cdot \dot{U} = \Sigma F_x - m_s \cdot (W \cdot q - V \cdot r) \quad (4.7)$$

$$\text{Lateral Dynamics : } m_s \cdot \dot{V} = \Sigma F_y - m_s \cdot (U \cdot r - W \cdot p) \quad (4.8)$$

$$\text{Vertical Dynamics : } m_s \cdot \dot{W} = \Sigma F_z - m_s \cdot (V \cdot p - U \cdot q) \quad (4.9)$$

$$\text{Roll Dynamics : } I_{xx} \cdot \dot{p} - I_{xz} \cdot \dot{r} = \Sigma M_x + (I_{yy} - I_{zz}) \cdot q \cdot r + I_{zx} \cdot p \cdot q \quad (4.10)$$

$$\text{Pitch Dynamics : } I_{yy} \cdot \dot{q} = \Sigma M_y + (I_{zz} - I_{xx}) \cdot r \cdot p - I_{xz} \cdot (p^2 - r^2) \quad (4.11)$$

$$\text{Yaw Dynamics : } I_{zz} \cdot \dot{r} - I_{zx} \cdot \dot{p} = \Sigma M_z + (I_{xx} - I_{yy}) \cdot p \cdot q - I_{zx} \cdot r \cdot q \quad (4.12)$$

All the terms in the right-hand side of equations (4.7) to (4.12) contain products of two unknown values of state variables which may be referred to as Gyroscopic terms, and hence they cannot be calculated directly from MATLAB. Otherwise neglecting these terms affects the accuracy of the results. Therefore, these terms are calculated downstream of the model in Simulink. The aforementioned six equations can be written in the following matrix form:

$$\left. \begin{aligned} \mathbf{A} \cdot [\dot{\mathbf{X}}] &= p \cdot \mathbf{A}_1 \cdot [\mathbf{X}] + q \cdot \mathbf{A}_2 \cdot [\mathbf{X}] + r \cdot \mathbf{A}_3 \cdot [\mathbf{X}] + [\mathbf{F}] \\ [\dot{\mathbf{X}}] &= p \cdot \underbrace{\mathbf{A}^{-1} \cdot \mathbf{A}_1}_{\mathbf{B}_1} \cdot [\mathbf{X}] + q \cdot \underbrace{\mathbf{A}^{-1} \cdot \mathbf{A}_2}_{\mathbf{B}_2} \cdot [\mathbf{X}] + r \cdot \underbrace{\mathbf{A}^{-1} \cdot \mathbf{A}_3}_{\mathbf{B}_3} \cdot [\mathbf{X}] + \underbrace{\mathbf{A}^{-1}}_{\mathbf{B}_4} \cdot [\mathbf{F}] \\ [\dot{\mathbf{X}}] &= \underbrace{p \cdot \mathbf{B}_1 \cdot [\mathbf{X}] + q \cdot \mathbf{B}_2 \cdot [\mathbf{X}] + r \cdot \mathbf{B}_3 \cdot [\mathbf{X}]}_{\text{Gyroscopic Terms}} + \underbrace{\mathbf{B}_4 \cdot [\mathbf{F}]}_{\text{Body Forces and Moments Term}} \end{aligned} \right\} \quad (4.13)$$

Where, $[\mathbf{X}]$ is the state vector, $[\dot{\mathbf{X}}]$ is the state vector derivative and $[\mathbf{F}]$ is the vector of external forces and moments affecting the vehicle body or sprung mass given as:

$$[\dot{\mathbf{X}}] = \begin{pmatrix} \dot{U} \\ \dot{V} \\ \dot{W} \\ \dot{p} \\ \dot{q} \\ \dot{r} \end{pmatrix} \quad [\mathbf{X}] = \begin{pmatrix} U \\ V \\ W \\ p \\ q \\ r \end{pmatrix} \quad [\mathbf{F}] = \begin{pmatrix} \Sigma F_x \\ \Sigma F_y \\ \Sigma F_z \\ \Sigma M_x \\ \Sigma M_y \\ \Sigma M_z \end{pmatrix} \quad (4.14)$$

$$\left. \begin{aligned}
 \mathbf{A} &= \begin{pmatrix} m_s & 0 & 0 & 0 & 0 & 0 \\ 0 & m_s & 0 & 0 & 0 & 0 \\ 0 & 0 & m_s & 0 & 0 & 0 \\ 0 & 0 & 0 & I_{xx} & 0 & -I_{zx} \\ 0 & 0 & 0 & 0 & I_{yy} & 0 \\ 0 & 0 & 0 & -I_{zx} & 0 & I_{zz} \end{pmatrix} \\
 \mathbf{A}_1 &= \begin{pmatrix} 0 & 0 & 0 & 0 & 0 & 0 \\ 0 & 0 & m_s & 0 & 0 & 0 \\ 0 & -m_s & 0 & 0 & 0 & 0 \\ 0 & 0 & 0 & 0 & I_{zx} & 0 \\ 0 & 0 & 0 & -I_{xz} & 0 & (I_{zz} - I_{xx}) \\ 0 & 0 & 0 & 0 & (I_{xx} - I_{yy}) & 0 \end{pmatrix} \\
 \mathbf{A}_2 &= \begin{pmatrix} 0 & 0 & -m_s & 0 & 0 & 0 \\ 0 & 0 & 0 & 0 & 0 & 0 \\ m_s & 0 & 0 & 0 & 0 & 0 \\ 0 & 0 & 0 & 0 & 0 & (I_{yy} - I_{zz}) \\ 0 & 0 & 0 & 0 & 0 & 0 \\ 0 & 0 & 0 & 0 & 0 & -I_{xz} \end{pmatrix} \\
 \mathbf{A}_3 &= \begin{pmatrix} 0 & m_s & 0 & 0 & 0 & 0 \\ -m_s & 0 & 0 & 0 & 0 & 0 \\ 0 & 0 & 0 & 0 & 0 & 0 \\ 0 & 0 & 0 & 0 & 0 & 0 \\ 0 & 0 & 0 & 0 & 0 & I_{xz} \\ 0 & 0 & 0 & 0 & 0 & 0 \end{pmatrix} \\
 \mathbf{B}_1 &= \mathbf{A}^{-1} \cdot \mathbf{A}_1 \\
 \mathbf{B}_2 &= \mathbf{A}^{-1} \cdot \mathbf{A}_2 \\
 \mathbf{B}_3 &= \mathbf{A}^{-1} \cdot \mathbf{A}_3 \\
 \mathbf{B}_4 &= \mathbf{A}^{-1}
 \end{aligned} \right\} \quad (4.15)$$

4.2.2 Unsprung Mass Dynamics:

As already mentioned the unsprung mass can be simplified by four masses distributed at each wheel. Each one has two degrees of freedom; the first represents the vertical movement of the wheel and the second represents the driving wheel speed, see figure 4.2.

4.2.2.1 Unsprung Mass Vertical Dynamics:

For vertical dynamics, a two-degree of freedom quarter-car model is used for each wheel. The quarter car model consists of an unsprung or wheel mass (m_{w_i}), which is connected to approximately a quarter of the vehicle's sprung mass (m_{q_i}) by a spring and a damper system as shown in figure 4.3. The quarter car model possesses two degrees of freedom which includes the vertical displacement of the vehicle quarter body sprung mass (z_{b_i}) and the vertical displacement of the wheel centre (z_{w_i}). All four wheel suspensions are assumed to be vertically directed. The equations of motion for the quarter car model can be derived easily by applying Newton's second law of motion. To derive the equation of motion in vertical direction firstly, suspension reaction must be calculated.

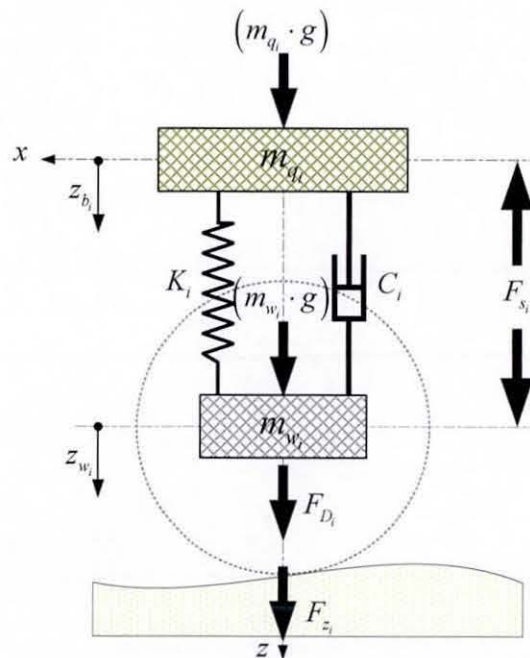


Figure 4.3 Two Degrees of Freedom Quarter-Car Model

Suspension forces (F_{s_i}) are calculated, based on the suspension spring stiffness (K_i), the shock absorber damping coefficient (C_i) and the vertical displacement and velocity difference between the sprung mass body corner and the wheel centre as (Gillespie, 1992)

$$F_{s_i} = C_i \cdot (\dot{z}_{b_i} - \dot{z}_{w_i}) + K_i \cdot (z_{b_i} - z_{w_i}) \quad (4.16)$$

Quarter-mass equation of motion:

$$m_{q_i} \cdot \ddot{z}_{b_i} = m_{q_i} \cdot g - F_{s_i} \quad (4.17)$$

$$m_{q_i} \cdot \ddot{z}_{b_i} = m_{q_i} \cdot g - \underbrace{C_i \cdot (\dot{z}_{b_i} - \dot{z}_{w_i}) - K_i \cdot (z_{b_i} - z_{w_i})}_{\text{Suspension Force}} \quad (4.18)$$

Unsprung mass equation of motion:

$$m_{w_i} \cdot \ddot{z}_{w_i} = m_{w_i} \cdot g + F_{s_i} + F_{D_i} + F_{z_i} \quad (4.19)$$

$$m_{w_i} \cdot \ddot{z}_{w_i} = m_{w_i} \cdot g + \underbrace{C_i \cdot (\dot{z}_{b_i} - \dot{z}_{w_i}) + K_i \cdot (z_{b_i} - z_{w_i})}_{\text{Suspension Force}} + \underbrace{b \cdot \dot{z}_{w_i}}_{\text{Soil Damping Force}} + F_{z_i} \quad (4.20)$$

Where (F_{z_i}) is the tyre vertical force calculated by the tyre model, see equations (3.30) or (3.33). The damping force (F_{D_i}) is computed from the wheel vertical speed (\dot{z}_{w_i}) multiplied by soil damping coefficient (b) in (N·s/m) (AESCO, 2005). The total equations of motion representing unsprung mass vertical dynamics are written as follows:

$$m_{w_1} \cdot \ddot{z}_{w_1} = m_{w_1} \cdot g + F_{s_1} + b \cdot \dot{z}_{w_1} + F_{z_1} \quad (4.21)$$

$$m_{w_2} \cdot \ddot{z}_{w_2} = m_{w_2} \cdot g + F_{s_2} + b \cdot \dot{z}_{w_2} + F_{z_2} \quad (4.22)$$

$$m_{w_3} \cdot \ddot{z}_{w_3} = m_{w_3} \cdot g + F_{s_3} + b \cdot \dot{z}_{w_3} + F_{z_3} \quad (4.23)$$

$$m_{w_4} \cdot \ddot{z}_{w_4} = m_{w_4} \cdot g + F_{s_4} + b \cdot \dot{z}_{w_4} + F_{z_4} \quad (4.24)$$

To implement the quarter car model into the full vehicle model, the effect of the vehicle body bounce (z), roll angle (φ) and pitch angle (θ) must be taken into consideration, to modify the body displacement at each corner. It can be written in the following form:

Vehicle body vertical position at each corner:

$$\begin{pmatrix} z_{b_1} \\ z_{b_2} \\ z_{b_3} \\ z_{b_4} \end{pmatrix} = \begin{pmatrix} z - \frac{t_{rf}}{2} \cdot \varphi - a \cdot \theta \\ z + \frac{t_{rf}}{2} \cdot \varphi - a \cdot \theta \\ z - \frac{t_{rr}}{2} \cdot \varphi + b \cdot \theta \\ z + \frac{t_{rr}}{2} \cdot \varphi + b \cdot \theta \end{pmatrix} = \begin{pmatrix} 1 & -\frac{t_{rf}}{2} & -a \\ 1 & \frac{t_{rf}}{2} & -a \\ 1 & -\frac{t_{rr}}{2} & b \\ 1 & \frac{t_{rr}}{2} & b \end{pmatrix} \cdot \begin{pmatrix} z \\ \varphi \\ \theta \end{pmatrix} \quad (4.25)$$

Vehicle body vertical velocity at each corner:

$$\begin{pmatrix} \dot{z}_{b_1} \\ \dot{z}_{b_2} \\ \dot{z}_{b_3} \\ \dot{z}_{b_4} \end{pmatrix} = \begin{pmatrix} W - \frac{t_{rf}}{2} \cdot p - a \cdot q \\ W + \frac{t_{rf}}{2} \cdot p - a \cdot q \\ W - \frac{t_{rr}}{2} \cdot p + b \cdot q \\ W + \frac{t_{rr}}{2} \cdot p + b \cdot q \end{pmatrix} = \begin{pmatrix} 1 & -\frac{t_{rf}}{2} & -a \\ 1 & \frac{t_{rf}}{2} & -a \\ 1 & -\frac{t_{rr}}{2} & b \\ 1 & \frac{t_{rr}}{2} & b \end{pmatrix} \cdot \begin{pmatrix} W \\ p \\ q \end{pmatrix} \quad (4.26)$$

Suspension force at each corner:

$$\begin{pmatrix} F_{s_1} \\ F_{s_2} \\ F_{s_3} \\ F_{s_4} \end{pmatrix} = \underbrace{\begin{pmatrix} K_f & 0 & 0 & 0 \\ 0 & K_f & 0 & 0 \\ 0 & 0 & K_r & 0 \\ 0 & 0 & 0 & K_r \end{pmatrix}}_{\text{Stiffness Matrix}} \cdot \begin{pmatrix} z_{b_1} - z_{w_1} \\ z_{b_2} - z_{w_2} \\ z_{b_3} - z_{w_3} \\ z_{b_4} - z_{w_4} \end{pmatrix} + \underbrace{\begin{pmatrix} C_f & 0 & 0 & 0 \\ 0 & C_f & 0 & 0 \\ 0 & 0 & C_r & 0 \\ 0 & 0 & 0 & C_r \end{pmatrix}}_{\text{Damping Matrix}} \cdot \begin{pmatrix} \dot{z}_{b_1} - \dot{z}_{w_1} \\ \dot{z}_{b_2} - \dot{z}_{w_2} \\ \dot{z}_{b_3} - \dot{z}_{w_3} \\ \dot{z}_{b_4} - \dot{z}_{w_4} \end{pmatrix} \quad (4.27)$$

It should be noted that, while the model calculates the suspension forces based on linear spring and shock absorber assumption, it would be relatively easy to implement suspension non-linearity and effect of bump rubber stops in the Simulink model by simply using look-up tables to accurately introduce all suspension system non-linearities.

4.2.2.2 Wheel Driving Speed:

Calculation of the wheel driving speed (ω_i) requires the calculation of wheel angular acceleration ($\dot{\omega}_i$). Wheel angular acceleration arises from driving torque, brake torque and tyre circumferential torque, as shown in figure 4.4.

From the wheel torque balance, using Newton's second law for rotational dynamics, the differential equation for the spin degree-of-freedom can be written as follows:

$$I_{w_i} \cdot \dot{\omega}_i = M_{w_i} - M_{B_i} - M_{U_i} \quad (4.28)$$

where:

- I_{w_i} : Wheel rotational moment of inertia (around the axle of spinning).
- $\dot{\omega}_i$: Wheel angular acceleration.
- M_{w_i} : Engine drive torque applied at each wheel hub, see section 4.2.8.
- M_{B_i} : Braking torque applied for each wheel.
- M_{U_i} : Tyre circumferential torque ($M_{U_i} = (F_{U_i} + F_{Ri}) \cdot r_{d_i}$), see equation (3.39).
- F_{U_i} : Circumferential force results from soil shear strength equation (3.38).
- F_{Ri} : Tyre internal rolling (flexing) resistance force.
- r_{d_i} : Wheel dynamic rolling radius (assumed to be constant value)

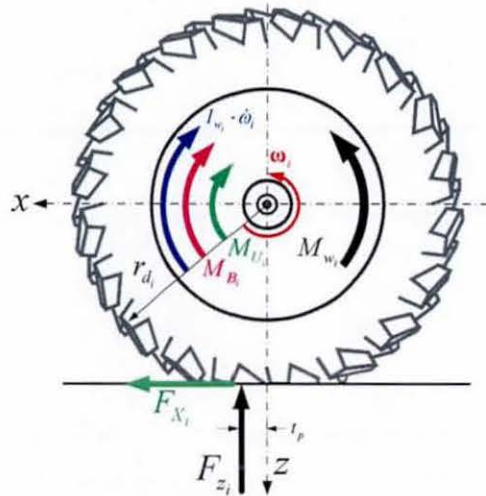


Figure 4.4 Driving Wheel Spin Degree of Freedom

4.2.3 Tyre Forces and Moments

The output force vector from the off-road tyre model is given at the wheel hub relative to the wheel coordinate system and calculated for each wheel in [N]. Transformation of the force vector from the wheel coordinate system to the local frame of reference is carried out based on the wheel steer angles as:

$$\begin{pmatrix} F_{x_1} \\ F_{x_2} \\ F_{x_3} \\ F_{x_4} \end{pmatrix}_{\mathbf{L}} = \begin{pmatrix} F_{X_1} \\ F_{X_2} \\ F_{X_3} \\ F_{X_4} \end{pmatrix}_{\mathbf{W}} \cdot \cos \begin{pmatrix} \delta_1 \\ \delta_2 \\ \delta_3 \\ \delta_4 \end{pmatrix} - \begin{pmatrix} F_{Y_1} \\ F_{Y_2} \\ F_{Y_3} \\ F_{Y_4} \end{pmatrix}_{\mathbf{W}} \cdot \sin \begin{pmatrix} \delta_1 \\ \delta_2 \\ \delta_3 \\ \delta_4 \end{pmatrix} \quad (4.29)$$

$$\begin{pmatrix} F_{y_1} \\ F_{y_2} \\ F_{y_3} \\ F_{y_4} \end{pmatrix}_{\mathbf{L}} = \begin{pmatrix} F_{X_1} \\ F_{X_2} \\ F_{X_3} \\ F_{X_4} \end{pmatrix}_{\mathbf{W}} \cdot \sin \begin{pmatrix} \delta_1 \\ \delta_2 \\ \delta_3 \\ \delta_4 \end{pmatrix} + \begin{pmatrix} F_{Y_1} \\ F_{Y_2} \\ F_{Y_3} \\ F_{Y_4} \end{pmatrix}_{\mathbf{W}} \cdot \cos \begin{pmatrix} \delta_1 \\ \delta_2 \\ \delta_3 \\ \delta_4 \end{pmatrix} \quad (4.30)$$

The total forces affecting the vehicle body sprung mass are given as:

$$\sum F_x = \underbrace{(F_{x_1} + F_{x_2} + F_{x_3} + F_{x_4})}_{\text{Tyre Forces in x-direction}} - F_{G_x} - F_a \quad (4.31)$$

$$\sum F_y = \underbrace{(F_{y_1} + F_{y_2} + F_{y_3} + F_{y_4})}_{\text{Tyre Forces in y-direction}} - F_{G_y} \quad (4.32)$$

$$\sum F_z = F_{G_z} - \underbrace{(F_{s_1} + F_{s_2} + F_{s_3} + F_{s_4})}_{\text{Suspension Forces}} \quad (4.33)$$

where:

$[\delta_1 \ \delta_2 \ \delta_3 \ \delta_4]$ are the wheel steering angles, calculated from equation (4.77)

$[F_{s_1} \ F_{s_2} \ F_{s_3} \ F_{s_4}]$ are suspension forces, calculated from equation (4.27)

$[F_{G_x} \ F_{G_y} \ F_{G_z}]$ is the gravitational force vector, calculated from equation (4.53)

F_a is the aerodynamics force due to air resistance, calculated from equation (4.55)

As already mentioned the tyre forces are calculated from the off-road tyre model at the wheel hub. These forces (after transformation relative to the vehicle body) cause moments with respect to the local frame of reference $\left(\mathbf{M}_i = \left(\vec{\mathbf{r}}_i \times \vec{\mathbf{F}}_i\right)_L\right)$. These moments affect the vehicle body roll, pitch and yaw motions. The position vector $\left(\vec{\mathbf{r}}_i\right)$ of each wheel hub with respect to the local frame of references can be written as follows, see figure 4.1:

$$\vec{\mathbf{r}}_1 = (a)\mathbf{i} - \left(\frac{t_{rf}}{2}\right)\mathbf{j} + (h_G - r_{d_1} - z + z_{w_1})\mathbf{k} \quad (4.34)$$

$$\vec{\mathbf{r}}_2 = (a)\mathbf{i} + \left(\frac{t_{rf}}{2}\right)\mathbf{j} + (h_G - r_{d_2} - z + z_{w_2})\mathbf{k} \quad (4.35)$$

$$\vec{\mathbf{r}}_3 = -(b)\mathbf{i} - \left(\frac{t_{rr}}{2}\right)\mathbf{j} + (h_G - r_{d_3} - z + z_{w_3})\mathbf{k} \quad (4.36)$$

$$\vec{\mathbf{r}}_4 = -(b)\mathbf{i} + \left(\frac{t_{rr}}{2}\right)\mathbf{j} + (h_G - r_{d_4} - z + z_{w_4})\mathbf{k} \quad (4.37)$$

The tyre forces affecting the vehicle body sprung mass with the following moments:

Roll Moments (M_x) :

$$M_{x_1} = -(h_G - r_{d_1} - z + z_{w_1}) \cdot F_{y_{l_1}} - \left(\frac{t_{rf}}{2}\right) \cdot F_{z_{l_1}} \quad (4.38)$$

$$M_{x_2} = -(h_G - r_{d_2} - z + z_{w_2}) \cdot F_{y_{l_2}} + \left(\frac{t_{rf}}{2}\right) \cdot F_{z_{l_2}} \quad (4.39)$$

$$M_{x_3} = -(h_G - r_{d_3} - z + z_{w_3}) \cdot F_{y_{l_3}} - \left(\frac{t_{rr}}{2}\right) \cdot F_{z_{l_3}} \quad (4.40)$$

$$M_{x_4} = -(h_G - r_{d_4} - z + z_{w_4}) \cdot F_{y_{l_4}} + \left(\frac{t_{rr}}{2}\right) \cdot F_{z_{l_4}} \quad (4.41)$$

Pitch Moments (M_y):

$$M_{y_1} = (h_G - r_{d_1} - z + z_{w_1}) \cdot F_{x_{L_1}} - (a) \cdot F_{z_{L_1}} \quad (4.42)$$

$$M_{y_2} = (h_G - r_{d_2} - z + z_{w_2}) \cdot F_{x_{L_2}} - (a) \cdot F_{z_{L_2}} \quad (4.43)$$

$$M_{y_3} = (h_G - r_{d_3} - z + z_{w_3}) \cdot F_{x_{L_3}} + (b) \cdot F_{z_{L_3}} \quad (4.44)$$

$$M_{y_4} = (h_G - r_{d_4} - z + z_{w_4}) \cdot F_{x_{L_4}} + (b) \cdot F_{z_{L_4}} \quad (4.45)$$

Yaw Moments (M_z):

$$M_{z_1} = \left(\frac{t_{rf}}{2} \right) \cdot F_{x_{L_1}} + (a) \cdot F_{y_{L_1}} \quad (4.46)$$

$$M_{z_2} = - \left(\frac{t_{rf}}{2} \right) \cdot F_{x_{L_2}} + (a) \cdot F_{y_{L_2}} \quad (4.47)$$

$$M_{z_3} = \left(\frac{t_{rr}}{2} \right) \cdot F_{x_{L_3}} - (b) \cdot F_{y_{L_3}} \quad (4.48)$$

$$M_{z_4} = - \left(\frac{t_{rr}}{2} \right) \cdot F_{x_{L_4}} - (b) \cdot F_{y_{L_4}} \quad (4.49)$$

The total moments affecting the vehicle sprung mass are given as follows:

$$\sum M_x = (M_{x_1} + M_{x_2} + M_{x_3} + M_{x_4})_L \quad (4.50)$$

$$\sum M_y = (M_{y_1} + M_{y_2} + M_{y_3} + M_{y_4})_L \quad (4.51)$$

$$\sum M_z = (M_{z_1} + M_{z_2} + M_{z_3} + M_{z_4})_L \quad (4.52)$$

4.2.4 Inclined Road Surfaces

Representing the road surface inclination is carried out by introducing the road surface profile vector ($\bar{\mathbf{n}}_B$) and the corresponding surface height (z_{R_i}) at each wheel-terrain contact patch with respect to the global frame of reference, figure 4.5. Since the gravitational force applies to the centre of mass of the vehicle, it is easy to introduce the effect of an inclined road by multiplying the gravitational vector by the transformation matrix given in equation (3.56), using the following conditions: ($\theta = \theta_R$, $\varphi = \varphi_R$, $\psi = 0$).

$$\left. \begin{aligned} \begin{pmatrix} F_{G_x} \\ F_{G_y} \\ F_{G_z} \end{pmatrix} &= \underbrace{\begin{pmatrix} \cos \theta_R & \sin \theta_R \cdot \sin \varphi_R & \sin \theta_R \cdot \cos \varphi_R \\ 0 & \cos \varphi_R & -\sin \varphi_R \\ -\sin \theta_R & \cos \theta_R \cdot \sin \varphi_R & \cos \theta_R \cdot \cos \varphi_R \end{pmatrix}}_{\text{Transformation Matrix}} \cdot \begin{pmatrix} 0 \\ 0 \\ m_s \cdot g \end{pmatrix} \\ \\ \begin{pmatrix} F_{G_x} \\ F_{G_y} \\ F_{G_z} \end{pmatrix} &= \underbrace{\begin{pmatrix} \sin \theta_R \cdot \cos \varphi_R \\ -\sin \varphi_R \\ \cos \theta_R \cdot \cos \varphi_R \end{pmatrix}}_{\bar{\mathbf{n}}_B} \cdot (m_s \cdot g) = \bar{\mathbf{n}}_B \cdot (m_s \cdot g) \end{aligned} \right\} \quad (4.53)$$

Where ($\bar{\mathbf{n}}_B$) is a downward normalized 3-dimensional vector, the length of the vector is 1, specifying the normal of the surface at the given position in the global coordinate system. A positive road inclination angle (θ_R) means an upward inclined road. A positive road camber angle (φ_R) means the road which raises the left-hand side of the vehicle. For a flat surface, ($\bar{\mathbf{n}}_B$) equals to $[0 \ 0 \ 1]^T$, consequently ($F_{G_x} = F_{G_y} = 0$, $F_{G_z} = m_s \cdot g$).

The road surface height (z_{R_i}) specifies the height of the surface with respect to the global frame of reference at the given position of a wheel (x_{w_i}, y_{w_i})_G as:

$$z_{R_i} = -x_{w_i} \cdot \sin \theta_R + y_{w_i} \cdot \sin \varphi_R \quad (4.54)$$

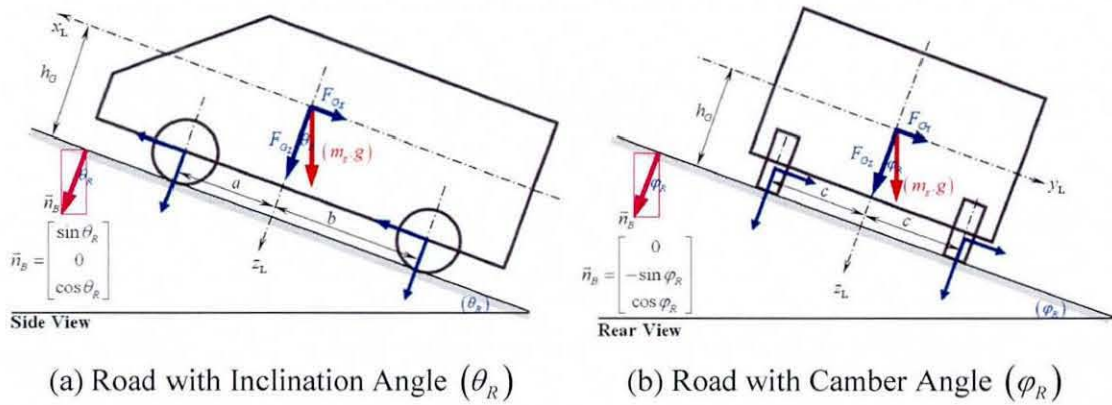


Figure 4.5 Gravitational Force Analyses for Inclined Road Surfaces

4.2.5 Aerodynamic Force

Aerodynamic forces have a major impact on the behaviour of a vehicle. Their effects include drag, lift, down load, lateral forces, moments in roll, pitch and yaw. These eventually influence the fuel economy, the handling and also the noise, vibration and harshness characteristics of the vehicle. Due to the aerodynamic shape of the vehicle body and the air flow, both normal pressure and shear stress are generated. This interaction causes an external aerodynamic resistance comprising two components. The former is the pressure drag arising from the component of the normal pressure acting against the motion of the vehicle. The later is the skin friction due to shear stress in the boundary layer adjacent to the external surface of the vehicle body. To simplify the calculations, only one component of the drag force, in longitudinal direction, is considered. Furthermore, the line of action is assumed to be at the vehicle body C.G. This force can be simply expressed as (Wong, 2001):

$$F_a = \left(\frac{\rho \cdot A \cdot C_d}{2} \right) \cdot U^2 \quad (4.55)$$

where (ρ) is the mass density of air, (C_d) is the coefficient of aerodynamic resistance that represents the combined effects of all the factors described above. (A) is the characteristic area of the vehicle, simply assumed to be the frontal area, which is the projected area of the vehicle in the direction of the travel (i.e. forward).

4.2.6 Vehicle and Tyre Kinematics

The AS²TM off-road tyre calculates forces and moments applied at the wheel hub relative to the wheel coordinate system. Consequently, the tyre model requires information about the velocity and position vector of each wheel hub. The velocity vector is defined with respect to the wheels' coordinate systems, while the position vector is defined with respect to the global frame of reference.

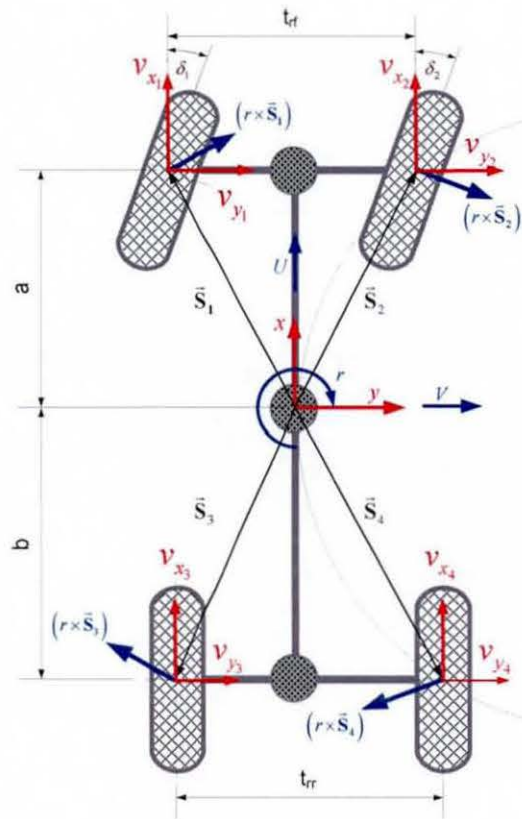


Figure 4.6 Velocities Transformation at the Wheel Hub

Once the differential equations of vehicle body motion are solved, both the translational and rotational velocity vectors of the vehicle body with respect to the local frame of reference are obtained. Subsequently, the velocity vector of the body corners can be calculated relative to the local frame of reference. Transformation of the velocity vector from the vehicle body local frame of reference to the wheel coordinate system can be easily carried out using the wheel steering angles as follows; see figure 4.6.

Longitudinal velocities vector with respect to the local frame of reference:

$$\begin{pmatrix} v_{x_1} \\ v_{x_2} \\ v_{x_3} \\ v_{x_4} \end{pmatrix}_L = \begin{pmatrix} 1 & 0 & \frac{t_{rf}}{2} \\ 1 & 0 & -\frac{t_{rf}}{2} \\ 1 & 0 & \frac{t_{rr}}{2} \\ 1 & 0 & -\frac{t_{rr}}{2} \end{pmatrix} \cdot \begin{pmatrix} U \\ V \\ r \end{pmatrix} \quad (4.56)$$

Lateral velocities vector with respect to the local frame of reference:

$$\begin{pmatrix} v_{y_1} \\ v_{y_2} \\ v_{y_3} \\ v_{y_4} \end{pmatrix}_L = \begin{pmatrix} 0 & 1 & a \\ 0 & 1 & a \\ 0 & 1 & -b \\ 0 & 1 & -b \end{pmatrix} \cdot \begin{pmatrix} U \\ V \\ r \end{pmatrix} \quad (4.57)$$

Longitudinal velocities vector with respect to the wheel coordinates system:

$$\begin{pmatrix} v_{x_1} \\ v_{x_2} \\ v_{x_3} \\ v_{x_4} \end{pmatrix}_W = \begin{pmatrix} v_{x_1} \\ v_{x_2} \\ v_{x_3} \\ v_{x_4} \end{pmatrix}_L \cdot \cos \begin{pmatrix} \delta_1 \\ \delta_2 \\ \delta_3 \\ \delta_4 \end{pmatrix} + \begin{pmatrix} v_{y_1} \\ v_{y_2} \\ v_{y_3} \\ v_{y_4} \end{pmatrix}_L \cdot \sin \begin{pmatrix} \delta_1 \\ \delta_2 \\ \delta_3 \\ \delta_4 \end{pmatrix} \quad (4.58)$$

Lateral velocities vector with respect to the wheel coordinates system:

$$\begin{pmatrix} v_{y_1} \\ v_{y_2} \\ v_{y_3} \\ v_{y_4} \end{pmatrix}_W = - \begin{pmatrix} v_{x_1} \\ v_{x_2} \\ v_{x_3} \\ v_{x_4} \end{pmatrix}_L \cdot \sin \begin{pmatrix} \delta_1 \\ \delta_2 \\ \delta_3 \\ \delta_4 \end{pmatrix} + \begin{pmatrix} v_{y_1} \\ v_{y_2} \\ v_{y_3} \\ v_{y_4} \end{pmatrix}_L \cdot \cos \begin{pmatrix} \delta_1 \\ \delta_2 \\ \delta_3 \\ \delta_4 \end{pmatrix} \quad (4.59)$$

Referring to figure 4.1, the position vector of each wheel hub with respect to the global frame of references $[\mathbf{r}_w]_G$ can be written as follows, (Day et al., 2001):

$$[\bar{\mathbf{r}}_w]_G = [\bar{\mathbf{r}}_{OL}]_G + \mathbf{R} \cdot [\bar{\mathbf{r}}_w]_L \quad (4.60)$$

where $[\bar{\mathbf{r}}_{OL}]_G$ is the position vector of the origin of the local frame of reference with respect to the global frame of reference. Referring to figure 4.1, it should be noted that, the global frame of reference is located directly beneath the local coordinate system at the point, where the manoeuvre has commenced. The initial position vector of local frame of reference relative to the global frame of reference can be given by: $[0 \ 0 \ -h_G]^T$.

$[\bar{\mathbf{r}}_w]_L$ is the position vector of each wheel hub with respect to the local frame of reference.

$$[\bar{\mathbf{r}}_w]_L = \left(\begin{array}{cccc} a & a & -b & -b \\ -\frac{t_{rf}}{2} & \frac{t_{rf}}{2} & -\frac{t_{rr}}{2} & \frac{t_{rr}}{2} \\ h_G - r_{d_1} - z + z_{w_1} & h_G - r_{d_2} - z + z_{w_2} & h_G - r_{d_3} - z + z_{w_3} & h_G - r_{d_4} - z + z_{w_4} \end{array} \right)_L \quad (4.61)$$

$$[\bar{\mathbf{r}}_w]_G = \left(\begin{array}{cccc} X_{w_1} & X_{w_2} & X_{w_3} & X_{w_4} \\ Y_{w_1} & Y_{w_2} & Y_{w_3} & Y_{w_4} \\ Z_{w_1} & Z_{w_2} & Z_{w_3} & Z_{w_4} \end{array} \right)_G$$

$$[\bar{\mathbf{r}}_{OL}]_G = \left(\begin{array}{cccc} X_{OL} & X_{OL} & X_{OL} & X_{OL} \\ Y_{OL} & Y_{OL} & Y_{OL} & Y_{OL} \\ Z_{OL} & Z_{OL} & Z_{OL} & Z_{OL} \end{array} \right)_G$$

(\mathbf{R}) is a relative transformation matrix used to transform the data from the local to the global frame of reference, see chapter 3. The transformation matrix is given as follows:

$$\mathbf{R} = \left(\begin{array}{ccc} \cos \theta \cdot \cos \psi & \sin \theta \cdot \sin \phi \cdot \cos \psi - \cos \phi \cdot \sin \psi & \sin \theta \cdot \cos \phi \cdot \cos \psi + \sin \phi \cdot \sin \psi \\ \cos \theta \cdot \sin \psi & \sin \theta \cdot \sin \phi \cdot \sin \psi + \cos \phi \cdot \cos \psi & \sin \theta \cdot \cos \phi \cdot \sin \psi - \sin \phi \cdot \cos \psi \\ -\sin \theta & \cos \theta \cdot \sin \phi & \cos \theta \cdot \cos \phi \end{array} \right) \quad (4.62)$$

For the transformation matrix (\mathbf{R}) given by equation (4.62), the order of rotations is yaw, pitch and roll. The angles between the local and global frames of reference are called the Euler angles (φ, θ, ψ) . Calculation of Euler angles requires integration of rotational velocity components (p, q, r) . Integration of these components along the axes of rotation of Euler angles yields their angular velocity as follows (Katz, 1997):

$$\dot{\varphi} = p + (q \cdot \sin \varphi + r \cdot \cos \varphi) \cdot \tan \theta \quad (4.63)$$

$$\dot{\theta} = q \cdot \cos \varphi - r \cdot \sin \varphi \quad (4.64)$$

$$\dot{\psi} = \frac{(q \cdot \sin \varphi + r \cdot \cos \varphi)}{\cos \theta} \quad (4.65)$$

4.2.7 The Steering System

Referring to figure 4.7, the steer angles at the rear wheels, $\delta_3 = \delta_4 = 0$ (assuming that, no camber or steer effects in the rear suspension geometry).

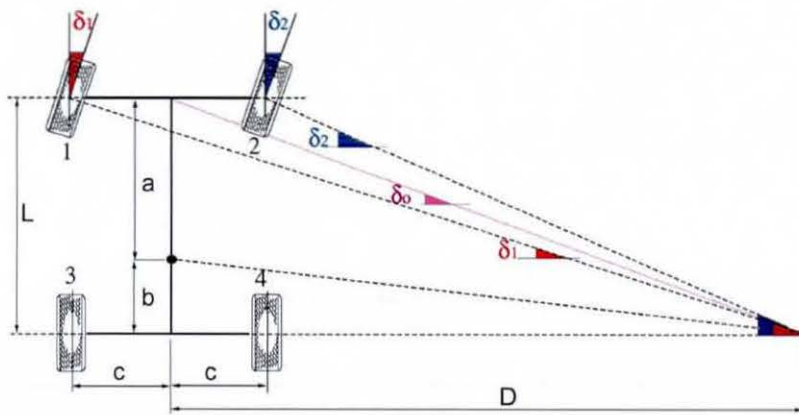


Figure 4.7 Ackerman Steering Corrections, adopted from (Gillespie, 1992)

The steering angle of the front wheels can be given as (Gillespie, 1992):

$$\tan \delta_0 = \frac{L}{D} \quad (4.66)$$

$$\tan \delta_1 = \frac{L}{(D+C)} \quad (4.67)$$

$$\tan \delta_2 = \frac{L}{(D-C)} \quad (4.68)$$

From equation (4.66): $\left(D = \frac{L}{\tan \delta_0} \right)$ and from equation (4.67): $\left(D + c = \frac{L}{\tan \delta_1} \right)$

$$\frac{L}{\tan \delta_0} + c = \frac{L}{\tan \delta_1} \quad (4.69)$$

$$\frac{L + c \cdot \tan \delta_0}{\tan \delta_0} = \frac{L}{\tan \delta_1} \quad (4.70)$$

$$\tan \delta_1 = \frac{L \cdot \tan \delta_0}{L + c \cdot \tan \delta_0} = \frac{\tan \delta_0}{1 + \frac{c}{L} \cdot \tan \delta_0} \quad (4.71)$$

For small δ_0 and δ_1 , and using the binomial expansion series:

$$(1+x)^n = 1 + n \cdot x + \frac{n \cdot (n-1) \cdot x^2}{2!} + \frac{n \cdot (n-1) \cdot (n-2) \cdot x^3}{3!} + \dots \quad (4.72)$$

$$(1+x)^{-1} \cong 1 - x \quad (4.73)$$

$$\delta_1 = \frac{\delta_0}{\left(1 + \frac{c}{L} \cdot \delta_0 \right)} = \delta_0 \cdot \left(1 + \frac{c}{L} \cdot \delta_0 \right)^{-1} \quad (4.74)$$

$$\delta_1 \approx \delta_0 \cdot \left(1 - \frac{c}{L} \cdot \delta_0 \right) \quad \text{and} \quad \delta_2 \approx \delta_0 \cdot \left(1 + \frac{c}{L} \cdot \delta_0 \right) \quad (4.75)$$

If (P_a) is the proportion of Ackerman, then (δ_1) and (δ_2) become:

$$\delta_1 \approx \delta_0 \cdot \left(1 - \left(\frac{P_a \cdot c}{L} \right) \cdot \delta_0 \right) \quad \text{and} \quad \delta_2 \approx \delta_0 \cdot \left(1 + \left(\frac{P_a \cdot c}{L} \right) \cdot \delta_0 \right) \quad (4.76)$$

The correction of steering input can be given as follows:

$$\begin{pmatrix} \delta_1 \\ \delta_2 \\ \delta_3 \\ \delta_4 \end{pmatrix} = \begin{pmatrix} 1 & -1 \\ 1 & 1 \\ 0 & 0 \\ 0 & 0 \end{pmatrix} \cdot \underbrace{\begin{pmatrix} \delta_0 \\ \left(\frac{P_a \cdot c}{L} \right) \delta_0^2 \end{pmatrix}}_{k_{steer}} \quad (4.77)$$

4.2.8 The Drivetrain Model

The drivetrain model embodies the dynamic characteristics of 4×4 vehicles including the engine, clutch, a manual five-speed gear-box, and three mechanical differentials, namely: central (open/locked), front (open) and rear (open) differentials, as well as the torque transmitting elements such as propeller shafts and axles, see figure 4.8.

The drivetrain model is implemented in a new toolbox called SimDriveline (The MathWorks Inc., 2004-2006), which is part of the Simulink Physical Modelling, encompassing the modelling and design of systems according to the basic physical principles. Physical Modelling runs within the Simulink environment and interfaces seamlessly with the rest of Simulink and with MATLAB. Unlike other Simulink blocks, which represent mathematical operations, Physical Modelling blocks represent physical components or relationships directly. With SimDriveline, it is possible to represent a drivetrain system with a connected block diagram, as shown in figure 4.9.

Rotational motion can be initiated and maintained in a driveline with actuators while measuring, via sensors, the motions of driveline elements and the torques acting on them. The SimDriveline libraries offer blocks to represent rotating bodies, gear constraints among bodies, special dynamic elements such as spring-damper forces, rotational stops, clutches, transmissions, sensors and actuators.

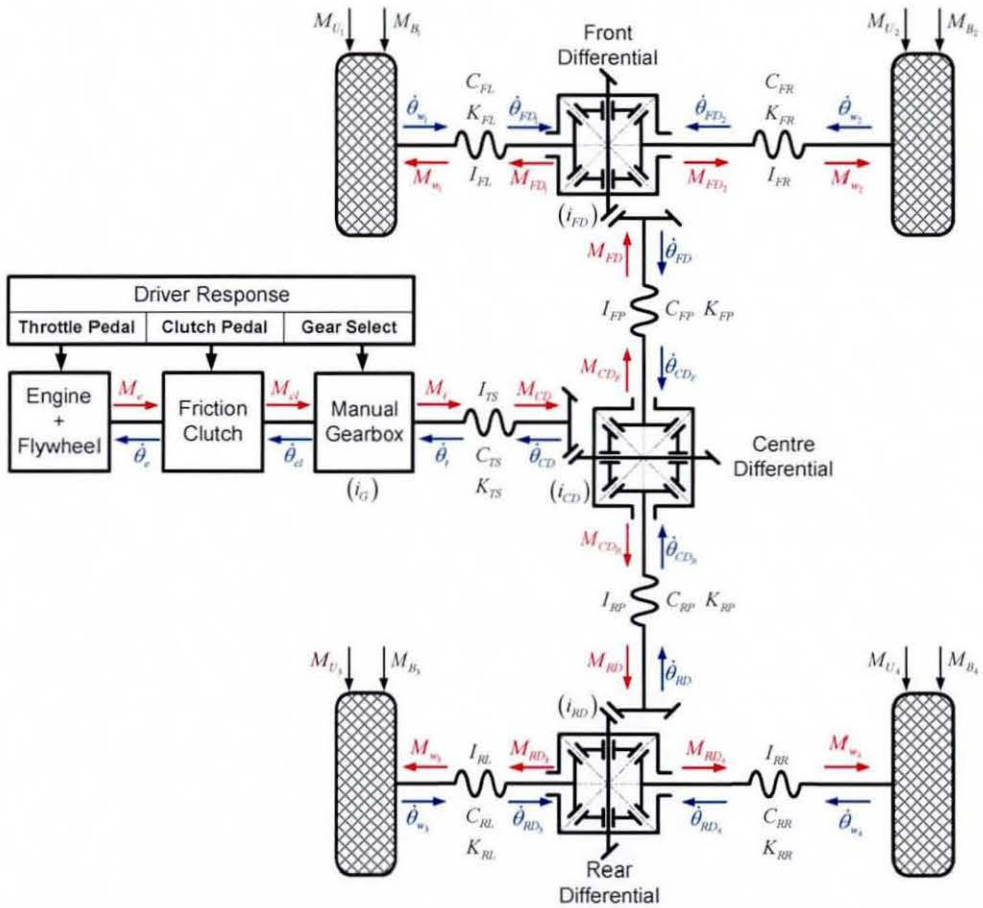


Figure 4.8 Mathematical Representation of 4x4 Drivetrain Model

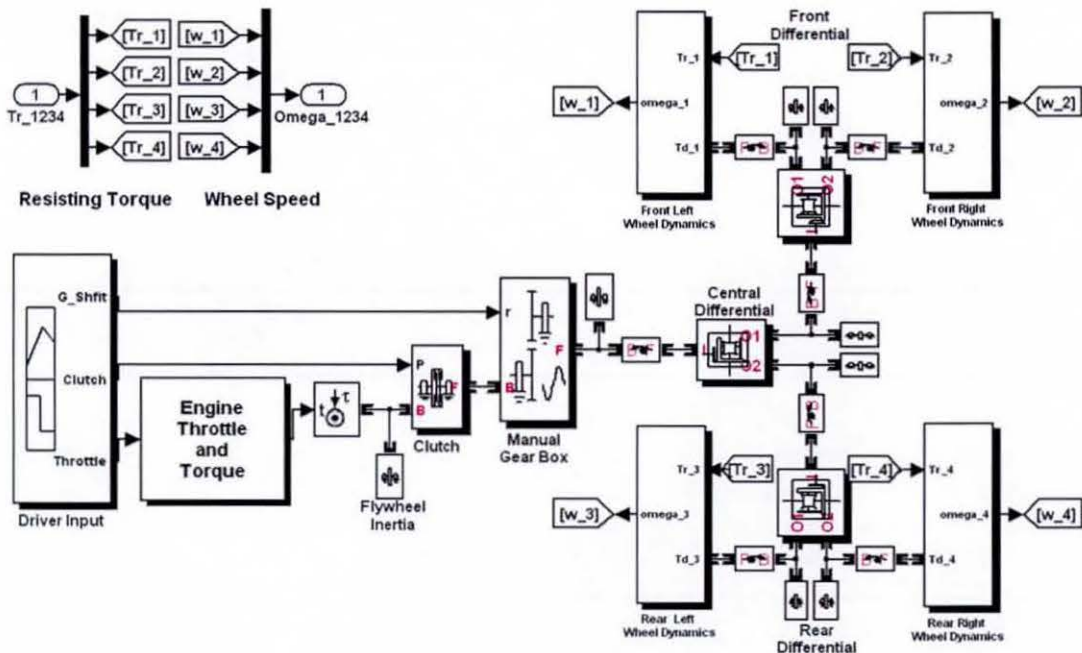


Figure 4.9 Development of 4x4 Drivetrain Model using SimDriveline

Engine:

Over the years, numerous computational models have been developed for the prediction of engine performance and fuel consumption. These models have different accuracies depending on the extension of details. Generally, engine modelling may be categorized into three groups. The first group incorporates static or steady state conditions which is widely acceptable for evaluation of performance. The second group implements simple dynamics with simple variables which is suitable for control system design. The third group deals with complex dynamics with large number of variables which is suitable for hardware in loop (HIL) simulations.

Traditionally, the static approach is based on steady state characteristics, which offers the advantage of high speed calculations and puts less demands on amount of required data entry. The accuracy of this approach depends on the available data from manufacturing.

The engine characteristics are included in the model as a look-up table of engine torque versus engine speed and throttle position. It should be noted that the engine model does not include the air-fuel mixture and the combustion process. The throttle signal directly controls the output torque that the engine generates and indirectly controls the speed at which the engine runs. If the engine speed exceeds the maximum specified speed the engine torque drops to zero. For the purpose of constant speed simulations, a proportional-integral-derivative (PID) controller is used. Based on the difference between the desired and actual speeds, the controller specifies the appropriate position of the throttle pedal to keep the vehicle speed constant.

The output torque of the engine is characterized by the driving torque (M_e) resulting from combustion, the internal friction torque (M_{fr}), and the external load (M_{cl}) from the clutch. Newton's second law of motion gives the following model:

$$I_e \cdot \ddot{\theta}_e = M_e - (M_{cl} + M_{fr}) \quad (4.78)$$

Where (I_e) is the mass moment of inertia of the engine and ($\ddot{\theta}_e$) is the flywheel angular acceleration.

Friction Clutch:

Friction clutch is commonly found in vehicles equipped with a manual transmission. It consists of friction disk connecting the flywheel of the engine and the transmission's input shaft. The clutch provides the capability to allow or restrict the transmission of engine torque to the drivetrain through clutch pedal. One of the simplest possible clutches is a set of two plates normal to the axis of transmission, one being the input and the other the output. The two plates can be pressed together so that friction causes the input to impart torque onto the output. The greater the pressure is, the higher the torque which can be transmitted.

The clutch requires a dimensionless input pressure signal (between zero and one) to modulate the applied friction. This signal is input as a function of time, which represents the driver response regarding clutch engagement and disengagement.

All the parameters required to describe the clutch are defined such as the number of friction surfaces (N_c), the effective torque radius (R_m), inner (r_1) and outer (r_2) plate radius, kinetic (μ_k) and static (μ_s) coefficients of friction. The clutch system is analyzed using a lumped-parameter model; the state equations for the coupled system are derived as follows:

$$\left. \begin{aligned} I_e \cdot \ddot{\theta}_e &= M_e - b_e \cdot \dot{\theta}_e - M_{cl} \\ I_t \cdot \ddot{\theta}_t &= M_{cl} - b_t \cdot \dot{\theta}_t \end{aligned} \right\} \quad (4.79)$$

Where; (I_e, I_t) are the mass moments of inertia of the engine and transmission system. (b_e, b_t) are the damping rates at the engine and transmission sides of the clutch.

The torque capacity of the clutch ($M_{f_{max}}$) is a function of its size, friction characteristics (μ) and the normal force that is applied between the friction plates (F_n) as follows:

$$\begin{aligned}
 M_{f_{\max}} &= \iint_A \frac{\mathbf{r} \times \mathbf{F}_f}{A} \cdot d\mathbf{a} \\
 &= \frac{F_n \cdot \mu \cdot N_c}{\pi \cdot (r_2^2 - r_1^2)} \cdot \int_{r_1}^{r_2} \int_0^{2\pi} r^2 \cdot dr \cdot d\theta \\
 &= F_n \cdot \mu \cdot N_c \cdot \underbrace{\frac{2}{3} \cdot \left(\frac{r_2^3 - r_1^3}{r_2^2 - r_1^2} \right)}_{R_m} \\
 &= F_n \cdot \mu \cdot N_c \cdot R_m
 \end{aligned} \tag{4.80}$$

When the clutch is slipping, the input and output remain independent, but some torque is transferred between them. The model uses the kinetic coefficient of friction (μ_k) and the full capacity ($M_{f_{\max}}$) is available in the direction that opposes slip.

$$M_{cl} = M_{f_{\max}} \cdot \text{sgn}(\dot{\theta}_e - \dot{\theta}_t) = \underbrace{F_n \cdot \mu_k \cdot N_c \cdot R_m}_{M_{f_{\max}}} \cdot \text{sgn}(\dot{\theta}_e - \dot{\theta}_t) \tag{4.81}$$

When the clutch applies static friction (μ_s) the frictional surfaces are locked together and do not slip. Both the input from the engine and the output to transmission effectively form a single axis ($\dot{\theta}_e = \dot{\theta}_t$). This state transfers the maximum torque possible and the system torque acts on the combined inertia of engine and transmission as a single unit. So, the equations (4.78) and (4.79) are combined into a single equation for the locked state:

$$(I_e + I_t) \ddot{\theta}_e = M_e - (b_e + b_t) \cdot \dot{\theta}_e \tag{4.82}$$

Solving equation (4.79) and equation (4.82) the torque transmitted by the clutch while locked can be given as follows:

$$M_{cl} = M_f = \frac{I_t \cdot M_e - (I_t \cdot b_e - I_e \cdot b_t) \cdot \dot{\theta}_e}{(I_e + I_t)} \tag{4.83}$$

The clutch thus remains locked unless the magnitude of (M_f) exceeds the static friction capacity ($M_{f_{\max}}$) where; ($M_{f_{\max}} = F_n \cdot \mu_s \cdot N_c \cdot R_m$)

Gear-Box:

The manual five-speed gear-box is modelled by a two-mass system, connected by a gear connection taking into account the gear ratios (i_G), gear efficiencies (η_G) and inertias.

A time signal is used to control the gear shifting sequence, while the program is running. Ultimately, the gear shifting instances are related to the engine speed, in order to achieve the best traction performance. If the maximum engine speed is reached, the gear box is shifted to a higher gear (lower gear ratios).

Both the angular velocity ($\dot{\theta}_{out}$) and acceleration ($\ddot{\theta}_{out}$) of the output shaft can be calculated as follows:

$$\left. \begin{aligned} \dot{\theta}_{out} &= \frac{\dot{\theta}_m}{i_G} \\ \ddot{\theta}_{out} &= \frac{\ddot{\theta}_m}{i_G} \end{aligned} \right\} \quad (4.84)$$

Torque loss due to friction between gears is calculated based on the following equation:

$$M_{loss} = M_m \cdot (1 - \eta) \quad (4.85)$$

Furthermore, drive shaft and axle inertias, as well as number of axles are considered in the model. Drive shaft and axles are modelled as rigid shafts.

Mechanical Differential:

The differential couples the rotational motion about the longitudinal axis with the rotational motion about two lateral axes. In normal use, the longitudinal shaft is the input, and motion, torque, and power flow out through the lateral shafts. The three rotational degrees of freedom, the longitudinal (ω_l) and the lateral ($\omega_{o_1}, \omega_{o_2}$), are subject to one gear constraint and thus reduce to two independent degrees of freedom. In terms of the differential gear ratio (i_D), the longitudinal motion is related to the sum of the lateral motions as shown in the following kinematic constraint:

$$\omega_l = i_D \cdot \left(\frac{\omega_{o_1} + \omega_{o_2}}{2} \right) \quad (4.86)$$

The driving output torques along the lateral axes (M_{o_1}, M_{o_2}) are constrained by the longitudinal input torque (M_l) in such a way that the power input equals the sum of the power outputs as follows:

$$M_l \cdot \omega_l = M_{o_1} \cdot \omega_{o_1} + M_{o_2} \cdot \omega_{o_2} \quad (4.87)$$

The combination of kinematic and power constraints yields the following relation:

$$M_l = \left(\frac{2}{i_D} \right) \cdot \left(\frac{M_{o_1} \cdot \omega_{o_1} + M_{o_2} \cdot \omega_{o_2}}{\omega_{o_1} + \omega_{o_2}} \right) \quad (4.88)$$

For an open differential the applied torques along the lateral axes are equal and limited by the lower adhesion between wheel and soil as follows:

$$M_{o_1} = M_{o_2} = i_D \cdot \frac{M_l}{2} \quad (4.89)$$

The locked differential has the same parts as an open differential, but adds an electric, pneumatic, hydraulic or frictional mechanism to lock the two output pinions together. This mechanism is usually activated manually, and when activated, both wheels spin at the same speed. If one wheel leaves the ground, the other wheel remains unaffected.

To model differential locking a controllable friction clutch is connected between the two output shafts. The clutch input signal can be programmed to represent full differential lock (the input pressure signal is a constant value) or a limited slip differential (the input pressure signal is variable, depending on the difference between the left and right rotational speeds). For full mechanical differential lock:

$$\omega_{o_1} = \omega_{o_2} = \frac{\omega_l}{i_D} \quad (4.90)$$

$$M_l = \frac{(M_{o_1} + M_{o_2})}{i_D} \quad (4.91)$$

Shafts and Axles:

The shaft is modelled as a rotational stiffness (k_{sh}) and damping (b_{sh}) in parallel and use the relative displacement ($\theta_{in} - \theta_{out}$) and relative velocity ($\dot{\theta}_{in} - \dot{\theta}_{out}$) across the end of the shaft to develop a windup torque. Shaft backlash may be also included to account for the shaft splines.

The general dynamic equation of output torque can be obtained as:

$$M_{out} = M_{in} - \underbrace{I_{sh} \cdot \ddot{\theta}_{sh}}_{\text{Inertia Effect}} - \underbrace{b_{sh} \cdot (\dot{\theta}_{in} - \dot{\theta}_{out})}_{\text{Stiffness Effect}} - \underbrace{k_{sh} \cdot (\theta_{in} - \theta_{out})}_{\text{Damping Effect}} \quad (4.92)$$

The above equation can be written for any shaft carrying torque, for example the propeller shaft or an axle shaft.

4.3 Numerical Simulation

Hitherto, modelling effort has concentrated on replicating individual component behaviour as closely as possible. This has, in the main, led to large multi-body dynamic models, created in codes such as ADAMS. Although very good agreement is often found with test data, the sheer size of such models often leads to long computation times.

For the purpose of the present study the model is implemented in the 'MATLAB/Simulink/SimDriveline' environment. This choice has added the possibilities of later incorporation of advanced control strategies and the use of the real-time toolbox. Also, it provides total control over the equations of the model and has facilitated the implementation of an in-house written code.

MATLAB is used to:

- Define the vehicle body, suspension, tyres and soil input data.
- Set the initial conditions of the states and define the testing manoeuvres.
- Carry out all basic calculations in matrix form to be used by the Simulink model.
- Execute the Simulink model.
- Read, save and plot the output results from Simulink model (postprocessing).

Simulink is used to:

- Integrate all the vehicle subsystems' modules with the off-road tyre model, where the tyre model is defined as a S-function in the Simulink environment, figure 4.10.
- Implementing the drivetrain model using SimDriveline toolbox, figure 4.9.
- Solve fourteen second-order non-linear differential equations with respect to time, and give the output in the form of time histories into the Matlab workspace.

Numerical simulation procedures are carried out using ODE4: Runge-Kutta solver with fixed-step integration size of (0.001s). The vehicle model contains (299) state variables.

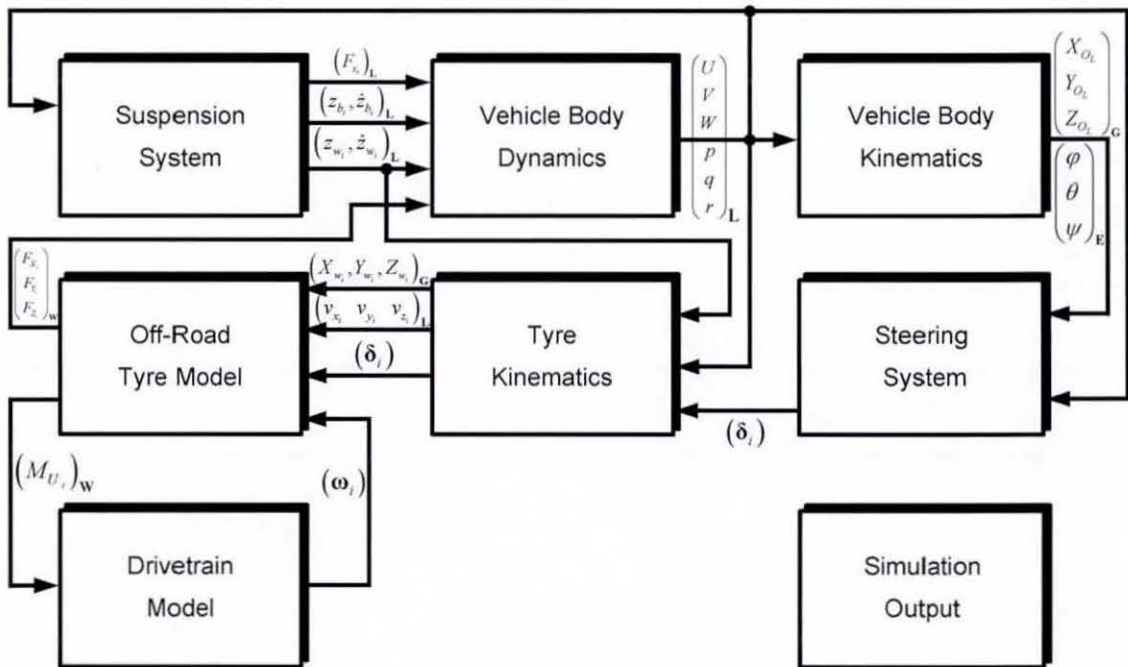


Figure 4.10 14-DOF 4x4 Off-Road Vehicle Simulink Model

4.4 Simulation Results and Analysis

Driving on soft terrains is very different to driving on prepared roads of solid construction. One main difference is the tyre sinkage, which is an important aspect of off-road terrains. Penetration of the wheel into the ground compresses the soil underneath the wheel, which is furrowed to the sides and to the front of the wheel, where a bow wave is built up. This plastic deformation of the soil produces the major part of the rolling resistance on soft grounds. The encountered rolling resistance not only reduces vehicle traction capabilities, but also affects the vehicle cornering behaviour and stability. At high slip angles the external rolling resistance has a lateral force component, which is added to the lateral force caused by shearing deformations, see equations (3.44) and (3.45). This lateral force rises with the sine of the slip angle (Harnisch, 2001).

Another difference in off-road operations is the restriction of the circumferential force on soft soils. Contrary to the conditions on rigid roads the tyre forces on soft soil are not only limited by the friction between the wheel and the ground surface, but also by the shear strength of the soil. The shear tension under the wheel is based on the local pressures and the local generated shear displacements. Furthermore, because the shear strength of soil is usually less than the friction between tyre and dry pavement, the maximum tyre forces (tractive and lateral) are reduced. Generally this can be noticed from the lower values of maximum lateral acceleration or by the limitation of the forward speed during off-road acceleration manoeuvres. As a result, the mechanism of tyre force generation greatly depends upon both wheel sinkage and the soil shear strength (depending on the soil type).

The aim of this section is to simulate an integrated 4×4 vehicle dynamics during various off-road manoeuvres and address the vehicle characteristics in terms of traction performance and cornering response. All simulations are carried out using 4×4 Land Rover Defender 110 (station wagon), see appendix (A). The baseline vehicle has three mechanical open differentials with a possibility to lock the centre differential. The static weight of the vehicle is distributed 40% on the front axle and 60% on the rear axle. The tyre inflation pressure is set to be 1.9 bar for the front axle tyres and 3.3 bar for the rear axle tyres.

As an integral part of off-road vehicle simulations, the soil mechanical properties should be defined, see appendix (A). Three different types of soils with distinct properties are used, namely clay, loam and sand soil (AESCO, 2005). The firm clay soil is characterized by moderate high shear strength properties, as well as a good sinkage resistance. The dry sand soil is characterized by relatively good shear strength properties, while it has a low sinkage resistance. The wet loam soil (grass grown) is characterized by relatively good sinkage resistance while it has low shear strength properties.

4.4.1 Traction Analysis

As a case-study, the traction performance of the vehicle at full throttle position is evaluated during acceleration in a straight line manoeuvre on firm clay soil, Figure 4.11. The throttle increases until the engine speed reaches its maximum value, at which stage the gearbox is shifted to a higher gear. This results in the saw-tooth diagram shown in figure 4.11.d. During shifting, the throttle is released and the clutch is disengaged.

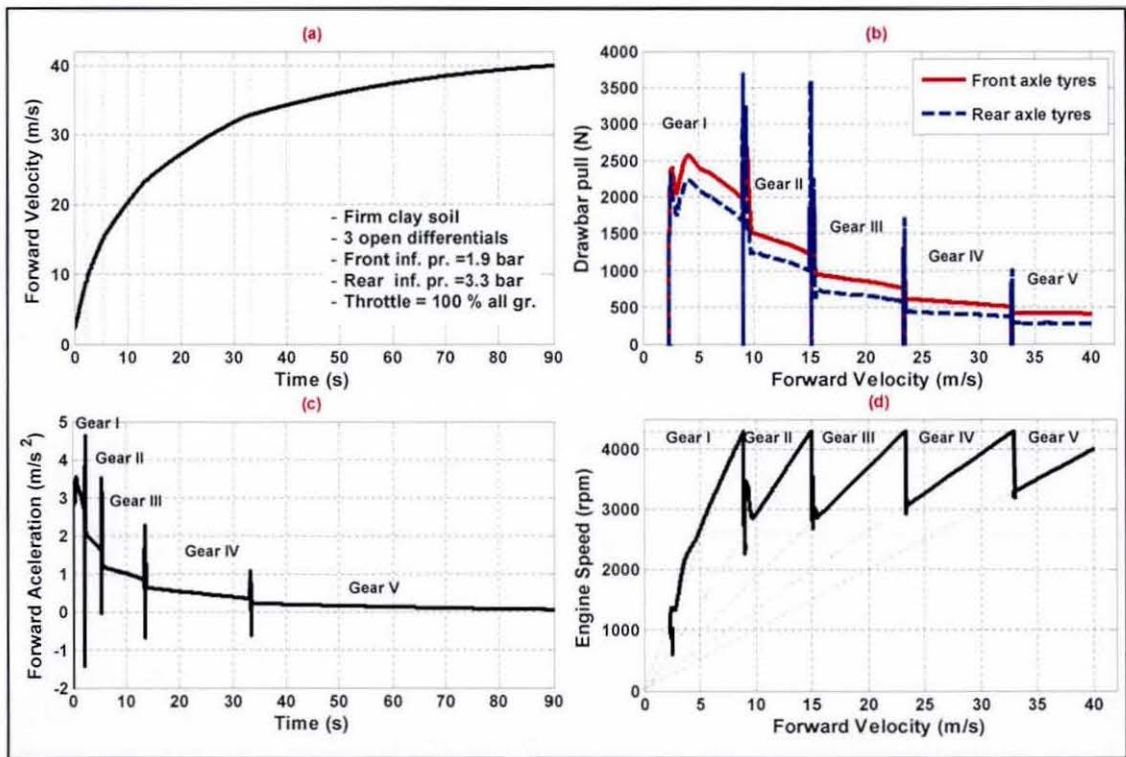


Figure 4.11 Traction Performance of the Baseline Vehicle Configuration

It should be noted that during the shifting process and until throttle reaches its maximum position the vehicle acceleration fluctuates. This results from an instantaneous drop in vehicle speed and the effect of clutch engagement and throttle pedal application. This causes wheel slip fluctuations which affects the vehicle acceleration. The amplitude of these fluctuations reflects the amplitude of tyre slip, which reaches its higher values in first gear and decreases as the gear box is up-shifted.

4.4.1.1 Effect of Soil Shear Strength Properties

The calculation of tractive force, as well as the drive torque is based on both the local ground pressure ($p(\vartheta)$) and the local shear displacement ($j_l(\vartheta)$) at the tyre contact patch. The local shear displacement can be calculated by time integration of the local rotational speeds (Wong and Reece, 1967a, 1967b). Based on the local shear displacement the local shear stress (τ) is computed by Bekker (1969) as follows;

$$\tau = \underbrace{(C + p \cdot \tan \varphi)}_{\tau_{\max}} \cdot \left(1 - e^{-\frac{j}{k}}\right) \quad (4.93)$$

The first part of equation (4.93) can be calculated from the Coulomb contribution, where (C) is the apparent cohesion of the soil and refers to the cohesive portion of the shear strength, ($p(\vartheta) \cdot \tan \varphi$) represents the frictional portion of the shear strength, where (ϑ) is the contact angle and (φ) is the soil angle of shearing resistance. The integration of shear stress (τ) over the contact patch gives the circumferential force. The horizontal portion of (τ) gives the horizontal force as follows; (Harnisch, 2001)

$$F_H = b \cdot \left(\frac{D^*}{2}\right) \cdot \int_{s_m}^{s_{el, \max}} (C + p(\vartheta) \cdot \tan \varphi) \cdot \left(1 - e^{-\frac{j_l(\vartheta)}{k}}\right) \cdot \sin(\vartheta) \cdot d\vartheta \quad (4.94)$$

The drawbar pull or net tractive force can be calculated as the difference between horizontal force (F_H) and the external rolling resistance.

Figure 4.12 shows the traction performance for different soils with different shear strength properties. As opposed to rigid road situations, the circumferential force on soft soil is not only limited by the friction between the wheel and the ground surface, but also by the shear strength of the soil. In soft loose soil the maximum shear tension is not immediately available at the beginning of the contact area, but is reached asymptotically with increasing shear displacement, equation (4.93). As a result, in the case of wet loam soil with lower shearing properties, it takes a longer time to achieve the same vehicle speed, followed by sand and clay soil, Figure 4.12.a. This is also apparent in the speeding up distance characteristics, Figure 4.12.b.

Another good indicator of traction performance is the vehicle forward acceleration, Figure 4.12.c. In general, acceleration is higher in first gear which is characterized by a higher ratio, whereas acceleration decreases as the gear is up-shifted. Comparison of acceleration results for different soils shows a difference which is more prominent in first gear, revealing the contribution of soil shearing properties. In the case of firm clay soil the shearing properties are such that the vehicle is propelled effectively, whereas the soft loam causes excessive slippage, which in turn increases sinkage and resistance.

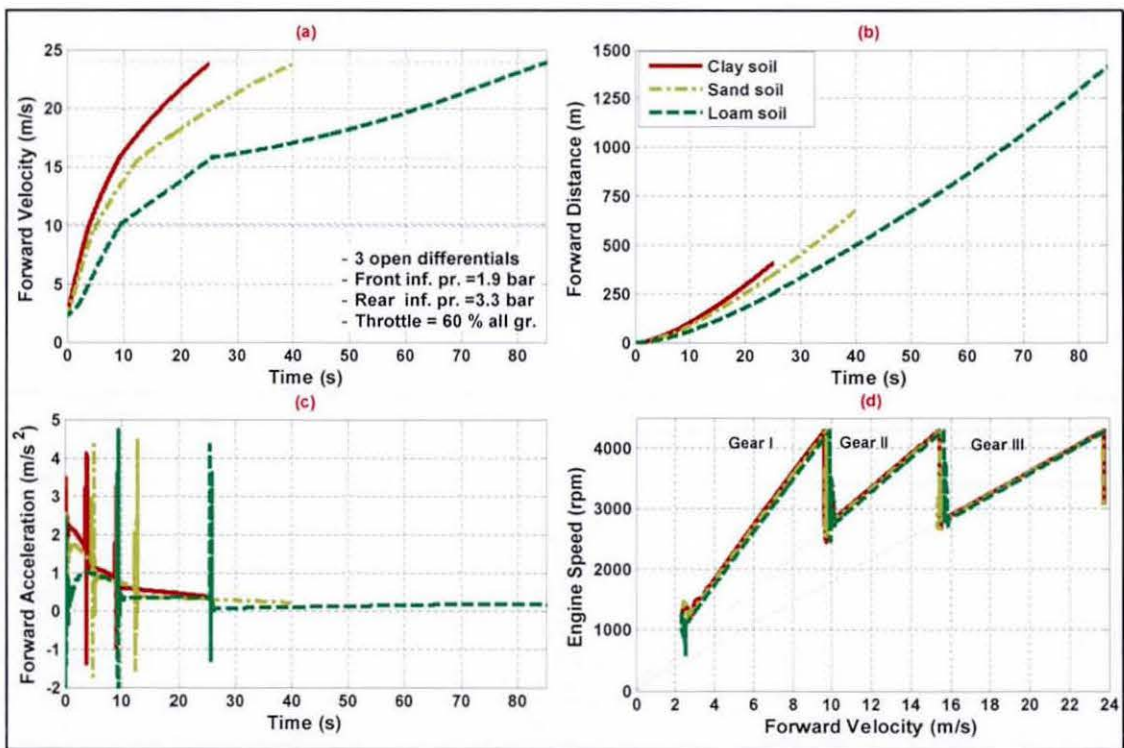


Figure 4.12 Effect of Soil Shear Strength on Traction Performance

4.4.1.2 Effect of Tyre Inflation Pressure

The main difference between driving on soft terrains and driving on rigid roads is the tyre sinkage. A wheel on soft soil penetrates into the ground deeply until the resultant ground pressure (p) balances the wheel load (F_z). The arising ground pressure is a result of the normal ground deformation (z). This can be described by the following equation, yielding the relationship between pressure and sinkage (Bekker, 1956, 1969):

$$p = \left(\frac{K_c}{b} + K_\phi \right) \cdot z^n = K \cdot z^n \quad (4.95)$$

Where: (K_c, K_ϕ) are the cohesive and frictional moduli of soil deformation, (n) is the soil sinkage exponent, and (b) is the width of the rectangular plate, or the radius of the circular plate. This equation shows that for the same soil parameters (K_c, K_ϕ, n), tyre sinkage (z) increases if the ground pressure or tyre vertical load rises. Another important parameter is the rolling resistance. The major part of the rolling resistance on soft ground results from the energy absorption of the soil, which is caused by the compaction and deformation of the soil. Therefore the rolling resistance can be calculated from the plastic soil deformation under the wheel as follows; (Bekker, 1956, 1969):

$$F_R = b \cdot \int_0^{z_0} p(z) \cdot dz = b \cdot \left(\frac{K_c}{b} + K_\phi \right) \cdot \left(\frac{z^{n+1}}{n+1} \right) \quad (4.96)$$

As tyre inflation pressure reduces, for the same vertical load, both the tyre contact length and contact area increase. Because of the enlarged contact area the ground pressure is reduced. As a result sinkage also decreases, equation (4.95), and, therefore, the rolling resistance is reduced, equation (4.96). In addition, the increase in contact area leads to the enlargement of the circumferential force, equation (4.94). Thus, it becomes obvious that the drawbar pull, which is the difference between circumferential force and rolling resistance, is affected favourably by a reduction in tyre inflation pressure (Lach, 1996).

Figure 4.13 shows how a reduction in tyre inflation pressure improves the straight-line performance on the loam soil. This can be seen clearly from an increase in vehicle acceleration for the same gear ratio, figure 4.13.c, and the improvement of speeding up time and distance, figure 4.13.a and figure 4.13.b.

It should be noted that wheel sinkage is the result of two different mechanisms. The first is called static sinkage representing the reaction to the wheel vertical load, as explained previously. The second mechanism is the slip sinkage due to excessive slipping, causing the wheel to penetrate into the ground, compressing the soil underneath the wheel, which is in turn furrowed to the sides and to the front of the wheel, where a bow wave is built up. This excessive slip leads to additional sinkage and rolling resistance and, hence, reduces the resulting tractive force. This explains why in soft deformable soils it is advisable to apply the throttle pedal gradually, especially when in first gear (section 3.2.9)

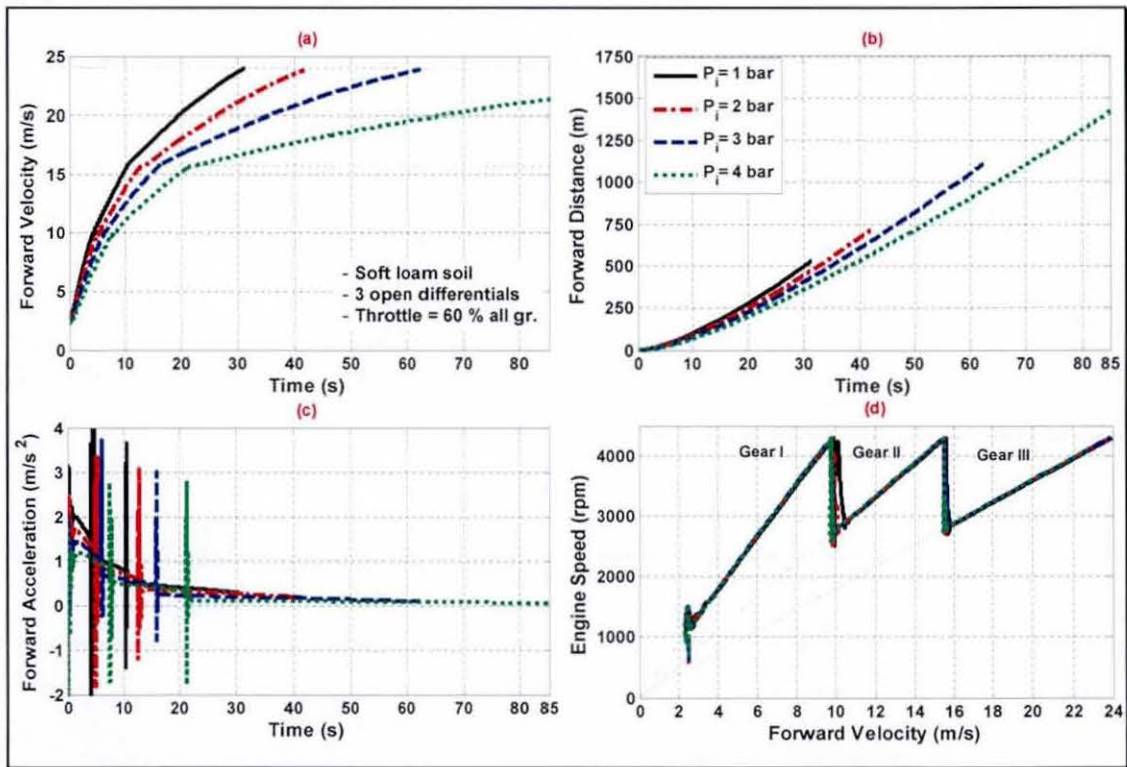


Figure 4.13 Effect of Tyre Inflation Pressure on Traction Performance

4.4.1.3 Effect of Differential Lock

Before discussing the effect of a locked differential on 4×4 off-road vehicles, it is useful to introduce the significant role of static load distribution between front and rear axles. In general, when the axle load increases, the ground pressure also increases, enhancing the maximum shear strength available by the soil, equation (4.93), and hence the circumferential force developed by the tyres, equation (4.94). This increases the ability of the tyres to develop higher driving torques without causing excessive slip. On the other hand, when the axle weight is increased, both tyre sinkage and rolling resistance also increase, equation (4.96). It should be mentioned that, for the reference vehicle, load distribution between front and rear axle is (40:60%) respectively.

To show the effect of differential locking, the reference vehicle is simulated in straight-line acceleration on dry sand soil. Vehicle traction performance is evaluated in two situations: first with an open central-differential and second with a locked central-differential, figure 4.14.

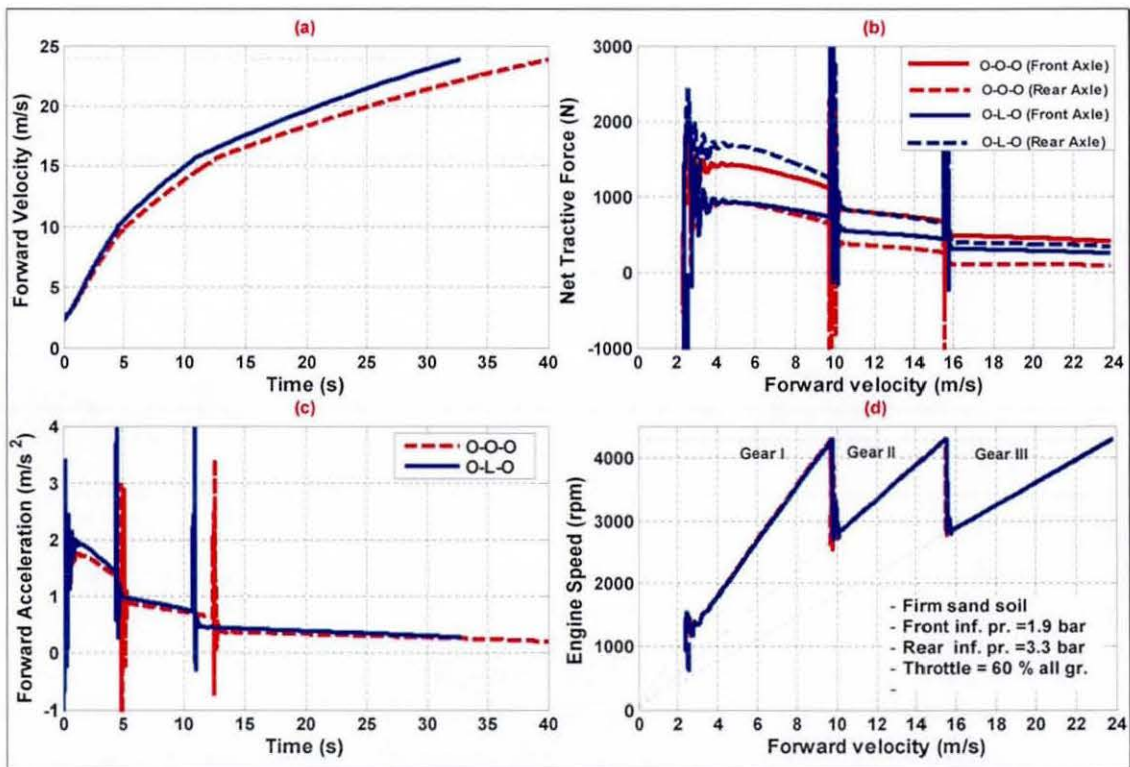


Figure 4.14 Effect of Differential Lock on Traction Performance

For open central-differential: the driving torque from the powertrain system is distributed equally between the front and rear axles, equation (4.89), therefore, the torque distribution is limited by the lower traction side or by the axle carrying the least weight. For the same driving torque, the rear axle-tyres suffer from higher rolling resistance due to higher vertical weight and sinkage. As a result, net tractive force at the front axle-tyres will be higher than that at the rear axle-tyres, figure 4.14.b.

For the locked central-differential: the driving torque from the powertrain system is distributed, based on the available traction at each axle, equation (4.91). Therefore, the rear axle with a larger weight and, therefore, relatively higher shear strength is able to develop a higher driving torque than the front axle. Hence, the generated drawbar pull at the rear axle-tyres would be higher than that at the front axle-tyres, figure 4.14.b. Another benefit of a locked differential is that all tyres are forced to rotate with the same driving speed, so the slip of all tyres is regulated by that of the tyre with most traction. Thus, the slip values at all four corners are automatically adjusted in favour of traction.

4.4.2 Handling Analysis

The rapidly increasing applications of AWD, particularly in the passenger vehicle sector demand the development of vehicles, not only with higher traction and acceleration capabilities, but also with better manoeuvrability over deformable soil. Although improving traction performance is a main consideration for off-road vehicle applications, handling behaviour is an important aspect of modern vehicles, which requires capability to undergo high lateral accelerations, whilst maintaining good level of directional stability. The desired increase in mobility must be reached without making any compromises regarding safety or ease of operation or driver comfort. This is particularly true as the driving torque affects the lateral behaviour of pneumatic tyres. It is anticipated that the handling response of these vehicles may be different from on-road vehicles. Furthermore, vehicle side-slip and yaw motions are dependent on, not only the vehicle design parameters and tyre characteristics, but also on the mechanical properties of the terrain. Therefore, study of handling characteristics of all-wheel drive vehicles, especially at high speeds, has become a significant point of research.

The prescribed 14-DOF model is used to simulate the handling behaviour of 4×4 vehicles subject to a steering input. The output is a time history of the vehicle motion variables such as lateral velocity, roll angle, yaw velocity, and lateral acceleration. Vehicle handling characteristics are examined under both steady state and transient conditions.

4.4.2.1 Steady State Handling Response

The steady-state handling behaviour of the 4WD vehicle is simulated by a given step steering angle of 2 degrees, within time interval of 1 second, applied at the front left wheel and then maintained for 30 seconds, see figure 4.18.a. The step input theoretically makes the vehicle, driven at constant speed, to follow a constant-curvature path at steady state, figure 4.18.b. The vehicle handling steady-state response is examined in terms of lateral acceleration gain and yaw velocity gain responses. Lateral acceleration gain is defined as the ratio of steady-state lateral acceleration to the input steering angle. Yaw velocity gain is defined as the ratio of steady-state yaw velocity to the input steering angle (Wong, 2001). Both lateral acceleration gain and yaw velocity gain cannot be calculated or predicted directly by a single execution of the model. Instead the vehicle is simulated by a given step steering input, similar to the one shown figure 4.18.a, at various vehicle longitudinal speeds. The steady-state lateral acceleration gain is determined from the steady-state lateral acceleration. A similar procedure is applied for obtaining yaw velocity gain. Furthermore, the off-road vehicle model is used to investigate the handling characteristics under different conditions as described below.

4.4.2.1.1 Static Weight Distribution Ratio:

Before discussing the effect of static weight distribution ratio between front and rear axles, it would be useful to introduce the significant role of tyre sinkage in soil terrain. Sinkage affects handling characteristics due to additional lateral loads generated at the tyre sidewalls. Tyre sinkage (z) varies non-linearly with tyre ground pressure (p_n) according to the well-known relationship: $\left(p_n = \left(\frac{K_c}{b} + K_\phi \right) \cdot z^n \right)$, (Bekker, 1956, 1960).

Where: (K_c, K_ϕ) are cohesive and frictional moduli of soil deformation, (n) is soil

sinkage exponent, (b) is width of the rectangular plate, or radius of the circular plate which represents the tyre width.

At higher sinkage, significant tyre sidewall forces may occur, which can be explained by the soil cutting theory (Wong, 2001). According to this theory a stress field occurs in the soil. Soil mechanics equations have been developed for this situation, based on passive soil failure, which is developed using the Mohr's circle technique. The additional lateral load capability is determined from integrating the passive soil pressure over the tyre sidewall for a given sinkage distribution of the tyre.

For very high slip angles, an additional effect is the bulldozing or build-up of soil at the tyre sidewalls, especially for soft soils, increasing the maximum lateral load. Furthermore, the tyre cornering stiffness and the maximum lateral load capacity both increase with the vertical load (Crolla and El-Razaz, 1987).

Vehicle weight distribution between front and rear axles plays a significant role in off-road vehicle handling, see figure 4.15. Generally, as the vehicle weight distribution on the front axle increases more than that on the rear, the generated yaw rate gain and lateral acceleration gain also increase. This may be explained as follows: as the vertical weight increases on the front axle, the ground pressure, sinkage and contact length also increase. The additional sinkage provides extra sidewall surface available for the build-up of passive soil pressure, which leads to a higher side-force (Metz, 1993; Liang et al., 2004). Due to these effects, the resulting cornering stiffness at the front axle increases with vertical load. Consequently, the under-steer coefficient is reduced and the vehicle becomes more over-steering with a reduced turning and increased yaw velocity. Depending on the values of understeer coefficients or the relationship between the slip angles of the front and rear tyres, the steady-state handling characteristics may then be evaluated (Wong, 2001).

It should be noted that the effect of weight distribution ratio on the steady state handling response appears clearly in the case of driving on sand soil (friction soil), figure 4.15.c. This is mainly due to the dependency of the mechanism of tyre shear forces generation on the vertical weight, which affects the tyre cornering stiffness, see equation (4.93).

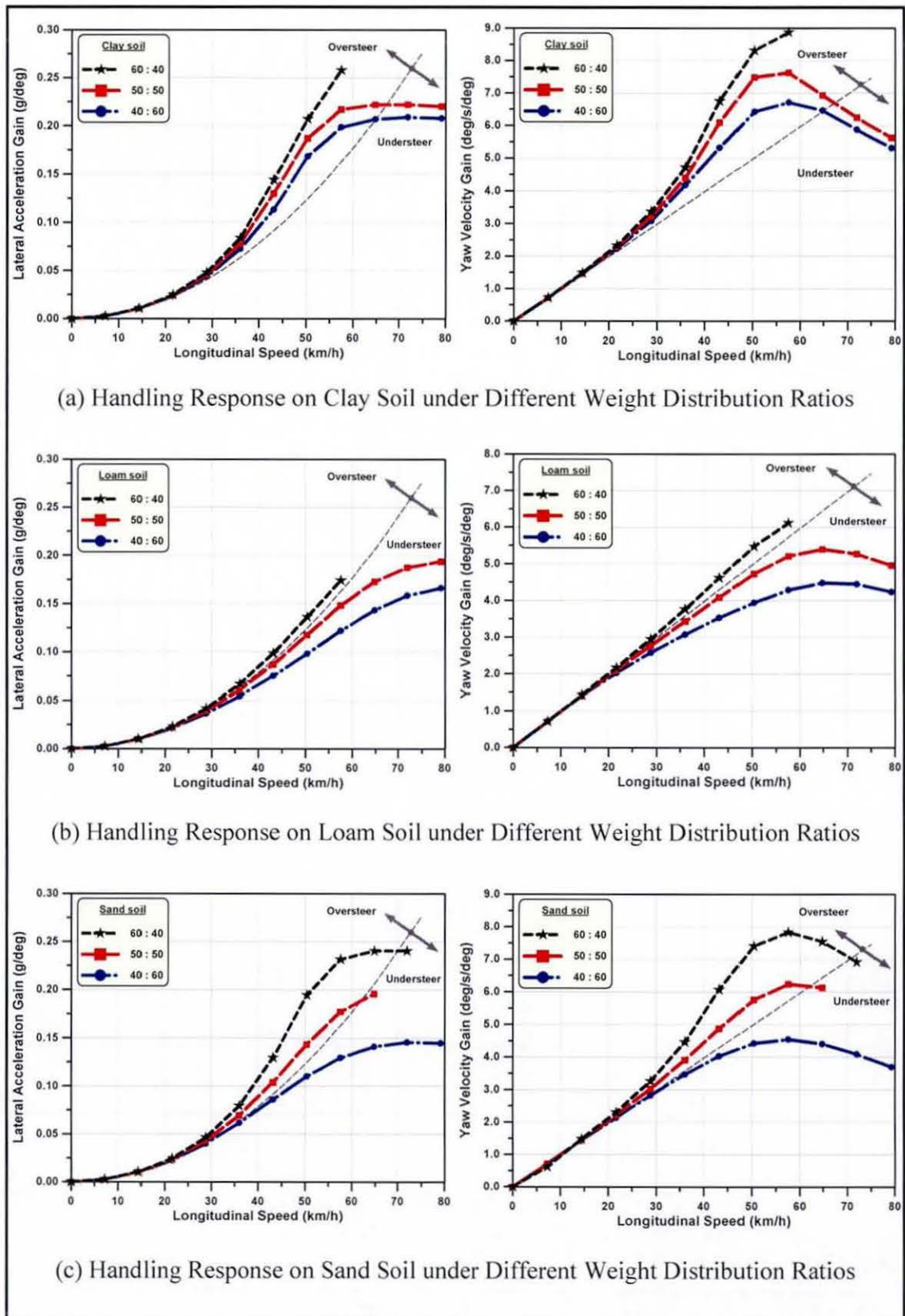


Figure 4.15 Effect of Static Weight Distribution Ratio between Axles

4.4.2.1.2 Soil Shear Strength Properties

The mechanism of lateral force generation is based not only on tyre sinkage (which is function of tyre vertical load), but also on the soil shearing strength (Bekker, 1956, 1960): $(\tau_{soil} = \tau_{max} \cdot (1 - e^{-j/k}))$, where (τ_{max}) is the soil maximum shear strength $(\tau_{max} = (c + p_n \tan \phi_s))$. Where also: (c, ϕ_s) are soil apparent cohesion and angle of internal shearing resistance, (j, k) are soil shear displacement and deformation moduli respectively. Therefore, it is important to examine the combined effect of sinkage (due to different weight distributions) for different cases of shear strength properties (different soils).

The effect of weight distribution is investigated over three types of soils with distinct mechanical properties, figure 4.16. These are firm clay soil with moderate shear strength properties, dry sand soil and wet loam soil. The results are obtained using drivetrain with a mechanical open differential and inflation pressure of 1.9 bar for the front axle tyres and 3.3 bar for the rear axle tyres.

Contrary to on-road, off-road tyre forces are affected by soil type, soil conditions (surface geometry, vegetation, etc.). Additionally, the terrain has a more significant effect than does the tyre parameters. Soil shear strength properties cause two significant effects on tyre cornering characteristics; a reduction in cornering stiffness and reduction in maximum lateral force (Crolla and El-Razaz 1987; Metz, 1993). Cornering stiffness is reduced since in addition to lateral tyre deformation, lateral soil deformation must occur for the soil to support load. Additionally, soil shear strength is typically less than the tyre/soil friction coefficient; hence the maximum lateral load capability is reduced.

Compared to sand and loam soils, due to its higher shearing strength, with clay soil higher maximum values for both the lateral acceleration gain and yaw velocity gain can be observed, as also noted by (Holloway et al., 1989; Harnisch et al., 2002). The vehicle handling behaviour is characterized by an oversteering characteristic, which appears clearly with shifting of more weight to the front axle, figure 4.16.c. It should be noted that compared to on-road handling manoeuvres, the maximum speed at which the vehicle is simulated is lower. Beyond this velocity significant lateral soil deformation occurs, resulting in a greater sinkage. This phenomenon is referred to slip sinkage (Metz, 1993).

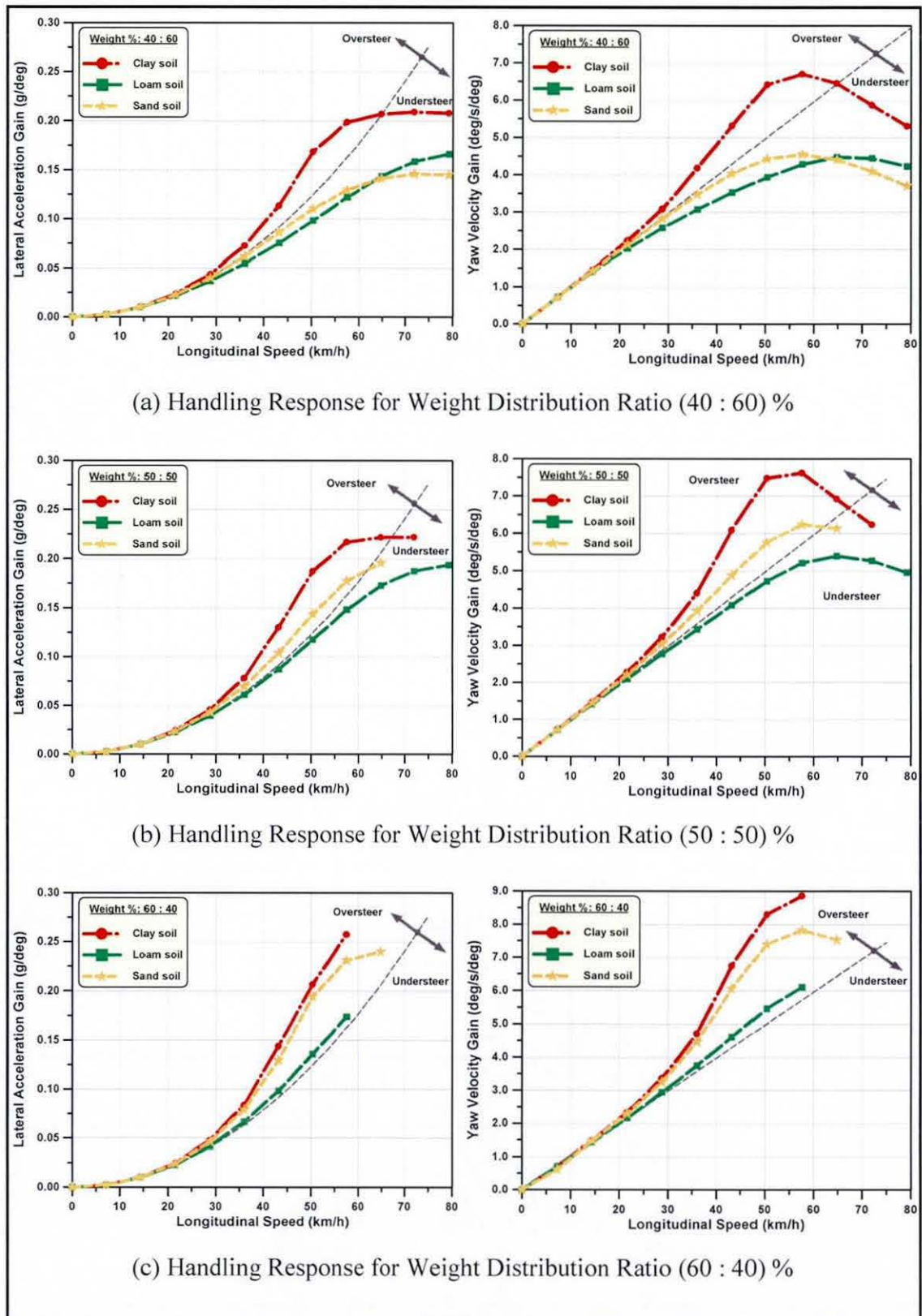


Figure 4.16 Effect of Soil Shear Strength Properties

4.4.2.1.3 Driveline Configurations:

The influence of different driveline configurations on the steady-state handling behaviour are depicted in figure 4.17. The simulations are carried out for both clay and sand soil with a fixed weight distribution of 40% and 60% for front and rear axles respectively.

Fundamentally, the cornering behaviour of any vehicle is mainly controlled by the generated lateral forces and slip angles at the tyre-ground contact patch. Furthermore, these lateral forces are regulated by the longitudinal slip and tractive force at each tyre according to the well known principle of friction circle (e.g., Crolla and El-Razaz, 1987). Both longitudinal and lateral tyre forces are restricted by the available soil shear strength properties, adhesion and the imposed tyre vertical force. Consequently, it is obvious that, biasing more driving torque to the rear axle would reduce the longitudinal slip at the front and therefore, increase the lateral force generating potential at the front. At the same time, the counteracting side force at the rear would be reduced. The additional yaw moment shifts the handling characteristics towards an oversteering response, a fact which in turn reduces both the stability and controllability of the vehicle.

It is clear from figure 4.17 that, front wheel drive (FWD) and rear wheel drive (RWD) represent the extremes of the aforementioned analysis. For FWD, the vehicle is biased to behave towards an understeering response, while for RWD the vehicle is biased to behave towards an oversteering response, which then deteriorates the vehicle stability.

Installing torque distribution devices between front and rear axles, e.g. mechanical differentials, would simply regulate the cornering response according to the criteria of torque distribution used, such that, the handling characteristics would be somewhere bounded by those resulting from FWD and RWD behaviours, depending on the axle weight distribution and the driving speed.

For open central differential (O-O-O): the driving torque is equally distributed between the axles, equation (4.89). Since the rear axle-tyres are subjected to a higher rolling resistance due to higher vertical weight and sinkage, both the longitudinal slip and tractive force at the front axle-tyres will be higher than those developed at the rear axle-

tyres. Consequently, the generated lateral forces at the rear axle will be higher than those at the front axle. On the other hand, the lateral load transfer from inward tyres to the outward tyres during cornering causes a considerable increase of the tractive force at the inward ones. The combined effect results in an under-steering tendency at high lateral accelerations

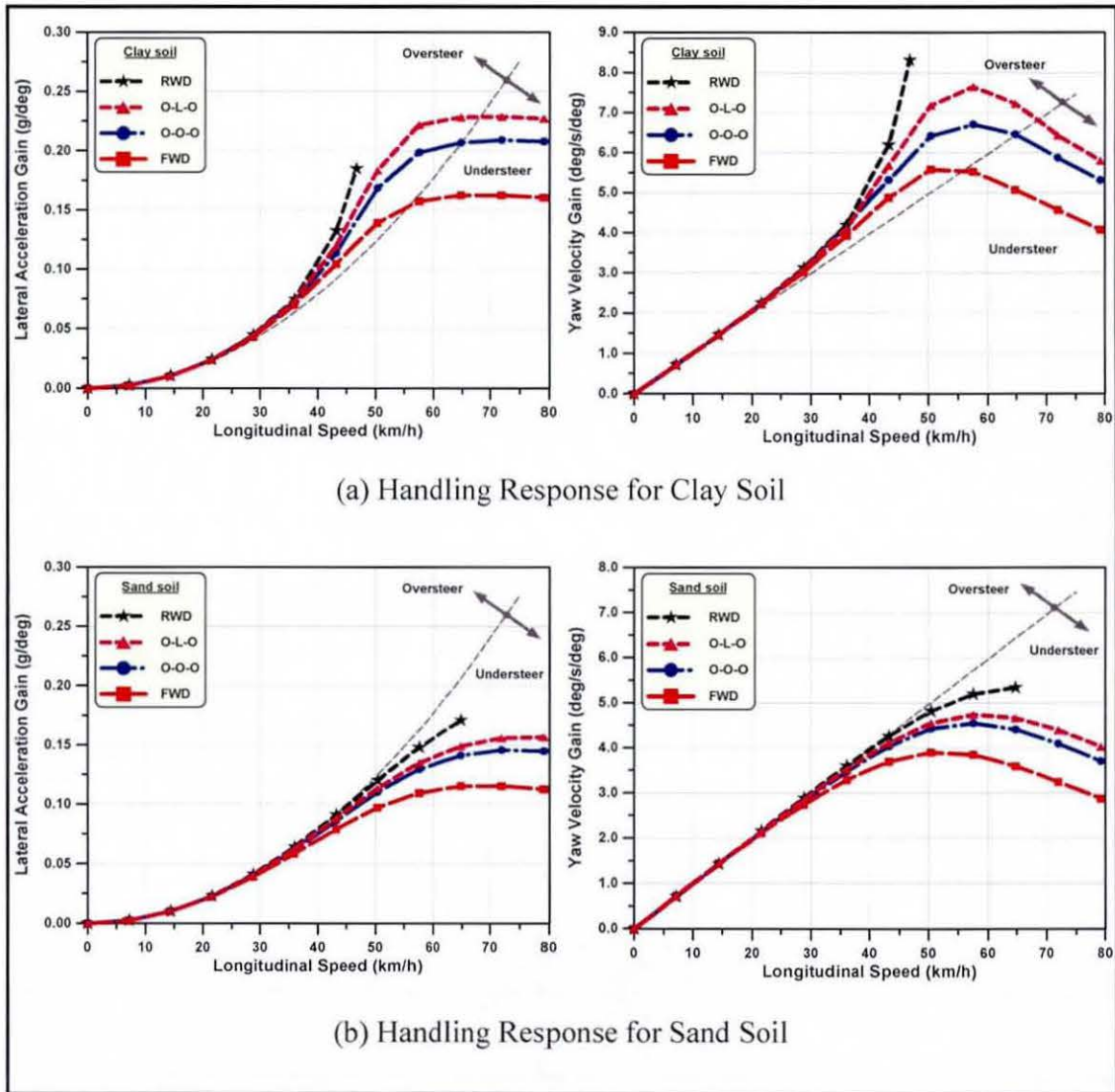


Figure 4.17 Steady State Handling Response for Different Driveline Configurations
(Weight Distribution 40% on front axle – 60% on rear axle)

For a locked centre differential (O-L-O): the driving torque is distributed between the front and rear wheels depending on the operating conditions, equation (4.91). Under the

condition of equal dynamic tyre radii for the front and rear tyres, the driving speed and thus the slip of all tyres equate and will be regulated by that of the tyre with the most traction. Under given steering conditions, the rear axle with a larger weight and, therefore, relatively higher shear strength would be able to develop a larger driving torque than the front axle. The slip at the front axle tyres, which is limited by the slip at the rear axle tyres would improve their potential to generate more lateral forces. This shifts the handling behaviour towards less understeer, when compared to that achieved by the open central differential configuration.

4.4.2.2 Transient Handling Response

Between the application of a steering input and the attainment of steady-state response, the vehicle is in a state of transience. The overall vehicle handling quality depends, to a great extent, on its characteristic transient response. The optimum transient response is that which has the fastest response with a minimum number of oscillations in the process of approaching the steady state condition. It is obvious from the steady-state analyses that the vehicle cornering behaviour not only depends on the static weight ratio but also on the soil mechanical properties especially for sand soils. In analyzing transient response for this case, two manoeuvres are considered: a step steer input manoeuvre (BS ISO 7401, 2003) and a lane change manoeuvre (El-Gindy and Woodrooffe, 1990).

4.4.2.2.1 Step Steer Manoeuvre

The step steering input is the simplest form of transient investigations, see figure 4.18.a. A steer angle of 2 degrees within rise time of a second is applied and maintained at the front left wheel while the angle of the front right wheel is calculated based on the Ackerman steering geometry (Wong, 2001). The manoeuvre is undertaken at a constant vehicle speed of 60 km/h. The vehicle forward speed is controlled by means of a PID controller. Initially, the forward speed drops due to the component of vehicle lateral velocity. Hence, an appropriate throttle input has to be applied in order to regain the velocity demand. This happens with an overshoot, with a settling time prior to reaching the steady state condition. Theoretically, the step steering input makes the vehicle follow a constant curvature path, figure 4.18.b.

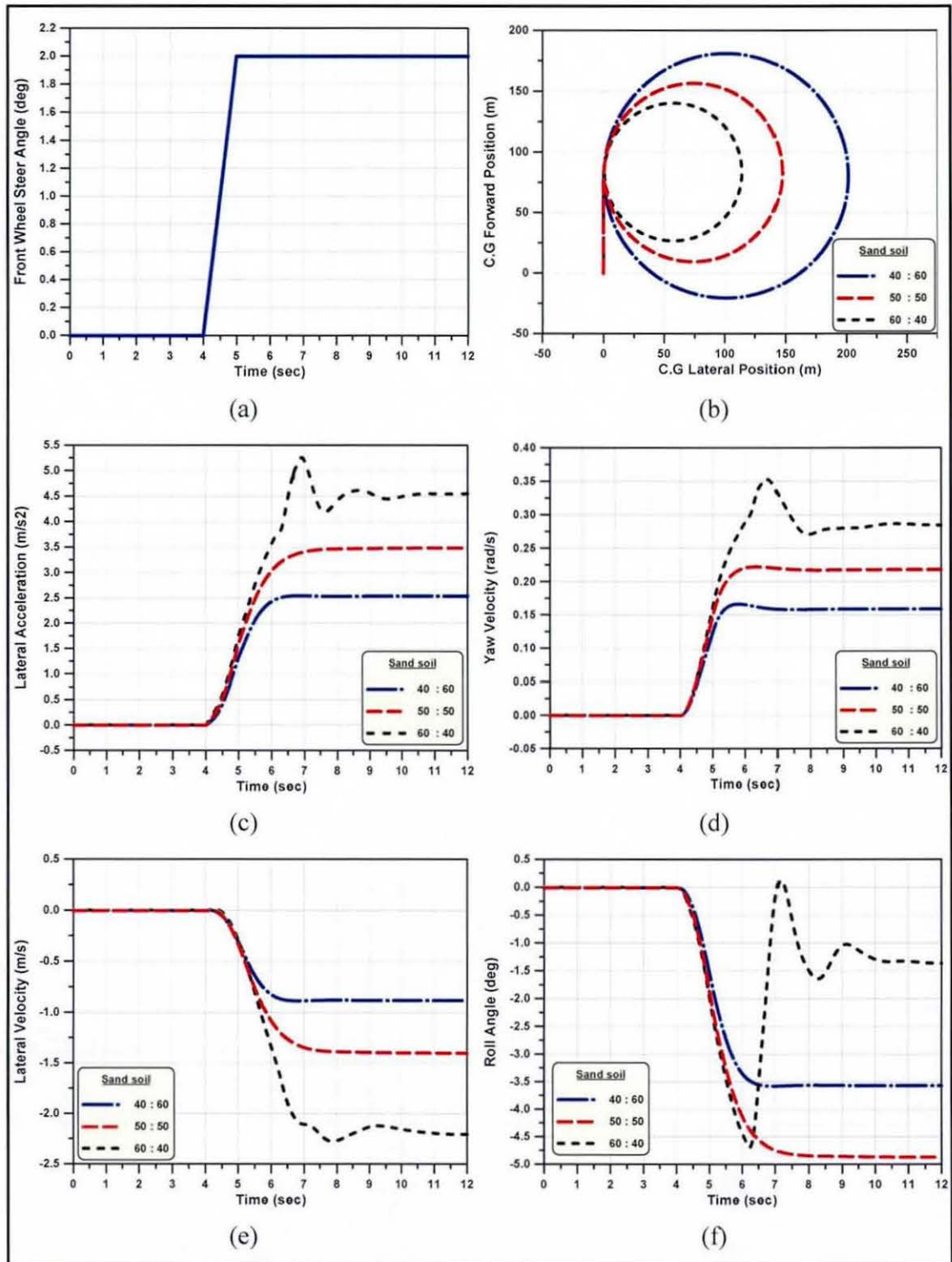


Figure 4.18 Transient Response of a Step Steer Input on Sand Soil at 60 km/h

As a result of applying the steering angle, a lateral acceleration is generated, figure 4.18.c. This lateral acceleration produces a centrifugal force, which induces the vehicle sprung mass to roll, figure 4.18.f, and move with a lateral velocity as shown in figure 4.18.e. As a reaction to this, a lateral force is generated at the tyre-ground contact patch, hence, slip angles are generated, which control the vehicle handling characteristics (under-steer or over-steer).

Referring to figure 4.18, generally, it is obvious that, increasing the static weight distribution on the front axle reduces the handling indicators' response, as explained before in the steady state analysis. However, it is clear that, this deterioration happens with a delay to reach steady state. For any change in wheel slip or slip angle, tyres have a finite response time relating to the time taken for the contact region to assume a new distorted shape. The lateral force delay of a side slip tyre is commonly called 'tyre lag' which has been explained by many researchers, e.g. Crolla and El-Razaz (1987).

Furthermore, it is observed that, for the simulation of weight distribution 60% on front and 40% on rear axle, both the lateral acceleration and yaw velocity transient responses perform an overshoot, although the curve still roughly follows the trend of the step steering input case. This phenomenon can be explained by observing the roll angle response of the sprung mass. Owing to the roll motion a lateral load transfer takes place so that the vertical force on the left and right tyres fluctuates.

At higher speeds, it is observed that sand soil behaves in an excessive manner. Since the sum of these fluctuated tyre lateral forces on all wheels is the only source that sustains the vehicle concerning, the vehicle's centrifugal or lateral acceleration also fluctuates as shown in figures 4.18.c and d. Because of the extra weight at the front axle, the equivalent cornering stiffness at the front axle increases due to extra sinkage. As a result the vehicle becomes excessively over-steering and momentarily stability is lost. Due to the complex interaction between the tyres and the sand, control is quickly re-gained and the vehicle stabilise at a different operation point. The oscillatory behaviour should not misinterpreted as an under-steering behaviour, as it is triggered by the roll motion of the vehicle due to the loss and subsequent re-gain of stability.

4.4.2.2 Lane Change Manoeuvre

The vehicle is subjected to a double triangular steering input, applied at the front left wheel, figure 4.19.a, with a constant angular speed of the steering wheel in both directions. The vehicle forward velocity is kept at 60 km/h and the simulation is performed for the duration of 18 seconds. The PID controller is used to maintain the vehicle speed, as previously described.

To demonstrate the transient cornering response of a 4×4 vehicle under off-road conditions, the handling characteristics of the same vehicle and weight distribution is simulated for different soils. The variations of typical indicators for transient handling in a lane change manoeuvre, such as yaw velocity, lateral acceleration, and roll angle of the sprung mass are plotted in figure 4.19.

Generally, it should be noted that the values of lateral acceleration are low compared to the same vehicle, when on-road, see figure 4.19.c. This is due to the restriction of the circumferential forces by the soil shearing strength, as a result of which the developed tyre lateral forces are remarkably lower than those for the case of the on-road manoeuvre.

Compared to the results obtained during step steer manoeuvre, there is a significant improvement in the time response of the lateral acceleration and yaw velocity. However, with regard to the simulation results of the sand soil, the vehicle cornering response shows quite sensitive behaviour to the static weight distribution and dynamic load transfer. According to (Bekker, 1960) soils can be classified to plastic soils (e.g. clay or loam), friction soils (e.g. dry sand) or mixture of plastic and friction properties. The maximum shear strength provided by the soil can be described by Mohr-Coulomb failure criterion, see equation (4.93). In contrary to clay and loam soils, the shear strength properties of sand soils and hence the mechanism of tyre forces generation are highly dominated by the imposed tyre vertical weight and the angle of internal friction. Increasing the tyre vertical load squeezes the sand grains against each other and improves its shear strength. As the tyres' vertical forces change, tyre lateral forces also vary.

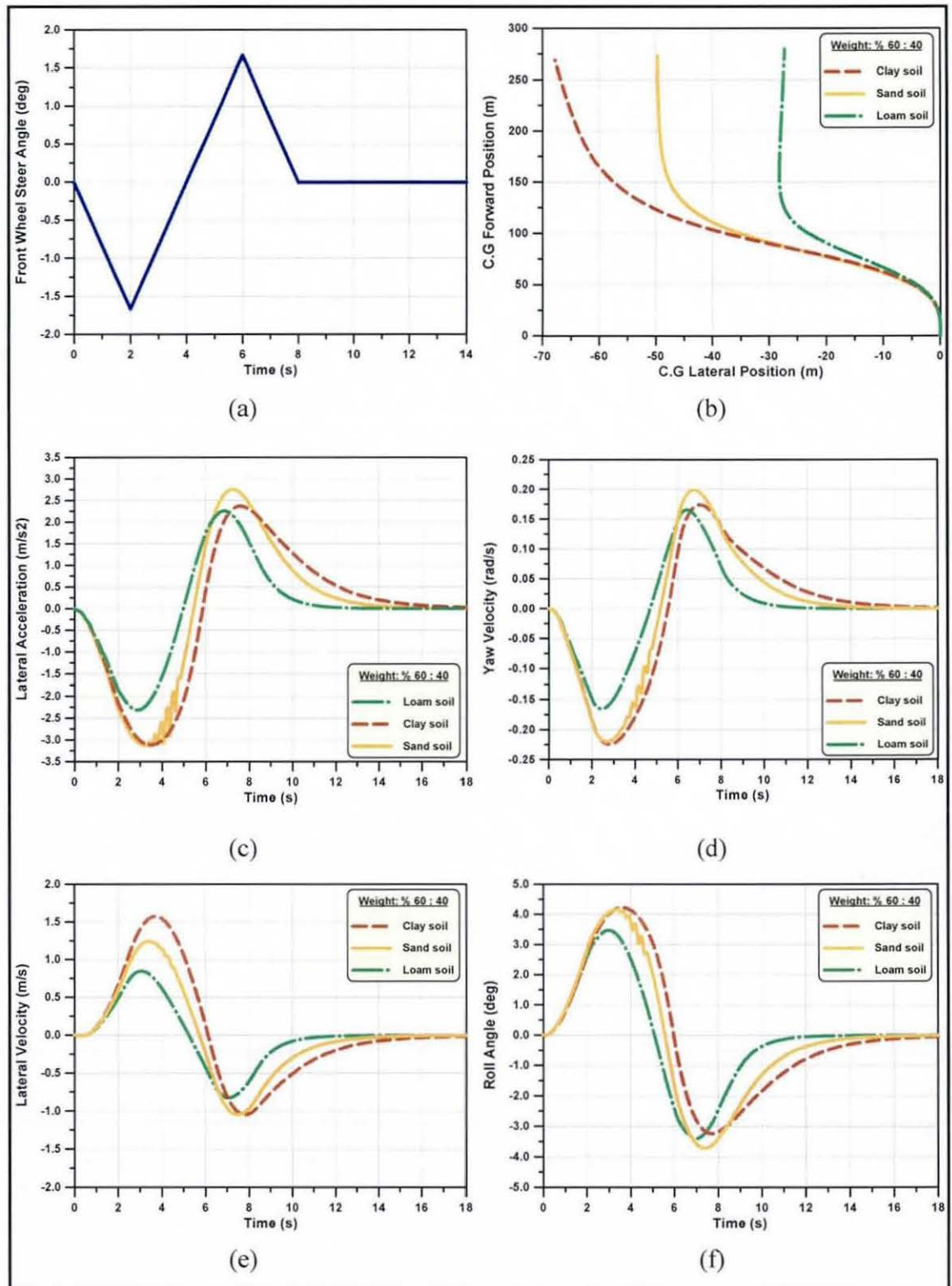


Figure 4.19 Transient Response of a Double Triangular Steering Input at 60 km/h

Chapter 5: Tribo-Dynamics' Modules of Visco-Lock Devices

Until 1980s the concept of 4WD was almost exclusively used for off-road vehicles. Today, nearly every American, European and Japanese vehicle manufacturer runs a special program for AWD vehicles. Systems used range from manually engaging second axle through to fully computerized traction control systems.

Among the wide variations of permanent AWD systems, visco-lock devices, including viscous couplings of shafts and visco-lock limited-slip differentials, offer a possibility to maintain permanent AWD relatively inexpensively, providing an automatically demand-adjusted tractive force distribution in a relatively wide range.

The main objective of this chapter is to develop tribo-dynamics' modules to describe visco-lock devices through to fully parameterised physical models, which capture the torque transmission mechanism represented by various thermodynamic, hydrodynamic, structural and mechanical modules. Therefore, the characteristics of these devices can easily be altered within a numerical simulation environment.

The mechanism of torque transmitted by visco-lock devices is modelled by considering two different modes of operation. One is the normal viscous shearing mode, whilst the other is the hump or self-torque amplification mode. The dependency of silicone fluid viscosity on both shear rate and temperature is taken into account.

In order to validate the proposed tribo-dynamics' modules, a test rig is devised to mimic the conditions of differential speed between axles. Furthermore, the transmitted shear torque and some related parameters are measured. The experimental results of typical components are compared with the numerical simulations results showing satisfactory agreement between them. It should be mentioned that the numerical modelling is based on an initial work carried by Mohan (1992, 2002, 2003, 2004), as well as through collaboration with him, resulting in two publications (Sharaf et al., 2007a, 2007b).

5.1 General Considerations

5.1.1 Automotive Applications of Visco-Lock Devices

The rotary viscous coupling is a component, which has been known in engineering for a long time for torque transmission or as torsional dampers. Recent developments of these couplings have been in the field of automotive drivelines in many cases. The main mechanism for torque transfer is based on the shearing friction of a high viscosity oil film and, therefore, the resistive torque of the viscous coupling, which is dependent on the relative speed of the rotating contacting elements. The viscous unit represents the basic element of an entire family of products. It can be connected within the driveline in series, called viscous transmission (VT), or in parallel, known as the viscous control (VC). On the basis of realized designs, some typical applications of the visco-lock devices are presented by, for example (Taureg and Herrmann, 1988; Garrett, 2001):

5.1.1.1 Viscous Transmission Device (VT):

Viscous coupling or transmission is commonly used to connect the rear axle of the vehicle to the front axle as illustrated in figure 5.1. The inner set of plates is splined to a shaft-end, driven by the front propeller shaft. The outer set of the plates is splined to the outer drum, which is rigidly connected to the rear propeller shaft.

When one set of wheels attempts to spin faster, perhaps because it is slipping, the set of plates corresponding to those wheels spins faster than the others. The fluid film, trapped between the plates, tries to adhere to the faster disks through entraining action, thus dragging the slower disks along. This transfers more torque to the slower moving wheels (the wheels that are not slipping).

During cornering manoeuvres, the difference in speed between the wheels is not as large as when one wheel is slipping. The faster the plates spin relative to each other, the more torque the viscous coupling transfers. The coupling does not interfere with vehicle turning, because the amount of torque transferred during a turn is usually quite small.

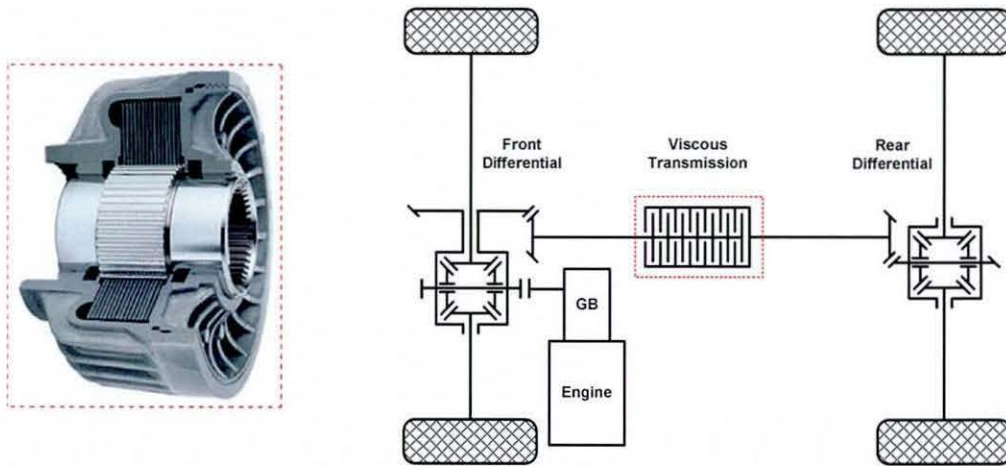


Figure 5.1 Viscous Transmission Devices (VT) in AWD Vehicles

5.1.1.2 Viscous Control Device (VC):

The shortcoming of a differential lock, used for axle-differentials or interaxle-differentials is that, it is either disengaged or fully engaged and has to be manually selected. However, combining a viscous coupling with a differential provides an automatic way of neutralizing the differential action whenever there is relative speed between the front and rear final-drives, or when one of the wheels loses its grip and commences to spin. The viscous coupling can be incorporated with either an interaxle-differential to transmit more torque to the final-drive whose axle retains good road wheel traction as shown in figure 5.2.a, or incorporated into a final-drive differential to transfer an increasing amount of torque to the wheel, which has traction whenever the wheel on the opposite side loses its grip and spins, see figure 5.2.b. The viscous unit can progressively and automatically lock out the differential action every time relative speed fluctuates between its two outputs.

In a differential, there are two common methods of installing the viscous unit as shown in figure 5.3. These are: the shaft-to-carrier and the shaft-to-shaft. In a shaft-to-carrier layout one set of plates is splined to the differential carrier, whilst the other set of plates is splined to the differential gear on one side, which in turn is splined to its shaft. On the other hand, with a shaft-to-shaft arrangement the plates are connected alternately, one set to each of the differential gears. With the latter arrangement; although the viscous

coupling is connected, in effect in series between the ends of the two half-shafts, the differential gear nevertheless still acts in parallel with it.

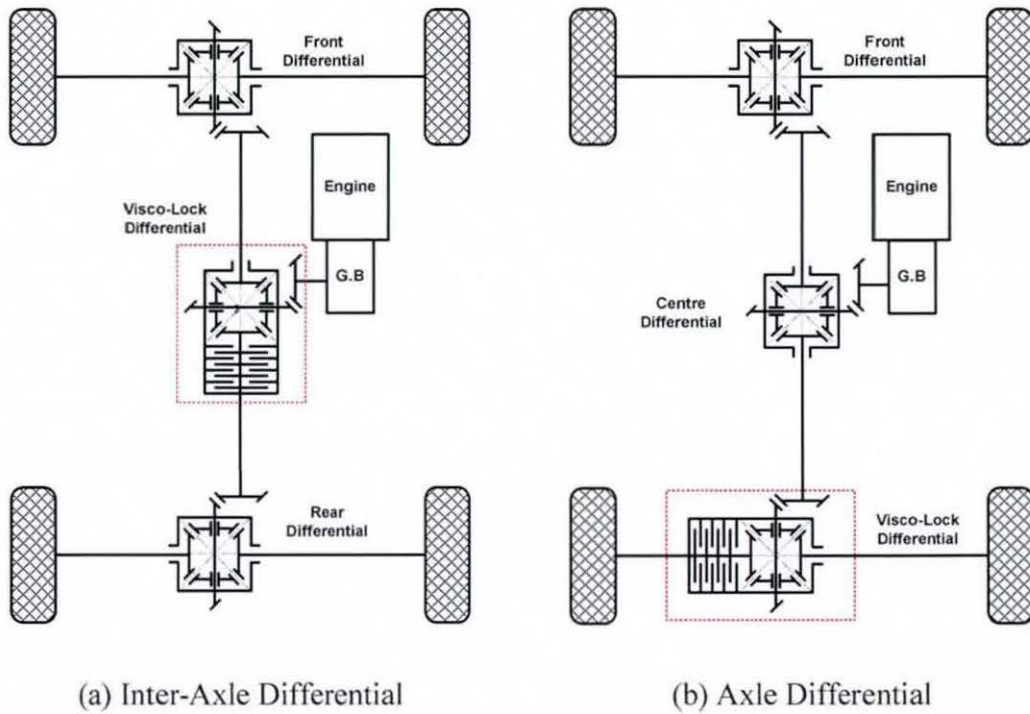


Figure 5.2 Configurations of the Viscous Control Devices (VC) in AWD vehicles

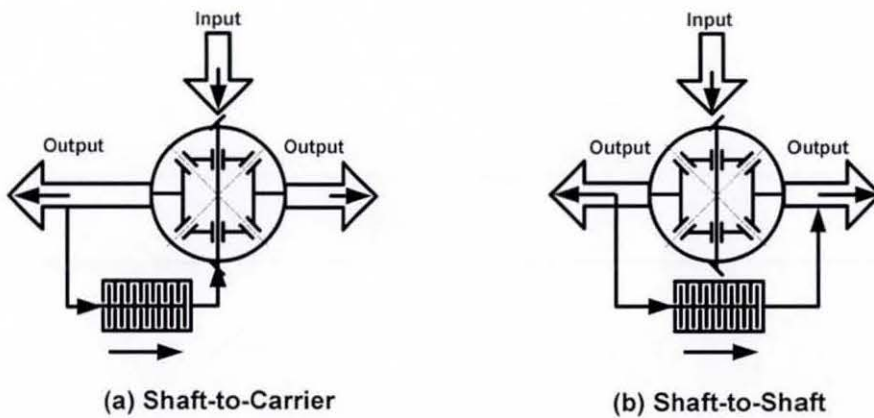


Figure 5.3 Common Methods of Installing the Viscous Unit within Differential

5.1.2 Strategies of Traction Control system

Basically, any traction control system may be classified according to the way the driving torque is regulated between the wheels (Holzwarth and May, 1994) as:

Proportion: the driving torque is distributed between the wheels in proportion to the adhesion properties at each wheel. However, drive torque still has the potential to exceed that available at the wheel with the lower adhesion properties, causing it to spin.

Limiting: the amount of driving torque delivered to the wheels is limited in order to prevent excessive slippage of the wheel. By limiting the torque the effective low adhesion side can be optimised at or near its peak value.

Optimal: provide the maximum utilization of the friction at each wheel independently through both proportion and limiting. In general limited slip differentials act proportionally, but cannot limit. Engine TCS systems can limit but cannot proportion, whilst the brake TCS systems are capable of proportioning and limiting.

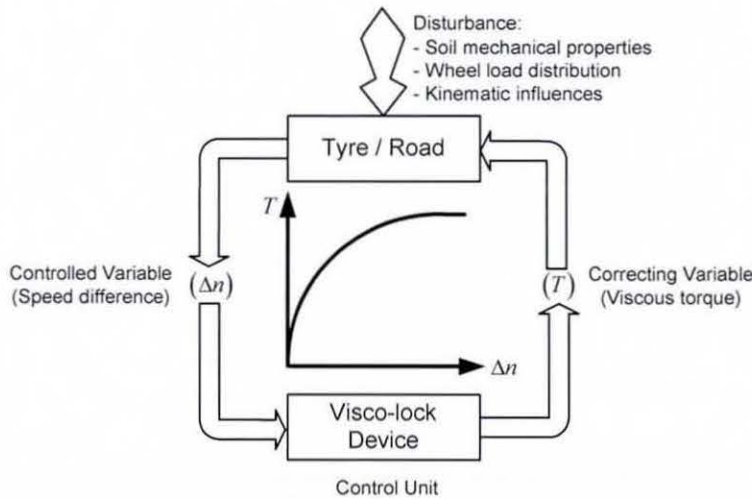


Figure 5.4 VC Traction Control Strategy, adopted from (Taureg and Herrmann, 1988)

A viscous unit can be considered as a passive traction control system, as shown in figure 5.4. The wheel-speed dependent parameter (Δn) is fed back, which gives the viscous coupling shear torque (T). Without a speed difference the torque distribution cannot be regulated. This means that the drive torque, which is transmitted to the axle or the wheel respectively, is automatically controlled in the sense of an optimized torque distribution

device. Factors causing disturbance in the tyre-road system are mainly the soil properties, the wheel load distribution, and the kinematic conditions (Taureg and Herrmann, 1988).

5.2 Rheology of Silicone Fluids

5.2.1 General Properties

Silicone fluid is an important element of the visco-lock devices. It has been selected because, in contrast to the mineral oils, the viscosity of silicone falls to a lesser degree with rising temperature. Furthermore, the fluid remains stable even at very high temperatures. This is mainly due to its resistance to oxidation and owing to its chemical inertness. Silicone fluids may be expressed as un-branched chains of alternate oxygen and silicon atoms or siloxane group (Si-O-Si), with methyl groups (CH₃) attached to the free valences of the silicon. The stability of the inorganic siloxane, Si-O-Si bonds, is a major contributor to the inert behaviour of the silicone fluids. The number of Siloxane units determines the molecular weight of the Silicone molecule, and to a great extent, the kinematic viscosity of the silicone. The molecular weight also affects the viscosity-shear rate characteristics. Poly-dim-ethyl-siloxane is a non-Newtonian, pseudo-plastic fluid. In such a fluid, viscosity decreases with increasing shear rate, stabilizing at some high shear rate (Tung and Linden, 1985).

5.2.2 Viscosity-Temperature Dependency

Calculation of the viscous shear torque depends, to a great extent, not only on the fluid viscosity, but also on its temperature dependency. Experimental data of silicone viscosity-temperature dependency is usually plotted in a logarithmic diagram, and then an empirical equation of the following forms is used to fit the measured data:

Equation (5.1) can be used to calculate the kinematic viscosity (ν_{θ}) at any temperature (θ) as a function of the nominal viscosity (ν_o), given at nominal temperature ($\theta_o = 25\text{ }^{\circ}\text{C}$), where (A) is an empirical constant and its value is determined empirically.

$$\log(v_{\theta}) = \log(v_o) \cdot 10^{A \cdot \log\left(\frac{\theta}{\theta_o}\right)} \quad (5.1)$$

Another empirical equation given by Dow Corning Corporation (1962) is as follows:

$$\log(v_{\theta}) = \left(\frac{722.5 + 0.000032 \cdot v_o}{\theta} \right) + 1.004 \cdot \log(v_o) - 2.447 \quad (5.2)$$

5.2.3 Viscosity-Shear-Rate Dependency

Generally, the relationship between the viscosity of silicones and shear rate is non-Newtonian, especially at higher shear rates. Moreover, silicones exhibit pseudo-plastic behaviour under shear strain, i.e. when the shear rate increases, the apparent viscosity decreases. However, the drop in apparent viscosity is noted for the higher viscosity fluids, which have a higher molecular weight.

The viscosity-shear rate characteristics for a given fluid at any temperature of interest are non-linear. A mathematical relationship defining this characteristic is, therefore, difficult to develop. Plotting viscosity versus shear rate on a logarithmic plot reduces the non-linearity only at low and extremely high shear rates, figure 5.5. However, it was found that, the logarithmic relationship between viscosity and shear rate for the entire shear rate range can be expressed mathematically using the following bode empirical equation (Tung and Linden, 1985).

$$\frac{\mu}{\mu_o} = \left(\frac{\dot{\gamma}_B}{\sqrt{\dot{\gamma}^2 + \dot{\gamma}_B^2}} \right)^{-m} \quad (5.3)$$

where:

- (μ) The dynamic viscosity at a specific temperature.
- (μ_o) The dynamic viscosity at a nominal temperature and nearly zero shear rate.
- (m) The slope of the regression line BC at the high shear rates
- ($\dot{\gamma}_B$) Critical shear rate (intersection of horizontal line passing through μ_o and line BC)

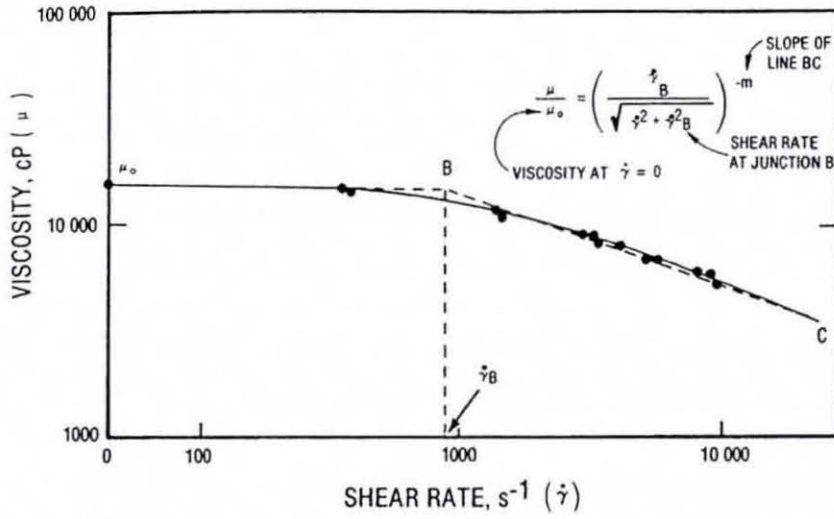


Figure 5.5 Mathematical Model of Viscosity Shear Rate Dependency
(after Tung and Linden, 1985)

Normally, silicone fluids can be distinguished by its nominal viscosity (ν_o) which is measured at room temperature (25°C) and approximately zero shear rate. For instance; silicone fluid with a kinematic viscosity of 30 [kcSt] may be referred to as 30 K. The kinematic viscosity is expressed in [centistokes] or [$\text{mm}^2 \cdot \text{s}^{-1}$]. The relation between the dynamic and kinematic viscosity can be specified using the fluid density as: ($\mu = \rho \cdot \nu$). Therefore, equation (5.3) can be expressed in terms of kinematic viscosity as follows:

$$\frac{\nu}{\nu_o} = \left(\frac{\dot{\gamma}_B}{\sqrt{\dot{\gamma}^2 + \dot{\gamma}_B^2}} \right)^{-m} \quad (5.4)$$

Equation (5.4) can be further simplified by assuming that at higher shear rates ($\dot{\gamma} \gg \dot{\gamma}_B$), the critical shear rate can be neglected accordingly, thus:

$$\nu = \nu_o \cdot \left(\frac{\dot{\gamma}_B}{\dot{\gamma}} \right)^{-m} = \nu_o \cdot \left(\frac{\dot{\gamma}}{\dot{\gamma}_B} \right)^m \quad (5.5)$$

It should be noted that, the relationship between shear stress and shear strain rate can be identified from the mathematical relationship between viscosity and shear rate. For the viscous shearing mechanism the transmitted shear torque is related to the shear stress between the input and output plates, and shear strain rate is proportional to the differential speed between the input and output plates.

5.3 Mathematical Model of Viscous Shear Torque

5.3.1 Newtonian Fluid Model

A well known test to establish the shear torque versus rotational speed characteristics is to drive the viscous coupling for 10 seconds with a ramp speed from zero to 100 rpm at a rate of 10 rpm/s. It is assumed that, the output shaft is kept at zero speed (i.e. locked). The mathematical model for viscous shear torque during such a test is developed in this section. General properties of the silicone fluid used here can be found in appendix (A).

The equation for the total viscous shear torque (T_V) from one side of the inner plate can be derived from basic principles by integrating the shear moment due to shear stress over the plates active area (A). The flow between the plates has a Reynolds Number ($\Re \ll 1$), thus, a linear velocity profile can be assumed in the gap (through the entrained lubricant film thickness). The inner plate has a relative rotational speed (ω) with a gap (S) from the adjacent outer plate, figure 5.6. Therefore:

$$T_V = \int_A \tau \cdot r \cdot dA = 2\pi \cdot \int_{r_1}^{r_2} \tau \cdot r^2 \cdot dr \quad (5.6)$$

The basic definition of the dynamic viscosity is given by: $\left(\mu = \frac{\tau}{\dot{\gamma}} = \left(\frac{F}{A} \right) / \left(\frac{du}{dy} \right) \right)$.

Therefore, an expression for the shear stress can be written as follows:

$$\tau = \mu \cdot \left(\frac{du}{dy} \right) \quad (5.7)$$

The shear strain rate ($\dot{\gamma}$) at any radius (r) over the gap (S) between inner and outer plates can be expressed as a function of the rotational speed difference (ω) as follows:

$$\dot{\gamma} = \frac{du}{dy} = \frac{\omega \cdot r}{S} \quad (5.8)$$

Form equations (5.7) and (5.8), a general form of the viscous shear torque may be obtained as follows:

$$T_V = \frac{2\pi \cdot \omega}{S} \cdot \rho \cdot v \cdot \int_{r_1}^{r_2} r^3 \cdot dr \quad (5.9)$$

$$T_V = \frac{\pi \cdot \rho \cdot v \cdot \omega}{2S} \cdot K_p \cdot (r_2^4 - r_1^4) \quad (5.10)$$

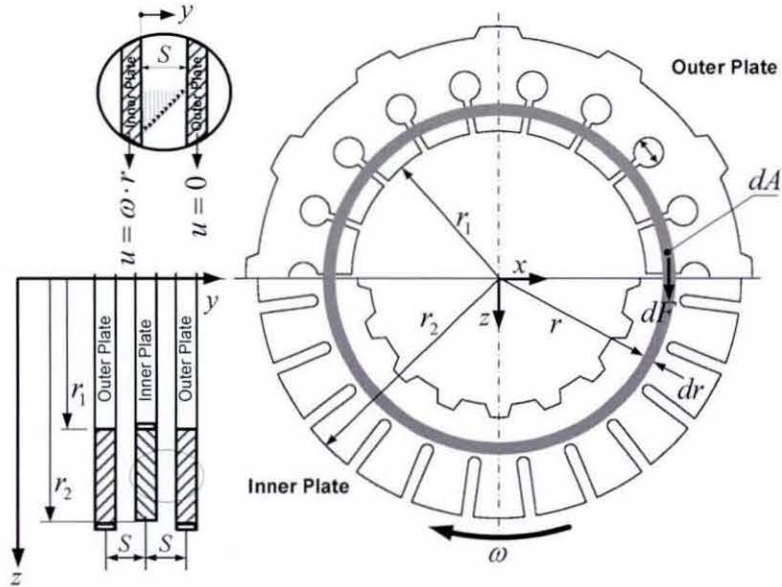


Figure 5.6 Simplified Model of One Inner and Two Outer Plates

In order to account for the reduction in the effective shear area due to the presence of the perforations and slots, an empirical correction factor ($K_p = 0.7:0.8$) is introduced in equation (5.10). This factor depends on the plate's slots and perforation dimensions.

$$\left(K_p = \frac{\text{Area of the wetted plate surface}}{\text{Area of the total theoretical surface}} \right) \quad (5.11)$$

Equation (5.10) shows that the transmitted shear torque (T_V) can be increased as follows:

- Using a fluid with a higher viscosity: During operation and as a result of heat generated, silicone's viscosity decreases, which in turn reduces the transferred torque. This justifies the employment of silicone fluid in rotary viscous couplings, as its viscosity remains constant over a long range of operating temperatures.

- The torque is proportional to the 4th power of the effective radius of the plates. Using plates with higher dimensions will increase the transmitted torque.
- When the differential speed between the plates increases.
- When the gap between the plates is reduced. It is noticed that if the gap reduces to a lower value the viscous torque rises sharply as shown later in figure 5.9.

5.3.2 Isothermal and Non-Newtonian Fluid Model

In section 5.3.1, it was assumed that the silicone fluid is Newtonian (the viscosity remains independent of the shear strain rate), so the calculated viscous torque is expected to be higher than its actual value. As mentioned previously, silicone fluids exhibit pseudo-plastic behaviour (i.e. viscosity decreases as shear strain rate increases, a non-Newtonian behaviour). Thus, a correction for viscosity must be carried out to take this effect into account. This is carried out by substituting the viscosity given by equation (5.5) and integrating over the shearing area. It should be noted that, the following derivation of shear torque does not take into account any thermal effects (i.e. isothermal).

$$v = v_o \cdot \left(\frac{\omega \cdot r}{S \cdot \dot{\gamma}_B} \right)^m \quad (5.12)$$

$$dT_V = \int_{r_1}^{r_2} \int_0^{2\pi} \rho \cdot v \cdot \frac{\omega}{S} \cdot r^3 \cdot d\phi \cdot dr \quad (5.13)$$

$$dT_V = \frac{2\pi \cdot \rho \cdot v_o}{\dot{\gamma}_B^m} \cdot \left(\frac{\omega}{S} \right)^{(1+m)} \cdot \int_{r_1}^{r_2} r^{3+m} \cdot dr \quad (5.14)$$

$$T_V = \underbrace{\frac{2\pi \cdot \rho \cdot v_o}{(4+m) \cdot \dot{\gamma}_B^m} \cdot K_p}_{K_1} \cdot \left(r_2^{(4+m)} - r_1^{(4+m)} \right) \cdot \left(\frac{\omega}{S} \right)^{(1+m)} \quad (5.15)$$

$$T_V = K_1 \cdot \left(\frac{\omega}{S} \right)^{(1+m)} \quad (5.16)$$

where (K_1) is given as follows:

$$K_1 = \left(\frac{2\pi \cdot K_p \cdot \rho \cdot V_o}{(4+m) \cdot \dot{\gamma}_B^m} \right) \cdot (r_2^{(4+m)} - r_1^{(4+m)}) \quad (5.17)$$

It should be noted that, if the slope of the regression line BC (m) at the high shear rates is equal to zero (slope of a straight line), then equation (5.15) will be reduced to equation (5.10) and in this case there is no effect due to shear strain rate (a Newtonian fluid).

5.3.3 Adiabatic and Non-Newtonian Fluid Model

The viscous shearing torque calculated by equation (5.15) is based on the assumption that the temperature of the fluid keeps constant at the room temperature. However, the work exerted by the plates in shearing the silicone fluid is converted into an equivalent amount of heat and therefore, increases the fluid's temperature. If the instantaneous torque and rotational speed are known, then the effective rate of heat generation can be equated to the shear work done as follows:

$$\frac{dQ}{dt} = T_v \cdot \omega \quad (5.18)$$

$$\int dQ = \int (T_v \cdot \omega) \cdot dt \quad (5.19)$$

Since the inner and outer plates are in permanent contact with the silicone fluid, the generated heat is transferred directly to the fluid and then to the surrounding air through the viscous coupling's housing. The rate of heat transfer through the viscous coupling is a time dependent process. Furthermore, it depends on the thermal properties of the components and the effective convective heat transfer coefficient on the fluid-solid interface. Since the test procedure is carried out within relatively small time (10 seconds), then it would be reasonable to assume that the thermal process is adiabatic. This means that, the work exerted by the plates is converted into heat which is absorbed by the core of the viscous coupling, consisting of the inner and outer plates, spacers, and the fluid trapped within the gap between the adjacent plates.

$$Q = (m_f \cdot c_f + m_c \cdot c_c) \cdot \Delta\theta = (T_v \cdot \omega) \cdot \Delta t \quad (5.20)$$

Where:

(m_f, m_c) : Masses of the silicone fluid and the steel core including the plates and the drum

(c_f, c_c) : Specific heat coefficients of the silicone fluid and core respectively

$(\Delta\theta)$: The incremental change in temperature corresponds to the time interval (Δt) .

During the computational scheme and at each time step (Δt) , the temperature rise $(\Delta\theta)$ is calculated. Accordingly, silicone's fluid viscosity is updated, based on equation (5.1) and then is used to compute the shear torque given by equation (5.15), see figure 5.8.

The viscous shear torque is calculated and plotted for all the aforementioned derived models during the speed ramp-rate test of 10 seconds run up to 100 rpm, see figure 5.7. It is obvious that, the model with an adiabatic assumption provides more realistic characteristics for the transmitted viscous shear torque.

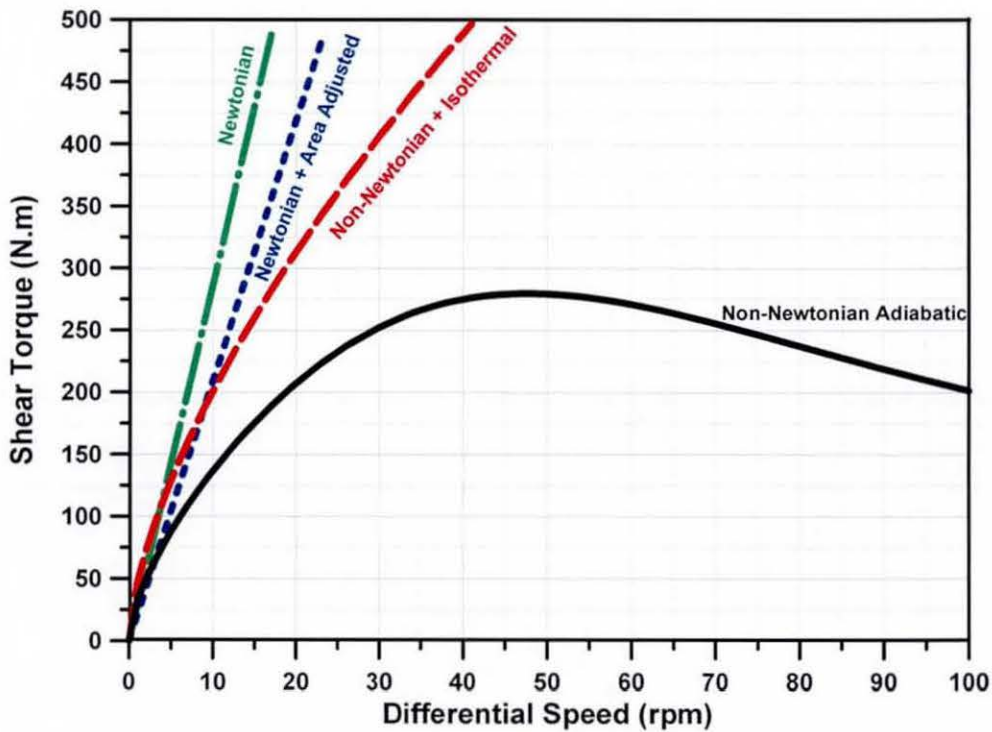


Figure 5.7 Viscous Shear Torque for Different Levels of Modelling Assumptions

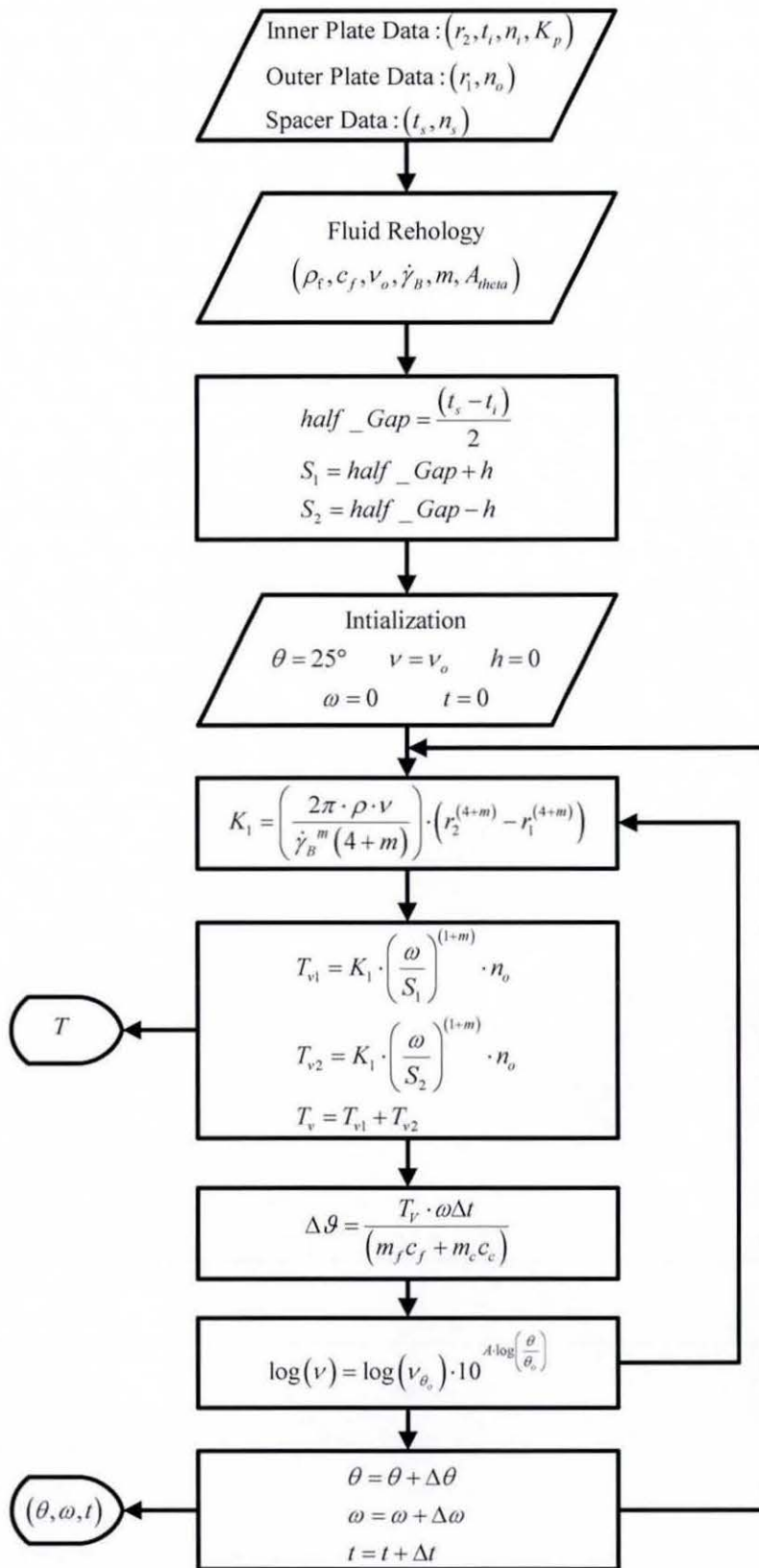


Figure 5.8 Flow Chart of Calculating Steps of the Viscous Torque.

5.4 Mathematical Model of Self Torque Induced Amplification

A viscous unit normally operates in the viscous shear mode, as described in section 5.3, where the generated torque is mainly due to the fluid shearing effect. Under certain circumstances, the coupling function changes into the so-called ‘Hump’ or ‘Induced Torque Amplification’ mode, which is characterized by a significant increase in torque. The advantage of this mode is that it works as a self-regulating mechanism to prevent the coupling from damage due to higher generated bulk pressures. In addition, it causes full locking of the unit, where there is no longer any relative motion between the plates. This causes the temperature to fall again, thereby reducing the pressure. Both temperature and pressure finally settle at a certain level according to the instantaneous traction effort.

In section 5.3, it was assumed that gaps between the plates remain constant i.e. there is no axial movements of the plates. However, in reality, these gaps vary randomly. As the gap between any pair of contiguous plates decreases, both the generated shear stress and shear torque increase accordingly as shown in figure 5.9.

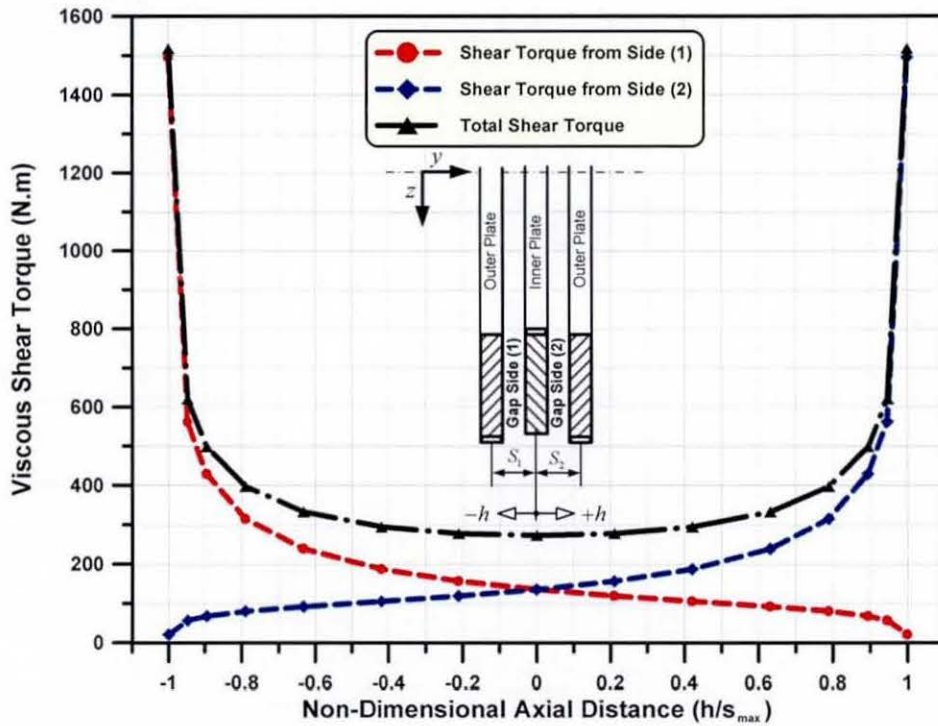


Figure 5.9 Effect of Inner Plate Axial Movement on the Viscous Shear Torque

A feature of the design of rotary viscous couplings is that their plates include slots and perforations. Also, the inner plate tabs are produced with an edge which encourages fluid entraining action through the hydrodynamic wedge effect and activates the initiation of the well known hump mode. The prescribed plate shape design is the key for developing the hump mode as described below, figure 5.10:

- Step (1): The slotted edge geometry of the tabs stimulates side-2 of the inner plate to have a narrower gap with side-3 of the outer gap.
- Step (2): The side with a narrower gap (side-2) generates a higher shear stress than the side with a larger gap (side-3).
- Step (3): The moment due to the resulting differential shear forces across the tab sides causes the plate tabs to twist around its centroid.
- Step (4): With the twisted shape of the inner plate tab and the differential speed between the inner and outer plates, the tabs act as a sliding pad bearing, generating a hydrodynamic pressure over them, which in turn, further increases the axial force. This force pushes the inner plates towards side-3 of the outer plates, until the leading edge of side-2 makes contact with side-3. The pressure drop might be limited by the effective local vapour pressure of the fluid/air mixture.
- Step (5): The introduced Coulomb friction at the rubbing leading edge increases the twisting moment and results in the twist of the tabs. The increased twist creates a higher differential pressure across side-1 and side-2 of the inner plate.
- Step (6): At room temperature, the coupling is only partially filled with the silicone fluid. At a certain critical temperature, when all the silicone fluid has expanded to fully fill the voids, the bulk pressure increases. Consequently, the hydrodynamic pressure and the net axial force increase rapidly until the plates contact each other.
- Step (7): This results in a sudden rise in the differential pressure across the inner plate. Side-2 would now be able to realize the full potential of the pressure drop instead of being limited by the local vapour pressure. The net torque is over twenty times the torque of a non-STA viscous coupling of a similar size. This self-induced torque amplification is sustained so long as the pressure and relative speed are maintained.

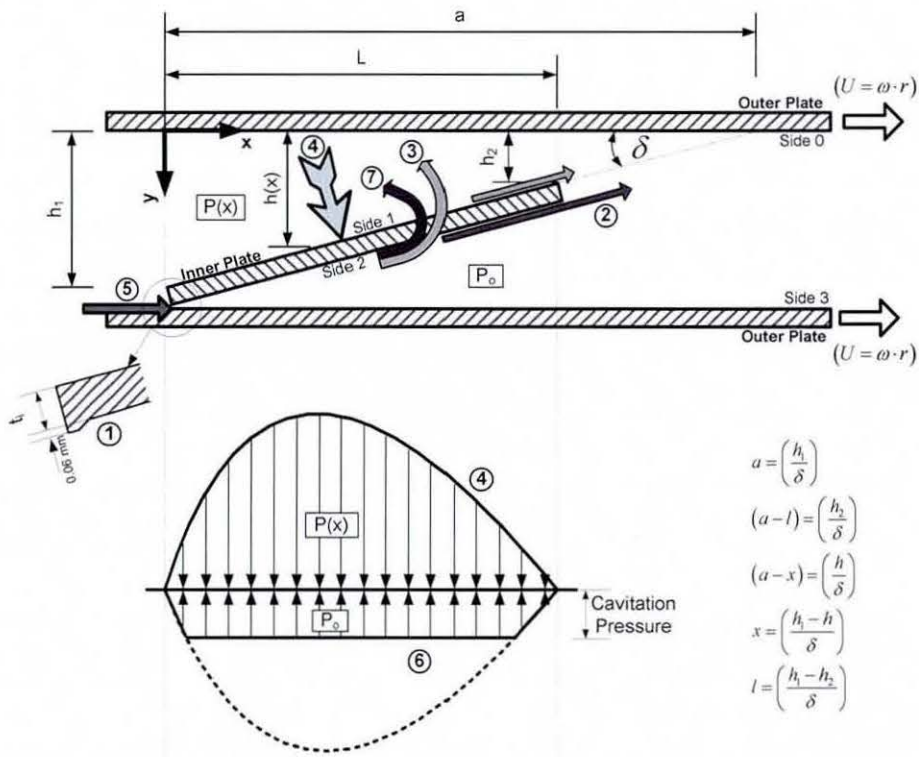


Figure 5.10 Model of Self Induced Torque Amplification (STA)

In view of the aforementioned hypothesis of self-torque amplification mode, appropriate mathematical models are required to be developed, as described below.

5.4.1 Hydrodynamic Pressure Model

The twisted shape of the inner plate tab in conjunction with the outer plate may be analyzed as a sliding pad bearing as shown in figure 5.10. The inner plate tab is assumed to be stationary and inclined with a small angle (δ), while the outer plate moves with a sliding velocity.

The axis system (X, Y, Z) represents the tangential, axial and radial directions of the flow field relative to the coupling respectively. It is also assumed that the tab depth is relatively large in the (Z) direction. The above assumptions allow the use of a two-dimensional rectilinear solution. The flow field is assumed to be an incompressible, isotropic, Newtonian, rectilinear, two-dimensional, steady-state flow.

The Navier-Stokes Equation:

According to the assumption of Newtonian behaviour of a fluid, the Navier-Stokes equations in rectangular coordinates can be written as follows (Hamrock, 2004):

$$\left. \begin{aligned} \rho \cdot \left(\frac{\partial u}{\partial t} + u \cdot \frac{\partial u}{\partial x} + v \cdot \frac{\partial u}{\partial y} + w \cdot \frac{\partial u}{\partial z} \right) &= -\frac{\partial p}{\partial x} + \mu \cdot \left(\frac{\partial^2 u}{\partial x^2} + \frac{\partial^2 u}{\partial y^2} + \frac{\partial^2 u}{\partial z^2} \right) + \rho \cdot g_x \\ \rho \cdot \left(\frac{\partial v}{\partial t} + u \cdot \frac{\partial v}{\partial x} + v \cdot \frac{\partial v}{\partial y} + w \cdot \frac{\partial v}{\partial z} \right) &= -\frac{\partial p}{\partial y} + \mu \cdot \left(\frac{\partial^2 v}{\partial x^2} + \frac{\partial^2 v}{\partial y^2} + \frac{\partial^2 v}{\partial z^2} \right) + \rho \cdot g_y \\ \rho \cdot \left(\frac{\partial w}{\partial t} + u \cdot \frac{\partial w}{\partial x} + v \cdot \frac{\partial w}{\partial y} + w \cdot \frac{\partial w}{\partial z} \right) &= -\frac{\partial p}{\partial z} + \mu \cdot \left(\frac{\partial^2 w}{\partial x^2} + \frac{\partial^2 w}{\partial y^2} + \frac{\partial^2 w}{\partial z^2} \right) + \rho \cdot g_z \end{aligned} \right\} \quad (5.21)$$

Where (u, v, w) are the fluid velocity components in (X, Y, Z) directions respectively. Navier-Stokes formulation contains three equations and four unknowns (u, v, w, p) . A fourth equation is provided by the continuity of flow condition in order to find the solution (Hamrock, 2004).

Continuity of Flow Condition:

$$\frac{\partial \rho}{\partial t} + \frac{\partial}{\partial x}(\rho \cdot u) + \frac{\partial}{\partial y}(\rho \cdot v) + \frac{\partial}{\partial z}(\rho \cdot w) = 0 \quad (5.22)$$

If density is assumed to be constant, the continuity equation may be written as follows:

$$\frac{\partial u}{\partial x} + \frac{\partial v}{\partial y} + \frac{\partial w}{\partial z} = 0 \quad (5.23)$$

Reynolds' Number:

The relative significance of inertial and viscous forces in any flow can be judged from the value of Reynolds' number (Munson et al., 2005). It is used to distinguish between laminar and turbulent flows. If the Reynolds' number is very small ($\Re \ll 1$), this indicates that the viscous force is dominant compared to the inertial and body forces and it may be possible to neglect them. Such low Reynolds' numbers are typical of narrow conjunctions. Furthermore, this means the fluid density is not an important variable,

since the pressures are quite high and the fluid may be considered to have become incompressible. Flow at a very small Reynolds' number is commonly referred to as creeping flow, and is typical of all lubrication problems.

The Reynolds' number for any flow is defined in terms of a characteristic length. The characteristic dimensions for the flow are the tab length (L) and the gap height (h) (i.e. the film thickness).

$$\Re = \frac{\text{Inertia}}{\text{Viscous}} = \frac{\rho \cdot U \cdot L}{\mu} = \frac{U \cdot L}{\nu} \quad (5.24)$$

The Reynolds' number expressed in equation (5.24) is the conventional Reynolds' number found in fluid mechanics. However, in fluid film lubrication because of the dominance of the viscous term the modified Reynolds' number is used. Considering the motion in the (x) direction, the modified Reynolds' number can be defined as follows:

$$\Re^* = \frac{\text{Inertia Force}}{\text{Viscous Force}} = \left(\rho \cdot u \cdot \frac{\partial u}{\partial x} \right) / \left(\mu \cdot \frac{\partial^2 u}{\partial y^2} \right) = \left(\rho \cdot \frac{u^2}{L} \right) / \left(\mu \cdot \frac{u}{h^2} \right) = \frac{\rho \cdot u \cdot h^2}{\mu \cdot L} \quad (5.25)$$

$$\Re^* = \frac{\rho \cdot u \cdot L}{\mu} \cdot \left(\frac{h}{L} \right)^2 = \Re_L \cdot \left(\frac{h}{L} \right)^2 = \Re_h \cdot \left(\frac{h}{L} \right) \quad (5.26)$$

where:

- (\Re) Reynolds' Number.
- (\Re^*) Modified Reynolds' Number ($\Re^* = 0.000105$).
- (\Re_h) Reynolds' Number defined for gap height ($\Re_h = 0.066$).
- (\Re_L) Reynolds' Number defined for tab length ($\Re_L = 4.2$).

It is obvious that, the Reynolds' number is very small which describes creeping flow, therefore, it would be reasonable to neglect the inertial terms in comparison with the viscous terms in the Navier-Stokes equation. Consequently, the left hand side of the Navier-Stokes equations may be neglected (set to zero). Equation (5.21) can be reduced to the following form:

$$\left. \begin{aligned} \frac{\partial p}{\partial x} &= \mu \cdot \left(\frac{\partial^2 u}{\partial x^2} + \frac{\partial^2 u}{\partial y^2} + \frac{\partial^2 u}{\partial z^2} \right) \\ \frac{\partial p}{\partial y} &= \mu \cdot \left(\frac{\partial^2 v}{\partial x^2} + \frac{\partial^2 v}{\partial y^2} + \frac{\partial^2 v}{\partial z^2} \right) \\ \frac{\partial p}{\partial z} &= \mu \cdot \left(\frac{\partial^2 w}{\partial x^2} + \frac{\partial^2 w}{\partial y^2} + \frac{\partial^2 w}{\partial z^2} \right) \end{aligned} \right\} \quad (5.27)$$

Assumptions:

- Since the dimension of the contact in the y-direction can be considered to be smaller compared to the direction of entraining motion (x-direction), the pressure gradient in that direction may be ignored $\left(\frac{\partial p}{\partial y} = 0 \right)$.
- In a semi-infinite flow field, both the velocity and pressure variations along the (z)-axis may be neglected (very small film thickness). Also, the velocity (w) in the (z) direction can be ignored (no side-leakage).
- Compared to the longitudinal velocity (u), the velocity component (v) is negligible (approach velocity). Furthermore, $\left(\frac{\partial^2 u}{\partial x^2} \right)$ can be neglected, because $\left(\frac{\partial^2 u}{\partial x^2} \ll \frac{\partial^2 u}{\partial y^2} \right)$.

Using the aforementioned assumptions, equation (5.27) can be simplified as follows:

$$\frac{\partial p}{\partial x} = \frac{\partial}{\partial y} \left(\mu \cdot \frac{\partial u}{\partial y} \right) \quad (5.28)$$

For steady-state conditions, the pressure has been shown to be a function of (x) only. Thus, equation (5.28) can be integrated directly to give a general expression for the velocity gradient as:

$$\frac{\partial u}{\partial y} = \frac{y}{\mu} \cdot \left(\frac{\partial p}{\partial x} \right) + \frac{A}{\mu} \quad (5.29)$$

Where (A) is the constant of integration. By integrating equation (5.29), the flow velocity (speed of entraining motion) can be obtained as:

$$u = \frac{y^2}{2 \cdot \mu} \cdot \left(\frac{\partial p}{\partial x} \right) + \frac{A}{\mu} \cdot y + B \quad (5.30)$$

If zero slip at the fluid-solid interface is assumed (in accordance with the Newtonian slow viscous motion), then the boundary values for the velocity are given by:

$$\left. \begin{array}{l} y = 0 \rightarrow u = U \\ y = h \rightarrow u = 0 \end{array} \right\} \quad (5.31)$$

$$\left. \begin{array}{l} B = U \\ A = -\frac{u}{h} \cdot \left(\frac{h^2}{2 \cdot \mu} \cdot \left(\frac{\partial p}{\partial x} \right) + U \right) \end{array} \right\} \quad (5.32)$$

The slider velocity (U) can be calculated from the tip speed of the tab $(U = \omega \cdot r_2)$, where (ω) is the relative rotational speed of the inner plate and (r_2) is the tip radius. With the boundary conditions obtained from equation (5.31), the velocity gradient (u) can be given as follows:

$$u = U \cdot \left(1 - \frac{y}{h} \right) - \left(\frac{y \cdot h}{2 \cdot \mu} \right) \cdot \left(\frac{\partial p}{\partial x} \right) \cdot \left(1 - \frac{y}{h} \right) \quad (5.33)$$

The volume flow rate per unit depth in the x-direction (q_x) may be derived from the reduced form of continuity equation as follows:

$$q_x = \int_0^{h(x)} u \cdot dy \quad (5.34)$$

Substituting equation (5.33) into equation (5.34) gives the volumetric flow rate per unit depth as follows:

$$q_x = \int_0^{h(x)} \left(U \cdot \left(1 - \frac{y}{h} \right) - \left(\frac{y \cdot h}{2 \cdot \mu} \right) \cdot \left(\frac{\partial p}{\partial x} \right) \cdot \left(1 - \frac{y}{h} \right) \right) \cdot dy \quad (5.35)$$

$$q_x = \frac{U \cdot h}{2} - \frac{h^3}{12\mu} \cdot \left(\frac{\partial p}{\partial x} \right) \quad (5.36)$$

So, $\left(\frac{\partial p}{\partial x} \right)$ may be rearranged and written in terms of (q_x) as follows:

$$\frac{\partial p}{\partial x} = 12\mu \cdot \left(\frac{U}{2h^2} - \frac{q_x}{h^3} \right) \quad (5.37)$$

$$p(x) = \int_0^x \frac{\partial p}{\partial x} dx = 6\mu \cdot U \cdot \int_0^x \frac{dx}{h^2} - 12\mu \cdot q_x \cdot \int_0^x \frac{dx}{h^3} + C \quad (5.38)$$

The boundary values for the pressure are given by:

$$x = 0 \quad \rightarrow \quad p(x) = p_o \quad \rightarrow \quad C = p_o \quad (5.39)$$

$$p(x) = p_o + 6\mu \cdot U \cdot \int_0^x \frac{dx}{h^2} - 12\mu \cdot q_x \cdot \int_0^x \frac{dx}{h^3} \quad (5.40)$$

Volume Flow Rate per Unit Depth (q_x) :

$$x = l \quad \rightarrow \quad p(x) = p_o \quad (5.41)$$

$$p_o = p_o + 6\mu \cdot U \cdot \int_0^l \frac{dx}{h^2} - 12\mu \cdot q_x \cdot \int_0^l \frac{dx}{h^3} \quad (5.42)$$

$$q_x = \frac{U}{2} \cdot \left(\frac{\int_0^l \frac{dx}{h^2}}{\int_0^l \frac{dx}{h^3}} \right) \quad (5.43)$$

The oil film thickness can be written as a function of (x) and the tab inclination angle (δ) as follows, see figure 5.10.

$$h(x) = \delta \cdot (a - x) \quad (5.44)$$

$$\left. \begin{aligned} x=0 &\rightarrow h(x)=h_1=\delta \cdot a \\ x=l &\rightarrow h(x)=h_2=\delta \cdot (a-l) \end{aligned} \right\} \quad (5.45)$$

$$q_x = \frac{U}{2} \cdot \left(\int_0^l \frac{dx}{\delta^2 \cdot (a-x)^2} \right) \Bigg/ \left(\int_0^l \frac{dx}{\delta^3 \cdot (a-x)^3} \right) \quad (5.46)$$

$$q_x = U \cdot \delta \cdot \frac{a \cdot (a-l)}{2a-l} \quad (5.47)$$

Hydrodynamic Pressure $p(x)$:

Substituting equation (5.47) into equation (5.38) yields the expression for hydrodynamic pressure distribution as:

$$p(x) = p_o + 6\mu \cdot U \cdot \int_0^x \frac{dx}{\delta^2 \cdot (a-x)^2} - 12\mu \cdot U \cdot \delta \cdot \frac{a \cdot (a-l)}{2a-l} \cdot \int_0^x \frac{dx}{\delta^3 \cdot (a-x)^3} \quad (5.48)$$

$$p(x) = p_o + \frac{6\mu \cdot U}{\delta^2} \cdot \left(\frac{1}{a-x} \right)_0^x - \frac{12\mu \cdot U}{\delta^2} \cdot \frac{a \cdot (a-l)}{2a-l} \cdot \left(\frac{1}{2 \cdot (a-x)^2} \right)_0^x \quad (5.49)$$

$$p(x) = p_o + \frac{6\mu \cdot U}{\delta^2} \cdot \left(\left(\frac{1}{a-x} - \frac{1}{a} \right) - \left(\frac{a \cdot (a-l)}{2a-l} \right) \cdot \left(\frac{1}{(a-x)^2} - \frac{1}{(a)^2} \right) \right) \quad (5.50)$$

From figure 5.10, the following terms can be substituted:

$$\left. \begin{aligned} x &= \frac{h_1 - h}{\delta} & a-x &= \frac{h}{\delta} & a &= \frac{h_1}{\delta} \\ l &= \frac{h_1 - h_2}{\delta} & a-l &= \frac{h_2}{\delta} \end{aligned} \right\} \quad (5.51)$$

$$p(x) = p_o + 6\mu \cdot U \cdot l \cdot \frac{(h_1 - h) \cdot (h - h_2)}{h^2 \cdot (h_1^2 - h_2^2)} \quad (5.52)$$

The Net Axial Force per Unit Depth (P):

The net axial force per unit depth can be obtained by integrating the hydrodynamic pressure distribution over the tab length (l).

$$P = \int_0^l p(x) \cdot dx = p_o \cdot l + \frac{6\mu \cdot U \cdot l}{(h_1^2 - h_2^2)} \cdot \int_0^l \frac{(h_1 - h) \cdot (h - h_2)}{h^2} \cdot dx \quad (5.53)$$

$$P = p_o \cdot l + \frac{6\mu \cdot U \cdot l}{(h_1^2 - h_2^2)} \cdot \int_0^l \frac{(h_1 - \delta \cdot (a - x)) \cdot (\delta \cdot (a - x) - h_2)}{(\delta \cdot (a - x))^2} \cdot dx \quad (5.54)$$

$$P = p_o \cdot l + \frac{6\mu \cdot U \cdot l}{(h_1^2 - h_2^2)} \cdot \left((a - x) - \left(\frac{h_1 \cdot h_2}{(a - x) \cdot \delta^2} \right) - \left(\frac{h_1 + h_2}{\delta} \right) \cdot \ln(a - x) \right)_0^l \quad (5.55)$$

$$P = p_o \cdot l + \frac{6\mu \cdot U \cdot l^2}{(h_1^2 - h_2^2)} \cdot \left(-2 + \left(\frac{\delta}{h_1 - h_2} \right) \cdot \left(\frac{h_1 + h_2}{\delta} \right) \cdot \ln \left(\frac{h_1}{h_2} \right) \right) \quad (5.56)$$

By introducing the variable: $k_1 = \left(\frac{h_1}{h_2} \right)$

$$P = p_o \cdot l + \frac{6\mu \cdot U \cdot l^2}{(k_1^2 - 1) \cdot h_2^2} \cdot \left(\ln(k_1) - \frac{2(k_1 - 1)}{k_1 + 1} \right) \quad (5.57)$$

Whilst side (1) of the inner plate tab undergoes pressure given by equation (5.52), side (2) experiences a corresponding drop in pressure below the ambient pressure such that it is limited by the effective vapour pressure of the silicone-air mixture, see figure 5.10. In other words, below this threshold pressure, the air comes out of the solution or the silicone would flash into vapour, especially at higher temperatures, when the silicone vapour pressure cannot be neglected.

The net axial force exerted on the tab is the sum of the integrated pressures on its side-1 and side-2. The total force per unit depth can be given as follows:

$$P_t = P_{1-2} = P_1 + K_c \cdot P_2 \quad (5.58)$$

The conditional factor (K_c) is introduced to modify the effect of the pressure on side-2, when the fluid bulk pressure is below the critical threshold in order to avoid formation of vapour.

5.4.2 Thermal Energy Calculations

The change in silicone temperature due to shear and Coulomb effects is calculated by making some simplifying assumptions of lumped-mass and one-dimensional thermal conduction model (Incropera, 2002).

The generated viscous shear and the Coulomb friction work done by the rotating plates are converted into heat (Q), which is calculated as follows:

$$\frac{dQ}{dt} = (T_v + T_c) \cdot \omega \quad (5.59)$$

Since the plates and the fluid are in contact, so it would be reasonable to assume that both remain at the same temperature (θ_f). Furthermore, the conducted heat (Q_1) from the viscous coupling core into the housing can be expressed using the following equation:

$$\frac{dQ_1}{dt} = \left[\frac{kA}{\Delta x} \right]_s \cdot (\theta_f - \theta_s) \quad (5.60)$$

Where; $\left[\frac{kA}{\Delta x} \right]_s$ is the equivalent conduction parameter through the housing.

The energy convected by the air (Q_2) from the housing outside surface at (θ_s) to the surrounding air at (θ_a) can be expressed using the following equation:

$$\frac{dQ_2}{dt} = [h \cdot A]_s \cdot (\theta_s - \theta_a) \quad (5.61)$$

Where, $[h \cdot A]_s$ is the corresponding convection parameter from the housing's outer surface. Two other relations can also be obtained from the heat balance from core to the housing and from the housing to air as follows:

$$\frac{dQ}{dt} - \frac{dQ_1}{dt} = [mc]_c \cdot \frac{d\theta_f}{dt} \quad (5.62)$$

$$\frac{dQ_1}{dt} - \frac{dQ_2}{dt} = [mc]_s \cdot \frac{d\theta_s}{dt} \quad (5.63)$$

Where, $(mc)_c$ and $(mc)_s$ are the equivalent thermal masses for the viscous coupling core and the steel housing respectively. During the simulation, Equations from (5.59) to (5.63) are solved numerically to obtain the fluid and housing temperatures.

The pressure rise inside the viscous coupling is established based on the silicone fluid temperature. The development of the mathematical models for pressure rise is carried out in two steps as described below.

5.4.2.1 Compression of The Gas Phase:

Initially, the coupling is partially filled with silicone fluid and air voids (V_a). With an increase in temperature (θ) the silicone fluid expands, compressing the air voids (P). A relationship can be obtained by applying the ideal gas law as follows (Mohan, 2004):

$$\left. \begin{aligned} P &= \frac{R \cdot \theta}{V_a} \\ dP &= \left(\frac{\partial P}{\partial \theta} \right) \cdot d\theta + \left(\frac{\partial P}{\partial V_a} \right) \cdot dV_a \\ dP &= \left(\frac{R}{V_a} \right) \cdot d\theta + \left(\frac{-R\theta}{V_a^2} \right) \cdot dV_a \\ dP &= P \cdot \left(\frac{d\theta}{\theta} - \frac{dV_a}{V_a} \right) \end{aligned} \right\} \quad (5.64)$$

Assumptions:

- Assume that both the air and silicone fluid are mixed together at the same temperature, thus: $((d\theta, \theta)_{air} = (d\theta, \theta)_{Fluid})$
- Thermal expansion of the steel housing may be neglected when compared to the thermal expansion of the fluid, , thus: $(dV_h \approx 0)$.
- The expansion volume of the fluid may be substituted for the reduction in the volume of air, thus: $(dV_a = -dV_f = -\beta_F \cdot V_F \cdot d\theta)$.

The volume of air at any temperature can be calculated as:

$$V_a = V_{hi} - V_F \tag{5.65}$$

(V_{hi}) is the initial volume of the viscous coupling housing, assumed to be constant, thus:

$$dP = P \cdot \left(\frac{d\theta_F}{\theta_F} + \frac{\beta_F \cdot V_F \cdot d\theta_F}{V_{hi} - V_F} \right) \tag{5.66}$$

For each time step, the incremental change in fluid temperature $(d\theta_f)$ is calculated and is used to update the bulk pressure rise (dP) and the expansion volume of the fluid (dV_f) , see figure 5.11. As the fluid temperature increases, the fluid expands and compresses the volume of air in the housing. The initial rate of pressure rise is small, because of the high compressibility of air.

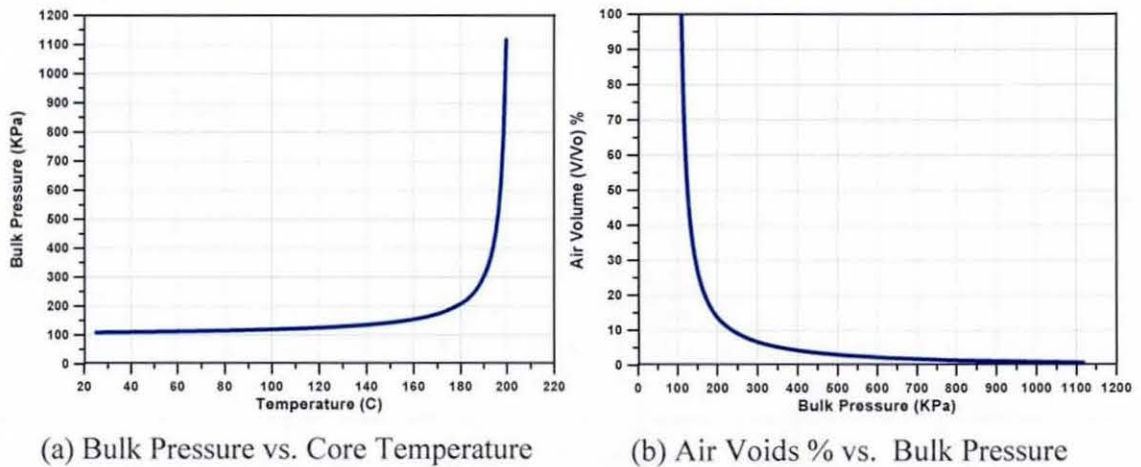


Figure 5.11 Effect of Core Temperature on Bulk Pressure and Air Voids %

5.4.2.2 Compression of The Liquid Phase:

After a certain critical temperature, the fluid completely fills the void volume. The expansion of the steel housing of the viscous coupling can no longer be neglected. The effective fluid compression may be calculated as the difference between the volume of the fluid (V_F) in its free state, and the smaller volume (V_h) of the viscous coupling's housing, which the fluid is made to occupy.

From the definition of the fluid bulk modulus (K_F), it follows that (Munson et al., 2005):

$$dP = K_F \cdot \left(\frac{dV_F}{V_F} \right) = K_F \cdot \left(\frac{V_{F\theta} - V_{h\theta}}{V_F} \right) \quad (5.67)$$

$$V_{F\theta} = V_{f_i} (1 + \beta_F \cdot \Delta\theta) \quad (5.68)$$

The initial fluid filling ratio (C_F) is defined as the ratio of the fluid (V_{f_i}) and the housing void volumes (V_h) at the filling temperature (θ_i). Thus:

$$C_F = \frac{V_{f_i}}{V_h} \quad (5.69)$$

For a temperature rise ($\Delta\theta = \theta - \theta_i$) both fluid and housing volumes can be calculated as:

$$V_{F\theta} = C_F \cdot V_h (1 + \beta_F \cdot \Delta\theta) \quad (5.70)$$

$$V_{h\theta} = V_h (1 + \beta_S \cdot \Delta\theta) \quad (5.71)$$

The pressure rise (ΔP) may be calculated, based on the following relations.

$$\Delta P = K_F \cdot \left(\frac{C_F \cdot (1 + \beta_F \cdot \Delta\theta) - (1 + \beta_S \cdot \Delta\theta)}{C_F \cdot (1 + \beta_F \cdot \Delta\theta)} \right) \quad (5.72)$$

5.4.3 Moments due to Coulomb Friction

As a result of the tab twisted shape and the differential speed, the plate tabs experience an axial force, causing their leading edge to be pushed against the outer plates. The total axial force (P_t) is calculated from equation (5.58) as the sum of the forces on side-1 and side-2. An equivalent differential pressure (P_e) may be introduced in the contact area of the plate, which would result in the same axial force acting on the tabs (Mohan, 2002), see figure 5.12, thus:

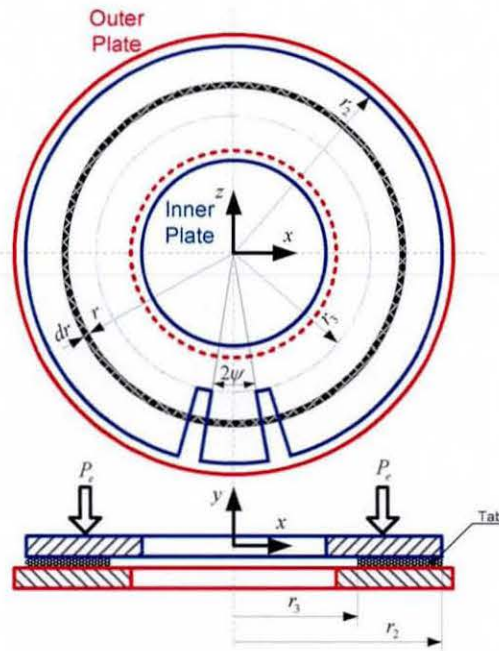


Figure 5.12 Coulomb Friction Torque Model

$$P_e = \frac{P_t}{\pi \cdot (r_2^2 - r_1^2)} \quad (5.73)$$

Consider an elemental annular ring area of width (dr) located at a radius (r). The elementary friction force (dF) resulting from the effective friction between the plates (η) can be calculated as follows:

$$dF = \eta \cdot P_e \cdot 2\pi \cdot r \cdot dr \quad (5.74)$$

The corresponding elemental torque (dT) is given as:

$$dT = dF \cdot r = \eta \cdot P_e \cdot 2\pi \cdot r^2 \cdot dr \quad (5.75)$$

The numerical integration of the elemental torque (dT) from the tab inner radius (r_3) to the outer radius (r_2) gives the Coulomb frictional torque (T_c) as:

$$T_c = \frac{2}{3} \cdot \pi \cdot \eta \cdot P_e \cdot (r_2^3 - r_3^3) \quad (5.76)$$

It should be noted that the calculated Coulomb frictional torque, equation (5.76), is added to the viscous shear torque (T_v) to provide the total torque provided per plate cell.

$$T_T = T_v + T_c \quad (5.77)$$

5.4.4 Structural Deformation of The Inner Plate Tab

Twisting Moment Due to Differential Shear Forces:

From equation (5.15), it is obvious that, when the inner plate moves away from the mid-point between the outer plates, side-1 and side-2 begin to experience different shear stresses. Referring to figure 5.13, the viscous shear forces acting on side-1 and side-2, with corresponding gaps (S_1) and (S_2), form a counter-clockwise twisting moment (M_{iv}) about the centroid of the base of the tab. The total twisting moment on one tab from the outer periphery up to a radius (r) is obtained as follows (Mohan, 2003):

$$M_{iv}(r) = \int_{-\psi}^{\psi} \int_r^{r_2} \left(\left[\mu \frac{du}{dy} \right]_2 - \left[\mu \frac{du}{dy} \right]_1 \right) \cdot \frac{t_i}{2} \cdot r \cdot dr \cdot d\psi \quad (5.78)$$

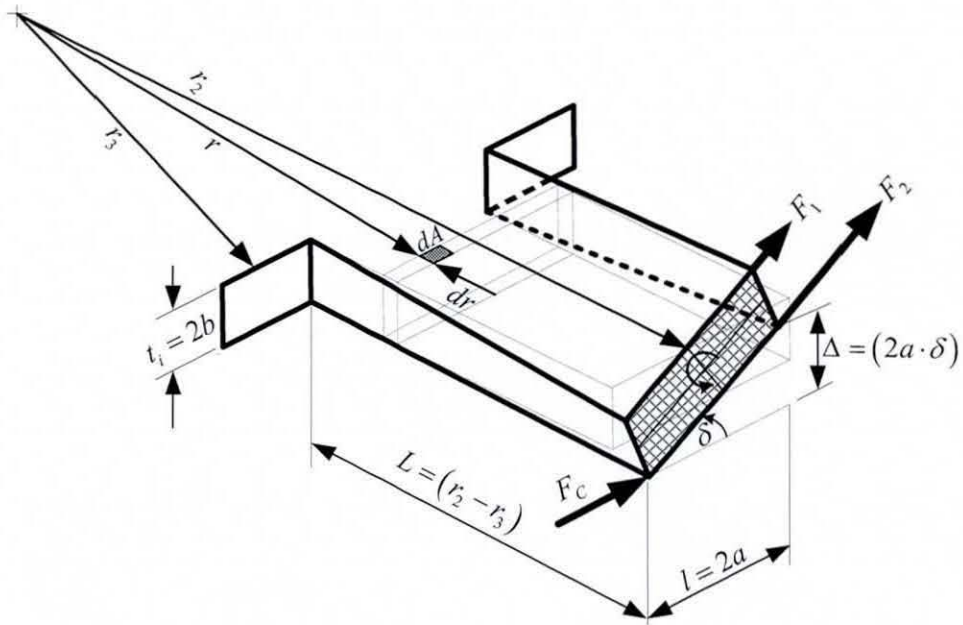


Figure 5.13 Structural Deformation of the Inner Plate Tab Model

From equations (5.5, 5.8), it follows that:

$$M_{iv}(r) = \frac{\rho \cdot V_o \cdot t_i \cdot \omega^{(1+m)}}{2 \cdot \dot{\gamma}_B^m} \cdot \int_{-\psi}^{\psi} \int_r^{r_2} r^{(2+m)} \cdot \left(\left(\frac{1}{S_2} \right)^{(1+m)} - \left(\frac{1}{S_1} \right)^{(1+m)} \right) \cdot dr \cdot d\psi \quad (5.79)$$

$$M_{iv} = \frac{\rho \cdot V_o \cdot t_i \cdot \psi \cdot \omega^{(1+m)}}{\dot{\gamma}_B^m} \cdot \left(\left(\frac{1}{S_2} \right)^{(1+m)} - \left(\frac{1}{S_1} \right)^{(1+m)} \right) \cdot \left(\frac{r_2^{(3+m)} - r_3^{(3+m)}}{3+m} \right) \quad (5.80)$$

Twisting Moment Due to Coulomb Friction:

As illustrated in figures 5.10 and 5.13, the tab is subjected to an additional twisting moment (M_{TC}), resulting from Coulomb friction at the tab's leading edge. This torque can be calculated according to the differential pressure induced force between side-1 and side-2 (P_{1-2}), the number of tabs on the inner plate (n), as well as tab's dimension as:

$$M_{TC} = \frac{P_{1-2}}{n} \cdot \eta \cdot \left(\frac{l \cdot \delta + t_l}{2} \right) \quad (5.81)$$

Once Coulomb friction comes into effect, the plates are irrevocably in the STA mode, even if the twisting moment due to viscous shear torque, (M_{TV}) reduces.

Inner Plate Tab Angle of Twist:

Calculation of the angle of twist is carried out by considering an elemental area (dA) subjected to a differential shear stress from both sides of the tab as:

$$\left. \begin{aligned} dF_1 &= \frac{2a \cdot \rho \cdot v_o}{\dot{\gamma}_B^m} \cdot \left(\frac{\omega}{S_1} \right)^{1+m} \cdot (r)^{1+m} \cdot dr \\ dF_2 &= \frac{2a \cdot \rho \cdot v_o}{\dot{\gamma}_B^m} \cdot \left(\frac{\omega}{S_2} \right)^{1+m} \cdot (r)^{1+m} \cdot dr \end{aligned} \right\} \quad (5.82)$$

The corresponding twisting moment $dM(r)$ around the tab's centroid can be obtained as:

$$\left. \begin{aligned} dM_{tv} &= (dF_2 - dF_1) \cdot b \\ dM_{tv} &= \frac{2a \cdot b \cdot \rho \cdot v_o}{\dot{\gamma}_B^m} \cdot \left(\frac{\omega}{S_2} - \frac{\omega}{S_1} \right)^{1+m} \cdot (r)^{1+m} \cdot dr \end{aligned} \right\} \quad (5.83)$$

This moment acts on an equivalent beam of length ($L = r - r_3$). The effective deflection at the section (r) is given by:

$$d\delta_{tv} = \frac{dM_{tv} \cdot L}{K_t \cdot G} = \frac{2a \cdot b \cdot \rho \cdot v_o}{\dot{\gamma}_B^m \cdot K_t \cdot G} \cdot \left(\frac{\omega}{S_2} - \frac{\omega}{S_1} \right)^{1+m} \cdot (r^{2+m} - r_3 \cdot r^{1+m}) \cdot dr \quad (5.84)$$

The total deflection at the tip may be computed by integrating it over the tab's radial length:

$$\delta_{iv} = \frac{\alpha \cdot t_i \cdot \rho \cdot v_o}{\dot{\gamma}_B^m \cdot K_t \cdot G} \cdot \left(\frac{\omega}{S_2} - \frac{\omega}{S_1} \right)^{1+m} \cdot \left(\frac{r_2^{4+m}}{3+m} - \frac{r_3 \cdot r_2^{3+m}}{2+m} + \frac{r_2 \cdot r_3^{3+m}}{(3+m) \cdot (2+m)} \right) \quad (5.85)$$

Twisting angle due to Coulomb friction moment around the tab's centroid can be calculated as:

$$\delta_{ic} = \frac{M_{ic} \cdot L}{K_t \cdot G} = F_C \cdot \left(\frac{\Delta + t_i}{2} \right) \cdot \frac{(r_2 - r_3)}{K_t \cdot G} \quad (5.86)$$

$$\delta_{ic} = \frac{\eta \cdot F_t \cdot (2a \cdot \delta_{tot} + t_i) \cdot (r_2 - r_3)}{2K_t \cdot G} \quad (5.87)$$

where (F_t) is the net total axial force per tab, (η) is the coefficient of Coulombic friction.

The total twisting angle due to the differential shear stress and Coulomb friction is given as:

$$\delta_{tot} = \delta_{iv} + \delta_{ic} \quad (5.88)$$

It should be noted that before a tab contact occurs, tab angle of twist is calculated based on equation (5.85). After contact, the tab angle of twist is calculated based on equation (5.88).

The net axial tip deflection (Δ) may be obtained by multiplying the angle of deflection by the width of the tab at the tip. This deflection can be measured during test and is used to characterize the deflected shape of the tab: $(\Delta = 2a\delta)$.

Figure 5.14 shows the general algorithm for simulating the viscous coupling during self-torque amplification mode. The numerical simulation procedures are carried out using ODE4: Runge-Kutta solver with fixed-step integration size of (0.001s), which was found adequate to ensure conversion of the algorithm.

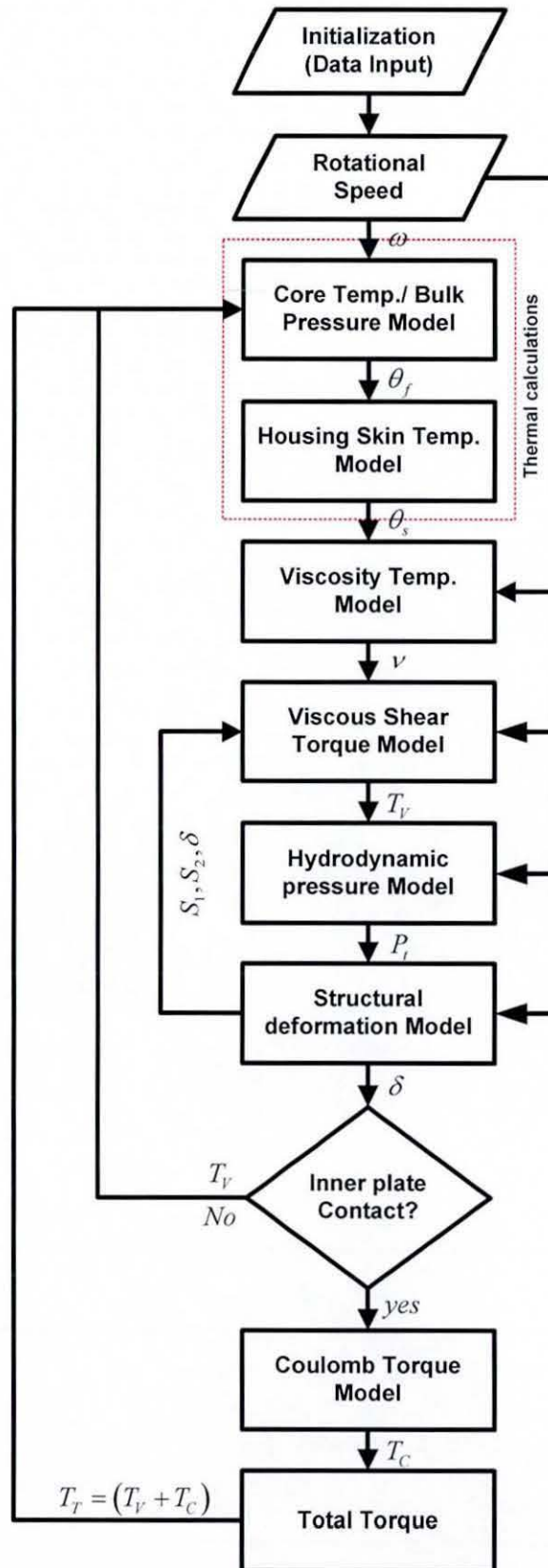


Figure 5.14 General Algorithm of Viscous Coupling Simulation in STA Mode.

5.5 Experimental Methodology

Validation of numerical modelling is an important step in any theoretical analysis work, as it imparts confidence to the users in employing the model for design purposes. In order to validate the tribo-dynamics' modules of the visco-lock devices, the simulated conditions described in sections 5.3 and 5.4 are applied to typical components, and then the experimental findings under similar conditions are compared with the simulation results.

5.5.1 Rheological Measurements for The Silicone Fluid

From the theoretical analysis of visco-lock devices, it is obvious that, the rheology of silicone fluid has a significant effect upon the generated shear torque, especially the fluid's viscosity-temperature and viscosity-shear rate characteristics. Consequently, it is of prime interest, to measure these characteristics for given samples of the silicone fluids used.

To measure these characteristics, AR1000 rheometer, from TA *Instruments*, is used, see appendix (B). The instrument consists of a main unit mounted on a cast metal stand and electronic control circuitry contained within a separate electronic control system as shown in figure 5.15.

The rheometer unit contains an electronically-controlled induction motor with an air bearing support for all the rotating parts. The drive motor is equipped with a hollow spindle which allows the geometry (cone and plate, parallel plate or concentric cylinders) to be securely attached. Measurement of angular displacement is made by an optical encoding device. The associated circuitry interpolates and digitizes the resulting signal to produce digital data which is directly related to the angular deflection of the rotating disk, therefore, the strain of the sample, see figure 5.16.

Temperature control is achieved using a Peltier plate system, which uses Peltier (thermo-electric) effect to rapidly and accurately control heating and cooling of the fluid trapped

in the gap (the film thickness). By controlling the magnitude and direction of electric current, the Peltier system can provide any desired level of active heating or cooling directly in the plate.

The concept of measurement is to drive the geometry under controlled torque, then, both the shear stress (function of driving torque and plate area) and rate of shear strain (measured rotational speed times the plate radius divided by the gap size or film thickness) are measured and plotted for different values of the controlled temperature.

The viscosity-shear rate characteristics are measured over the temperature range of (25:150) °C as depicted in figure 5.17. It is obvious that, at a lower shear strain rate, the fluid is characterized by Newtonian behaviour, where the viscosity is independent of the rate of shear strain. Furthermore, for each temperature, viscosity decreases as rate of shear strain increases. The observed drop in viscosity under shear strain rate is attributed to the elongation and orientation in shear direction of the initially randomly convolute chain molecules under the influence of shear loading. Moreover, and as a typical behaviour of pseudo-plastic fluids, the rate of decrease in apparent viscosity is more pronounced at the lower range of measured temperatures.

The viscosity-shear rate characteristics at temperature 25 °C can be represented by the mathematical relationship given in equation (5.5). Therefore, the following parameters can be estimated from the measurements; the nominal kinematic viscosity ($\nu_o = 80 \text{ KcSt}$), the critical shear rate ($\dot{\gamma}_B = 80 \text{ s}^{-1}$) and the slope of the regression line ($m = -0.85$).

The viscosity-temperature relationship can be predicted from viscosity-shear rate characteristics at nearly zero shear-strain rate, as shown in figure 5.18. The data obtained are plotted against temperature, and then, equations (5.1) and (5.2) are used to mathematically represent the relationship. Coefficient ($A = -1.37$) can be obtained by fitting the measured data. Figure 5.18 shows a sufficient accuracy when using both equations to predict viscosity as function of temperature.

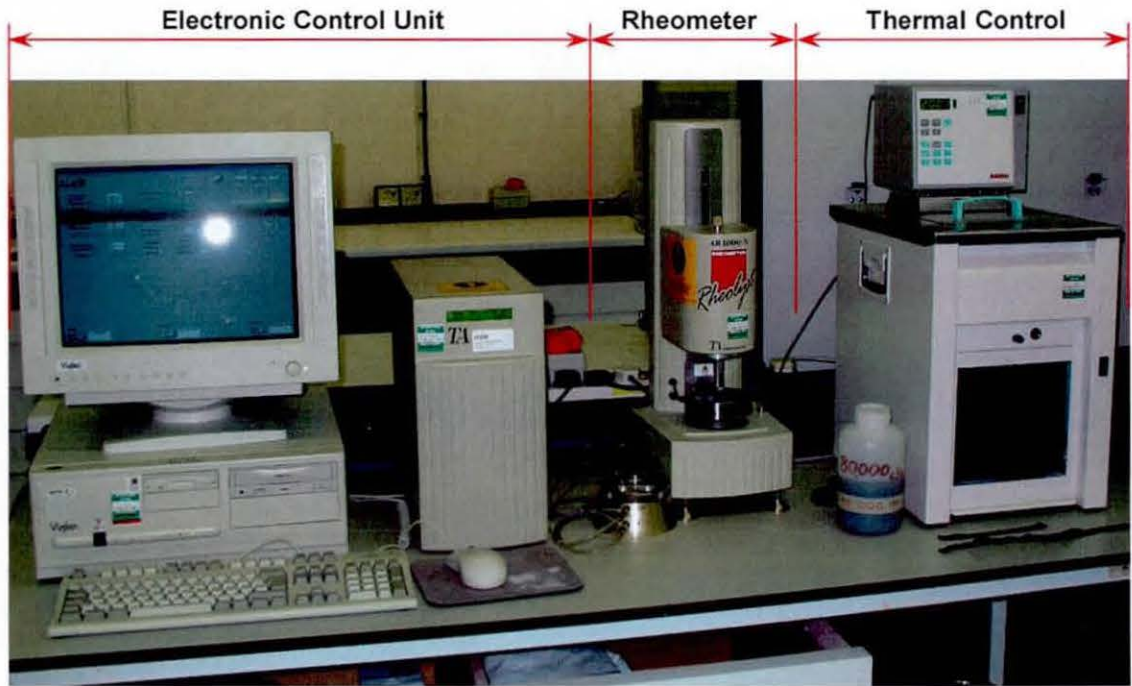


Figure 5.15 Silicone Fluid Rheology Measurements

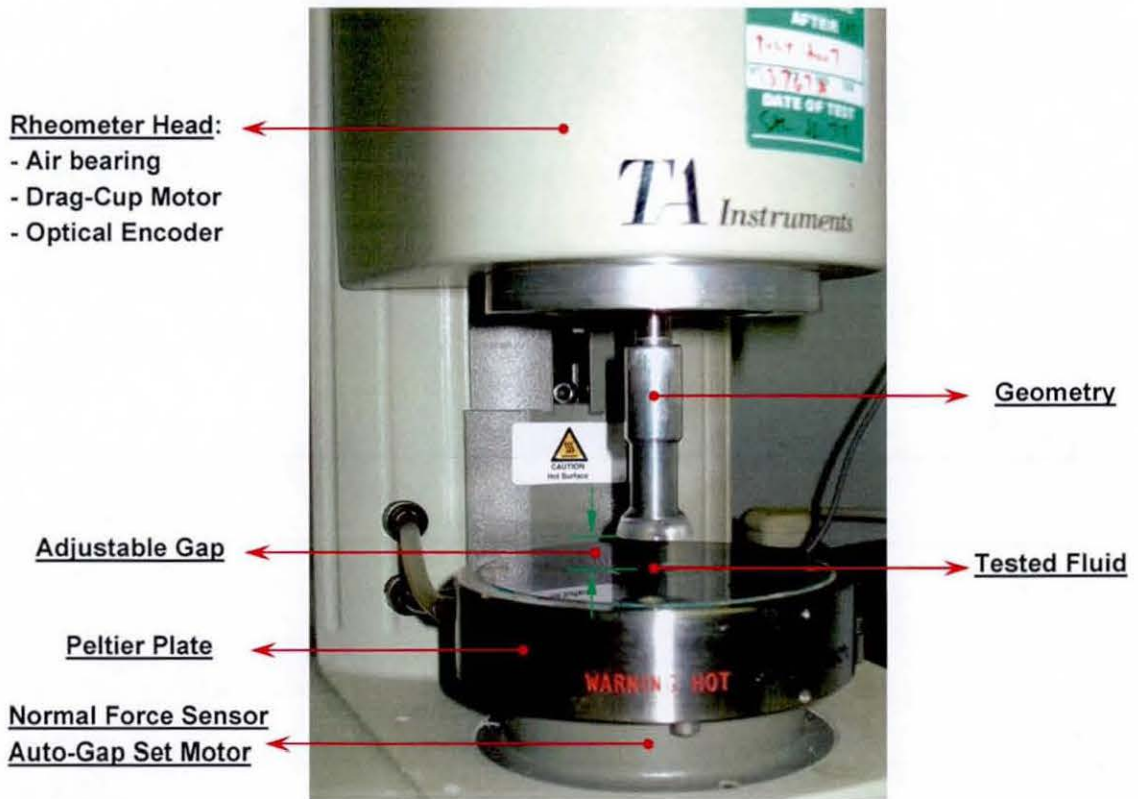


Figure 5.16 The AR1000 Rheometer

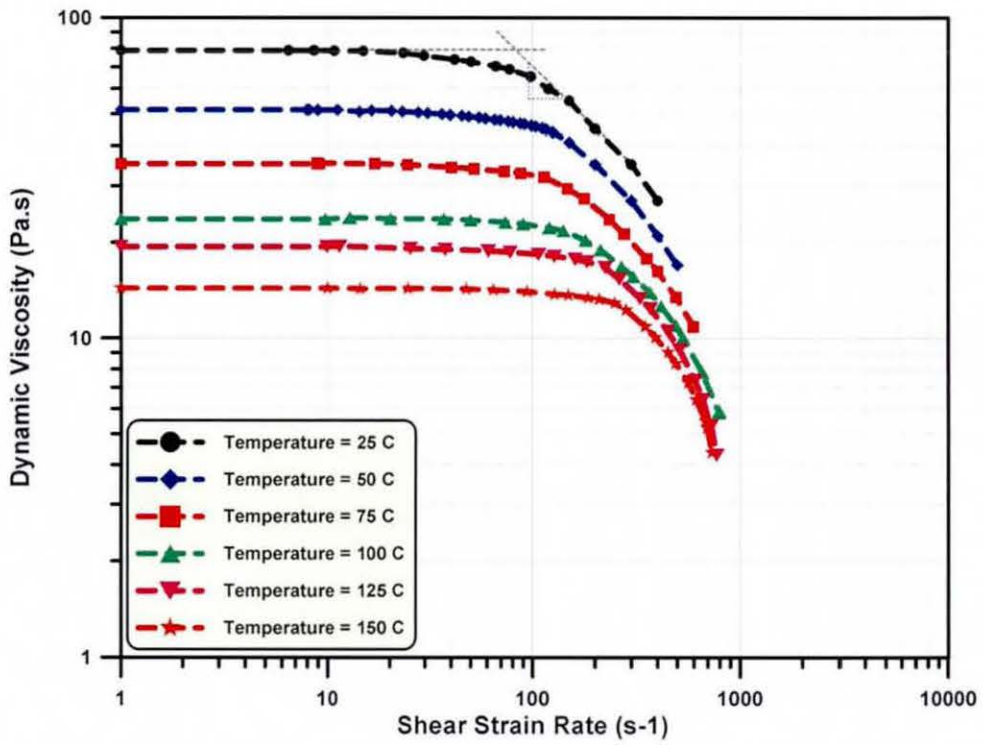


Figure 5.17 Viscosity-Shear Strain Rate Dependency at Different Temperatures

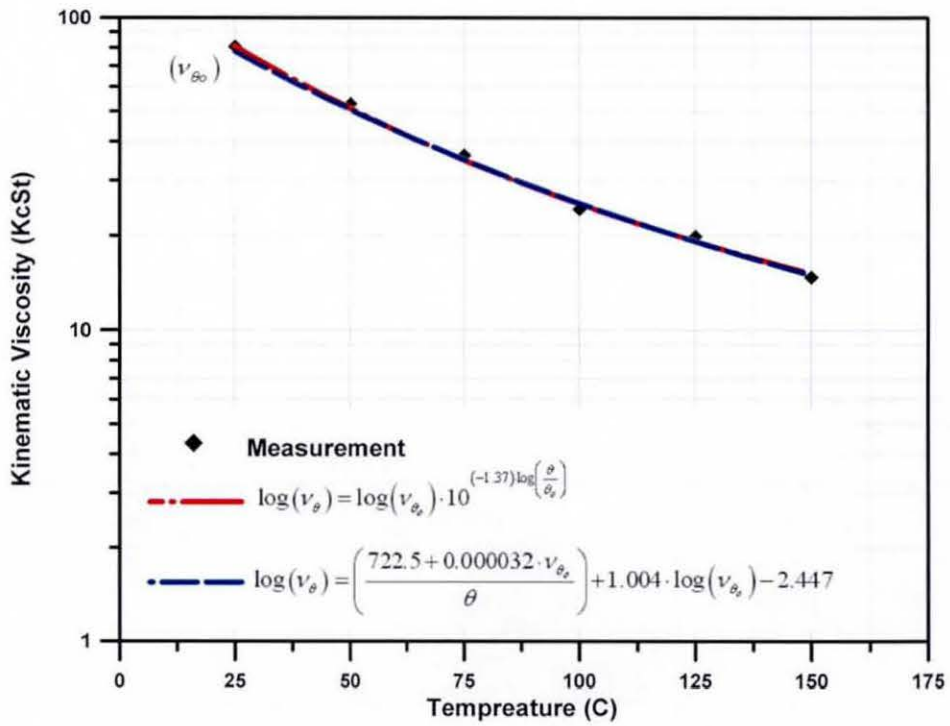


Figure 5.18 Viscosity-Temperature Dependency at Nearly Zero Shear Rate

5.5.2 Test Rig Design

To capture the characteristics of the viscous-shear torque mechanism transmitted by visco-lock devices, it is essential to represent the condition of differential speed or slip between the input and output of these devices. However, in practice these components are installed within axles or integrated with full transmission systems. Therefore, it would be an advantage to consider their performance separately, rather than dealing with complex systems with many interacting parameters with manifold of effects. For this purpose, a special casing was designed to hold the differential unit as described later. Furthermore, different aspects associated with viscous-shear phenomenon, such as shear torque, shear rate and thermal effects are measured. The following sections deal with these issues in some detail, providing justification for use of the given configuration.

5.5.2.1 Visco-lock Differential Casing

The idea of the differential casing design, to a great extent, was based on the construction layout of the differential itself and the functional implementation of the viscous unit. The viscous coupling unit is incorporated into a rear axle differential to provide an automatic way of neutralizing the differential action, whenever one of the wheels loses its grip and commences to spin. The manner of installation of the viscous unit was based on the shaft-to-carrier layout such that, the plates are connected alternately; one set of plates was splined to the differential carrier, whilst the other set of plates was splined to the differential gear on one side, which in turn was splined to its shaft.

In order to simulate and test the operation of such a configuration, the differential can be analyzed as a set of planetary gears. The gear, attached to the right half-axle, can be considered as a sun gear, which drives the gearing system, as well as the inner plates of the viscous coupling. The other gear, attached to the left half axle, can be considered as a ring gear. The crown wheel is considered as the planet carrier, which is attached to the outer plates of the viscous coupling.

For the purpose of viscous torque measurement, the crown wheel was locked to the casing, whilst the ring gear was free. Therefore, the net differential speed can be

measured from the speed of the sun gear and the driving torque is totally consumed by the viscous shear resistance, see figure 5.19.

For the purpose of lubrication, the differential assembly was covered with a sealed plastic sheet and partially filled with gear oil. Furthermore, a hole was tapped to lubricate the input shaft through an oil cup.

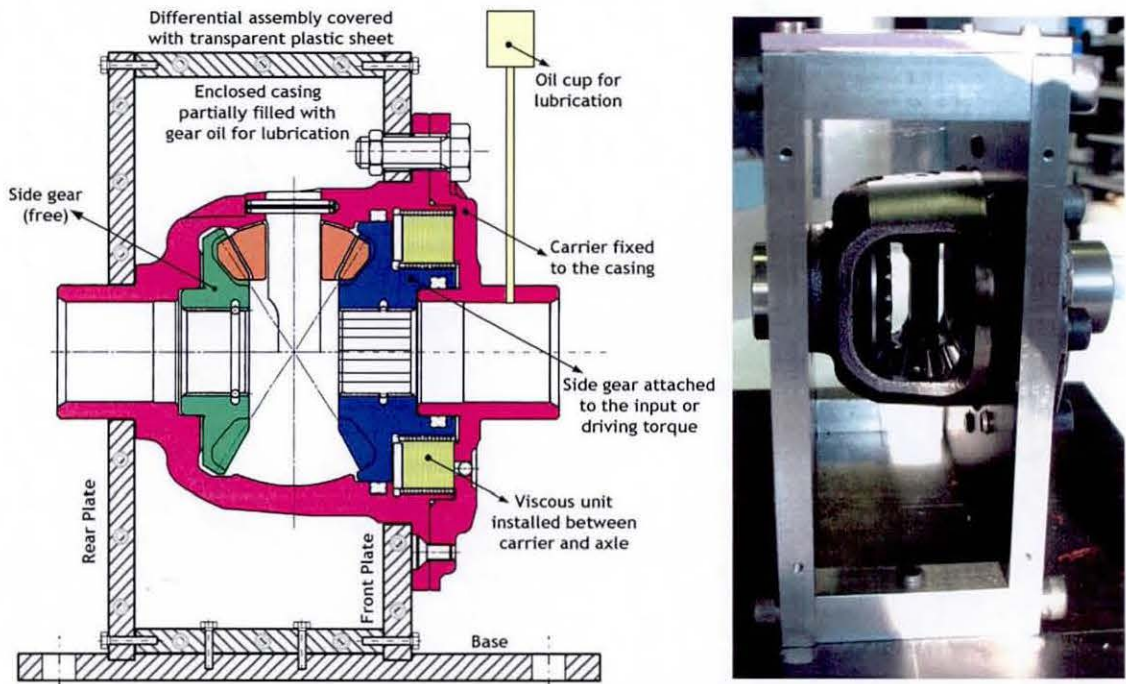


Figure 5.19 Visco-Lock Differential Casing Assembly

5.5.2.2 Torque Unit Assembly

The differential unit, described earlier, was driven and measured at the same time via the torque unit assembly as shown in figure 5.20. The unit consists of a torque transducer, which was installed between two self-aligning plummer block bearings. In addition, the unit assembled the propeller shaft and the input shaft to the differential unit. To improve the alignment and flexibility of the rig, a constant velocity joint was introduced between the visco-lock differential casing and the torque unit.

Torque was measured (up to 500 N·m), using the 420 series torque transducers, supplied by the Datum Electronics Ltd., see appendix (B). The torque transducer operates as a non-contact device (no direct contact between the rotor and the stator) using strain gauges. Both the rotary shaft and the stator are built into a static housing, which is mounted onto the shaft via bearings. Therefore, the housing of the transducer was locked by means of a metallic plate.

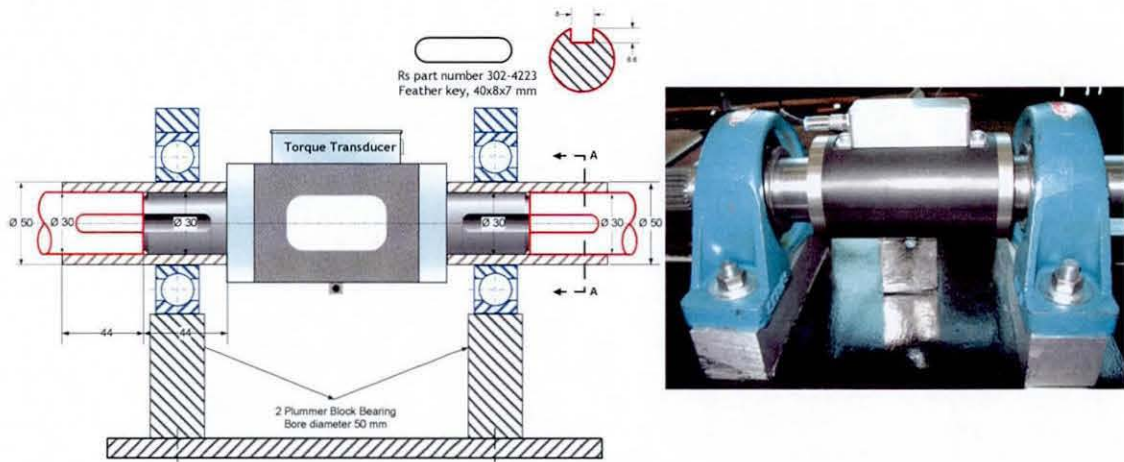


Figure 5.20 Torque Unit Assembly

5.5.2.3 The Drive Unit

The drive unit was a part of a previous research aimed at measuring the induced vibration (clonk) in vehicular drivetrain systems (Gnankumarr, 2004). The drive unit consists of AC electric motor, motor control, self-lubricating cast iron pillow block, hydraulic clutch and a gear box, figure 5.21. Some modifications were carried out for the drive input shaft to be accommodated with the differential rig. The following are brief notes about the drive unit.

Electric motor: A 22 KW, three phase, four pole AC electric motor provides the opportunity to apply fully controllable torque conditions. The maximum delivered torque 143 N·m at 1470 rpm is more than sufficient to drive the viscous differential at the low speed of (100 rpm).

Motor Controller: an inverter 'IMO Jaguar VX 2200 –P-EN' is used to achieve the smoothness in motor's performance. Using the controller, it would be possible to obtain certain speed-time profiles necessary to investigate the viscous shear characteristics.

Flexible Coupling: A flexible rubber coupling was installed in-line between the motor and the input shaft of the gearbox. The rubber coupling helps to dampen torsional vibration and to isolate the drivetrain from the operational frequencies of the electric motor. The coupling is fitted with a shear pin in order to protect the electric motor from any sudden reversals or over-loading conditions. The propeller shaft is mounted rigidly on a pair of angular contact thrust ball bearings in back-to-back arrangement to provide high dynamic stiffness.

Bearing: In order to support the propeller shaft and the weight of the coupling unit, it is necessary to use the bearings. Therefore, two self-lubricating cast iron pillow block units with angular contact thrust ball bearings were selected. Both bearing are mounted into the bedplate with motor and the transmission.

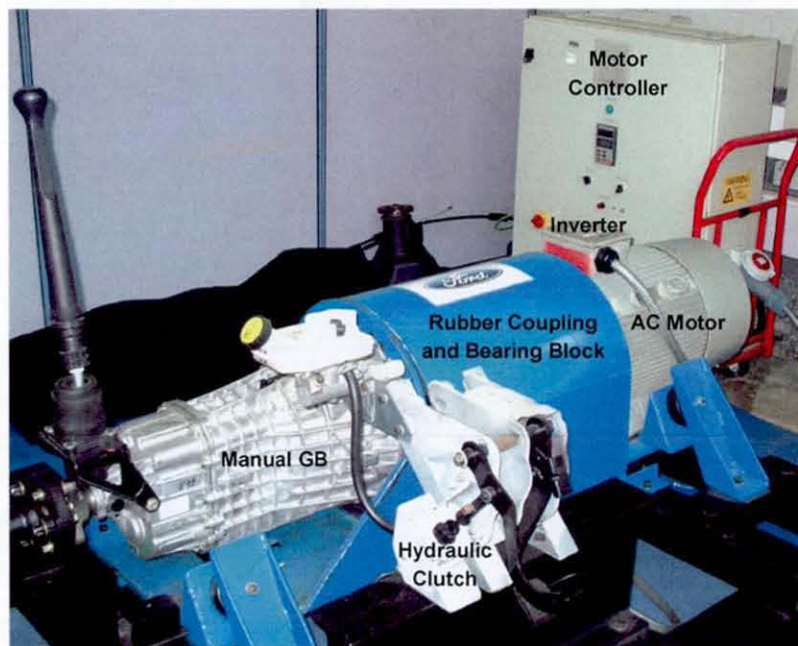


Figure 5.21 The Drive Unit Main Components

Hydraulic Clutch system: The standard vehicle hydraulic clutch system has been fitted in the test rig to provide time-controlling and altering clutch engagement-disengagement. For the present research, the clutch was assumed to be fully engaged.

Gear Box: A five speed manual gear box is installed to provide a wide variation of torque, depending on the selected gear ratio. Normally, the first gear provides enough torque to drive the rig components.

5.5.3 Measuring Instruments

5.5.3.1 Temperature Measurement

Temperature was measured using type K thermocouples (Nickel-Chromium / Nickel-Aluminium) of accuracy ($\pm 0.25\%$ of F.S) and resolution ($\pm 0.1\%$ of F.S). To obtain more accurate and reliable measurements, three thermocouples were attached to the outer surface of the differential at different places, such that all of them were as close as possible to the viscous unit as shown in figure 5.22. Thermocouples were plugged into a multi-channels microprocessor thermometer (Comark, series 6201), which provides the ability to read the temperature digitally. Furthermore, this instrument provides an analogue representation of the digital display of 1 volt which is equivalent of $100\text{ }^{\circ}\text{C}$.



Figure 5.22 Temperature Measurements using Comark Microprocessor Thermometer

5.5.3.2 Speed Measurement

The angular speed of the driving shaft was measured using a laser torsional vibrometer, which is an effective non-contact alternative to the use of an Eddy current probe or traditional contacting vibration transducers. The principle of the Laser Doppler Vibrometry (LDV) relies on the detection of a doppler shift in the frequency of the coherent light scattered by a moving target, from which a time-resolved measurement of the target velocity is obtained (Halliwell, 1996).

The laser beam is divided into two parallel beams which are separated by a small gap. The instrument is held so that the plane of the incident laser beams is parallel to the shaft's cross-section. The Doppler frequency demodulation of the photo-detector output provides a time resolved analogue voltage of the rotational speed of the shaft, figure 5.23.



Figure 5.23 Rotational Speed Measurements using Laser Rotational Vibrometer

5.5.3.3 Torque Measurement

For the measurement of torque, a non-contact rotary torque transducer with bearings (series M420 metric) was employed. The transducer provides a digital output (via RS232 serial port) directly proportional to the torque. In addition, the transducer can measure torque up to values 500 N·m with an accuracy of 0.1% full scale with sampling rate of 10:100 samples per second. For the purpose of display and data logging facilities, special software is provided to monitor and record speed, torque and power values as depicted in figure 5.24.



Figure 5.24 Torque Measurements using Datum Torque Transducer and Torque Log

To collect data from the thermocouples and the laser Doppler vibrometer, the NI USB-6008 data acquisition device was used. The device provides connection to eight analogue input channels, two analogue output channels, twelve digital input/output channels, and a 32-bit counter with a full-speed USB interface. The system was connected to a Pentium IV 2 GHz laptop computer. Raw data were transferred into various data analysis software such as National Instruments LabVIEW 7.0 and Microsoft Office Excel.

The overall test rig arrangement, as well as the instrumentation is shown in figure 5.25.

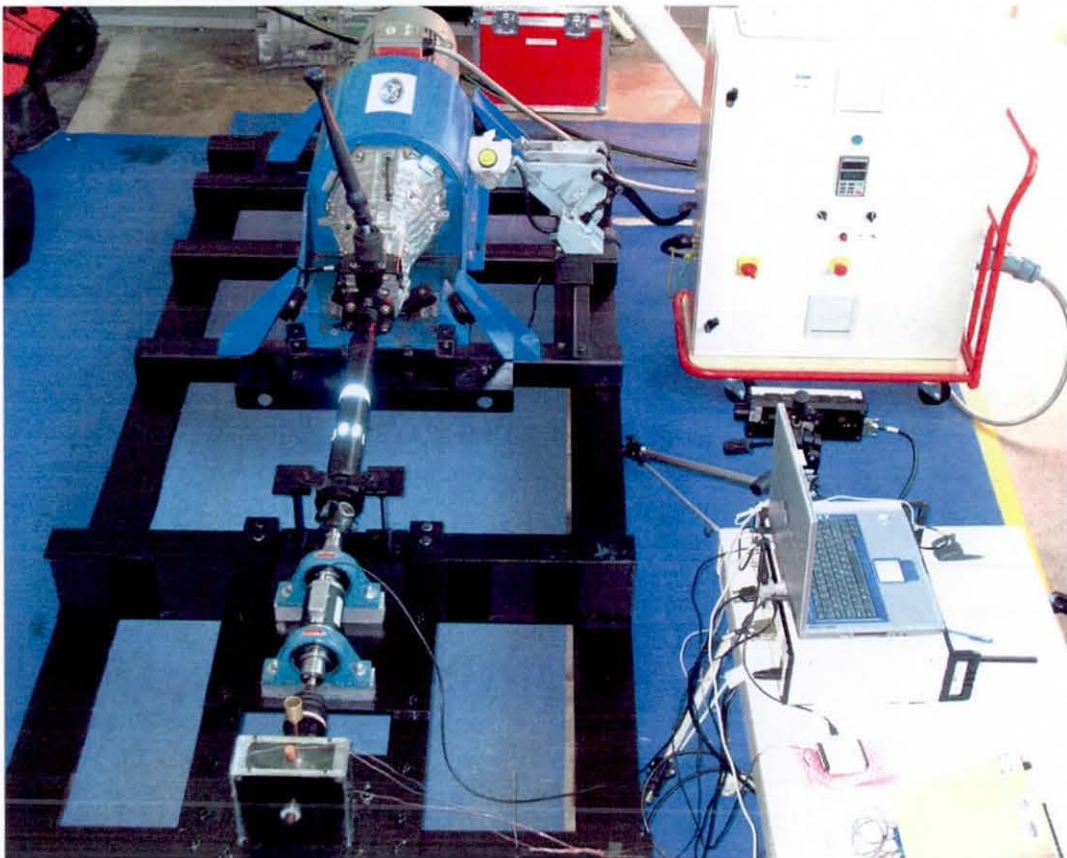


Figure 5.25 Test Rig Arrangement with Instrumentations

5.6 Results and Analysis

Several different methods can be considered for evaluating the shear torque transmission characteristics of visco-lock devices. The method used in the present research is to consider the output shaft, connected to the outer plates, to be fully locked, whilst the input shaft, connected to the inner plates, is driven with a speed ramp rise rate of 10 rpm/sec.

The controlled rotational speed was increased from zero up to 100 rpm within 10 seconds. The speed was hold at 100 rpm for another 25 seconds and then decreased again to zero. The variations in the transmitted shear torque during this process was recoded and examined. Limitations in the measured data are related to instrument accuracy and sensor placement. Furthermore, a filter was used to reduce noise in the data set, without creating any significant lag in the data recording rate. The accuracy of the calculated results is verified through comparisons with the experimental measurements.

5.6.1 Visco-Lock Limited Slip Differential

Figure 5.26 demonstrates a time history of the numerical simulation results of a rear axle limited slip differential for a short duration of 10 seconds. Based on Non-Newtonian and full thermal model assumptions, both shear torque and temperature of core, as well as that of the housing were calculated. The behaviour of the shear torque can be best explained by observing the changes in fluid viscosity. In the first three seconds, where both shear rate and fluid temperatures are low, the rate of increase of shear torque is quite high. However, an equivalent amount of heat is generated, which can be estimated by multiplying the instantaneous shear torque, rotational speed and time, see equation (5.19). The resultant heat raises the silicone fluid temperature and hence reduces its viscosity. Moreover, similar effect on the apparent viscosity occurs due to the shear thinning effect. The continual reduction of fluid viscosity limits the rate of increase of shear torque.

The comparisons between the numerical simulation results and the experimental measurements during a long period of time are depicted in figure 5.27. The test is carried out at initial skin temperature of 26°C. Good agreement can be observed for both the skin temperature and the rotational speed.

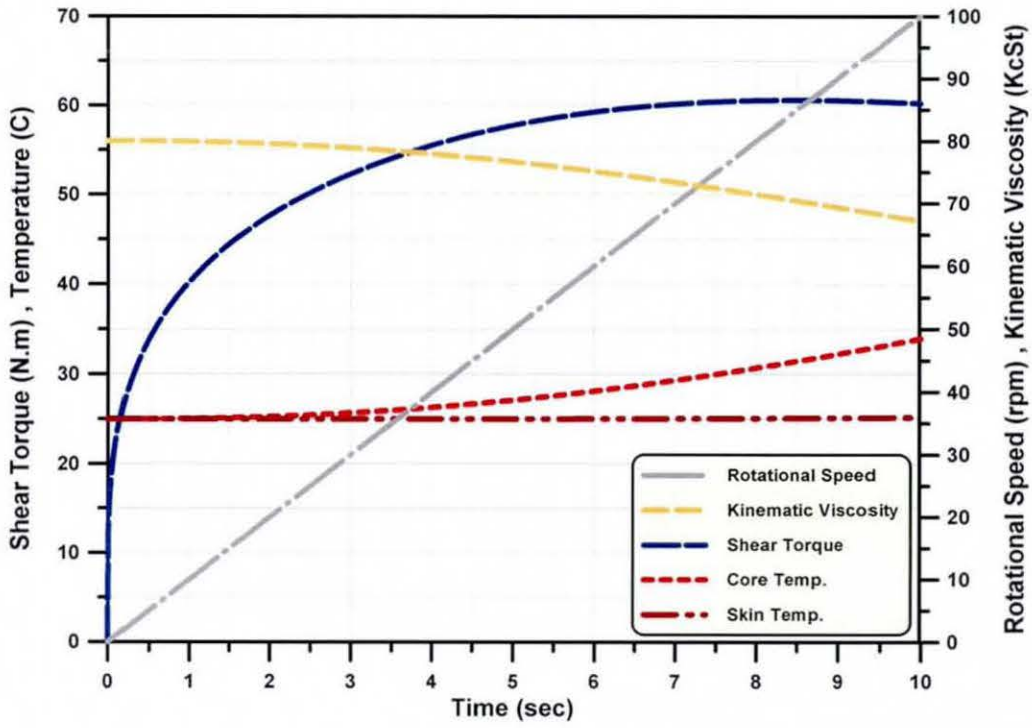


Figure 5.26 Time History of Numerical Simulation Result during Short Time of Period

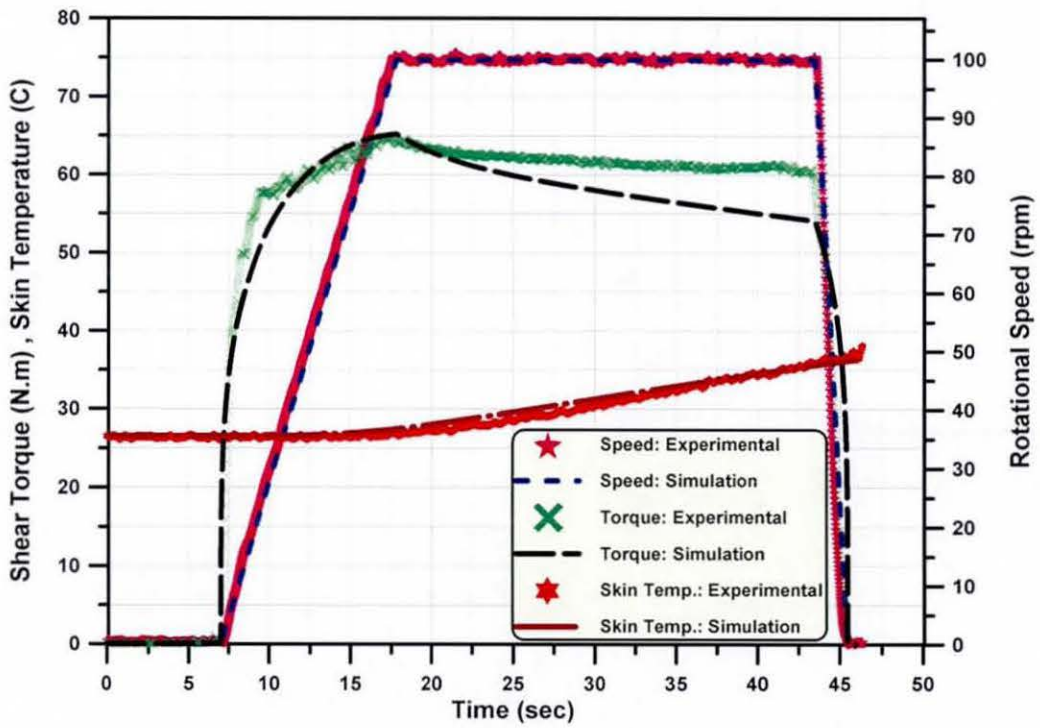


Figure 5.27 Comparisons between the Numerical and the Experimental Results During Long Period of Time

For shear torque characteristics; while the numerical simulation values follow that of the experimental measurements during short period, for longer period of time a small difference is observed which may be considered to be due to the approximate nature of the thermal model due to its simplifying assumptions.

Referring to figure 5.27, it is obvious that, during the speed-ramp period (up to 18 seconds) a minute change in housing temperature occurs, which justifies the assumption of an adiabatic thermal process, see section 5.3.3. During experiments, it was observed that, the coupling does not hump (the phenomenon described in section 5.4). In addition, the measured value of shear torque is comparatively low. This performance is desired by the manufacturers in order to reduce the over-steer effect of the vehicle during cornering manoeuvre as described later in chapter 6.

Another important characteristic to describe the behaviour of viscous coupling is to construct the relationship between shear torque and rotational speed. Figure 5.28 shows a comparison for both the numerical and experimental results for the short duration tests, which reveals an acceptable confidence about the developed numerical model.

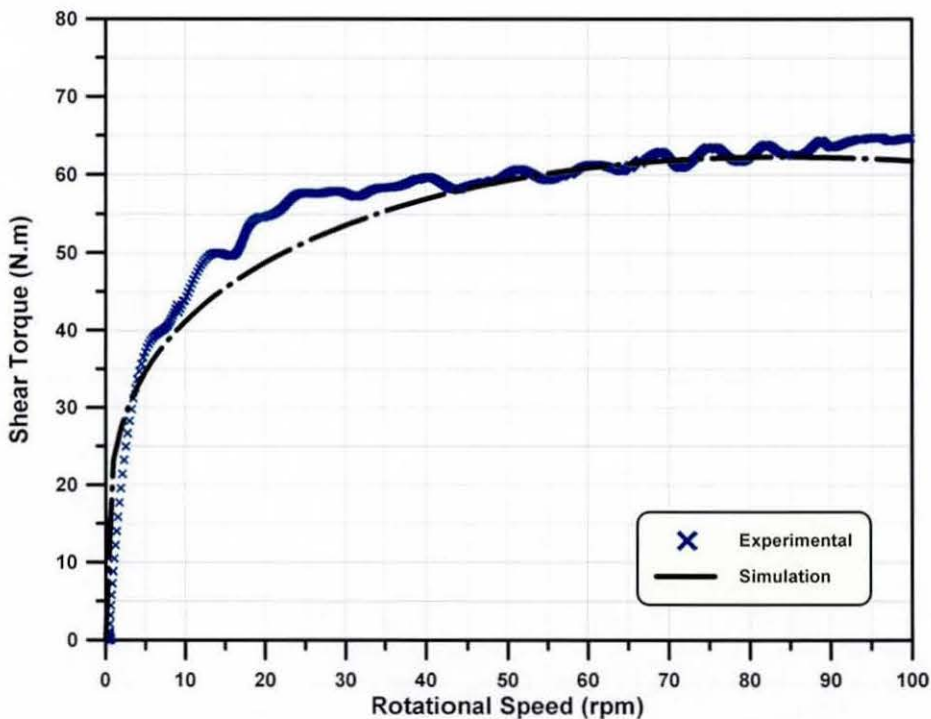


Figure 5.28 Shear Torque-Speed Characteristics (Model versus Experiment)

To investigate the effect of temperature on the torque capacity of the visco-lock limited slip differential, several tests were carried out at different skin temperatures, as shown in figure 5.29. As expected, performing the shear-test at higher temperatures would reduce the torque capacity of the unit from 65 N·m at 25°C to 50 N·m at 150°C. The reduction in shear torque is mainly due to the decrease in viscosity of the siloxane, which is added to the thixotropic behaviour, see equations (5.1), (5.2) and figure 5.18.

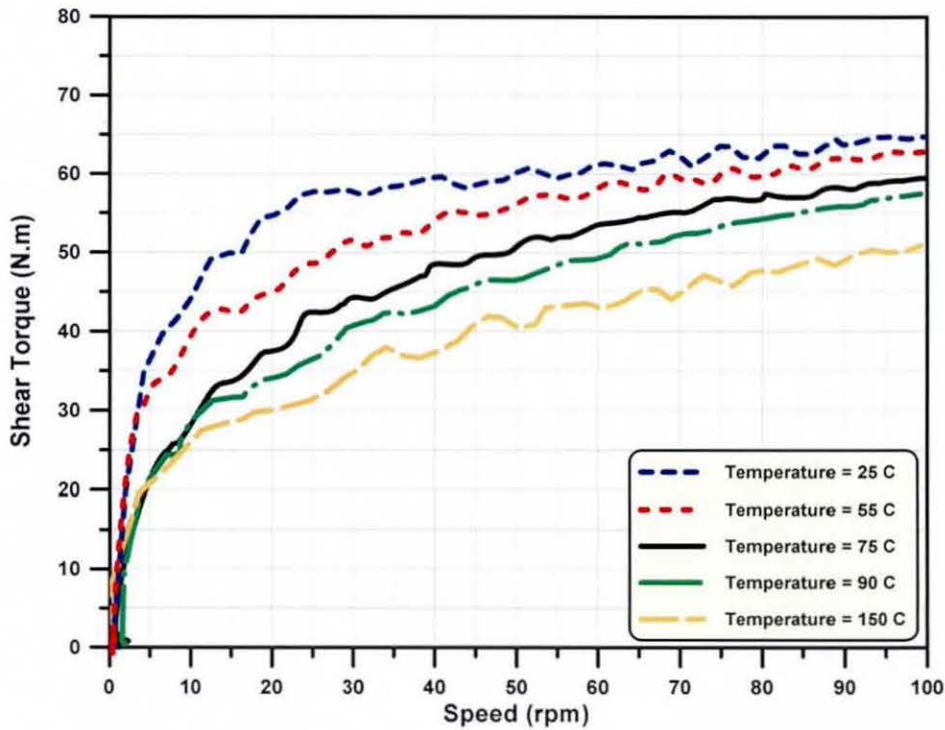


Figure 5.29 Temperature Effect on Torque capacity of the Visco-Lock Differential

5.6.2 Viscous Coupling

The viscous coupling behaviour is investigated during ramp speed input, from 0 to 100 rpm, with an angular acceleration of 10 rpm/sec. Thereafter, the speed is maintained constant as depicted in figure 5.30.a.

The torque is the primary characteristic of the operation of the viscous coupling. Referring to figure 5.30.c, the torque characteristics can be divided into three distinct phases as follows:

- The initial: is the normal viscous shearing phase, which is characterized by an increased rate of shear torque as previously explained in section 5.6.1.

- The intermediate: is characterized by a noticeable reduction in the shear torque. This effect can be explained by noting the relationship between shear torque, heat, and viscosity-temperature dependency, see figure 5.30.b. However, with continual shearing of the fluid as well as the slotted edge geometry of the tabs, the inner plates are made to move axially, creating non-symmetrical gaps around their tabs as shown in figure 5.30.d. The resulting change in the gap between the contiguous plate pairs causes differential shear stresses and twisting moments across the inner plate tabs. This tends to twist the tabs around their centroids, see figure 5.30.f. With the twisted shape of the inner plate tab and the differential speed between the inner and outer plate, the tabs act as a sliding pad bearing, generating hydrodynamic pressures. The resulting differential pressure across the plate tabs creates a further axial force, see figure 5.30.e.

- The final: is the self-torque amplification phase, which is characterized by a sudden and sharp increase in the transmitted torque. The generated hydrodynamic pressures are limited by the bulk pressure inside the viscous coupling. At the room temperature, the coupling is only partially filled with the silicone fluid. At a certain critical temperature, when the volume of silicone fluid has expanded to fully fill the voids, the bulk pressure increases, see figure 5.11. Consequently, both the differential pressure and the net axial force increase rapidly until the plates come into direct contact with each other, figure 5.30.d. At this point, a Coulomb friction torque is generated, which adds to the viscous torque to form a sharp increase in torque, known as the humping torque, figure 5.30.c.

For the purpose of verifying the numerical model in hump mode, the simulation results are compared with some of the well known published experimental results (Mohan, 2002, 2003, 2004) as shown in figure 5.30.a and b and c. It can be seen that the numerical results conform well with the reported experimental findings.

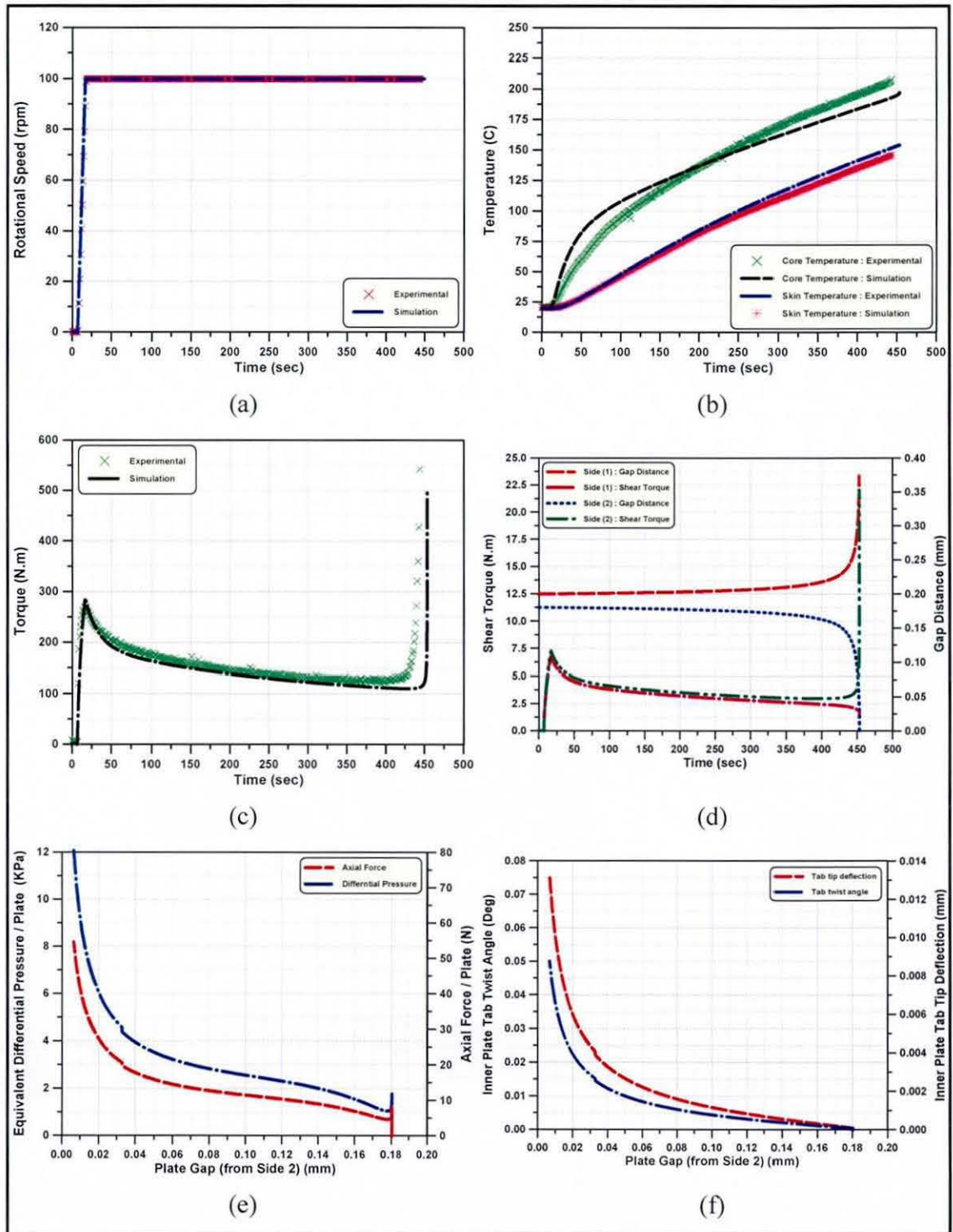


Figure 5.30 Self-Torque Amplification in Rotary Viscous Couplings

Chapter 6: Analysis of AWD Vehicle Dynamics Augmented by Visco-Lock Devices

The rapidly increasing applications of AWD, particularly in the passenger vehicle sector, necessitates the development of vehicles not only with higher traction potential but also with better manoeuvrability over deformable soil. Although improving traction performance is a main consideration for off-road vehicle applications, handling behaviour is an important aspect of modern vehicles, which requires capability to undergo high lateral accelerations, whilst maintaining good level of directional stability. The desired increase in mobility must be reached without making any compromises regarding safety or ease of operation or driver comfort. It is anticipated that, the performance of AWD off-road vehicles depends not only on the total tractive effort available by the power-plant, but also on its distribution between the driving wheels.

An innovation in the field of permanent AWD is the use of visco-lock devices not only to fulfil the function of torque split and transfer, but also to work as self-controlling devices. The tuning and setting up of these devices is usually based on a trial and error approach, which is time consuming and expensive. In such a situation a computer simulation can usually offer a tool not only for speeding up this process, but also to develop a deeper understanding of the problem. The characteristics of these devices can easily be altered so that comparison can be made between their different types. In addition, the influence of a wide range operating conditions and vehicle design parameters can easily be examined and therefore optimized for better performance.

The main objective of this chapter is to implement the tribo-dynamic modules, derived in chapter 5, into the overall vehicle multi-physics model, derived in chapter 4. Furthermore, the dynamic performance of AWD off-road vehicles, coupled with different drivetrain layouts, is addressed in terms of traction and directional stability. Additionally, the tuning process for visco-lock devices is established in a full numerical simulation environment by altering the rheology of the silicone fluid to achieve the required vehicle performance.

6.1 Implementation of Visco-Lock Devices into Dynamic Drivetrain Model

Biasing the driving torque between axles/wheels has serious consequences on the vehicle behaviour. Generally, 4WD systems may be classified according to the way driving torque is divided between their axles as follows:

Static torque split devices: characterized by a fixed ratio of torque-split between axles, which is predetermined by the gearing design. The conventional (straight) bevel geared differential, without additional control mechanism, has an equal torque distribution between its axles, i.e. (50:50) %. Different static split torque ratios can be obtained by using an angular bevel gear or a planetary gear set as described later, see figure 6.3.

Dynamic torque split devices: characterized by a variable ratio of torque-split between axles, which is predetermined by the device's locking characteristics, i.e. softer or stiffer. While the visco-lock devices can dynamically split the driving torque between their axles/wheels, the range of torque split is constrained by the rheological characteristics of the viscous unit. Therefore, an optimal solution is achieved by incorporating a viscous control element into the static torque split devices. The mathematical modelling of some of the well-known mechanisms for torque distribution is derived as described below.

6.1.1 Viscous Control Differentials with Equal Torque Distribution:

As previously described in section 5.1, the viscous unit may be installed within the conventional open differential to act as a viscous controlled element for distribution of torque. Either arrangement of shaft-to-carrier or shaft-to-shaft leaves the differential carrier and pinions to function normally, except when there is a significant speed difference between the half-shafts, where the viscous unit operates.

6.1.1.1 Shaft-To-Carrier Layout:

Referring to figure 6.1, the input torque (T_C) is applied at the differential carrier through the ring gear. According to the differential rotational speed between left and right axles,

the viscous torque (T_v) is developed. Therefore, the torques applied at right axle (T_1) and left axle (T_2) can be calculated from the principles of mechanics as follows:

Since the side gears of the differential have equal diameters (or symmetrical geometry), then from the balance of forces acting on differential gears, the following relationship is obtained:

$$T_1 + T_2 = T_c \quad (6.1)$$

From the balance of moments, the following relationship is found:

$$T_1 = T_2 - T_v \quad (6.2)$$

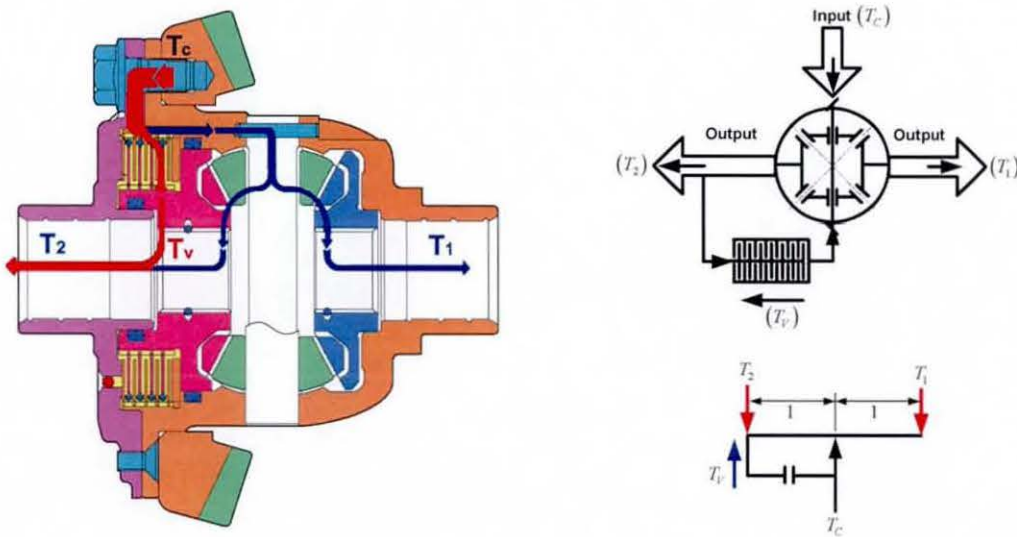


Figure 6.1 Viscous Control Differential with Shaft-To-Carrier Arrangement

By solving equations (6.1) and (6.2), expressions for the axles' torques (T_1) and (T_2) can be obtained as follows:

$$T_1 = \frac{T_c - T_v}{2} \quad (6.3)$$

$$T_2 = \frac{T_c + T_v}{2} \quad (6.4)$$

$$T_v = |T_2 - T_1| \quad (6.5)$$

6.1.1.2 Shaft-To-Shaft Layout:

Since the side gears of the differential have equal diameters (or symmetrical geometry), then from the balance of forces acting on differential gears, the following relationship can be obtained:

$$T_1 + T_2 = T_c \quad (6.6)$$

From the balance of moments, the following relationship is found:

$$T_1 + T_v = T_2 - T_v \quad (6.7)$$

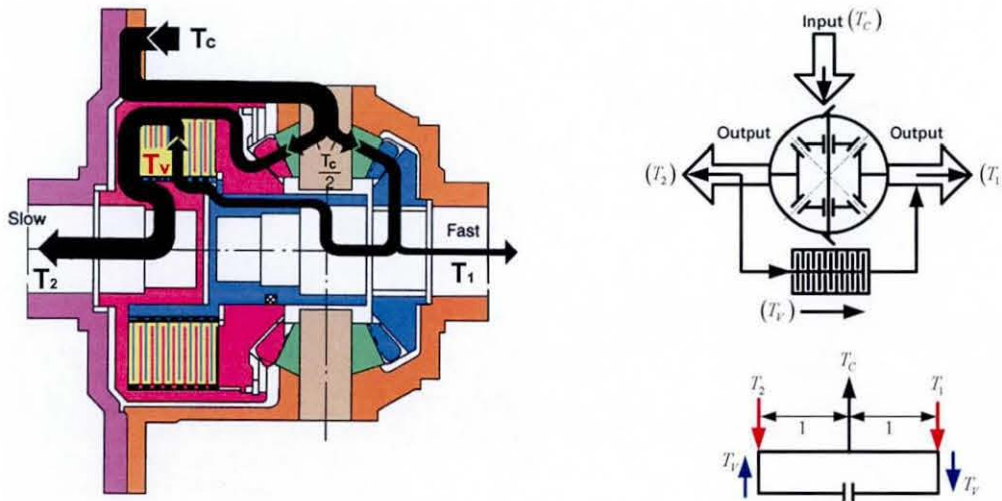


Figure 6.2 Viscous Control Differential with Shaft-To-Shaft Arrangement

By solving equations (6.6) and (6.7), expressions for the axles' torques (T_1) and (T_2) can be obtained as follows:

$$T_1 = \frac{T_c}{2} - T_v \quad (6.8)$$

$$T_2 = \frac{T_c}{2} + T_v \quad (6.9)$$

$$T_v = \frac{|T_2 - T_1|}{2} \quad (6.10)$$

For the purpose of comparison between the two aforementioned arrangements and for a given speed difference, the shaft-to-shaft layout has approximately three times the locking torque of the shaft-to-carrier design. It is, therefore, the preferred arrangement for applications in which sufficient space is available and a high torque is to be transmitted.

If the viscous unit is assumed to have a torque capacity (K) in $\left(\frac{kN \cdot m}{rad/s}\right)$, given at certain operating conditions where side-1 is fully slipping and side -2 is completely stationary, then, as an example of calculation, the axles' torque may be found as:

– For Shaft-To-Carrier Layout:

$$\left. \begin{array}{lll} \omega_2 = 0 & \omega_1 = 2\omega_c & \Delta\omega = |\omega_2 - \omega_c| = \omega_c \\ T_2 = K \cdot \omega_c & T_1 = 0 & Torque\ Bias = |T_2 - T_1| = K \cdot \omega_c \end{array} \right\} \quad (6.11)$$

– For Shaft-To-Shaft Layout:

$$\left. \begin{array}{lll} \omega_2 = 0 & \omega_1 = 2\omega_c & \Delta\omega = |\omega_2 - \omega_1| = 2\omega_c \\ T_2 = 2K \cdot \omega_c & T_1 = 0 & Torque\ Bias = |T_2 - T_1| = 2K \cdot \omega_c \end{array} \right\} \quad (6.12)$$

6.1.2 Viscous Control Differentials with Non-Equal Torque Distribution:

As previously mentioned, an ordinary mechanical differential with straight bevel gears cannot bias torque between its output axles. However, in certain situations to improve the driving capabilities, it is required to statically split the driving torque between the axles. Under such a condition, angular bevel gears or a planetary gear set can provide torque split features as shown in figure 6.3. This feature of static torque split is normally adhered to the central distribution element between the axles such as in a transfer-case or a central differential.

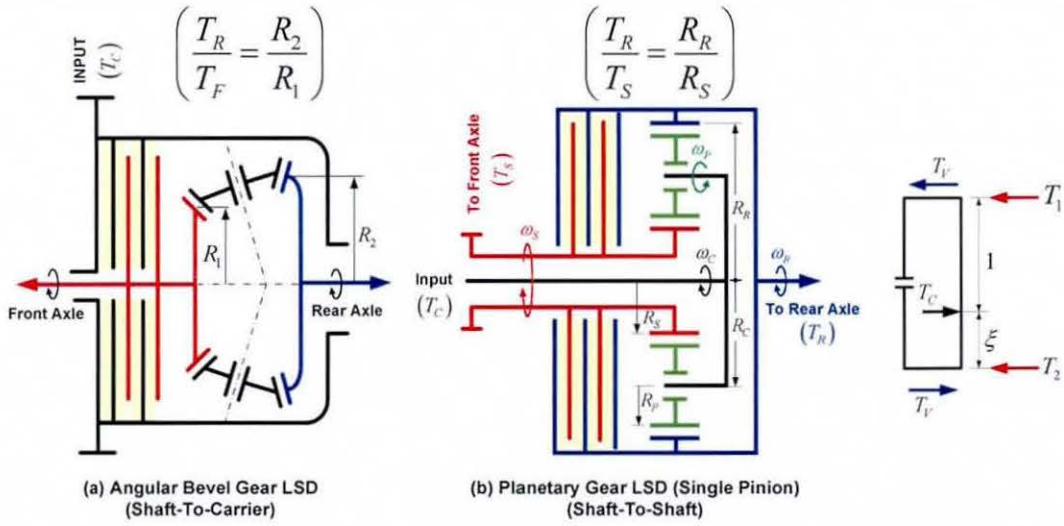


Figure 6.3 Viscous Control Differentials with Non-Equal Torque Distribution

Planetary gear (single pinion) is commonly used as a centre differential to mechanically split the driving torque between the front and rear axles. The viscous unit is installed between the sun gear (connected to the front axle) and the ring gear (connected to the rear axle) to control excessive slip between front and rear axles as illustrated in figure 6.3.

The planetary gear imposes two kinematic and two geometric constraints on the three connected axes and the fourth constraint; the internal wheel (planet): see figure 6.3.b.

$$R_C \cdot \omega_C = R_S \cdot \omega_S + R_P \cdot \omega_P \quad (6.13)$$

$$R_R \cdot \omega_R = R_C \cdot \omega_C + R_P \cdot \omega_P \quad (6.14)$$

$$R_C = R_S + R_P \quad (6.15)$$

$$R_R = R_C + R_P \quad (6.16)$$

In terms of the ring-to-sun gear ratio ($\xi_{RS} = R_R / R_S$), the key effective kinematic constraint is given as:

$$(1 + \xi_{RS}) \cdot \omega_C = \omega_S + \xi_{RS} \cdot \omega_R \quad (6.17)$$

The four degrees of freedom are reduced to two independent degrees of freedom, therefore, the input torque is distributed between the front and rear axles as follows:

$$\frac{T_R}{T_F} = \frac{R_R}{R_S} = \xi_{RS} \quad (6.18)$$

Referring to equation (6.18), the ratio of torque split between the rear and front axles is statically fixed and can be determined from the ratio of the ring-to-sun gear diameters.

Due to the effect of viscous unit (shaft-to-shaft), torque distribution between the front and rear axles can be dynamically varied according to the speed difference. Assume (ξ) to be the torque split ratio, given by:

$$\xi = \frac{\text{Split Output Torque 1}}{\text{Split Output Torque 2}} \quad (6.19)$$

For example, a differential with a mechanical split ratio (38:62) % between front and rear axle ($\xi = 0.619$). The output torque applied to the output axles can be calculated as:

$$T_1 = \left(\frac{\xi}{1+\xi} \right) \cdot T_C - T_V \quad (6.20)$$

$$T_2 = \left(\frac{1}{1+\xi} \right) \cdot T_C + T_V \quad (6.21)$$

It should be noted that, for a conventional straight bevel gear differential, the split ratio between its outputs is (50:50) % with a mechanical split ratio of ($\xi = 1.0$) equations (6.20) and (6.21) are reduced to equations (6.8) and (6.9) respectively.

6.1.3 Permanent Wheel Drive with Viscous Coupling Transmission

To demonstrate the implementation of viscous coupling transmission in permanent AWD drivetrain, a simplified model is derived as follows, see figure 6.4.

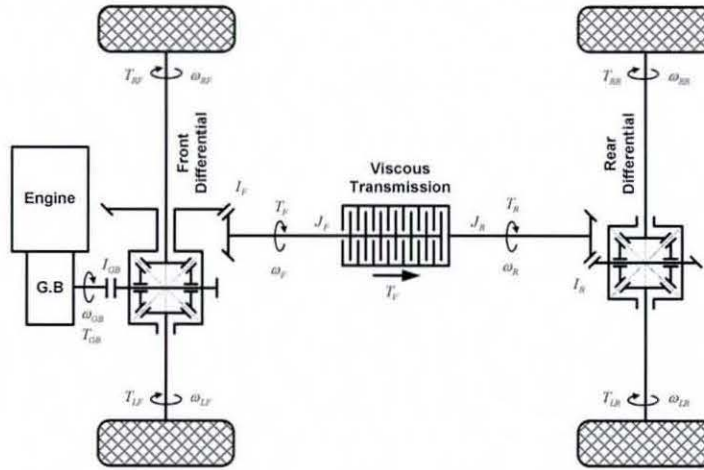


Figure 6.4 Permanent Drivetrain System with Viscous Coupling Transmission

Gear box:

$$\left. \begin{aligned} T_{GB} &= \left(\frac{T_{RF} + T_{LF}}{I_{GB}} \right) + \left(\frac{T_F}{I_{GB} \cdot I_F} \right) \\ \omega_{GB} &= \left(\frac{\omega_{LF} + \omega_{RF}}{2} \right) \cdot I_{GB} \end{aligned} \right\} \quad (6.22)$$

Front open differential:

$$T_{RF} = T_{LF} = 0.5 \cdot (T_{GB} \cdot I_{GB} - T_F / I_F) \quad (6.23)$$

Front propeller shaft:

$$\left. \begin{aligned} T_F &= J_F \cdot \dot{\omega}_F + T_V \\ \omega_F &= \left(\frac{\omega_{GB}}{I_{GB} \cdot I_F} \right) = \left(\frac{\omega_{LF} + \omega_{RF}}{2 \cdot I_F} \right) \end{aligned} \right\} \quad (6.24)$$

Rear propeller shaft:

$$\left. \begin{aligned} T_R &= T_V - J_R \cdot \dot{\omega}_R \\ \omega_R &= \left(\frac{\omega_{LR} + \omega_{RR}}{2 \cdot I_R} \right) \end{aligned} \right\} \quad (6.25)$$

Rear open differential:

$$T_{RR} = T_{LR} = \left(\frac{T_R \cdot I_R}{2} \right) = \left(\frac{T_V - J_R \cdot \dot{\omega}_R}{2} \right) \cdot I_R \quad (6.26)$$

Viscous coupling:

$$T_V = \mathbb{F}(|\omega_F - \omega_R|) \quad (6.27)$$

The viscous shear torque (T_V) is calculated according to the models derived earlier in chapter (5), which are functions of the differential speed between the front and rear propeller shafts, as well as the design parameters of the viscous coupling unit.

Figures 6.5 and 6.6 illustrate the traction performance of an AWD vehicle, incorporating a viscous coupling transmission. The drivetrain layout is depicted in figure 6.4. The simulation is carried out at full throttle position during acceleration in a straight line manoeuvre on firm clay soil. The throttle increases until the engine speed reaches its maximum value, at which stage the gearbox is shifted to a higher gear (lower ratio).

Compared to the results obtained in section 4.4.1, see figure 4.11, it is obvious that the difference between the tractive forces developed at the front and rear axles are not constant, see figure 6.5.b. This can be best explained by observing the shear torque characteristics as shown in figure 6.6.b, and its strong dependency on fluid viscosity figure 6.6.a. Initially, in first gear, a high speed difference between the front and rear axles is noted, figure 6.6.d, due to different resisting moments applied at each tyre. Therefore, a high rate of shear torque is transferred to the rear axle via the viscous coupling unit, figure 6.6.b. An equivalent amount of heat is generated which is proportional to the rate of shearing torque. This has as its consequence an increase in fluid temperature, figure 6.6.c, thus reducing the apparent viscosity in a similar manner, figure 6.6.a.

In general, acceleration is higher in first gear, which is characterized by its higher gearing ratio, whereas acceleration decreases as the gear is up-shifted. Therefore, the differential rotational speed across the viscous coupling and hence the shear torque is reduced by a similar rate. On the other hand, the noticeable reduction in the apparent viscosity has its consequence on the reduction in shear torque. The combined effect of gear up-shifting and lowering of viscosity result in eliminating the difference between the tractive forces at the front and rear axles.

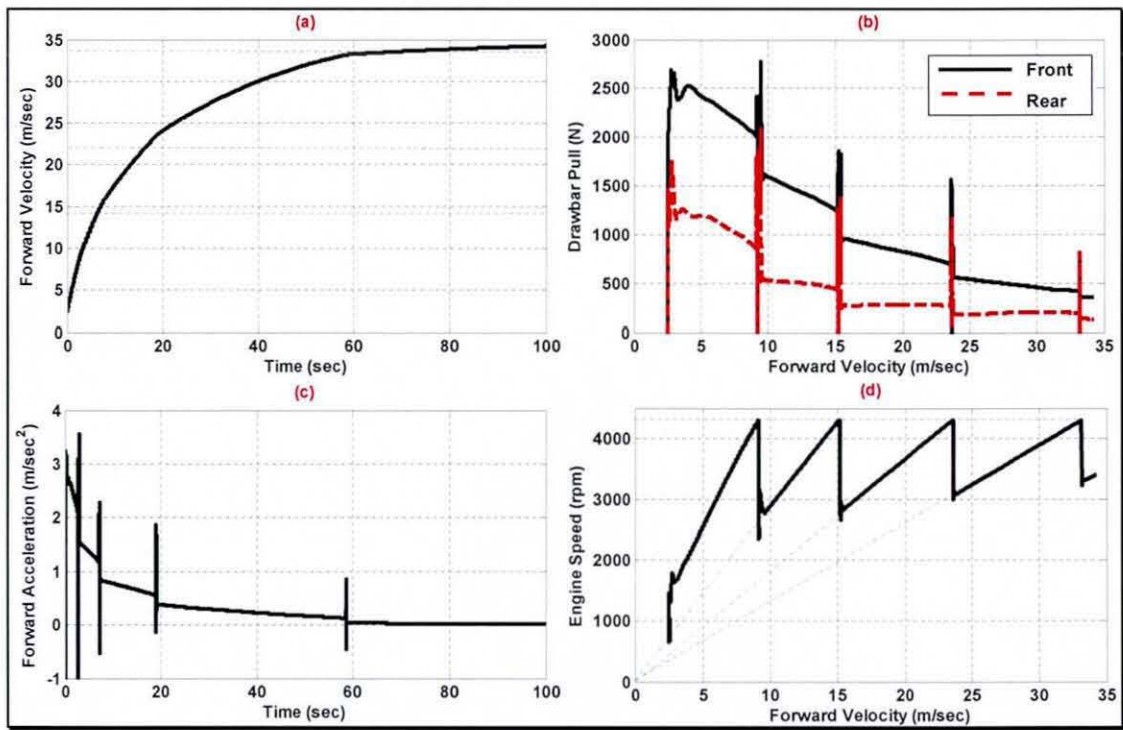


Figure 6.5 Traction Performance of the Vehicle Fitted with Viscous Coupling

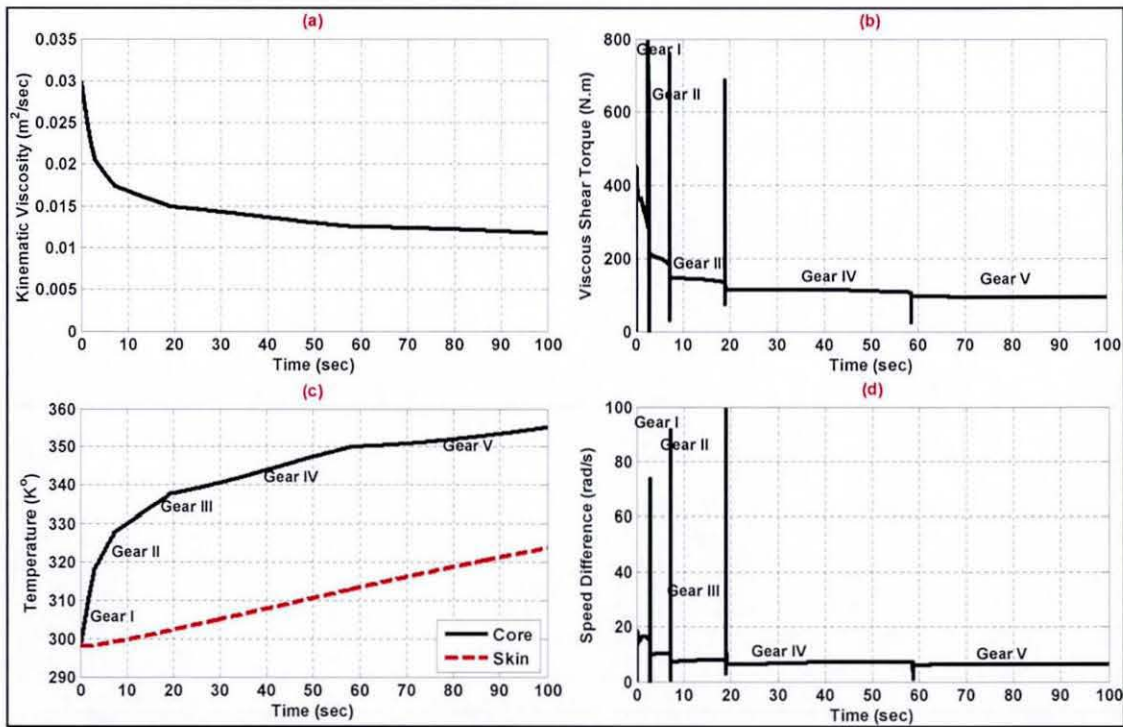


Figure 6.6 Viscous Coupling Operational and Torque Characteristics

For the purpose of the present investigation, a special library is created including custom-made blocks, representing the different mechanical and visco-lock torque distribution devices. In addition to open and mechanically locked ordinary differentials, a mechanical transfer-case is modelled to statically split the driving torque from the gear-box between the front and rear axles, see figure 6.7. The derived library is implemented using a new toolbox called SimDriveline, which is a part of Simulink Physical Modelling, encompassing the modelling and design of systems according to basic physical principles.

With the derived library, it is possible to simulate any drivetrain configuration. The concepts of modularity, flexibility, and user-friendliness were emphasized during the model development. The viscous coupling unit forms the heart of all these units, which are successfully linked with the drivetrain system developed in chapter 4.

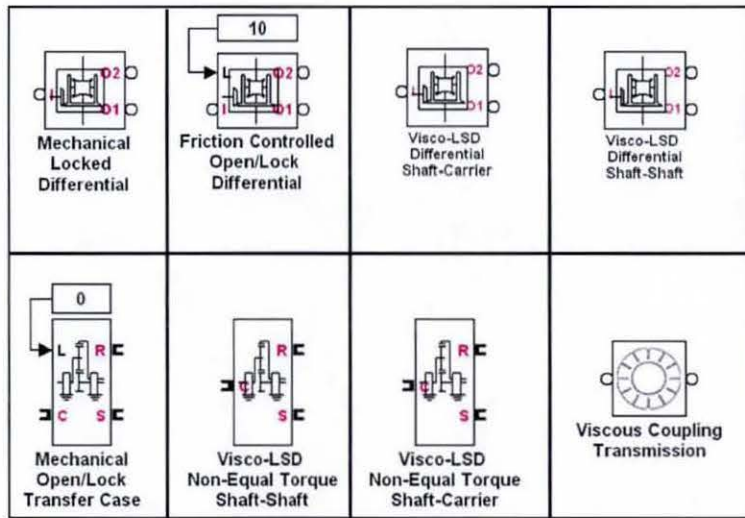


Figure 6.7 Physical Simulation Library of Visco-Lock Devices

6.2 Evaluation Criteria

While there are plenty of established criteria which are developed to evaluate vehicle behaviour over prepared roads of solid construction, for 4x4 off-road vehicles, there are limited investigations to evaluate the entire vehicle behaviour over soft soils. Furthermore, most of the reported relevant investigations are devoted to the prediction and optimization of vehicle behaviour from point of view of traction only, ignoring the

critical consequence on directional stability. It is anticipated that the cornering response of these vehicles may be different from on-road vehicles. Furthermore, vehicle side-slip and yaw motions are dependent on the driving torque distributed between the axles/wheels, as well as the mechanical properties of the terrain.

A methodology for comparison of longitudinal performances, as well as lateral stability of AWD vehicles is introduced and implemented into the overall model. The results of this virtual evaluation method would assist in optimizing AWD vehicle performance in terms of drivetrain architectural choice and component specifications.

6.2.1 Traction Criterion

Over the years, different criteria have been developed to evaluate traction performance of off-road vehicles, depending on the vehicle functional requirements. In chapter 4, section 4.4.1, a method was introduced to assess the traction performance in terms of maximum speed, acceleration, speeding-up time and speeding-up distance. While this method is adequate to predict the traction capabilities for a specific power plant and given transmission characteristics, it is observed that, limitations are encountered in differentiating between various drivetrain configurations, see figure 4.15. Therefore, it is of prime interest to employ different criteria, which would provide the opportunity to investigate the traction characteristics over the entire range of tyres longitudinal slip.

Based on the efficiency calculation of the power transmitted from the engine to the driven wheels, Wong et al. (1970, 1998b, 2000, 2001) presented a validated criterion for predicting the tractive performance of cross-country vehicles. In this section Wong's methodology is briefly highlighted, in addition to some results of its implementation in the current vehicle model.

6.2.1.1 Drawbar Pull Characteristics

Drawbar pull (F_d) is defined as the force available at the drawbar, and is equal to the difference between the total tractive forces developed by the driving wheels and the total driving resistance as follows:

$$F_d = \sum_{i=1}^4 F_{xi} - \sum R \tag{6.28}$$

Where: $(\sum R)$ is the total resisting force acting on the off-road vehicle, including the rolling resistance of the tyres, resistance due to vehicle-terrain interaction, grade resistance, as well as aerodynamic drag. The rolling resistance of the tyre consists of an internal component caused by the flexing work of the tyre (due to hysteresis losses) and an external component caused by soil deformation or compaction (Wong, 2001).

It should be mentioned that, the employed off-road tyre model internally calculates the net tractive force by considering the internal resistance of the tyre and the resistance due to tyre-terrain interactions such as resistance due to compaction of the terrain and the bulldozing effect. In this case the resisting force $(\sum R)$ is reduced to the aerodynamic drag and grade resistance.

Also, in cross-country operations the maximum tractive effort is often limited by the shear characteristics of the tyre-terrain interaction. Furthermore, the development of thrust often results in considerable slip over unprepared terrain, thus the drawbar pull and vehicle speed are functions of slip. The product of the drawbar pull and the vehicle speed is usually referred to as the drawbar pull power: $(P_d = F_d \cdot V)$

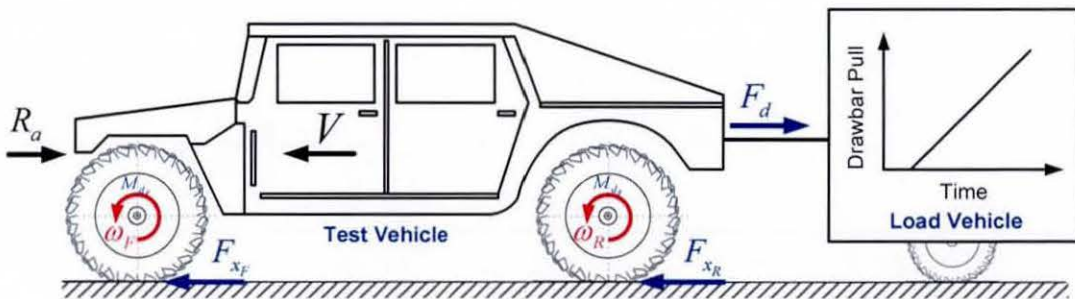


Figure 6.8 Concepts of Tractive Forces–Slip Characteristics Measurement

In reality and for the purpose of measuring tractive forces over entire range of longitudinal slip, a drawbar load is applied by pulling a loaded vehicle as depicted in figure 6.8. The drawbar hitch was set at a low level to minimize load transfer effects between the axles. By shifting gear in the transmission and by applying brakes to the

loaded vehicle, different drawbar loads are experienced. The driver of the test vehicle applies the throttle pedal such that the engine revolutions and hence the vehicle speed is maintained, noting that normally a low speed (around 15 km/h) is desired to eliminate dynamic effects. By measuring the drawbar pull, the driving torques applied on the front and rear axles, the angular speeds (or displacements) of the front and rear tyres, the ground speed (or distance travelled) of the vehicle, the tractive force-slip characteristics can be obtained.

The numerical simulation of the aforementioned procedures involves adding a slowly growing towing capacity with time for the vehicle, driven at a low constant speed of 15 km/h in the lowest gear as shown in figure 6.8. The test is terminated, when full wheel slip is considered to have reached. The advantage of this test is that it provides a complete picture of traction performance over the entire range of tyre longitudinal slip. To keep the vehicle speed constant, a PID controller is employed, which controls the engine torque through the proper position of the throttle pedal. As the towing load increases, the engine torque also increases, as well as the tractive force. The relationship between the tractive force and longitudinal slip for each tyre can then be plotted as shown in figure 6.9.

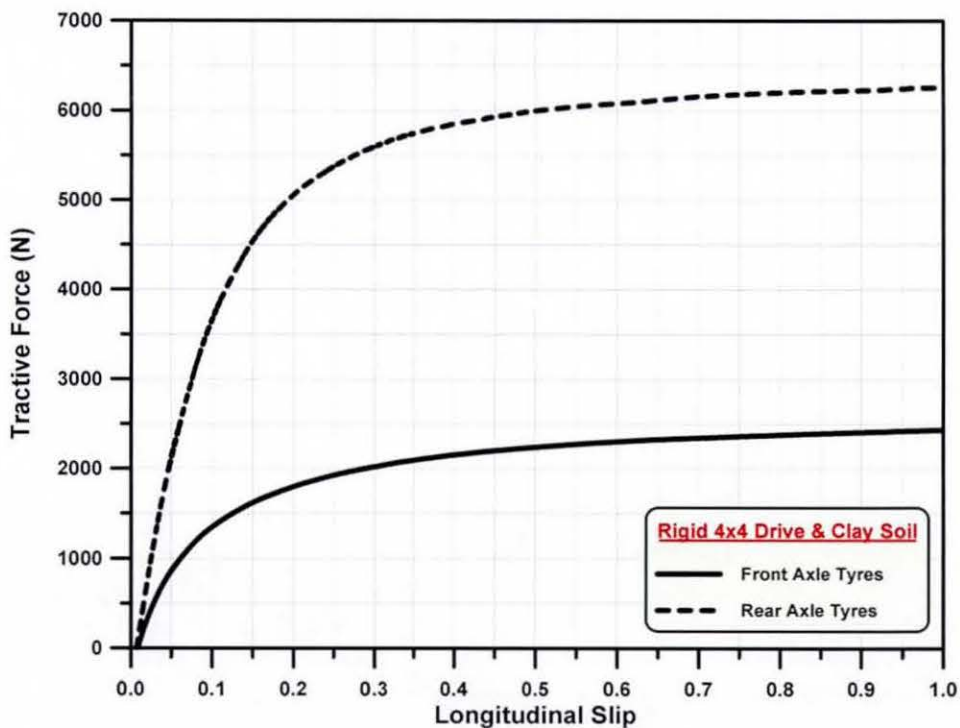


Figure 6.9 Tractive Force–Slip Characteristics (Locked Centre Differential on Clay Soil)

6.2.1.2 Tractive Efficiency

The tractive efficiency (η_d) of a wheeled vehicle under constant speed and straight line motion conditions on horizontal ground may be expressed as:

$$\eta_d = \eta_t \cdot \eta_s \cdot \eta_m \quad (6.29)$$

Transmission Efficiency (η_t): represents the efficiency of the transmission, which characterizes the losses in power from the engine to the driven wheels, given as follows:

$$\eta_t = \left(\sum_{i=1}^4 M_{di} \cdot \omega_i \right) / (M_E \cdot \omega_E) \quad (6.30)$$

Slip Efficiency (η_s): represents the efficiency, which characterizes the power losses and also the reduction in forward speed of the vehicle due to slip of the driven wheels. This part of the power dissipates through the sliding of the tyre relative to the terrain surface and internal shearing of the terrain between the tyre lugs. The slip efficiency not only affects the drawbar power, but also closely relates to tyre wear. Usually, slip is a major source of power loss during the operation in the field. In general, the slip efficiency can be determined from the ratio of power loss due to slip to the power available at the driven wheel. For a 4WD vehicle, the slip efficiency may be calculated as:

$$\eta_s = 1 - \left(\frac{i_f \cdot M_{df} \cdot \omega_f + i_r \cdot M_{dr} \cdot \omega_r}{M_{df} \cdot \omega_f + M_{dr} \cdot \omega_r} \right) \quad (6.31)$$

Motion Efficiency (η_m): represents the efficiency which is a measure of losses incurred in transforming the available driving torque at the driven wheels (M_{di}) to that successfully pulled at the drawbar (F_d).

$$\eta_m = \left(\sum_{i=1}^4 F_{xi} - \sum R \right) / \left(\sum_{i=1}^4 \frac{M_{di}}{r_{di}} \right) \quad (6.32)$$

Figures 6.10 and 6.11 show the variation of efficiency and longitudinal slip with drawbar pull. The simulation is carried out for a rigid-drive 4×4 vehicle on firm clay and wet loam soils respectively. It is observed that, motion efficiency reflects the ability of the soil (in terms of shear and sinkage properties) to support the thrust force, while slip efficiency reflects the utilization of the distributed torque to propel the vehicle forward.

Another interesting conclusion can be derived from equation (6.31) that when the slip of either the front or rear wheels reaches 100% the slip efficiency and the tractive efficiency fall to zero. Furthermore, the maximum slip efficiency is only achieved when the slip ratio of the front axle (i_f) is equal to the slip ratio of the rear axle (i_r). At this moment the slip efficiency is no longer affected by the torque distribution between the front and rear axles. In other words, the optimum torque distribution is that which makes both the front and rear axle tyres to attain the same slip ratio.

By comparing the results obtained in figures 6.10 and 6.11, it is obvious that, for the same concept of a drivetrain, higher maximum values of drawbar pull and tractive efficiency can be observed in the case of clay soil. This may be due to the higher shearing strengths and lower sinkage properties of clay soil, when compared to the loamy soil. These mechanical properties essentially affect the motion efficiency which is equal to (0.9) in the case of clay soil, and (0.756) in the case of loam soil.

6.2.2 The Handling Criterion

A typical off-road AWD vehicle with a ramp-steer manoeuvre, at a constant forward speed of 75 km/h, is considered to assess its handling performance. The steer-angle is gradually increased, whilst driving on a deformable clay soil. The vehicle's response in terms of lateral acceleration is calculated and plotted against the commanded steer angle in order to obtain a picture of its handling performance (Wong, 2001).

It should be noted that the vehicle is considered to understeer when the slope of the generated curve is greater than that for the neutral steering case, and to oversteer when the slope is less than the same.

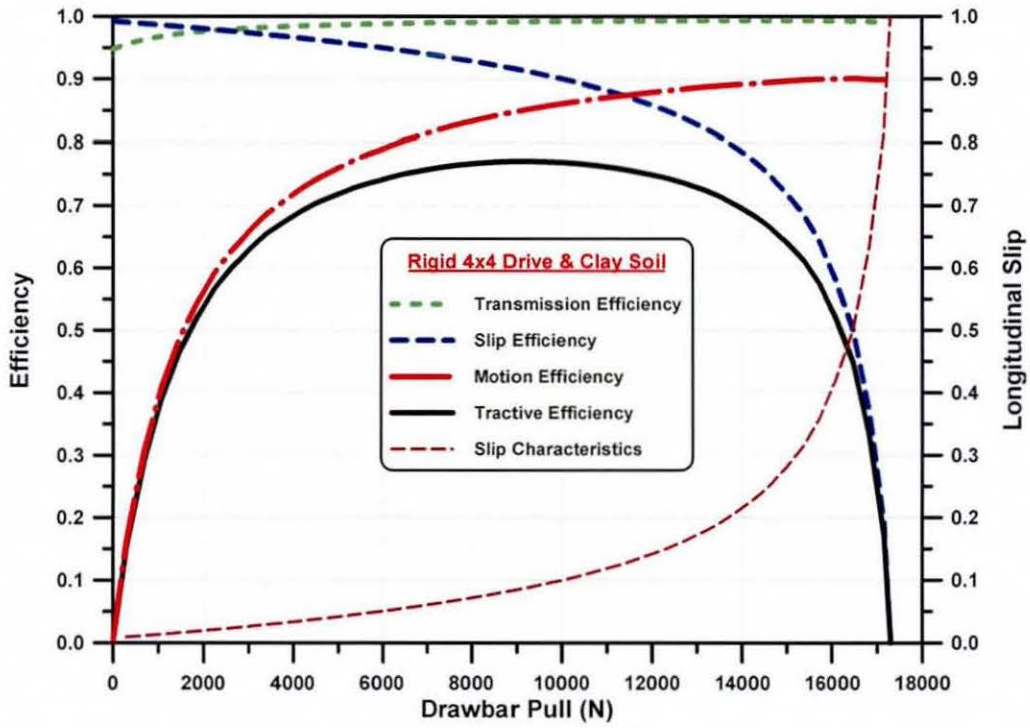


Figure 6.10 Variation of Tractive Efficiency with Drawbar Pull on Clay Soil

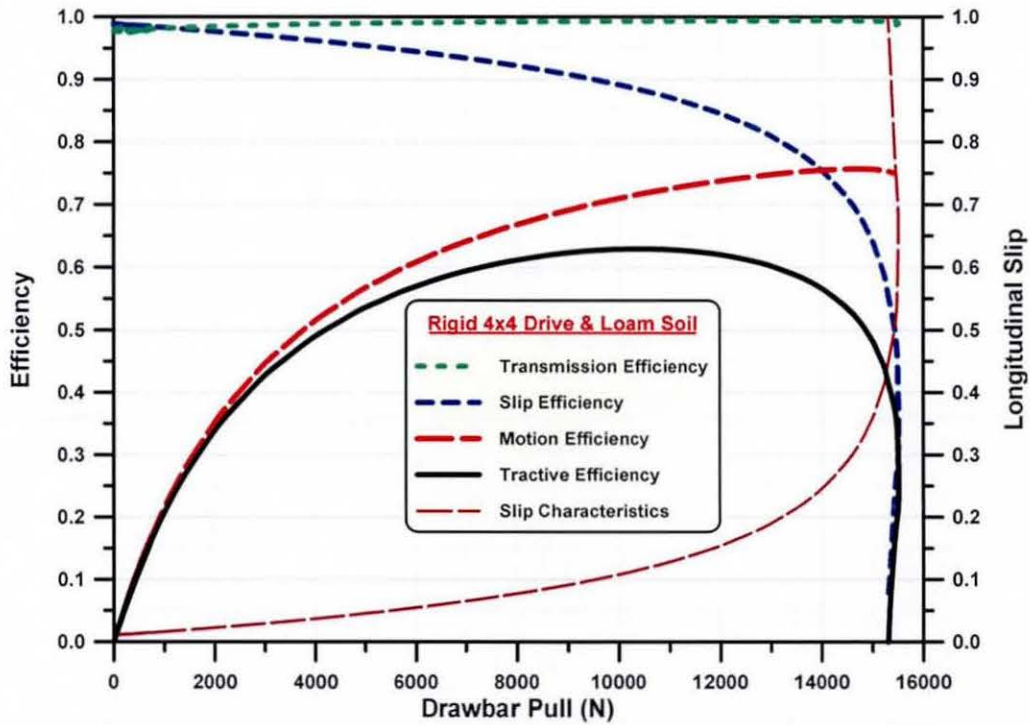


Figure 6.11 Variation of Tractive Efficiency with Drawbar Pull on Loam Soil

6.3 Result and Analysis

With regard to the aforementioned criteria, both the traction capability and the directional stability of a typical 4×4 vehicle are investigated. The vehicle's main design parameters are kept the same as before, except for the way the driving torque is distributed between the axles. The inflation pressure is assumed to be 1 bar for all tyres. The static weight distribution between the front and rear axles is (40:60%) respectively.

Simulation results for a visco-lock device include viscous coupling and a visco-lock differential are plotted and compared with ordinary mechanical devices such as a differential (open/locked), as well as the transfer-case with a mechanically biased torque.

6.3.1 Different Drivetrain Configurations:

Before discussing the influence of torque distribution devices on the performance of a 4×4 off-road vehicle, it would be helpful to highlight the significant consequences of static weight distribution between the front and rear axles.

When the vertical load, applied on a tyre increases, both the contact area and ground pressure increase accordingly. Consequently, the maximum soil shear strength and thus the circumferential force developed by the tyre are enhanced. This increases the ability of the tyre to develop additional driving forces without causing excessive slip. On the other hand, when the tyre vertical load is increased, both the tyre sinkage and rolling resistance also increase.

Handling characteristics are affected by sinkage due to additional lateral forces generated at the tyre sidewalls. At higher sinkage, significant tyre sidewall forces may occur, which can be explained by the soil cutting theory (Wong, 2001). According to this theory a stress field occurs in the soil, based on passive soil failure, which is developed using the Mohr's circle technique. This additional lateral force is determined by integrating the passive soil pressure over the tyre sidewall for a given sinkage distribution of the tyres.

In general, the reference vehicle has more weight on its rear axle, and due to these effects, the resulting equivalent cornering stiffness is higher than that developed at the front axle. Consequently, the under-steer coefficient is increased and the vehicle becomes more under-steering with a increased turning radius and a reduced yaw velocity.

The effects of different concepts of drivetrain, for the same vehicle, on both traction performance and handling responses are depicted in figures 6.12 to 6.14. To have an expressive designation of different drivetrain configurations, a set of letters are appointed to differentiate between each case. The symbol 'O' stands for open differential, 'L' for mechanically locked differential, 'VC' for viscous coupling transmission, 'LSD(SS)' for visco-lock limited slip differential shaft-to-shaft layout, 'LSD(SC)' for visco-lock limited slip differential shaft-to-carrier layout, 'FWD' for front wheel drive and 'RWD' for rear wheel drive.

Open Central-Differential (O-O-O):

The main characteristic of this type of drivetrain is that the ratio of angular velocity of the front wheels to that of the rear wheels may vary depending on the operating conditions, but the ratio of the torque distribution between the front and rear wheels is invariable and limited by the lowest traction side (carrying the least weight). Therefore, drivetrain torsional wind-up never occurs under any conditions. This means that a rigid driveline model used is justified, unless impulsive conditions due to lash take-up takes place, which is outside the remit of this research and is adequately covered by Menday (2003) and Gnanakumarr (2004). Nevertheless, both the maximum drawbar pull and the tractive efficiency still depend on the slips of both front and rear wheels and will only be high if these are equal. In order to achieve high operational efficiency, the weight distribution and other factors should be carefully controlled.

For equal torque distribution, and assuming equal dynamic radii for the front and rear tyres, the rear axle-tyres are subjected to higher rolling resistance due to higher vertical weight and sinkage. As a result, both the longitudinal slip and tractive force at the front axle-tyres will be higher than those developed at the rear axle-tyres. Consequently, the generated lateral forces at the rear axle will be higher than those at the front axle. On the

other hand, the lateral load transfer from inward wheels to those at the outside during cornering causes a considerable increase in the tractive force at the inside. The combined effect results in a greater tendency to understeer, especially at high lateral accelerations, see figure 6.14.

Locked Central-Differential (O-L-O):

The main characteristic of this type of drivetrain is that the ratio of angular velocity of the front wheels to that of the rear wheels is invariable, but the ratio of the torque distribution between the front and rear wheels may vary depending on operating conditions. Under the assumption of equal dynamic tyre radii for the front and rear tyres, they would be forced to rotate at the same rotational driving speed (theoretical speed), thus the slip of all tyres would equate and would be regulated by that of the tyre with the most traction. Therefore, the slip values at all four corners are automatically adjusted in favour of traction and the vehicle performance is no longer affected by its weight distribution, see figure 6.12.

However, under given steering conditions, the kinematics of the vehicle require that the front and rear wheels follow different paths with different translational speeds. In this case, tractive slip at the front will reduce and skidding might occur in extreme cases, with the subsequent generation of braking forces at the front. On the other hand, the rear wheels slip, generating a forward thrust. Under these circumstances, torsional wind-up in transmission occurs, resulting in premature failure of the driveline components and/or excessive wheel slippage depending on tyre-soil conditions (Wong, 2001).

For lower shear strength or slippery soils, the wind-up torque results in an excessive slippage and tyre wear. For higher shear strength soils or rigid roads, the wind-up torque exerts so much stresses on the drivetrain shafts and gears in addition to undesirable resistance sensed by the steering wheel. This may also affect the structural performance of driveshaft tubes, meaning that an elastodynamic model of these may be required.

The rear axle with a larger weight and, therefore, relatively higher shear strength would be able to develop a larger driving torque than the front axle. The slip at the front is limited by the slip at the rear and the front tyres improve their potential of lateral force

generation. This shifts the handling behaviour towards less understeer, when compared to that achieved by the open central differential configuration, see figure 6.14.

Visco-Lock Devices:

The common feature of such devices is that the torque cannot be transmitted unless there is a speed difference between the input and output shafts. Therefore, these are termed speed sensitive devices. In other words, visco-lock devices act as a passive traction control system to regulate torque distribution between the axles according to the speed (or slip) difference between them. If the speed difference between the axles increases, visco-lock devices bias or transfer more torque to the side with a lower speed (i.e. the front axle). The effect is, therefore, to deliberately introduce a ratio (smaller than unity) for the theoretical speed of the front wheel to that of the rear. This ratio can be tuned or optimised according to the viscous unit design parameters (as described later) to meet the required characteristics.

For the viscous coupling layout (O-VC-O) the vehicle behaviour, to a great extent, depends on the way the viscous coupling is installed in the drivetrain. For this analysis, the driving torque from the engine is primarily directed to the rear axle. This torque is transferred to the front axle via the viscous coupling unit. This arrangement would improve the traction performance, especially at higher values of longitudinal slip, see figure 6.12.

For the visco-lock differentials layout the effect of a viscous control unit at the central differential, shaft-to-shaft (O-SS-O) or shaft-to-carrier (O-SC-O), is considerably less severe than that of a viscous coupling transmission (O-VC-O) for direct torque transfer. However, even this rather “soft” characteristics result in a substantial improvement in the traction performance compared with the ordinary open central differential configuration. It should be noted that, for a given speed difference, the shaft-to-shaft layout exhibits approximately three times the locking torque of the shaft-to-carrier design. It, therefore, represents the preferred option for applications in which sufficient space is available and a high torque is to be transmitted, see figure 6.12.

The handling characteristics provided by visco-lock devices are similar to that of the vehicle fitted with open differentials. In addition, it depends not only on the amount of viscous torque, but also on the way that the viscous unit is installed. However, because there is no rigid connection between the axles (like a viscous transmission), the tyres are still free to rotate with different velocities, so the problem of drivetrain wind-up is minimized.

When the vehicle corners at 75 km/h, the transmitted torque by the visco-lock device is relatively small, since the speed differences imposed on the output shafts are small. Figure 6.14 shows the effect of different scenarios with visco-lock devices on the handling characteristics.

It should be noted that, the speed difference across the axle differentials increases with lateral acceleration. At higher lateral accelerations the angular speed of the inner wheels begins to increase due to the additional lateral and traction forces imposed on the tyres in relation to the reducing vertical load. Moreover, the rear outer wheel, which experiences the highest vertical load, begins to slow down due to a combination of lateral weight transfer and a large slip angle at the rear axle. This generates a very high rolling resistance, which eventually exceeds the traction applied to the wheel. As a result of these effects, the handling characteristics become more sensitive particularly in the case of (O-VC-O).

Additional results are depicted in figure 6.13, revealing the effect of soil mechanical properties on the maximum drawbar pull for different drivetrain layouts. It is obvious that, clay soil, with comparatively good sinkage resistance and shearing properties, affords better opportunity for improved traction performance. Furthermore, compared to sand and loam, clay soil is less sensitive to the variation of drivetrain layouts. Since the maximum traction performance is attained using a rigid or a locked centre differential, a rating of 100% is allocated to that layout, while all other layouts are compared accordingly.

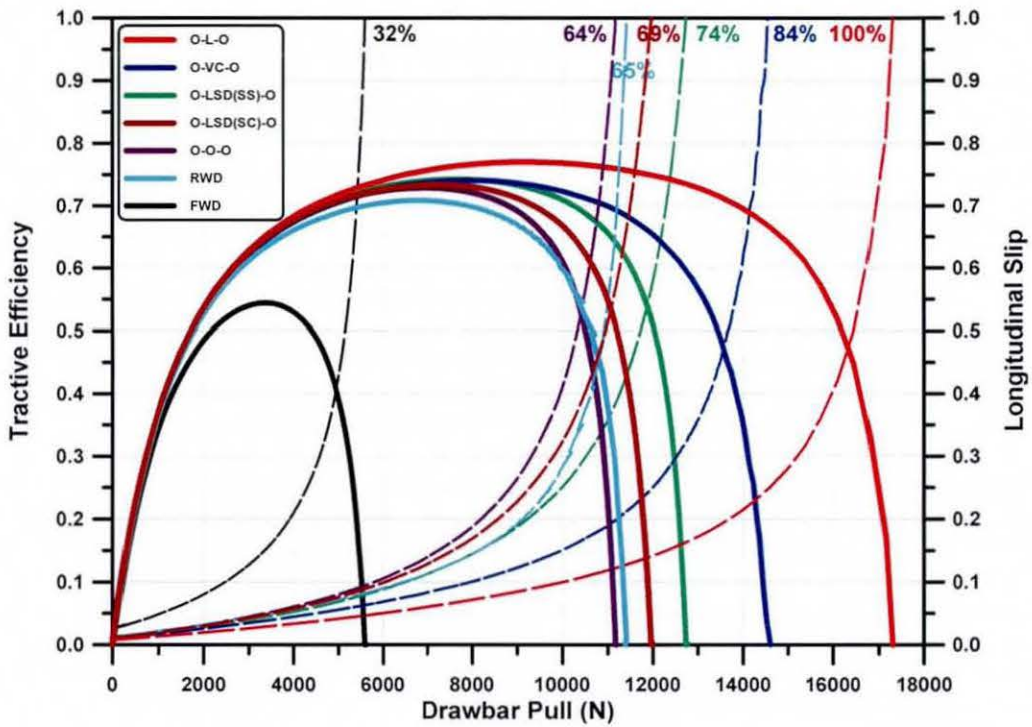


Figure 6.12 Effect of Drivetrain Layouts on Traction Performance on Clay Soil

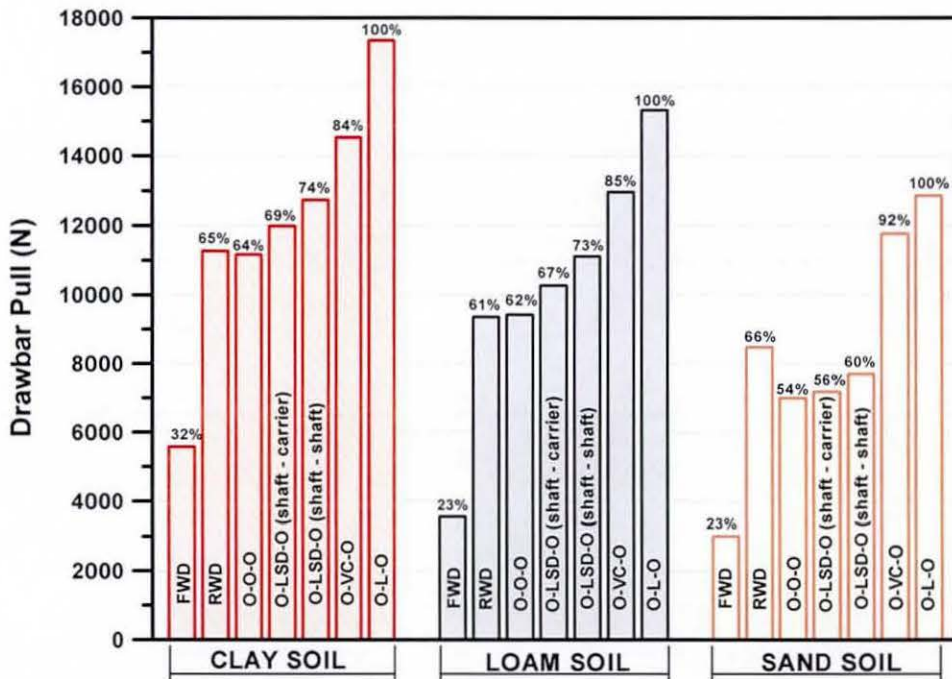


Figure 6.13 Effect of Drivetrain Layouts on Traction Performance on different Soil

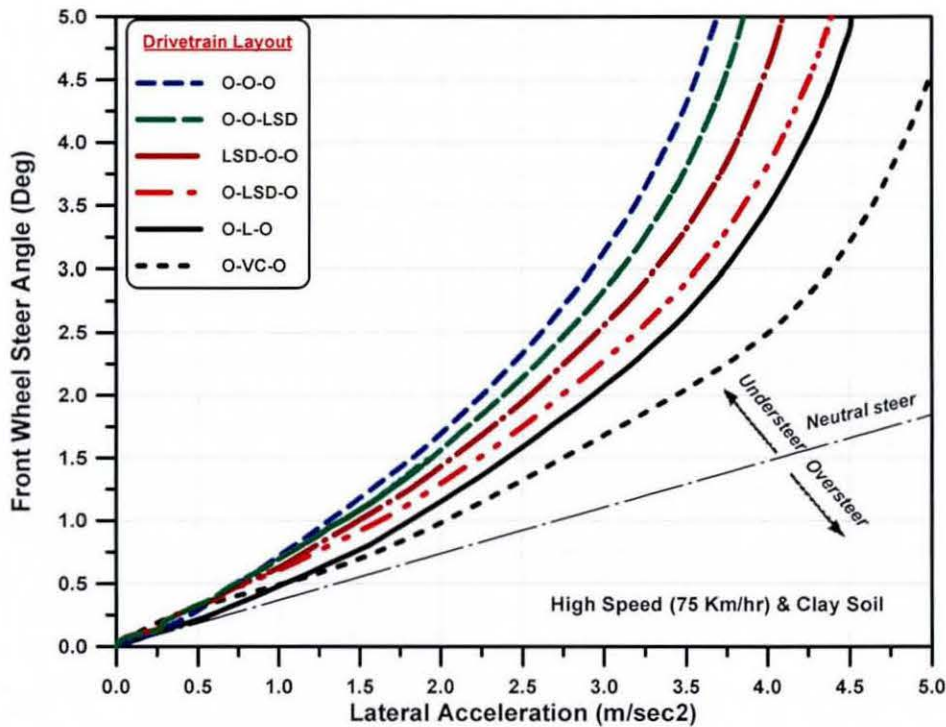


Figure 6.14 Effect of Drivetrain Layouts on Handling on Clay Soil at High Speed

6.3.2 Static Split Ratio of Driving Torque Distribution:

For the purpose of this analysis, a transfer case is used to statically split the driving torque between the axles at different fixed ratios, as explained earlier in section 6.1.2. The gear-box output is fed into a single pinion planetary gear transfer case which in turn drives, through planetary gears, the front and rear propeller shafts. The wheels are driven via a mechanical open differential. It should be mentioned that, while the transfer-case can split the torque between the front and rear axles, there is no constraint imposed on the rotational speed of these axles. This feature is mainly due to the inherent characteristics of the planetary gears. The importance in analysing the effect of static distribution of driving torque is that it improves understanding and aids optimisation of visco-lock devices.

The numerical results of the computations depicted in figures 6.15 to 6.18 reveal that, a slight variation in torque distribution between the axles causes considerable changes in traction performance, as well as the handling characteristics as described below.

From the Traction Performance View Point:

Biasing more driving torque to the axle with a greater vertical load improves the drawbar pull, as well as the tractive efficiency (particularly the slip efficiency). Since the reference vehicle has a greater weight on the rear axle, it is obvious that in order to improve the tractive efficiency, the driving torque should also be distributed in a matching manner (according to the weight distribution) as shown in figure 6.15. However, in reality, it is unacceptable to design the vehicle with a fixed scenario of weight distribution between the axles, as both static and dynamic variations in weight distribution would alter the optimum value of torque distribution between the axles.

Figure 6.16 shows a comparison of the traction performance under the different conditions for static torque split ratios on different soils. As expected, the maximum value of drawbar pull is achieved for the case of driving on clay soil. Furthermore, it seems that the split ratio of 30% on the front and 70% on the rear axle provides an acceptable level of traction over different soils. It should be pointed out that, the inefficient distribution of the driving torque not only wastes power, but also can cause excessive tyre wear.

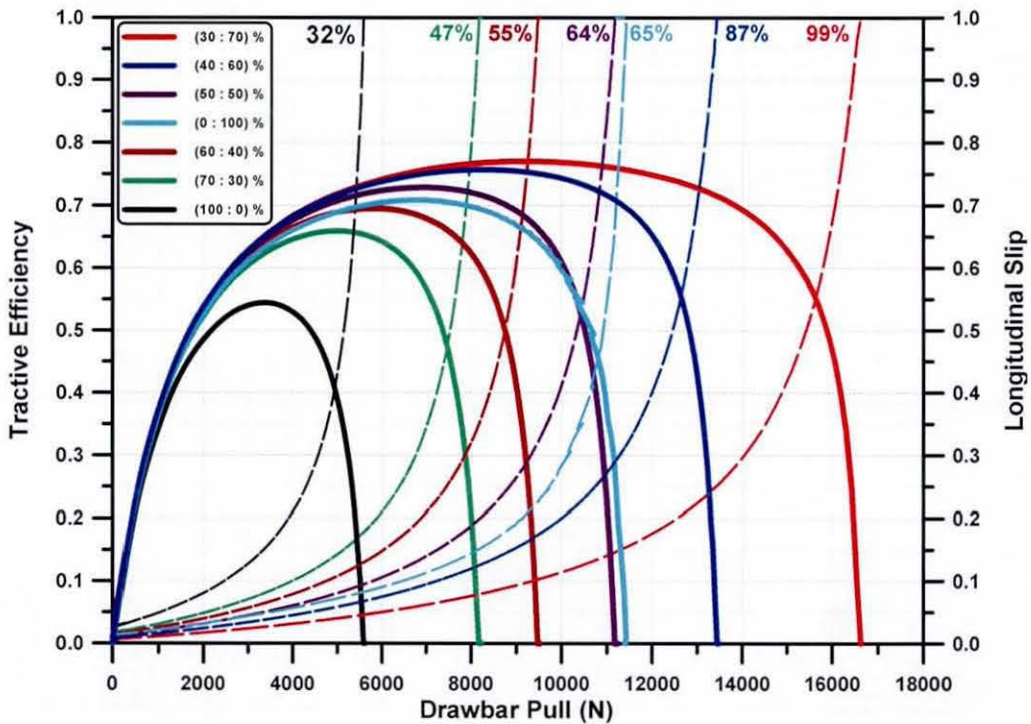


Figure 6.15 Effect of Static Split Ratio on Traction Performance on Clay Soil

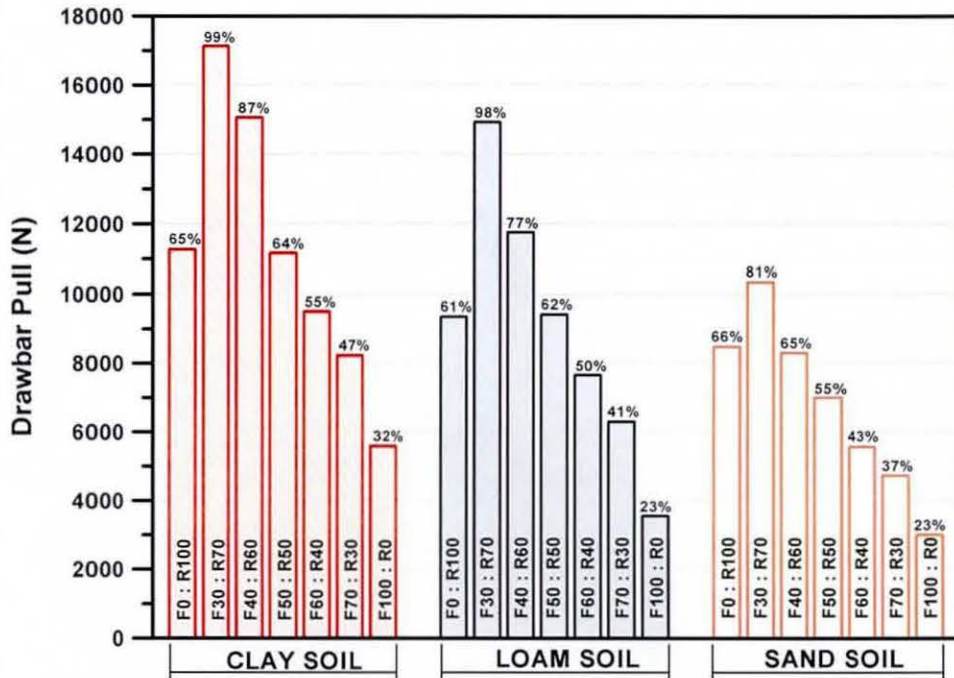


Figure 6.16 Effect of Static Split Ratio on Traction Performance on different Soils

From the Handling Characteristics View Point:

Splitting the driving torque between the front and rear axles has a serious consequence on handling characteristics. For the purpose of this analysis, the cornering response is investigated at both low speed (40 km/h) and high speed (75 km/h) during ramp-steer manoeuvre over clay soil as shown in figures 6.17 and 6.18.

The depicted results reveal that biasing more torque to the rear axle would reduce the longitudinal slip at the front and, consequently, increase the lateral force generating potential at the front. At the same time, the counteracting side force at the rear would be reduced. The additional yaw moment shifts the handling characteristics towards oversteer, a fact which in turn reduces the stability and controllability of the vehicle. While this effect is not clear for low speed cornering manoeuvres, see figures 6.17, at higher speeds the cornering response is sensitive to static torque split ratio as shown in figures 6.18.

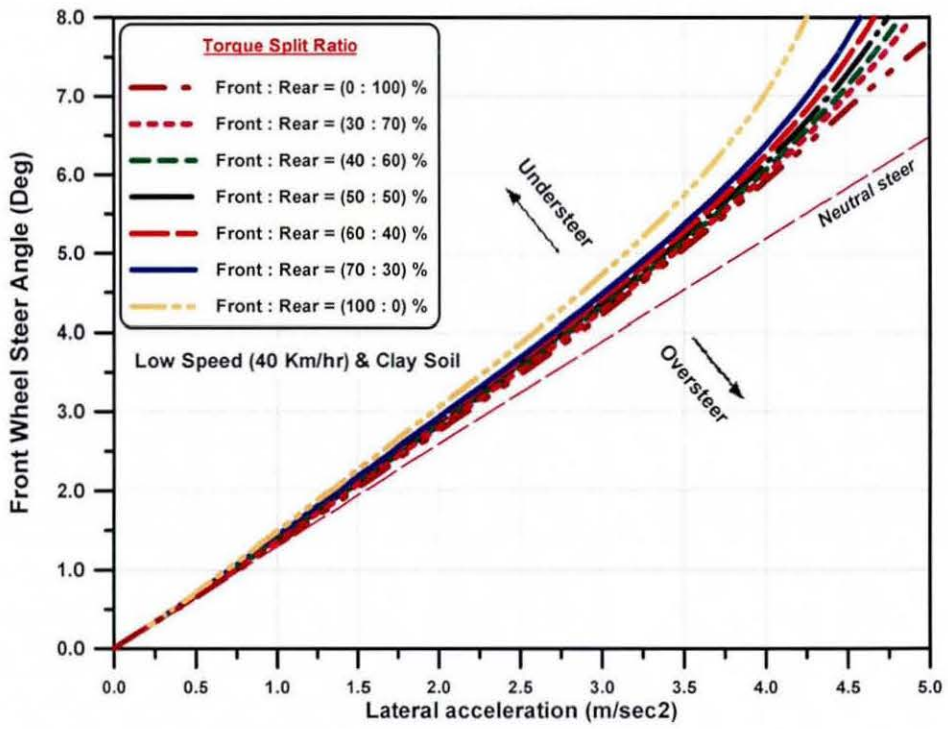


Figure 6.17 Effect of Static Split Ratio on Handling on Clay Soil at Low Speed

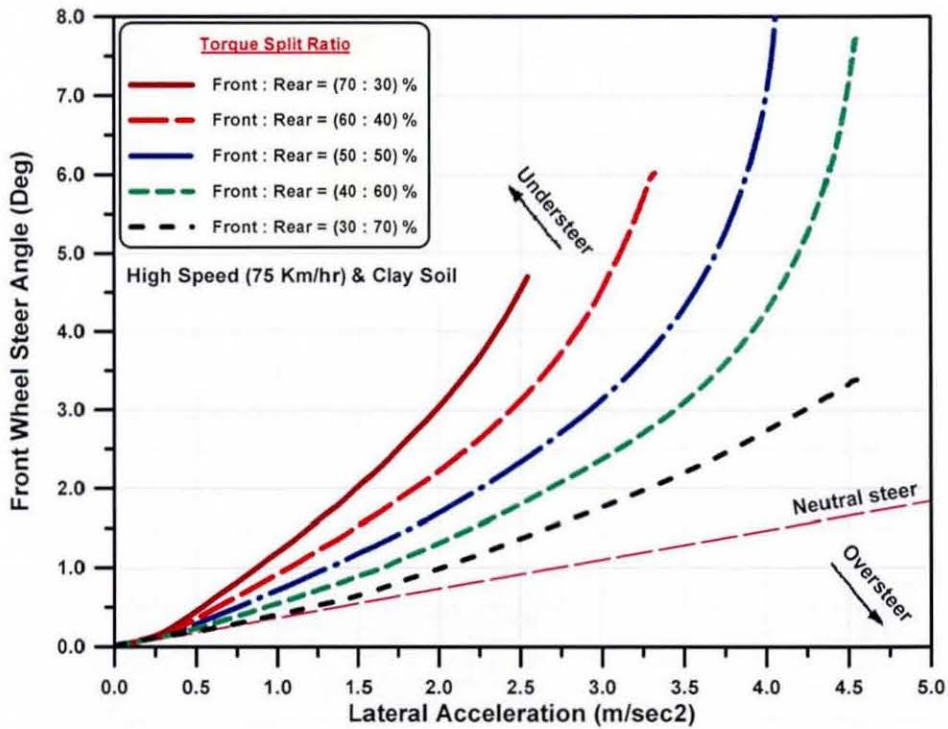


Figure 6.18 Effect of Static Split Ratio on Handling on Clay Soil at High Speed

As a general conclusion, in order to optimise a 4×4 vehicle behaviour in terms of traction performance and cornering stability, the ratio of torque distribution between the front and rear axles must be carefully controlled in order to guarantee, not only a higher traction, but also an acceptable level of controllability and stability.

6.3.3 Visco-Lock Device Tuning:

Visco-lock devices are designed not only to transmit torque, but also to control its distribution. The transmitted torque must satisfy certain requirements for vehicle performance. The viscous shear torque characteristics depend on the fluid rheology, dimensions and number of plate pairs, the gap between them (clearance) and the fluid filling percentage. However, because these devices act as passive control systems, they require tuning (optimisation) before installation into the drivetrain system.

In reality, this process is simply carried out empirically, changing the silicone fluid in a trial and error approach, which is time consuming and expensive.

For the purpose of this investigation, different silicone fluids (A, B, C, and D) with different rheological properties, in terms of kinematic viscosity, as well as shear and thermal properties are used. The silicone fluids can be distinguished according to their nominal kinematic viscosity as follows: (Fluid A: 1.0 m²/s), (Fluid B: 0.1 m²/s), (fluid C: 0.01 m²/s), and (Fluid D: 0.001 m²/s).

If the viscous unit is assumed to have a torque capacity factor (K) expressed in $\left(\frac{N \cdot m}{rad/s}\right)$, given at operating conditions with rotational speed difference ($\Delta\omega$), the torque bias ratio between the two shafts $|T_2 - T_1|$ can be expressed by: $(K \cdot |\Delta\omega|)$. Using a silicone fluid with a higher nominal viscosity (for example, fluid A) makes the unit stiffer with a higher torque capacity factor. This enables larger torques to be transmitted. Depending on the functional installation of the viscous unit within the drivetrain, both the traction performance and cornering stability of the vehicle would vary accordingly.

6.3.3.1 Viscous Coupling (O-VC-O):

As previously explained, the way the viscous coupling is installed within the drivetrain depends on the static ratio of weight distribution between the axles. Since the reference vehicle carries more static weight on the rear axle, the primary drive is dedicated to the rear axle and the secondary drive axle (front axle) is used via the viscous coupling.

Figure 6.19 illustrates the consequences of employing different silicone fluids with altered rheological properties on the tractive efficiency, as well as the drawbar pull-slip characteristics. It is apparent that, by using a fluid with stiffer characteristics (e.g. fluid A), the traction performance can be regulated to approach that obtained in the case of a locked centre differential (O-L-O). On the other hand, by using a fluid with softer characteristics (e.g. fluid D), the traction performance can be regulated to approach that obtained in the case of a rear wheel drive (RWD).

As a critical step during the optimization procedures, the same simulation is repeated for different soils as shown in figure 6.20. It is obvious that while the clay soil offers comparatively improved conditions for traction, over the same type of soil, traction sensitivity to the variation of fluid's properties remains unaltered.

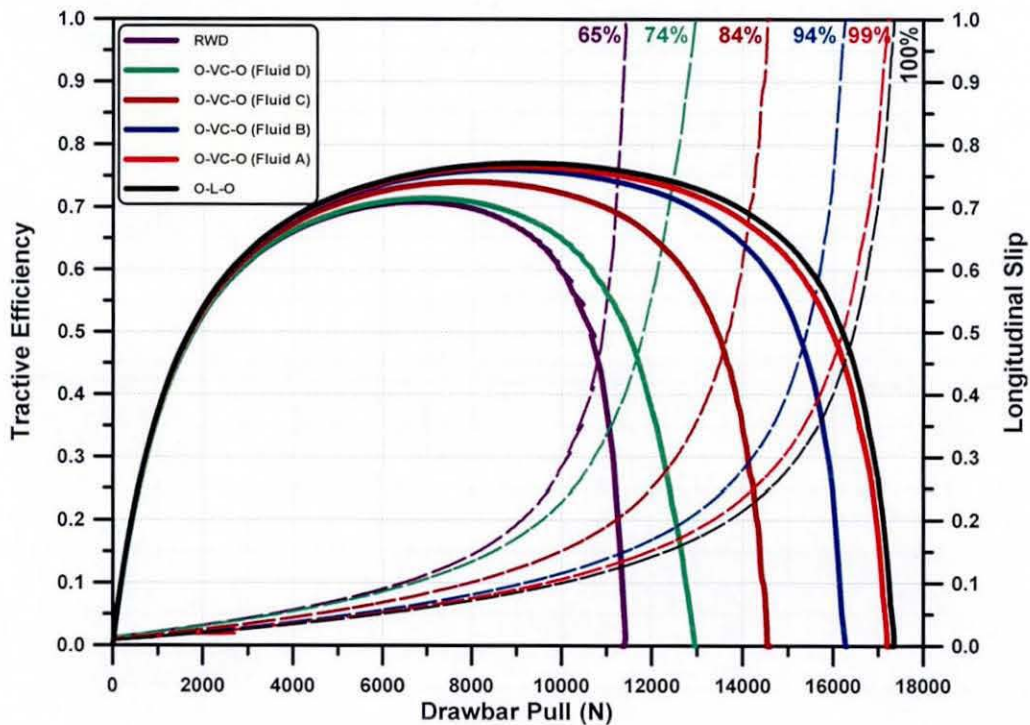


Figure 6.19 Effect of Viscous Coupling Fluid Rheology on Traction on Clay Soil

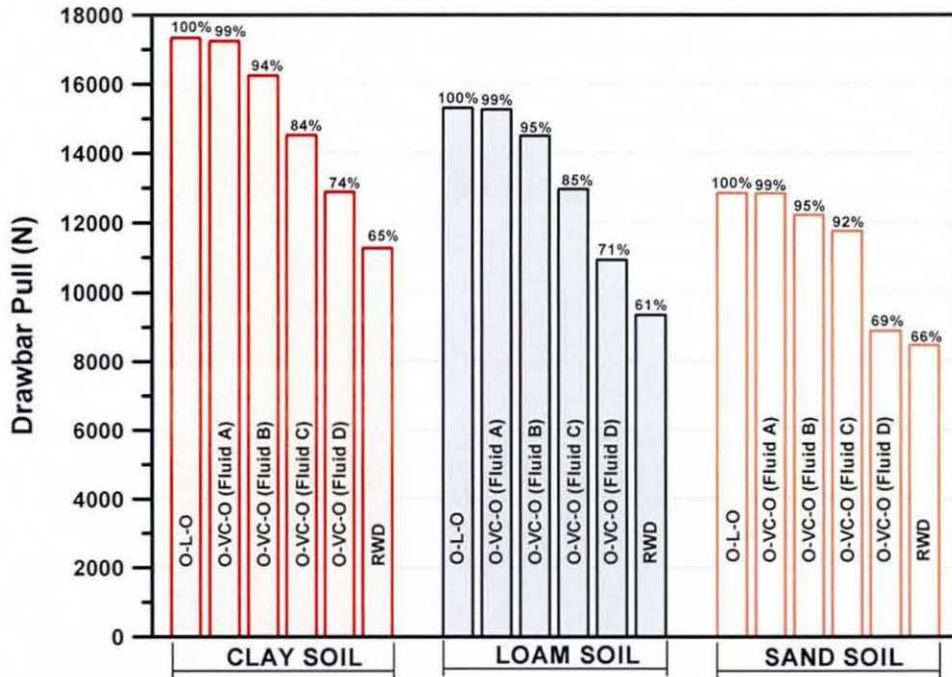


Figure 6.20 Effect of Viscous Coupling Fluid Rheology on Traction on Different Soils

As introduced earlier in chapter 5, the viscous coupling has two modes of operation; shear mode and hump mode. While the shear mode is primarily speed and temperature dependent, the hump mode is additionally time dependent. In other words, for the viscous coupling to hump or experience self-torque amplification, the unit should operate a long time, through which the generated heat (due to front and rear speed difference) can cause the silicone fluid to expand and fully fill the voids inside the viscous coupling.

During the computation, it was observed that, sometimes the longitudinal slip of the vehicle tyres reaches its ultimate value (100%), while the viscous unit still performed in the normal shear mode. Furthermore, it was noted that for loose or slippery soils (e.g. sand and loam), time for the driven tyres to reach their critical longitudinal slip value is relatively short compared to that achieved over relatively firm soil like the clay soil.

Figures 6.21 and 6.22 demonstrate an example of the consequences of the hump mode on both longitudinal slip and tractive force. When the rear axle tyres reach the utmost value of longitudinal slip, the differential rotational speed, across the viscous coupling shafts

also increases. Subsequently, the total torque and the resulting heat rises the temperature of the silicone fluid. At certain critical temperature, when all air has been dissolved, the bulk pressure drives the unit into the STA mode, see figures 5.11 and 5.30.

The suddenly increased bulk pressure and thus the total torque across the viscous coupling shafts bring the rotating plates together such that the unit acts as a rigid coupling. Under these conditions both the front and rear axle tyres rotate at the same driving speed and, hence the same slip ratio. Therefore, the driving torques and the resulting tractive forces are redistributed according to the wheel-soil contact conditions.

Two favourable advantages are gained from the STA mode. First advantage relates to the safety of the viscous unit, where the relative slip between its plates diminishes, so the core temperature and thus the bulk pressure of the unit stop rising. These would guard against damage to the coupling. The second advantage relates to traction performance, where the excessive slippage of the tyres is eliminated, reducing the slip sinkage and offer a better chance to recover traction.

The cornering response of the reference vehicle at 75 km/h with different silicone fluids is illustrated in figure 6.23. As expected, the handling response is also bounded by the characteristics acquired for rear wheel drive (RWD) and that achieved by locking the central differential (O-L-O).

By employing a silicone fluid with stiffer characteristics (e.g. fluid A), more of the driving torque is biased to the front axle. Consequently, both longitudinal slip and tractive force at the front axle-tyres tend to increase. Accordingly, the generated lateral forces at the rear axle also increase. On the other hand, the lateral load transfer from the inside wheels to those at the outside during cornering causes a considerable increase in the tractive force at the inside tyres. The combined effect results in shifting the handling diagram towards the understeer side, especially at high lateral accelerations.

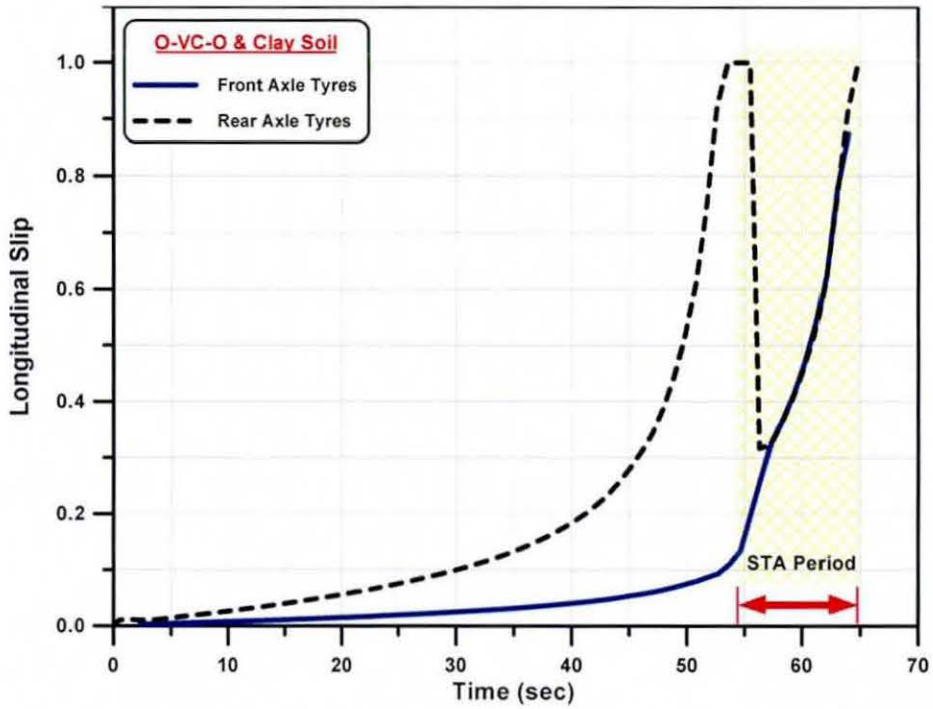


Figure 6.21 Consequences of the Hump Mode on the Longitudinal Slip of the Tyres

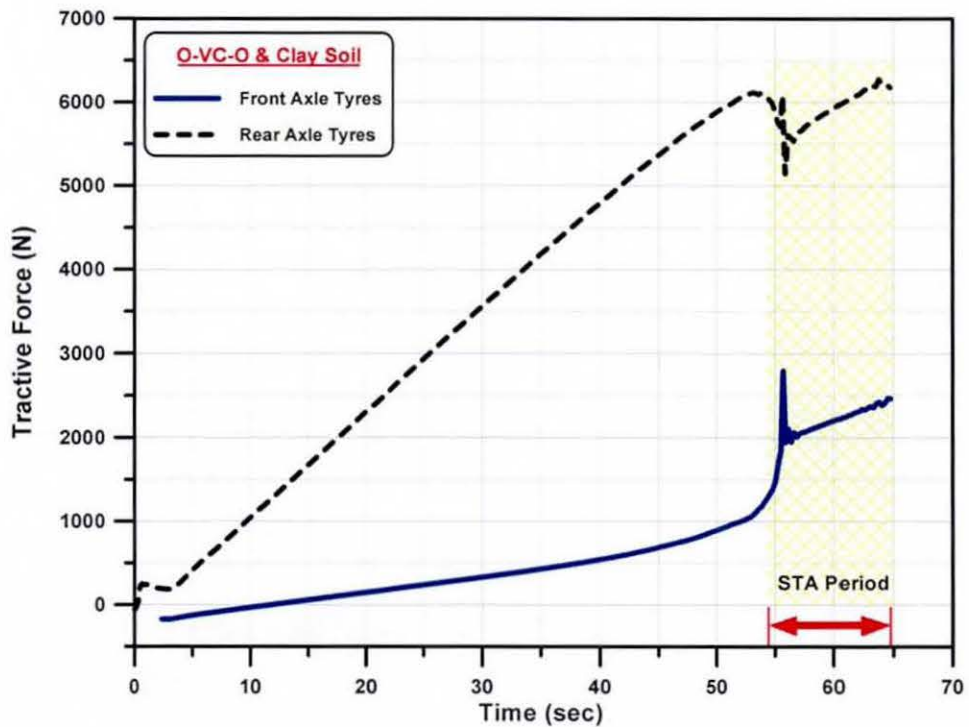


Figure 6.22 Consequences of the Hump Mode on the Distribution of the Tractive Forces

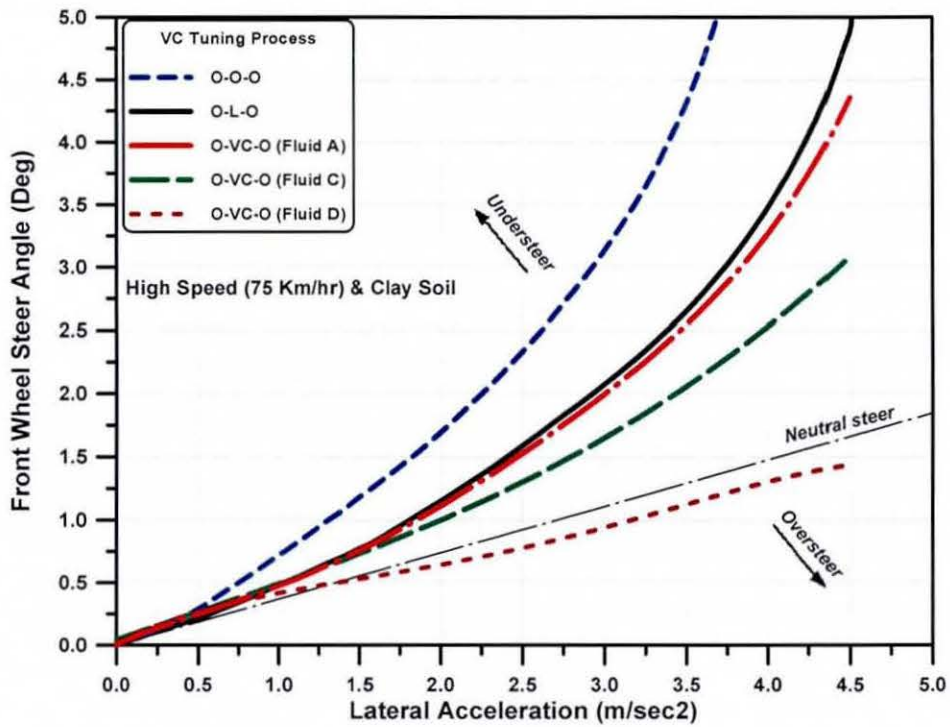


Figure 6.23 Effect of Viscous Coupling Fluid Rheology on Handling on Clay Soil

As a general conclusion, in order to optimise the behaviour of the presented reference vehicle fitted with drivetrain layout (O-VC-O), the viscous coupling should be filled with the silicone fluid (A), which would ensure not only a sufficient traction performance, but also an acceptable level of cornering stability.

6.3.3.2 Visco-Lock Limited Slip Differential (O-LSD-O):

As already mentioned, the viscous unit can be integrated within the ordinary mechanical differential to act as a control element. In this section, the employed layout is a visco-lock limited slip differential in shaft-to-shaft configuration, which is used as a central distributing element (O-LSD-O). Similar to the viscous coupling, different types of silicone fluids are used to establish the vehicle behaviour.

As shown in figure 6.24, employing silicone fluids with a higher nominal viscosity sets the performance close to that obtained by a mechanically locked central differential (O-L-O). On the other hand, selecting a silicone fluid with a lower nominal viscosity sets the performance close to that obtained by a mechanically open central differential (O-O-O).

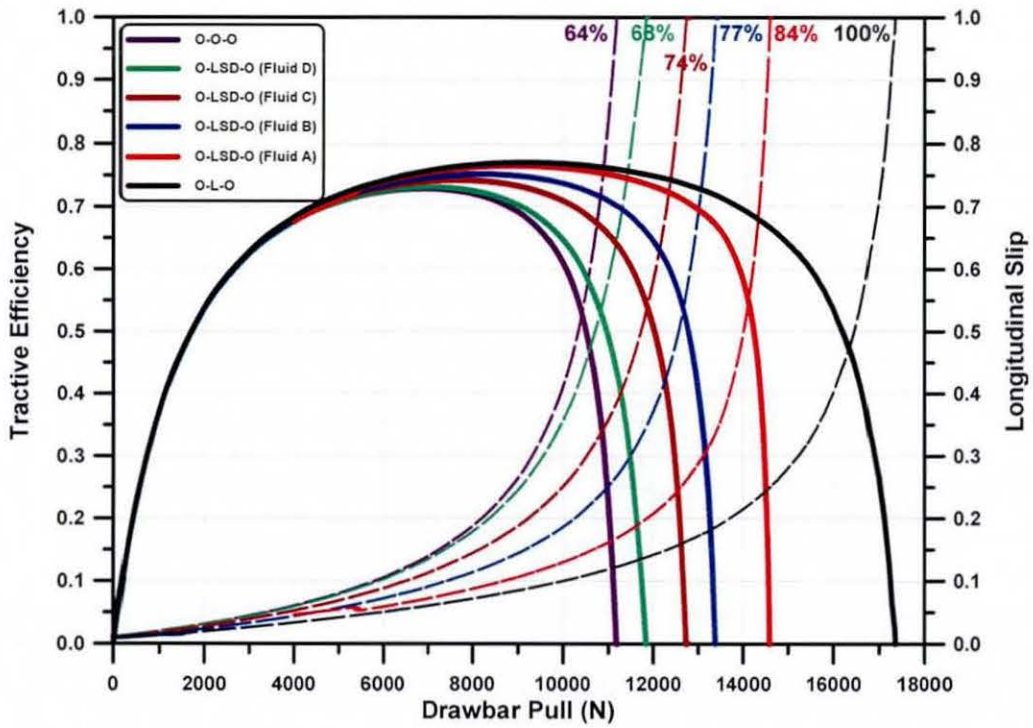


Figure 6.24 Effect of Visco-Lock LSD Fluid Rheology on Traction on Clay Soil

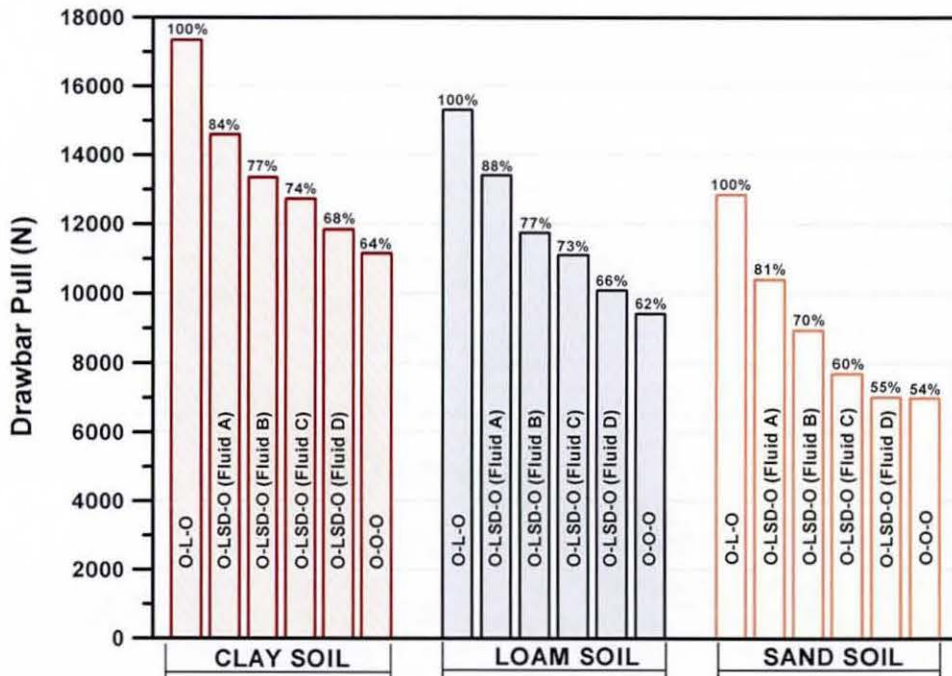


Figure 6.25 Effect of Visco-Lock LSD Fluid Rheology on Traction on Different Soils

The same trend is obtained over different soils with a noticeable reduction in traction performance provided by sand and loam soil in comparison to that with clay soil, see figure 6.25. Furthermore, for the case of sand soil, using silicone fluids with different values of viscosity has shown less influence on traction performance.

Before discussing the influence of silicone fluid properties on the cornering response of a 4×4 off-road vehicle, fitted with a visco-lock differential, it would be helpful to highlight the significant consequences of an ordinary mechanical differential lock.

The main significance of differential lock is that the driving torque is distributed according to the conditions of the tyre-soil contact. This affects primarily the longitudinal slip and, therefore, the tractive force. According to the well known principle of friction circle, both the longitudinal and lateral forces are limited by the maximum adhesion provided by the soil. This implies that increasing the tractive force should result in a noticeable reduction in the lateral forces. As a result, locking the differential not only regulates the tractive force distribution, but also the lateral forces.

The effect of differential locking on the cornering stability, to a great extent, depends on the location of the differential used within the drivetrain. Based on a 4×4 drivetrain with three mechanical differentials, there are eight possible configurations of differential locking as shown in figure 6.26.

In general, locking the central differential regulates the driving forces between the front and rear axles and the cornering response would be determined according to the static weight distribution between the axles. Since the reference vehicle has a greater static weight on the rear axle, locking the differential would constitute greater tractive forces developed at the rear axle, while more lateral forces would be expected to be developed at the front axle. The effect due to the moments generated by these forces would reduce the understeer moment as previously explained.

Locking the axle (front or rear) differential regulates the tractive and, hence, the lateral forces between the tyres of the same axle and the cornering response would be

determined according to the dynamic lateral weight transfer from the inside wheels in a turn to the outside wheels, which in turn are functions of lateral acceleration. If the axle differential is locked, more driving torques are transferred to the outer wheels, which would experience larger vertical weights and, hence, rolling resistance. Consequently, the generated tractive forces at the inside wheels are reduced. The effect of the moments of these forces would be to reduce understeer.

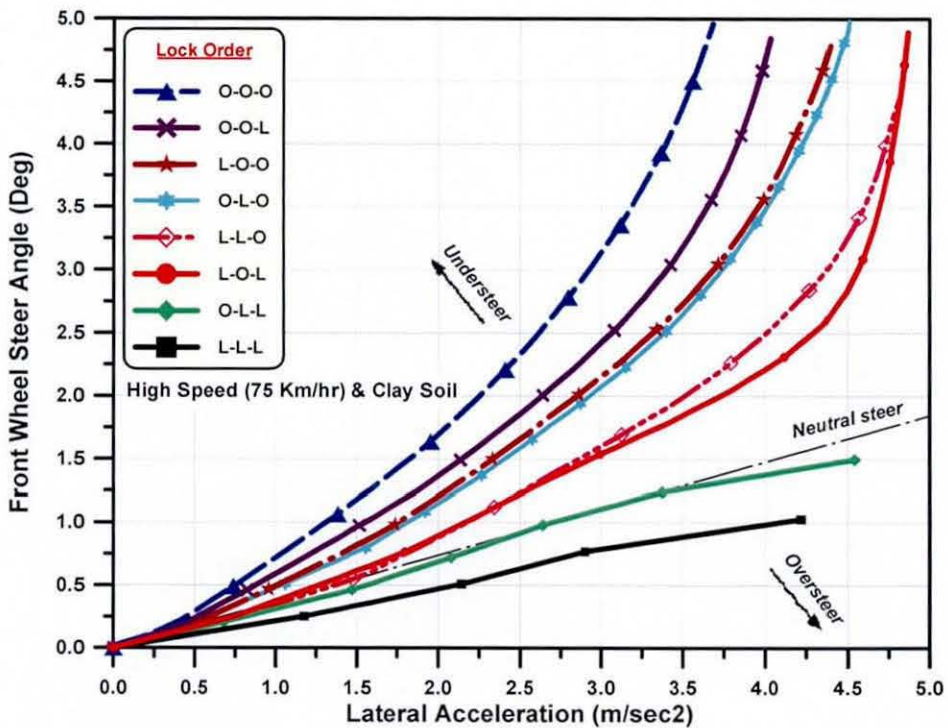


Figure 6.26 Effect of Mechanical Differential Locking on Handling Characteristics

Referring to figure 6.26, different scenarios are simulated to represent the possible layouts of differential locking. According to the aforementioned analysis, it is obvious that, locking the three differentials represents the extreme condition of oversteering, while unlocking the three differentials represents the extreme condition of understeering. The handling characteristics provided by other possibilities are somewhere in between these extremes, depending on the weight distribution and lateral dynamic weight transfer.

As depicted in figure 6.27, it is obvious that, by changing the silicone fluid it is possible to tune the visco-controlled limited slip differential (LSD) to achieve the required

handling characteristics. A higher torque capacity factor shifts the cornering response towards that expected of a rigid 4x4 coupling (O-L-O) characteristics, while a lower torque capacity factor shifts the vehicle performance towards the open central differential (O-O-O) characteristics.

As a general conclusion: in order to optimise the behaviour of the reference vehicle in this study, fitted with the drivetrain layout (O-LSD-O), silicone fluid (C) seems to be a reasonable choice which would ensure not only sufficient traction performance, but also an acceptable level of cornering stability.

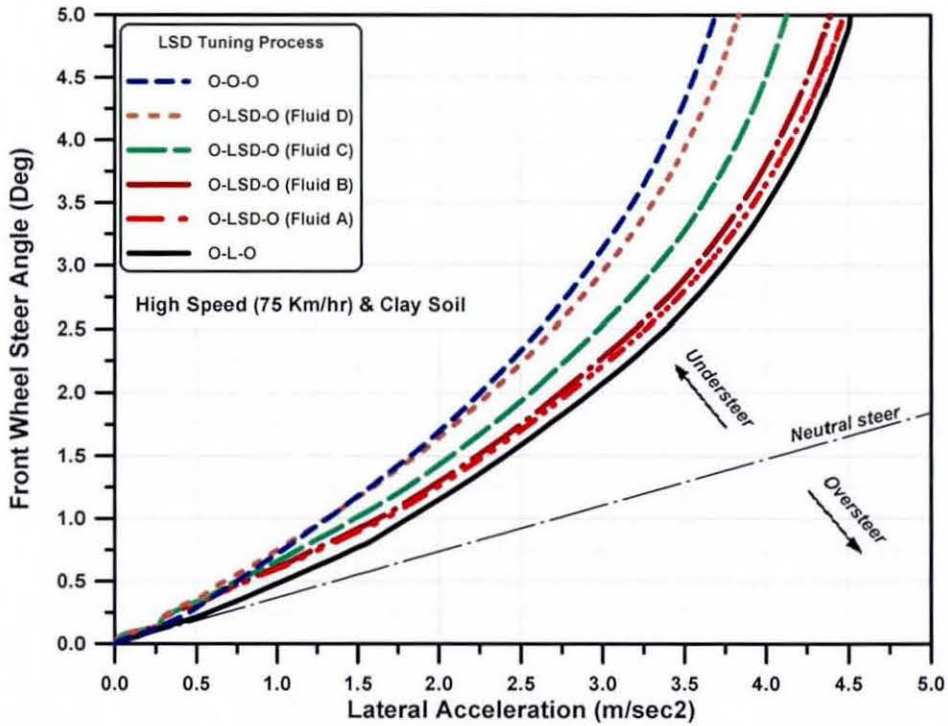


Figure 6.27 Effect of Visco-Lock LSD Fluid Rheology on Handling on Clay Soil

Chapter 7: Conclusions and Suggestions for Future Work

7.1 Achievement of Aims and Contributions to Knowledge

The thesis reports on an integrated investigation of the dynamic behaviour of all-wheel-drive vehicles, whilst negotiating deformable soil terrains. A comprehensive model is devised with parameterised physical models of visco-lock devices, which is used in full vehicle simulations.

The vehicle is represented by a 14-DOF model, integrating all important subsystems such as vehicle body, suspension, steering system and wheel dynamics. The vehicle model also incorporates body dynamics of 4×4 full drivetrain systems, including sources of torsional damping and stiffness in axles/shafts. The drivetrain model also allows provisions for the inclusion of conventional torque distribution devices.

Within the drivetrain model, the driving torque is transmitted/regulated by the various torque distribution devices. At the output end of the system, the torque is regulated by the interaction between the tyres and the soft soil.

The employment of a detailed model of any drivetrain system would be meaningless without an equally elaborate representation of the tyre-soil interaction. For this reason, the newly developed AS²TM soft soil tyre model was employed. The model accounts for the pressure-sinkage in the vertical direction and the shear-tension-displacement in the horizontal direction. Both phenomena are particular to off-road terrains and affect the tyre-force generation process to such an extent that typical tyre models for rigid roads cannot be employed for the simulation of the contact between tyres and soils.

The proposed model was successfully extended to assimilate a special library of tribodynamics' modules of visco-lock devices including viscous couplings of shafts and visco-

lock limited-slip differentials. The mechanism of torque transmitted by visco-lock devices was modelled, considering the viscous shear mode, as well as the hump or self-torque amplification mode. The dependency of silicone fluid rheology on both shear rate and temperature was taken into account.

In order to validate the proposed tribo-dynamics' modules, an experimental test rig was devised. The measurements were carried out to capture torque characteristics of these devices. Experimental findings for typical components were compared with the numerical simulation results, showing satisfactory conformity for the predictions.

The integration of all modules resulted in a fairly complex generic multi-physics model, which was implemented in a MATLAB/Simulink/SimDriveline environment. Hitherto, this is the only numerical approach developed reported, which incorporates tribo-dynamics' modules for visco-lock devices with the capability of simulating 4×4 off-road vehicles. This unique modelling approach can be used to support the design engineers and manufacturers in the following manner:

- Simulation of a wide variety of conditions including ride, traction and handling tests using medium degree of sophistication for 4×4 off-road vehicle models. However, the main strength of the model is the inclusion of a detailed drivetrain dynamics for accurate representation of traction forces.
- Investigation of components' selection, particularly those related to drivetrain gearing/coupling design, which would produce the characteristics, best suited to a proposed vehicle.
- Assessment of vehicle behaviour in accordance to the detailed design parameters of visco-lock devices. Subsequently, the requirements for tuning of such devices can easily be achieved in a purely numerical environment, which would eliminate time and money wasted in the otherwise empirical trial and error implementations.
- Feasibility for the future incorporation of advanced control strategies and automatic optimization techniques for off-road 4×4 vehicles. This is in addition to the possibility of integrating such control strategies with an in-house written code rather than using complex/commercial models, which often require special know-how in order to be adapted to particular design requirements.

7.2 Overall Findings and Conclusions

The numerical analysis has been successfully employed in order to predict both traction and handling characteristics of a typical 4×4 off-road vehicle. The traction performance is evaluated based on two alternative approaches. One is to assess vehicle traction capabilities for a specific power plant system in terms of maximum speed, acceleration. The other is to assess the efficiency of torque distribution devices in terms of drawbar pull and tractive efficiency. The handling characteristics have been examined under both transient and steady state conditions during standard cornering manoeuvres such as lane change, step steer and ramp steer manoeuvres.

Contributions of a number of significant parameters such as mechanical properties of soil, static weight distribution and tyre inflation pressure have been ascertained. Particular attention is paid to various types of conventional drivetrain configurations, as well as different scenarios for torque distribution between front and rear axles, including mechanical and visco-lock devices.

While it was not possible to conduct field tests to verify the simulation model, the findings conform to general observations and natural intuition and to those reported in well known published research work. Based on the results obtained, the following main conclusions have been drawn:

- Contrary to on-road vehicles' performance, it is noted that both the longitudinal and lateral behaviour of off-road vehicles are dominated by the mechanical properties of the soil. To explore the vehicle behaviour over wider range of soil terrains, three different types of soils with distinct properties were employed. The findings confirmed that traction performance, as well as cornering stability are seriously deteriorated when driving on loose soil with poor shear properties.
- The analysis results also show that quite different characteristics compared to those obtained on rigid road are obtained for soft terrains, particularly for higher speed manoeuvres. Generally, a lower magnitude of lateral acceleration is observed which is mainly attributed to the resisting circumferential forces due to soil shear strength, as a

result of which the developed tyre lateral forces are remarkably lower than those on the made roads.

- A significant improvement in the handling stability was noted when the vehicle has more static weight on the rear axle. This is mainly due to the higher resultant equivalent cornering stiffness at the rear axle, which tends to shift the handling characteristics towards an understeering behaviour.
- The cornering response of AWD vehicles is highly affected by the way the driving torque is distributed between the axles/wheels. This is particularly true where the lateral forces are regulated by the longitudinal slip and the tractive forces at the tyres. It was observed that, biasing more driving torque to the rear axle would reduce both the longitudinal slip and tractive force at the front axle-tyres and therefore, increase the lateral force generating potential at the front. The additional yaw moment shifts the handling characteristics towards an oversteering response, a fact which in turn reduces both the stability and controllability of the vehicle.
- Results of traction analysis have shown that vehicle weight distribution is a crucial parameter, which must be taken into account during the design process of AWD off-road vehicles. For a given ratio of static weight distribution, except for the case of a locked central differential configuration, the traction capabilities are adversely affected. In order to achieve the maximum tractive efficiency, the driving torque should be distributed to match the weight distribution between the front and rear axles in a manner that would minimize the slip difference between them.
- In the case where more torque is biased to the rear axle, a conflict with the handling characteristics would be inevitable, and the vehicle stability would be adversely affected.
- Towards the end of the numerical investigation it was noted that, for mechanical torque distribution devices, a fixed ratio of torque bias can be carefully selected by appropriately setting the gearing design. On the other hand, for visco-lock devices the torque bias ratio can be tuned by carefully selecting the silicone fluid rheological parameters.

7.3 Critical Assessment of Approach

The thesis presents an integrated numerical approach to simulate AWD off-road vehicles fitted with visco-lock devices. A model of medium degree of sophistication is validated against existing typical vehicle parameters and experimental results obtained during the study. Furthermore, the thesis demonstrated the usefulness of visco-lock devices not only to improve traction performance but also to maintain vehicle stability. The present research is characterised by certain limitations, as follows:

- The suspension system is simply represented by a linear spring and shock absorber model with purely vertically directed forces. This assumption is clearly not accurate due to the complicated design of the suspension system, including, bushing non-linearities, geometry and compliance. However, it should be noted that, evaluation of vehicle behaviour for ride comfort was not the main concern of the present research. Therefore, the current formulation of suspension system may be reasonable. Additionally, due to the modular structure of the model, it would be relatively easy to incorporate complex suspension models to achieve more accurate dynamic load transfer and hence tyre forces.
- The presented numerical model is devoted to the wheeled vehicles, whilst traversing on soft soil terrains. This limitation is mainly attributed to the employed off-road tyre model. Therefore, the current model cannot be employed for on-road research requirements. However, by carefully selecting the soil terrain input parameters, simulation of hard soil could still give useful qualitative predictions for vehicle behaviour on-road.
- While the proposed approach seems capable of predicting off-road vehicle behaviour, under combined lateral and longitudinal manoeuvres, the experimental verifications of the vehicle model are inevitably required. This would enable its use for a wide range of applications. It is commonly recognized that, field tests of off-road vehicles are quite difficult, which would requires measurements not only the vehicle response, but also of the soil properties and terrain profile.

- The vehicle behaviour in terms of traction performance and cornering stability has been predicted under the assumption of homogeneous and isotropic surfaces. However, it is obvious that, this assumption is not valid particularly for cross country terrains. It is, therefore, expected that the actual performance to be less effective than the indicated simulated results.

7.4 Suggestions for Future Work

- With respect to the aforementioned limitations, the potential of the model can clearly be extended. The generic formulation and modular structure of the model permits interactions between sub-models, whereby the design time is concentrated upon the subsystem currently under investigation. These features enable the future incorporation of detailed subsystems such as complex suspensions, tyre inflation pressure system, engine dynamics and so forth. Additionally, to broaden the applications of the model, it is suggested to integrate it with an on-road tyre module such that it would be easy for the user to switch between different conditions.
- Another major improvement would involve the extension of the vehicle model to represent features of multi-axle all-wheel-drive off-road vehicles such as 6×6 and 8×8. It is widely recognized that, there is an increasing demand for such vehicles with efficient capabilities for dual operations on both rigid and soft roads. It is anticipated that, the appropriate numerical model to predict traction performance and cornering stability of such configurations would be a complex task.
- With the rapidly growing applications of electronic control systems and automatic optimization in the field of AWD vehicles, the devised model would represent a suitable environment for such indicated developments. It is encouraged that, various traction control strategies and active torque distribution devices should be implemented in the presented model.
- Conducting field test and measuring vehicle behaviour in both longitudinal and lateral directions during typical manoeuvres, aimed at verification of the entire vehicle model, can be another avenue for further research.

List of References

AESCO, GbR (2005) '*Matlab/Simulink module AS²TM user's guide version 1.12*', <http://www.aesco.de/>, viewed 15 April, 2007.

Ahlvin, R. B. and Haley, P. W. (1992) 'NATO Reference Mobility Model Edition II, NRMM II user's guide', Technical Report GL-92-19, U.S. Army Waterways Experiment Station, Vicksburg, MS.

Alexander, T. and Monkaba, V. (2000) 'Development and implementation of a tool for modelling driveline systems', SAE Technical Paper Series No. 2000-01-3525.

Alexander, T., Liu, C. and Monkaba, V. (2002) 'Multi-body dynamic modelling methods and applications for driveline systems', SAE Technical Paper Series No. 2002-01-1195.

Assanis, D., Bryzik, W., Chalhoub, N., Filipi, Z., Henein, N., Jung, D., Liu, X., Louca, L., Moskwa, J., Munns, S., Overholt, J., Papalambros, P., Riley, S., Rubin, Z., Sendur, P., Stein, J. and Zhang, G. (1999) 'Integration and use of diesel engine, driveline and vehicle dynamics models for heavy duty truck simulation', SAE Technical Paper Series No. 1999-01-0970.

Aubel, Th. (1994) 'The interaction between the rolling tyres and the soft soil FEM simulation by VENUS and validation', 6th European Conference of the ISTVS, Vienna.

Bekker, M. G. (1956) '*Theory of land locomotion*', The University of Michigan Press, Ann Arbor, USA.

Bekker, M. G. (1960) '*Off-the-road locomotion*', The University of Michigan Press, Ann Arbor, USA.

Bekker, M. G. (1969) '*Introduction to terrain-vehicle systems*', The University of Michigan Press, Ann Arbor, USA.

Borio, P., Delcaro, U., Frediani, S., Ricci, C. and Caviasso, G. (2004) 'Evaluation criteria for AWD vehicles system analysis', SAE Technical Paper Series No. 2004-01-2086.

Borutzky, W. (1992) 'The Bond graph methodology and environments for continues system modelling and simulation', ESM92 Proc. European simulation Multi-conference, York, UK, pp. 15-21.

BS ISO 7401 (2003) 'Road vehicles—lateral transient response test methods—open loop test methods', British Standard BS ISO 7401.

Chen, S. T. (1993) '*Analysis of the tractive performance of pneumatic tires over soft terrain*', PhD thesis, Department of Mechanical and Aeronautical Engineering, Carlton University, Canada.

Chocholek, S. E. (1988) 'The development of a differential for the improvement of traction control', *Proceedings of the Institution of Mechanical Engineering*, No. C368/88, pp. 75-82.

Ciesla, C. R. and Jennings, M. J. (1995) 'A modular approach to powertrain modelling and shift quality analysis', SAE Technical Paper Series No. 950419, pp. 139-147.

Crolla, D. A. (1975) 'The performance of off-road vehicle under fluctuating load conditions', *Proceedings of the Institutional Mechanical Engineering*, No. C206/75, pp. 91-99.

Crolla, D. A. and Hales, F. D. (1979) 'The lateral stability of tractor and trailer combinations', *Journal of Terramechanics*, Vol. 16, No. 1, pp. 1 - 22.

Crolla, D. A. (1983a) 'The steering behaviour of off-road vehicles', Proc. of the 8th Int. Conf. on the Dynamic of Vehicle on Road and Railway Tracks, pp. 99-115.

Crolla, D. A. and Horton, D. N. L. (1983b) 'The steering behaviour of articulated body steer vehicles', *Proceedings of the Institutional Mechanical Engineering*, No. C123/83, pp. 139-146, London.

Crolla, D. A. and EL-Razaz, A. S. A. (1987a) 'A Review of the combined lateral and longitudinal force generation of tyres on deformable surfaces', *Journal of Terramechanics*, Vol. 24, No. 5, pp. 199–225.

Crolla, D. A. and El-Razaz, A. S. A. (1987b) 'A model to predict the combined lateral and longitudinal forces on an Off-road tyre', Proceedings of the 9th International ISTVS Conference, International Society for Terrain Vehicle Systems, pp. 362–372, New Hampshire, USA.

Crolla, D. A. (1991) '*Off-road vehicle dynamics*', D. Tech. Thesis, Loughborough University of technology, Loughborough, UK.

Danesin, D., Girardin, C., Sorniotti, A., Morgando, A. and Velardocchia, M. (2004) 'Driveline layout influence on four wheel drive dynamics', SAE Technical Paper Series No. 2004-01-0860.

Day, T. D., Roberts, S. G. and York, A. R. (2001) 'SIMON: A new vehicle simulation model for vehicle design and safety research', SAE Technical Paper Series No. 2001-01-0503.

Dick, W. M. (1995) '*All-wheel and four-wheel-drive vehicle systems*', Society of Automotive Engineers, Warrendale, PA, USA, ISBN 1560916133.

Dow Corning (1962) 'Silicone notes', Bulletin: 05-021, Dow Corning Corporation, Midland, Michigan.

Drogies, S. and Bauer, M. (2002) 'Modelling road vehicle dynamics with Modelica', SAE Technical Paper Series No. 2002-01-1219.

Egnaczak, B. (1994) 'The new Torsen II traction technology', SAE Technical Paper Series No. 940736, pp. 107-114.

El-Gawwad, K. A., Crolla D. A., Soliman, A. M. A. and El-Sayed, F. M. (1999a) 'Off-road tyre modelling: I The multi-spoke tyre model modified to include the effect of straight lugs', *Journal of Terramechanics*, Vol. 36, No. 1, pp 3-24.

El-Gawwad, K. A., Crolla D. A., Soliman, A. M. A. and El-Sayed, F. M. (1999b) 'Off-road tyre modelling : II Effect of camber on tyre performance', *Journal of Terramechanics*, Vol. 36, No. 1, pp 25-39.

El-Gawwad, K. A., Crolla D. A., Soliman, A. M. A. and El-Sayed, F. M. (1999c) 'Off-road tyre modelling: III Effect of angled lugs on tyre performance', *Journal of Terramechanics*, Vol. 36, No. 2, pp 63-76.

El-Gawwad, K. A., Crolla D. A., Soliman, A. M. A. and El-Sayed, F. M. (1999d) 'Off-road tyre modelling: IV Extended treatment of tyre-terrain interaction for the multi-spoke model', *Journal of Terramechanics*, Vol. 36, No. 2, pp 77-90.

El-Gindy, M. and Woodrooffee, J. H. (1990) 'The effect of tractor parameter variations on the dynamic performance of B-train double', The Winter Annual Meeting of the American Society of Mechanical Engineering, Dallas, TX.

Ellis, J. R. (1994) '*Vehicle handling dynamics*', Mechanical Engineering Publications Limited, London, ISBN: 0852988850.

Elmqvist, H., Mattsson, S. E., Olsson, H., Andreasson, J., Otter, M., Schweiger, C. and Brück, D. (2004) 'Realtime simulation of detailed vehicle and powertrain dynamics', SAE Technical Paper Series No. 2004-01-0768.

Garcia, O. M. and Kargar, K. (2000) 'Simulation tool for transmission and driveline systems design', SAE Technical Paper Series No. 2000-01-0832, pp. 1-10.

Garrett, T. K. (2001) '*Motor vehicle*', Butterworth-Heinemann, Oxford, ISBN 0750644494.

Gill, S. S., Kalsi, N. S., Singh, B. and Singh, N. (2002) 'Improved differential function for avoiding slippage of motor vehicles in a muddy trench', SAE Technical Paper Series No. 2002-01-0988.

Gillespie, T. D. (1992) '*Fundamentals of vehicle dynamics*', Society of Automotive Engineers, Warrendale, Pa., USA, ISBN – 1560911999.

Gnanakumarr, M. M. (2004) '*Integrated investigation of impact-induced noise and vibration in vehicular drivetrain systems*', PhD Thesis, Wolfson School of Mechanical and Manufacturing Engineering, Loughborough University, Loughborough, UK.

Gradu, M. (2003) 'Torque bias coupling for AWD applications', SAE Technical Paper Series No. 2003-01-0676.

Grechenko, A. (1969) 'Slip and drift of the wheel with tyre on soft ground', Proceedings of 3rd International ISTVS Conference, Vol. 2, Essen, W. Germany.

Hall, L. C. (1986) 'The influence of limited slip differential on torque distribution and steady state handling of four-wheel drive military vehicles', *Proceedings of IMechE*, International Conformance on All-Wheel Drive, No. C05/86, pp. 595-66, London, U.K.

Hall, L. C. and Moss, P. J. (1988), 'The use of viscous couplings to alleviate transmission wind in military vehicles when driven on-road', *Proceedings of IMechE*, International Conformance on All-Wheel Drive, No. C362/88, pp. 23-32.

Halliwell, N. A. (1996) 'The LASER torsional vibrometer: A step forward in rotating machinery diagnostics', *Journal of Sound and Vibration*, Vol. 190, No. 3, pp. 288-307.

Hamrock, B. J. (2004) '*Fundamentals of fluid film lubrication*', 2nd ed., Marcel Dekker, New York, ISBN – 0824753712.

Harnisch, C. (1997) 'Drive line concepts for multi-axle-off-road vehicles – simulation with ORIS', Proceedings, 7th European Conference of the ISTVS, Ferrara.

Harnisch, C. (1999) 'Strategies for intelligent multi-axle steering in terrain', Proceedings, 13th International Conference of the ISTVS, Munich.

Harnisch, C. (2001) '*Dynamic real time simulation of the off road driving of wheeled vehicles*', PhD thesis, The Institute of Automotive Engineering, (IKK), Federal Armed Forces, Hamburg, (In Germany).

Harnisch, C. and Lach, B. (2002a) 'Off road drive of wheeled vehicles in dynamic realtime simulation', NATO SCI Panel Symposium, Berlin.

Harnisch, C. and Lach, B. (2002b) 'Off road vehicles in a dynamic three-dimensional realtime simulation', 14th International Conference of the ISTVS, Vicksburg – USA.

Harnisch, C., Lach, B. and Jakobs, R. (2003) 'ORSIS - news and further developments', 9th European Conference of the ISTVS, Harper Adams, UK.

Harnisch, C., Lach, B., Jakobs, R., Troulis, M. and Nehls, O. (2005) 'A New tyre–soil interaction model for vehicle simulation on deformable ground', *Vehicle System Dynamics*, Vol. 43, Supplement, pp. 384 – 394.

Harnisch, C., Lach, B. and Jakobs, R. (2007) 'ORSIS - news and further developments', *Journal of Terramechanics*, Vol. 44, Issue 1, pp. 35-42.

Heiming, G. W. (1987) 'Statistical procedures for evaluation of terrain measuring data', 9th International Conference of the ISTVS, Barcelona.

Heiming, G. W. (1989) 'Statistical mobility analysis' 4th European Conference of the ISTVS, Wageningen.

Heisler, H. (1885) '*Vehicle and engine technology*', British Library Catalogue, United Kingdom, ISBN 0713135425.

Heisler, H. (2002) '*Advanced vehicle technology*', Butterworth-Heinemann, Oxford, ISBN 0750651318.

Hintze, D. (1990) 'The influence of seasonal moisture changes on soil strength', 10th International Conference of the ISTVS, Kobe.

Hintze, D. (1991) 'The prediction of soil strength with the aid of climatic data'. 5th European Conference of the ISTVS, Budapest.

Hintze, D. (1994) 'Simulation of climatic influences on ground strength and trafficability', 6th European Conference of the ISTVS, Vienna.

Hirschberg, W., Rill, G. and Weinfurter, H. (2002) 'User-appropriate tyre-modelling for vehicle dynamics in standard and limit situations', *Vehicle System Dynamics*, Vol. 38, No. 2, pp. 103 – 125.

Holloway, D. C., Wilson, W. H. and Drach, T. J. (1989) 'Examination of ATV tire forces generated on clay, grass and sand surfaces', SAE Technical Paper Series No. 891106.

Holzwarth, R. K. and May, K. A. (1994) 'Analysis of traction control systems augmented by limited slip differentials', SAE Technical Paper Series No. 940831.

Hopkins, P. and Metz, L. D. (1994) 'Oversteer/understeer characteristics of a locked differential', SAE Technical Paper Series No. 492485, pp. 97-107.

Huchtkotter, H. and Taureg, H. (1994) 'The effect of a viscous coupling used as a front-wheel drive limited-slip differential on vehicle traction and handling', SAE Technical Paper Series No. 940875, pp. 13-21.

Huchtkotter, H. and Klin, H. (1996) 'The effect of various limited-slip differential in front-wheel drive vehicles on handling and traction', SAE Technical Paper Series No. 960875, pp. 131-140.

Huchtkoetter, H. and Gassmann, T. (2004) 'Vehicle dynamics and torque management devices', SAE Technical Paper Series No. 2004-01-1058.

IMAGINE (1995-2006) '*AMESim: Powertrain Library*', viewed 15 April 2007, http://www.amesim.com/software/libraries/lib_powertrain.aspx

Incropera, F. P. (2002) '*Introduction to heat transfer*', 4th ed., Wiley, New York, ISBN – 0471386499.

Janosi, Z. and Hanamoto, B. (1961) 'The analytical determination of draw bar pull as a function of slip for tracked vehicles in deformable soils', Proceedings of the 1st International Conference on the Mechanics of Soil-Vehicle Systems, Italy.

Katz, A. (1997) '*Computational rigid vehicle dynamics*', Krieger Publishing company, Inc, Florida. ISBN: 1-57524-016-5.

Kinsey, J. (2004) 'The advantages of an electronically controlled limited slip differential', SAE Technical Paper Series No.2004-01-0861.

Lach, B. (1996) 'The influence of tyre inflation pressure - A comparison between simulation and experiment', 1st East Europe Conference of the ISTVS, Wroclaw.

Lach, B. (1997) 'Strategies for automatic tire inflation pressure control', 7th European Conference of the ISTVS, Ferrara.

Lach, B. (1999) 'Individual tire inflation management for multi-axle vehicles', 13th International Conference of the ISTVS, Munich.

Lanzer, H. (1986) 'Permanent and part-time four wheel drive and typical tractive force distribution', SAE Technical Paper Series No. 861369, pp. 5.263-5.273.

Lee, S. K. and Atkinson, N. M. (2002) 'Understanding the interaction between passive four wheel drive and stability control systems', SAE Technical Paper Series No. 2002-01-1047.

Liang, C. Y., Allen, R. W., Rosenthal, T. J., Christos, J. P. and Nunez, P. (2004) 'Tire modeling for off-road vehicle simulation', SAE Paper No. 2004-01-2058.

Liu, C., Monkaba, V., Lee, H., Alexander, T., and Subramanyam, V. (2001) 'Co-simulation of driveline torque bias controls', SAE Paper No. 2001-01-2782.

Liu, C., Monkaba, V., McKenzie, C., Lee, H. and Suo, S. (2002) 'Driveline torque-bias-management modelling for vehicle stability control', SAE Technical Paper Series No. 2002-01-1584.

Lugner, P. Lanzer, H. and Bösch, P. (1987) '4 wheel drive with visco coupling elements', Proceedings of the 10th IAVSD Symposium, pp. 239-251.

MacLaurin, E. B. and Crolla, D. A. (1988) 'Wheel-spin control for on/off-road vehicles', *Proceedings of the Institution of Mechanical Engineers*, Conference on Traction Control and Anti-Wheel Spin Systems for Road Vehicles, London, No. C363/88, pp.33-46.

MacLaurin, E. B. and Hall, L. C. (1993) 'The effect of a controllable double differential on the handling and traction properties of a 4x4 vehicle', *Proceedings of the Institution of Mechanical Engineering*, No. C466/010/93, pp. 61-74.

Maretzke, J. and Richter, B. (1986) 'Direction control of 4WD passenger cars-A study by computer simulation', SAE Technical Paper Series No. 861370.

Menday, M. T. (2003) '*Multi-body dynamics analysis and experimental investigations for the determination of the physics of drivetrain vibro-impact induced elasto-acoustic coupling*', PhD Thesis, Wolfson School of Mechanical and Manufacturing Engineering, Loughborough University, Loughborough, UK.

Metz, L. D. (1993) 'Dynamics of four-wheel-steer off-highway vehicles', SAE Technical Paper Series No. 930765, pp. 1193-1221.

Minabe, H., Hashimoto, T. and Yamanoto, M. (1986) 'Four-wheel drive vehicle dynamics computer simulation', *Proceedings of the Institution of Mechanical Engineering*, No. C09/86, pp. 17-24.

Modelica Association '*Modelica and MathModelica*', <http://www.modelica.org>, viewed 15 April 2007.

Mohan, S. K., Ramarao, B. V., Stephens, C. F., Varma, S. K. and Gokul, B. V. (1992) 'Viscous couplings in 4WD vehicles: application of computational modelling', SAE Technical Paper Series No. 920611, pp. 787-796.

Mohan, S. K. and Williams, R. C. (1995) 'A survey of 4WD traction control systems and strategies', SAE Technical Paper Series No. 952644, pp. 59-76.

Mohan, S. K. (2002) '*A comprehensive study of self-induced torque amplification in rotary viscous couplings*', PhD. thesis, Syracuse University, Syracuse, NY.

Mohan, S. K. and Ramarao, B. V. (2003) 'A comprehensive study of self-induced torque amplification in rotary viscous couplings', *Transactions of the ASME, Journal of Tribology*, Vol. 125, pp. 110-120.

Mohan, S. K. (2004) 'Comprehensive theory of viscous coupling operation', SAE Technical Paper Series No. 2004-01-0867.

MSC Software Corporation 'ADAMS/Driveline', viewed 15 April 2007,
<http://www.cad.ltu.se/help/swdocuments/adams/driveline/drivegs/drive.pdf>

MSC Software Corporation 'Easy5', viewed 15 April 2007,
<http://www.mscsoftware.com/products/easy5.cfm>

Munson, B. R., Young D. F., Okiishi, T. H. (2005) 'Fundamentals of fluid mechanics', 5th ed., Wiley, New York, ISBN – 0471675822.

Nakaoka, M., Kikuyama, K., Hasegawa, Y. and Kojima, K. (1993) 'Torque amplification phenomenon in viscous couplings: Effects of camber of inner disk blade', *Transactions of the Japan Society of Mechanical Engineers*, Part B Vol. 59, No. 561, pp. 44-51 (in Japanese).

Nakashima, H. and Wong, J. Y. (1993) 'A three dimensional tire model by the Finite Element Method', *Journal of Terramechanics*, Vol. 30, No. 1, pp. 21-34.

Nobrant, P. (2001) 'Driveline modelling using MathModelica', MSc. Thesis, Department of Electrical Eng., Linköpings Universitet, LINKÖPING, Sweden.

Park, J. and Kroppe, W. J. (2004) 'Dana torque vectoring differential dynamic trak™', SAE Technical Paper Series No. 2004-01-2053.

Perumpral, J. V., Liljedal, J. B. and Perloff W. H. (1971) 'A numerical method for predicting the stress distribution and soil deformation under a tractor wheel', *Journal of Terramechanics*, Vol. 8, No. 1, pp. 81-98.

Peschke, W. (1986) 'A viscous coupling in the drive train of an all-wheel-drive vehicle', SAE Technical Paper Series No. 860386, pp. 2.788-2.800.

Pettersson, C. (1996) 'Driveline modeling and principles for speed control and gear-shift control', MSc. Thesis, Department of Electrical Engineering, Linköpings Universitet, LINKÖPING, Sweden.

Rahnejat, H. (1998) 'Multi-body dynamics vehicles, mechanics, and mechanisms', Society of Automotive Engineering Inc., U.S.A. ISBN: 0-7680-0269-9.

Rubin, Z. J. and Moskwa, J. J. (1999) 'A modular HMMWV dynamic powertrain system model', SAE Technical Paper Series No. 1999-01-0740.

Ruff, K. (1991) 'Interactive simulation of the driver-vehicle-terrain-system', Proceedings of the 5th European Conference of the ISTVS, pp. 351–358, Budapest.

Ruff, K. and Jakobs, R. (1993) 'Interactive simulation of vehicle movement in terrain', Proceedings of the 11th International ISTVS Conference, Lake Tahoe.

Ruff, K. (1994) 'The simulation of the phenomena between tyre and terrain with the simulation system ORIS', Proceedings of the 6th European ISTVS Conference, Vol. 1, pp. 190–207, Vienna.

Ruff, K. (1997) '*Fahrzeugbewegung im gelände mit dem simulationssystem ORIS*'. Dissertation, Universität der Bundeswehr Hamburg, Institut für Kraftfahrwesen und Kolbenmaschinen, Hamburg, (in Germany).

SAE J670e (1976) 'Vehicle dynamic terminology', SAE International, PA, USA.

Schmid, I. C. and Ludewig, J. (1991) 'Improved calculation of sinkage of a wheel on soft ground', 5th European Conference of the ISTVS, Budapest.

Schmid, I. C. (1995) 'Interaction of vehicle terrain results from 10 years research at IKK', *Journal of Terramechanics*, Vol. 32, No. 1, pp. 3-26.

Schwanghart, H. (1968) 'Lateral forces on steered tyres in loose soil', *Journal of Terramechanics*, Vol. 5 No. 1, pp. 9-29.

Shih, S. and Bowerman, W. (2002) 'An evaluation of torque bias and efficiency of Torsen differential', SAE Technical Paper Series No. 2002-01-1046.

Somayaji, L. (1993) 'Simulating drivetrain performance of off-highway dump trucks', SAE Technical Paper Series No. 932416.

Stone, R. and Ball, J. K. (2004) '*Automotive engineering fundamentals*', Society of Automotive Engineers, Warrendale, PA, USA, ISBN 0768009871.

Subramanyam, V., Monkaba, V. and Alexander, T. (2000) 'A unique approach to all-wheel drive vehicle dynamics model simulation and correlation', SAE Technical Paper Series No. 2000- 01-3526.

Sullivan, P. M. (1999) 'Impact of weather data accuracy on NRMII vehicle performance predictions', Proceeding of the 13th ISTVS International Conference, Vol. 1, pp. 55-62.

Takemura, T. and Niikura, Y. (1990) 'An analysis of viscous coupling torque transmission characteristics and hump phenomenon', SAE Technical Paper Series No. 900558, pp. 767-776.

Tani, M., Yuasa, H. and Isoda, K. (1987) 'Controllability and stability of various types of four wheel drive cars', SAE Technical Paper Series No. 870542.

Taureg, H. and Herrmann, G. (1988) 'Application of viscous couplings for traction control in passenger cars', *Proceedings of the Institution of Mechanical Engineering*, No. C377/88, pp. 151-161.

Taureg, H. and Horst, J. (1990) 'Induced torque amplification in viscous couplings', SAE Technical Paper Series No. 900557, pp. 758-766.

Taylor, J. H. and Burte, E. C. (1987) 'Total axle load effect on soil compaction', *Journal of Terramechanics*, Vol. 24, No. 3, pp. 179-186.

The MathWorks Inc. (2004-2006) '*SimDriveline for use with Simulink user's guide version 1*', <http://www.mathworks.com>, viewed 15 April 2007.

Tung, S. C. Y. and Linden, J. L. (1985) 'Modelling torque converter clutch viscous damper performance', SAE Technical Paper Series No. 850459, pp. 3.469-3.483.

Vantsevich, V. V. (1997) 'Actuating vehicle systems and unified limited slip differentials', SAE Technical Paper Series No. 9727751, pp.1-8.

Vijayakumar S. and Chandran R. S. (2002) 'Analysis of a 4-DOF vehicle model using Bond Graph and Lagrangian technique', SAE Paper No. 2002-01-0809.

Wakamatsu, M., Yoshida, K., Kojima, Y., Murata, O. and Mori, H. (1992) 'Flow analysis of viscous coupling', *Proceedings of the Institution of Mechanical Engineering*, No. C389/221, pp. 135-142.

Wallén, J. (2004) '*Modelling of components for conventional car and hybrid electric vehicle in Modelica*' MSc. Thesis, Department of Electrical Engineering, Linköpings Universitet, LINKÖPING, Sweden.

Wehrwein, D. and Mourelatos, Z. P. (2005) 'Modeling and optimization of vehicle drivetrain dynamic performance considering uncertainty', SAE Technical Paper Series No. 2005-01-2371.

WES (1973) 'The AMC Mobility Model', U.S. Army Tank Automotive Command (ATAC), Warren, Michigan, USA.

Williams, R. C., Socin, R. J. and Varma, S. K. (1995) 'A building block approach for understanding four wheel drive systems: past-present-future', SAE Technical Paper Series No. 952643, pp. 21-42.

Wong, J. Y. and Reece, A. R. (1966) 'Soil failure beneath rigid wheels', Proceedings of the 2nd Conference of the International Society for Terrain-Vehicle Systems, pp. 425-445, University of Toronto Press.

Wong, J. Y. and Reece, A. R. (1967a) 'Prediction of rigid wheel performance based on the analysis of soil-wheel stresses - Part I, Performance of driven rigid wheels', *Journal of Terramechanics*, Vol. 4, No. 1, pp. 81-98.

Wong, J. Y. and Reece, A. R. (1967b) 'Prediction of rigid wheel performance based on the analysis of soil-wheel stresses - Part II, Performance of towed rigid wheels', *Journal of Terramechanics*, Vol. 4, No. 2, pp. 7-25.

Wong, J. Y. (1970) 'Optimization of the tractive performance of four wheel-drive off-road vehicles', SAE Technical Paper Series No. 700723, Vol. 79, pp. 2238-2245.

Wong, J. Y. and Preston-Thomas, J. (1983) 'On the characterization of the shear stress-displacement relationship of terrain', *Journal of Terramechanics*, Vol. 19, No. 4, pp. 255-234.

Wong, J. Y. and Preston-Thomas, J. (1986) 'Development of vehicle performance predicating software', Unpublished report of Vehicle Systems Development Corporation, prepared for the National Research Council of Canada.

Wong, J. Y. (1989) '*Terramechanics and off-road vehicles*', Elsevier Science Publishers, Amsterdam, The Netherlands, ISBN 0-444-88301-0.

Wong, J. Y. (1995) 'Application of the computer simulation model NTVPM-86 to the development of a new version of the infantry fighting vehicle ASCOD', *Journal of Terramechanics*, Vol.32, No. 1, pp. 53-61.

Wong, J. Y. (1998a) 'Optimization of design parameters of rigid-link track systems using an advanced computer aided method', *Proceedings of the Institution of Mechanical Engineers*, Vol. 212, Part D: J. Automobile Engineering, pp. 153-176.

Wong, J. Y., McLaughlin, J. N. B., Knezevic, Z. and Burt, S. (1998b) 'Optimization of the tractive performance of four-wheel-drive tractors: Theoretical analysis and experimental substantiation', *Proceeding Institution of Mechanical Engineers*, Part D, Journal of Automobile Engineering, Vol. 212, No. D4.

Wong, J. Y., Zhao, Z., McLaughlin, J. N. B. and Burt, S. (2000) 'Optimization of the performance of four-wheel-drive tractors: correlation between analytical prediction and experimental data', SAE Technical Paper Series No. 2000-01-2596.

Wong, J. Y. (2001) '*Theory of ground vehicles*', 3rd ed., John Wiley, New York.

Wong, J. Y. and Huang, Wei (2006a) 'Wheels vs. track – A fundamental evaluation from the traction perspective', *Journal of Terramechanics*, Vol. 43, pp. 27-42.

Wong, J. Y. and Huang, Wei (2006b) 'An investigation into the effects of initial track tension on soft ground mobility of tracked vehicles using an advanced computer simulation model', *Proceedings of the Institution of Mechanical Engineers*, Vol. 220 Part D: J. Automobile Engineering, pp. 695-711.

Wu, Yeun-Chung (2000) '*Handling of multi-axle, all-wheel-drive off-road vehicles*', PhD thesis, Mechanical and Aerospace Engineering, Carleton University, Ottawa, Ontario, Canada.

Yong, R. N., Fattah, E. A. and Boosinsuk, P. (1978) 'Analysis and prediction of tyre-soil interaction and performance using finite element', *Journal of Terramechanics*, Vol. 15, No. 1, pp. 43-63.

Appendix A: Numerical Simulation Parameters

A.1 Vehicle Parameters

A.1.1 General Description:

Model		<u>1996 Land Rover Defender 110</u> (Station Wagon-Top, 5+4 seats, 5 doors)
Unladen weight	[Kg]	1923
Gross vehicle weight	[Kg]	2950
Towing capabilities	[Kg]	– 750 (Un-braked) – 3500 (Overrun) – 4000 (Coupled)
Ground clearance	[mm]	215
Angle of approach	[°]	50
Angle of departure	[°]	35
Minimum turning radius	[m]	6.4
Maximum speed	[Km/hr]	145

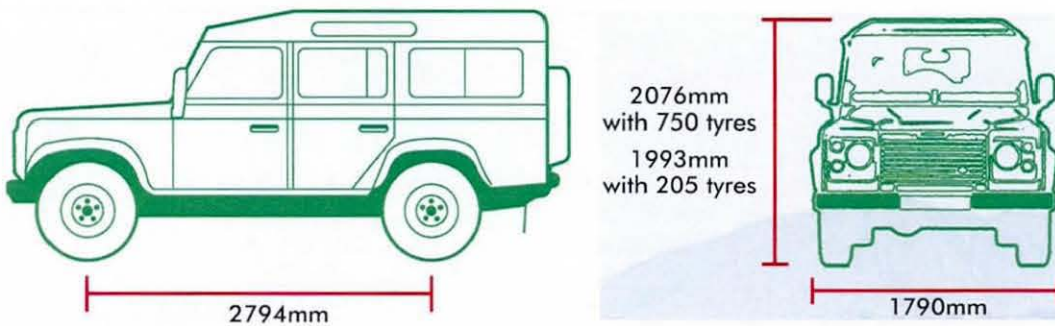


Figure A.1 Basic Dimensions of the Reference Vehicle

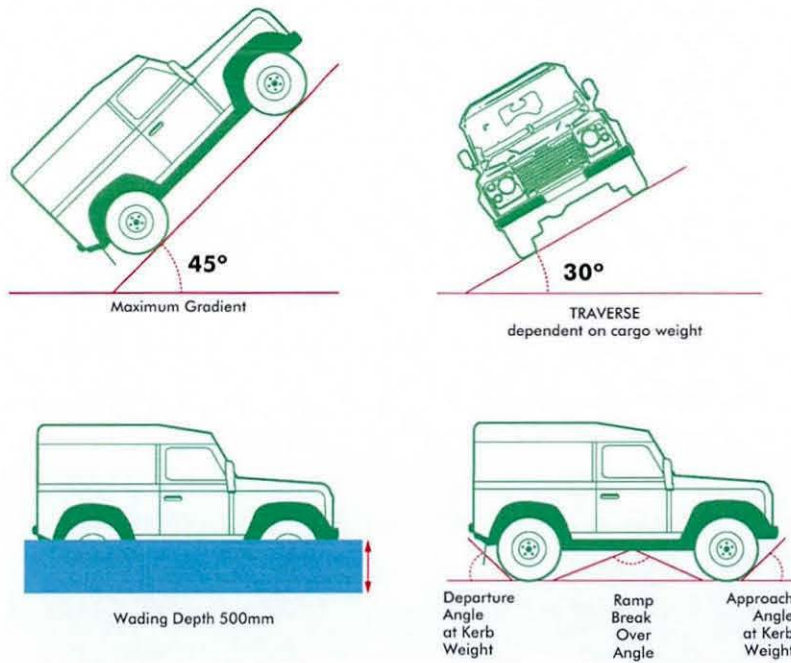


Figure A.2 Performance Limitations of the Reference Vehicle

A.1.2 Dimensions

Track front/rear (t_{ff}, t_{rr})	[mm]	1486
Interior width	[mm]	1430
Interior height	[mm]	1175
Width between wheel boxes	[mm]	925
Tailgate aperture width	[mm]	864
Largest box length	[mm]	1100/1470
Largest box width	[mm]	660
Largest box height	[mm]	1050
Width	[mm]	1790
Height with 205 tyres	[mm]	1993
Height with 750/235 tyres	[mm]	2076
Overall length	[mm]	4599
Wheelbase (L)	[mm]	2794

A.1.3 Sprung Mass

Sprung mass (m_s)	[Kg]	2,709.9
Roll moment of inertia (I_{xx})	[Kg · m ²]	1170
Pitch moment of inertia (I_{yy})	[Kg · m ²]	4511
Yaw moment of inertia (I_{zz})	[Kg · m ²]	4803
Product moment of inertia (I_{xy})	[Kg · m ²]	-6.519
Product moment of inertia (I_{xz})	[Kg · m ²]	45.04
Product moment of inertia (I_{yz})	[Kg · m ²]	-1.106
Sprung mass C.G. height (h_G)	[m]	0.98277
Sprung mass initial yaw angle (ψ)	[°]	0.00
Sprung mass initial pitch angle (θ)	[°]	1.1115
Sprung mass initial roll angle (ϕ)	[°]	0.00

A.1.4 Unsprung Mass

Front unsprung mass (m_{w_f})	[Kg]	218.82
Front unsprung mass C.G. height	[mm]	371.67
Front roll centre height	[mm]	394.42
Rear unsprung mass (m_{w_r})	[Kg]	211.25
Rear unsprung mass C.G. height	[mm]	375.88
Rear roll centre height	[mm]	372.53

A.1.5 Axle Weight Distribution

Front axle	[Kg]	1200
Rear axle	[Kg]	1750
Front axle at kerb	[Kg]	1026
Rear axle at kerb	[Kg]	1029

A.1.6 Suspension System

Front	<p>Model: <u>NRC9448</u> – Damper model: <u>RNB104320</u>.</p> <p>Live beam axle – dual rate coil springs – telescopic hydraulic dampers. Panhard rod – Heavy Duty Suspension – Load capacity: 585.00 Lb – Spring rate: 39431 – N/m Free length: 388.62 mm – No. of coils: 8 turns.</p>
Rear	<p>Model: <u>NRC6389</u> – Damper model: <u>ANR3538</u>.</p> <p>3050kg live beam axle – multi-rate coil springs – telescopic hydraulic dampers – "A" frame – Spring: Heavy Duty – Load capacity: 643.97 Lb – Spring rate: 57816 N/m – Free length: 407.00 mm – No. of coils: 8 turns.</p>

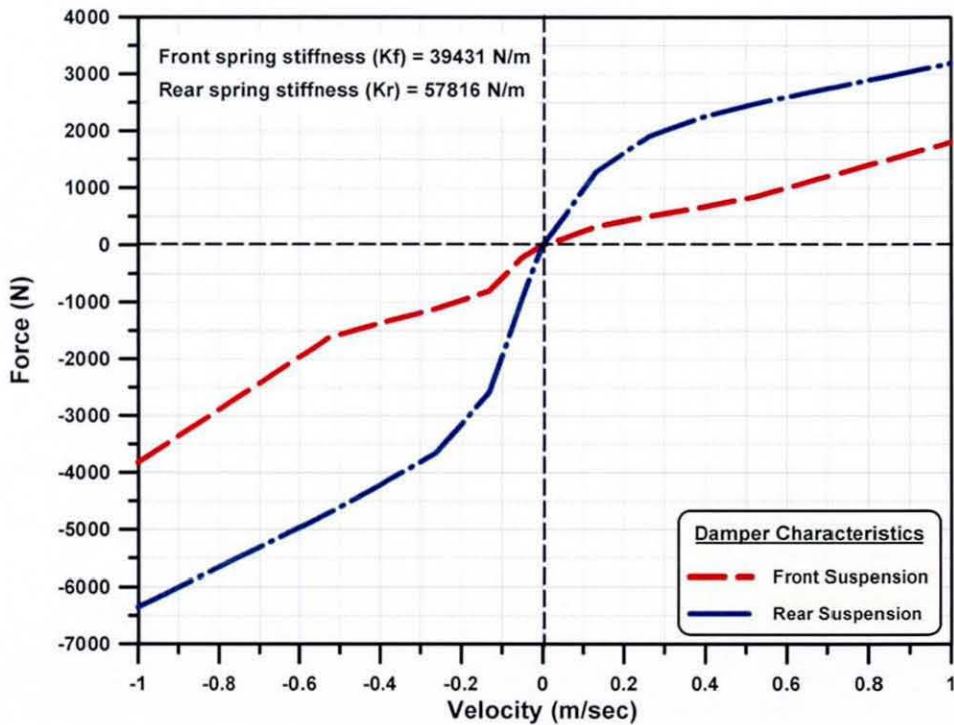


Figure A.3 Suspension System Characteristics

A.1.7 Wheel and Tyre

Description	Symbol	Units	Data
Tyre free (unloaded) radius	r_o	[<i>cm</i>]	38
Tyre width (manufacture)	b	[<i>cm</i>]	25.8
Contact area average width		[<i>cm</i>]	24.8
Moment of Inertia	I_w	[<i>kg · m²</i>]	1.0
Profile factor	-----	-----	0.85
Profile depth	-----	[<i>cm</i>]	1.0
Grip, coefficient of friction	-----	-----	0.9
Maximum pressure	p_i	[<i>bar</i>]	4.0

Tyre Characteristics

a1	a_1	-----	10
a2	a_2	-----	40
b1	b_1	-----	250
b2	b_2	-----	3000
b3	b_3	-----	0.23
Tyre vertical damping	[<i>N · s / m</i>]	-----	50
Dynamic radius	r_d	[<i>cm</i>]	37.9

Rill Approach Parameters

Nominal wheel load	F_z	[<i>N</i>]	6000
Lambda (F_z)	λ_N	-----	1.0
Lambda ($2 \cdot F_z$)	λ_{2N}	-----	1.0

	Front	Rear
Wheel	Standard steel	Standard steel
Tyre	205R16	205R16
Inflation Pressure	1.9 [<i>bar</i>]	3.3 [<i>bar</i>]

A.1.8 Engine

Model		TD5 Diesel 2.5 [Litre]
Type		Inter-Cooled Direct Injection
Max Power (DIN Net)	[KW]	101 @ 4,200 [rpm]
Max Torque	[N·m]	300 @ 1950 [rpm]
Number of Cylinders		5
Compression Ratio		19.5:1
Cylinder Bore	[mm]	84.5
Stroke	[mm]	89.0
Cubic Capacity	[cm ³]	2495



Figure A.4 Engine Torque-Speed Characteristics

A.1.9 Drivetrain System

- The drivetrain system can be described as a full-time 4WD system including lockable centre differential and transfer case model LT230. This arrangement allows both the front and rear transfer-case output shafts to rotate at different driving speeds. In addition, it permits the 4WD system to be used at low-range of speed without transmission wind-up. The transfer case has two gear positions; high (1.411:1) and low (3.320:1)
- A differential lock engages the shafts together when wheel slip is a problem; in fact it locks the front shaft to the differential carrier. This differential-lock does not act on the axle differentials. Later a viscous coupling in place of the centre differential lock is used.
- If the differential-lock is engaged on good roads it will cause sever transmission/tyre wear. If the differential-lock is not engaged (early enough) on loose surfaces it may allow the centre differential (which is small and rotates 3.5 times more rapidly than the road wheels) to overheat and eventually fail. This explains the importance of later incorporation of viscous coupling which not only improves vehicle performance but also adds strength and durability.
- The transfer case uses the standard arrangement of input shaft (from the gearbox), intermediate shaft and output shafts, the latter embody the centre differential. Later a ‘silent chain’ or ‘Morse chain’ to carry the drive from the input shaft directly to the output shaft. A viscous coupling replaces the centre differential lock. The high/low range selection is done by epicyclic gears at the end of the gearbox output-shaft/transfer case input shaft, where a PTO would normally fit.
- A manual 5-speeds gear box of model (R380) is incorporated:

First	3.321:1
Second	2.132:1
Third	1.397:1
Fourth	Direct (1:1)
Fifth	0.77:1

- Both the front and rear differentials of model (FTC2750) are used with gear reduction (3.54:1).
- Rotational moment of inertia about it's axis of rotation $[kg \cdot m^2]$:

Engine and flywheel	0.1		
Gear Box	0.0897		
Axle from GB to central Dif.	0.001	Central differential	0.1957
Front propeller shaft	0.002320	Front differential	0.0845
Rear propeller shaft	0.001304	Rear differential	0.0845
Front axle	Left: 0.001	Right: 0.001	
Rear axle	Left: 0.001	Right: 0.001	
Wheel and tyre	1.0		

- Shafts/axles elasticity properties:

	Stiffness $\left[\frac{N \cdot m}{rad} \right]$	Damping $\left[\frac{N \cdot m \cdot s}{rad} \right]$	Initial Offset $[rad]$	Backlash $[rad]$
Axle from GB to central Dif.	1200	1	0	0
Front propeller shaft	1000	10	0	0
Rear propeller shaft	1000	10	0	0
Front left axle	7200	50	0	0
Front right axle	7200	50	0	0
Rear left axle	7200	50	0	0
Rear right axle	7200	50	0	0

Stiffness: The spring constant or rate for the restoring torque imposed by the spring.

Damping: The damping constant of the kinetic frictional torque imposed by the spring

Initial Offset: The initial angular offset of the relative displacement.

Backlash: The angular free playback allowed in the torsional spring.

A.2 Visco-Lock Devices

Parameter	Symbol	Unit	VC	LSD I	LSD II
-----------	--------	------	----	-------	--------

1- Inner Plate Parameters:

Inner plate thickness	t_i	[m]	0.0005588	0.0005588	0.00040
Inner plate outer radius	r_2	[m]	0.058530	0.058530	0.03980
Inner plate slot inner radius	r_3	[m]	0.045470	0.045470	0.02750
Inner plate slot width	d_i	[m]	0.002790	0.002790	0.00216
Inner plate tap angle	$2 \cdot \psi$	[°]	15.00	15.00	15.00
Inner plate edge height	t_{edge}	[m]	0.000033	0.000033	0.000033
Inner plate number of tabs	N_{Tabs}	---	24	24	24
Inner plate mass	m_{Inner}	[Kg]	0.02758	0.02758	0.0085
Coefficient of Coulomb friction	η	---	0.1	0.1	0.1
Number of inner plates	N_{Inner}	---	27	10	13

2- Outer Plate Parameters:

Outer plate thickness	t_o	[m]	0.0005588	0.0005588	0.00040
Outer plate inner radius	r_1	[m]	0.035584	0.035584	0.02725
Outer plate perforated holes diameter	d_o	[m]	0.007400	0.007400	0.00740
Number of perforated holes	N_{holes}	---	18	18	18
Outer plate mass	m_{Outer}	[Kg]	0.02669	0.02669	0.0106
Number of outer plates	N_{Outer}	---	28	11	14

3- Spacers Parameters:

Spacer thickness	t_{spacer}	[m]	0.0009398	0.0009398	0.0007
Spacer mass	m_{Spacer}	[Kg]	0.00235	0.00235	0.0005
Number of spacers	N_{Spacer}	---	26	9	13

4- Fluid Rheology (Silicone Parameters)

Nominal kinematic viscosity	ν_o	$\left[\frac{m^2}{s}\right]$	0.03	0.1	0.08
Critical shear rate (in viscosity model)	γ_B	$[s^{-1}]$	100	100	80
Slope of viscosity-shear rate curve	m	---	0.3586	-0.4716	-0.85

Parameter	Symbol	Unit	VC	LSD I	LSD II
Density (at temperature = 25°C)	ρ_F	$\left[\frac{Kg}{m^3}\right]$	976.00	976.00	976.00
Empirical constant (log-log equation)	A_{theta}	---	1.84	1.40	1.37
Coefficient of thermal expansion	β_F	$[K^{-1}]$	0.00096	96E-05	0.00096
Bulk modulus	K_F	$[Pa]$	6.25E+08	6.25E+08	6.25E+08
Thermal conductivity	k_F	$\left[\frac{W}{m \cdot K}\right]$	0.145	0.174	0.145
Specific heat	c_F	$\left[\frac{J}{Kg \cdot K}\right]$	1444	1444	1444
Total mass of silicone fluid	m_F	$[Kg]$	0.1195	0.0278	0.0163

5- Housing Parameters:

Housing length	$L_{housing}$	$[m]$	0.06441	0.036605	0.033
Housing outer diameter	D_{o_hous}	$[m]$	0.1397	0.1397	0.10224
Housing inner diameter	D_{in_hous}	$[m]$	0.1245	0.1245	0.05450
Thickness of end wall	t_{end_wall}	$[m]$	0.011	0.011	0.011
Effective area factor of plates	K_p	---	0.73	0.73	0.85
Hub outer diameter	D_{o_hub}	$[m]$	0.068	0.068	0.0325
Hub inner diameter	D_{in_hub}	$[m]$	0.0410	0.0410	0.0112
Percentage of fluid filling ratio	C_F	$[\%]$	0.86	0.86	0.85
Mass of housing and hub	$m_{hsg+hub}$	$[Kg]$	4.4690	2.9069	2.0532
Conduction coefficient	h_{C_S}	$\left[\frac{W}{m^2 \cdot K}\right]$	400.0	400.0	400.0
Convection coefficient	h_{S_A}	$\left[\frac{W}{m^2 \cdot K}\right]$	10.0	10.0	10.0
Steel Density	ρ_s	$\left[\frac{Kg}{m^3}\right]$	7832	7832	7832
Steel Modulus of Rigidity	G_S	(Pa)	1.0E+011	1.0E+011	1.0E+011
Steel Thermal conductivity	k_S	$\left[\frac{W}{m \cdot K}\right]$	63.9	63.9	63.9
Steel Specific heat	c_S	$\left[\frac{J}{Kg \cdot K}\right]$	434.0	434.0	434.0
Coefficient line thermal expansion	α_S	$\left[\frac{m/m}{K}\right]$	16.2E-06	16.2E-06	16.2E-06
line contact to volume		---	3	3	3

VC stands for data of viscous coupling used in section 5.6.2 and section 6.3

LSD I stands for data of visco-lock limited slip differential used in section 6.3

LSD II stands for data of visco-lock limited slip differential used in section 5.6.1

Silicone Fluid Rheology Parameters used in Section 6.3.3 (tuning procedures)

			Fluid (A)	Fluid (B)	Fluid (C)	Fluid (D)
Nominal kinematic viscosity	ν_o	$\left[\frac{m^2}{s}\right]$	1.00	0.10	0.01	0.001
Critical shear rate	γ_B	$[s^{-1}]$	15	100	2000	10 000
Slope of viscosity-shear rate curve	m	---	-0.5622	-0.4716	-0.412	-0.39
Density at room temperature	ρ_F	$\left[\frac{Kg}{m^3}\right]$	976	976	976	976
Empirical constant	A_{theta}	---	0.92	1.4	2.5	Table
Coefficient of thermal expansion	β_F	$[K^{-1}]$	0.00099	0.00099	0.00099	0.00099
Bulk modulus	K_F	$[Pa]$	6.25E08	6.25E08	6.25E08	6.25E08
Thermal conductivity coefficient	k_F	$\left[\frac{W}{m \cdot K}\right]$	0.174	0.174	0.174	0.174
Specific heat coefficient	c_F	$\left[\frac{J}{Kg \cdot K^\circ}\right]$	1444	1444	1444	1444

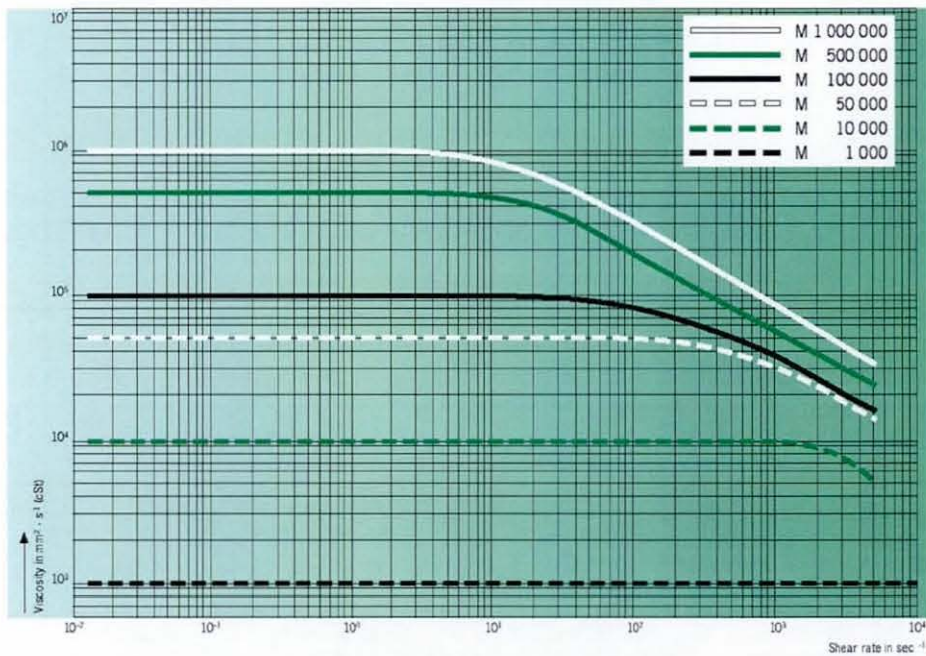


Figure A.5 Silicone Fluid Shear Properties at 25 °C (after Payer, 2006)

A.3 Soil Mechanical Properties

Parameters	Symbol	Unit	Clay	Loam	Sand
Density of the soil	ρ	$\left[\frac{g}{m^3}\right]$	2.0	2.0	1.9
Cohesive module of deformation	K_C	$\left[\frac{N}{cm^{n+1}}\right]$	35	18	20
Frictional module of deformation	K_ϕ	$\left[\frac{N}{cm^{n+2}}\right]$	30	6.0	23
Exponent of sinkage	n	-----	0.18	0.50	0.55
Cohesion	C	$\left[\frac{N}{cm^2}\right]$	3.5	2.5	1.0
Angle of friction	ϕ	$[\circ]$	18	25	28
Slip coefficient	K	-----	2.5	2.5	2.5
Stiffness coefficient	C_B	$\left[\frac{N}{cm^3}\right]$	7600	70	560
Damping coefficient	b	$\left[\frac{N \cdot s}{m}\right]$	4000	4000	10000
Slippery coefficient	-----	-----	0.2	0.3	0.8
Compaction capability	-----	-----	1.0	0.9	0.4
Rolling resistance correction	-----	-----	0.078	0.144	0.230
Shearing offset	-----	$[cm]$	0.0	0.5	5.0

Appendix B: Measuring Instruments Specifications

B.1 The AR1000 Rheometer

Supply Voltage	230V AC 5 amps 120V AC 10 amps
Frequency	50 to 60 Hz
Power	800 V AC
Torque Range	0.1 μ N·m to 100 m N·m
Shear Stress Range (Geometry Dependent)	0.0008 to 508000 Pa
Frequency Range	0.1 mHz to 100Hz
Angular Velocity Range	Controlled stress: 10^{-8} to 100 rad·s Controlled strain: 10^{-2} to 100 rad·s
Angular Displacement Resolution	0.62 μ ·rad·s
Shear Rate Range (Geometry, material and technique dependent.)	10^{-6} to 11,000 s^{-1}
Minimum strain	Range: 0.00006
Normal force	1g to 5000g
Peltier system range (Ramp rate)	-10 °C to 99 °C (20 °C min)
Internal resolution of Pt100	0.016 °C

B.2 Non-Contact Rotary Torque Transducer

Model	Size 2 / M420 Torque Transducer (0 – 500Nm)	
Torque Rating	0 - 500Nm	
Operating Speed	100 rpm	
Data Output	Digital Output RS232	
Optional Output	Analogue Output 4-20mA / 0 – 10VDC – Type 686 Analogue Output Module Required	
Accuracy	0.1% Full Scale	
Sampling Rate	10 - 100 samples per second	
Operating Temperature	-10°C to +70°C	
IP Rating	IP54	
Cable Length	4 metres	
Supply Voltage	12V (15V if supplied Type 686 module)	
Compatible with	Type 370 Torque, Speed & Power Indicator, Type 300 Digital Torque Indicators and TorqueLog Software.	
Delivery	Standard delivery is 4 – 6 weeks from receipt of order	
Shaft Dimensions	Overall Length	240mm
	Shaft Diameter	25mm (150–450Nm) 30mm (400–750Nm)
	Body Diameter	75mm
	Body Length	85mm 150mm

Calibration Record

Torque lbft	Torque Nm	CW mV/V	CCW mV/V	CW Error % FSD	CCW Error % FSD
0	0.0	0.000	0.000	0.00	0.00
75	101.7	0.364	-0.360	0.32	-0.12
150	203.4	0.728	-0.724	0.64	-0.02
225	305.1	1.075	-1.085	-0.01	-0.09
300	406.7	1.433	-1.450	-0.03	0.07
375	508.425	1.792	-1.811	0.00	0.00

Calibration Figure: **1.762**

B.3 The Microprocessor Thermometers

Model	Comark (6201)
Output	Analogue signal
Response	0.5 second to full accuracy
Reading rate	4 per second
Range	0.0001 to 9.9999
Accuracy	$\pm 0.05\%$ of setting
Analogue output	1 Volt out = 100 °C or 1 mV
Resolution	$\pm 0.1\%$ of F.S. (1 volt)
Temp. coefficient	$\pm 0.05\%$ per 1 °C
Thermocouple	K Type Nickel-Chromium / Nickel-Aluminium

B.4 The Data Acquisition (USB-6008/6009)

Converter typeSuccessive approximation
 Analog inputs.....8 single-ended, 4 differential,

software selectable

Input resolution

USB-600812 bits differential,

11 bits single-ended

USB-600914 bits differential,

13 bits single-ended

Max sampling rate

Single channel

USB-6008.....10 kS/s

USB-6009.....48 kS/s

Multiple channels (aggregate)

USB-6008.....10 kS/s

USB-6009.....42 kS/s

AI FIFO512 bytes

Timing resolution41.67 ns (24 MHz timebase)

Timing accuracy100 ppm of actual sample rate

Input range

Single-ended..... ± 10 V

Differential ± 20 V, ± 10 V, ± 5 V, ± 4 V, ± 2.5 V, ± 2 V, ± 1.25 V, ± 1 V

Working voltage ± 10 V

Input impedance144 k Ω

Overvoltage protection ± 35

B.5 The Rotational Vibrometer

Sensor Head: OFV-400 (Polytec)	
Operating distance	400 mm \pm 50 mm (200 or 600 mm optional)
Beam separation	8 mm (standard)
Laser class	II (less than 1 mW per exiting beam)
Wavelength	633 nm
Environmental Temp.	+5 °C...+40 °C
Controller: OFV-4000 (Polytec)	
Main supply	100/115/230 V
Power consumption	Max. 150 VA
Interface	RS-232 (8 data bits, baud rate 4800)
Speed Measurement (rpm)	
Measurement range	-7000 rpm...+11 000 rpm
Display range	-7000 rpm...+9 999 rpm
Slope	1 mV/rpm
Analog output	+/- 12 V, $R_j=100 \Omega$, BNC min. load impedance 10 K Ω
Calibration error	< +/- 1% \pm 5 rpm at 25 °C \pm 5 degrees
Linearity error	< 0.5%
Limit frequency	1 Hz (slow) / 2500 (fast)
Vibrational velocity	Range: 100, 1000, 10 000, 60 000 °/s full scale value
Vibrational angle	Range: 0.1° / : 1.0° /: 10° full scale value

Appendix C: Publications

C.1 Publications Related to MSc Point of Research:

- [1] **Sharaf, A. M.**, Hossamel-deen, Y. H., El-Haddad, M. A. and Moussa, M. M. (1999) 'Evaluation of the dynamic performance of heavy articulated vehicles (case study)', *Proceedings of the 8th ASAT conference*, Military Technical College, Cairo, Egypt, 4-6 May, pp. 419-439.
- [2] **Sharaf, A. M.**, Hossamel-deen, Y. H. and El-Haddad, M. A. (2000) 'Minimizing input data cost of UMTRI Yaw/Roll Model', *Proceedings of the 9th AMME conference*, Military Technical College, Cairo, Egypt, 16-18 May, pp. 693-718
- [3] **Sharaf, A. M.**, Hossamel-deen, Y. H. and El-Haddad, M. A. (2001) 'Effect of payload parameters on the dynamic performance of heavy vehicles', *Proceedings of the 9th ASAT conference*, Military Technical College, Cairo, Egypt, 8-10 May, pp. 1033-1050

C.2 Publications Related to PhD Point of Research:

- [1] **Sharaf, A. M.**, Mavros, G., Rahnejat, H. and King, P. D. (2006) 'Multi-physics modelling approach in all terrain vehicle longitudinal dynamics', paper IMECE2006-13578, *Proceedings of IMECE06*, ASME International Mechanical Engineering Congress and Exposition, Chicago, Illinois, USA.
- [2] **Sharaf, A. M.**, Mavros, G., Rahnejat, H., King, P. D. and Mohan, S. K. (2007a) 'Direction control and stability of AWD off-road vehicles fitted with visco-lock devices', poster paper, 20th International Symposium: Dynamics of Vehicles on Roads and Tracks, Berkeley, California, USA.
- [3] **Sharaf, A. M.**, Rahnejat, H. and King, P.D. (2007b) 'Analysis of handling characteristics of all-wheel drive off-road vehicles', *International Journal of Heavy Vehicle Systems*, (Accepted for publication)
- [4] **Sharaf, A. M.**, Mavros, G., Rahnejat, H., King, P. D. and Mohan, S. K. (2008) 'Optimization of AWD off-Road vehicles performance using visco-lock devices', *International Journal of Heavy Vehicle Systems*, Special issue on 'The Performance and Dynamics of Diversified Land Vehicle Systems', (Accepted for publication)

